Three Dimensional Characterization and Multi-scale Modelling of Deformation in Biomaterials



Liye Yan

Linacre College

University of Oxford

A thesis submitted for the degree of

Doctor of Philosophy

Hilary Term, 2019

Abstract

Three Dimensional Characterization and Multi-scale Modelling of Deformation in Biomaterials

Liye Yan

Linacre College, Oxford

A thesis submitted for the degree of Doctor of Philosophy

Hilary Term, 2019

Mollusc shell and bone are two interesting materials with complicated morphological geometries and hierarchical microstructures, which present a good combination of stiffness, strength and toughness and therefore attract interests of researchers from engineering and clinic fields.

In this work, in-situ mechanical tests during X-ray tomography have been done on common British limpet and bones (cortical bone and trabecular bone), which provide geometric and microstructural information for modelling. The 3-D displacement fields within deformed biomaterials have been extracted by digital volume correlation (DVC), which provides either boundary conditions for modelling or experimental comparison for simulated results. Different modelling approaches have been employed in order to provide a comprehensive understanding of mechanical properties of biomaterials.

A value for the elastic modulus of the mollusc shell, which is consistent with literature, has been obtained using a finite element (FE) model with simple boundary conditions (experimental load) which incorporates the morphological information of limpet. Additional information of possible fracture sites within limpet have also been successfully predicted from the model, and the strain field within the deformed shell has been calculated using FE model with the 3D full displacement field from DVC analysis as boundary conditions. FE models of indentation tests on cortical bone have also been built which provide insight into the mechanical behavior of bone under indentation loading. A cellular model, PReMISe, which was designed for the prediction of elastic modulus of quasi-brittle and porous materials, has been employed in cortical bones. From this, the intrinsic elastic moduli of cortical bone have been obtained, with a good agreement with literature measurements by nanoindentation. To characterize the fracture resistance of trabecular bone, which has a very complex porous microstructure, in situ tomographs of a pre-notched test specimen were analysed to extract the averaged displacement fields from DVC to allow J integral calculation using the JMAN code. The obtained critical stress intensity factor (K) has a good agreement with literature.

Preface

The work presented in this doctoral thesis has been carried out at the Department of Materials, University of Oxford from August 2015 to January 2019, under the supervision of Prof. James Marrow. All of the research carried out for this thesis is original, and where the work of others has been included has been clearly referenced and acknowledged. No part of thesis has been submitted for a degree at this or any other university. Some of the work has been submitted and peer-reviewed in journals and presented at conferences as details below:

Journal Article:

Oliver R Boughton, Shaocheng Ma, Xiran Cai, **Liye Yan**, Laura Peralta, Pascal Laugier, **James Marrow**, Finn Giuliani, Ulrich Hansen, Richard Abel, Quentin Grimal, Justin P Cobb. *Computed tomography porosity and spherical indentation for determining cortical bone millimetre-scale mechanical properties*. Scientific Review. Decision Letter: SREP-19-04995A. Accepted on 23-04-2019.

Conference:

Liye Yan, Luis Saucedo Mora, O. R. Boughton, R.L. Abel, T.J. Marrow. Three Dimensional Characterization and Multi-scale Modelling of Damages in Nature Biomaterials. 14th International Conference of Fracture, Greece. Oral presentation.

Acknowledgements

This work was made possible by a generous financial support from my parents and enormous mental support from my husband. I hope my pursuit of work is justified on their merits.

The work present in this thesis was made possible through the great support from many people. First, I would like to thank my supervisor Prof. James Marrow for his outstanding support, great guidance and enormous passion through the project. James has been patient on teaching me to become a good researcher and provided me with priceless knowledge of science. James have also organized BBQ events for all group members and made me feel like in a family. Second, I would like to thank all my colleagues in Oxford who help me through the difficulties from study and life. I want to thank Dr. Luis Saucedo Mora, Dr. Yelena Vertyagina and Mathew Jordan who generously provided me technical and scientific supports in my research. I also want to thank Phil Earp and Dr. Selim Barhli who not only help me a lot in research but also bring me so much happiness and good memories in my life. Third, I want to thank my collaborator: Dr. Oliver Boughton. We spent such a wonderful research time together and went through a lot of hard time during experiments. I also want to thank Dr. Shaocheng Ma for helping me collect useful data of trabecular bone.

Apart from academic work, I want to thank all my friends that I met in Oxford. Their kindness makes my life in Oxford full of love and happiness.

At last, I want to thank again my loving husband Qifeng Yang. You are always there for me. I cannot finish this thesis without your help.

Contents

1 Introduction 1

1.1 Motivation 1

1.2 Scope of the project 2

2 Literature review 5

2.1 Mollusc Shells 6

2.1.1 Factors that influence mechanical behaviours of mollusc shells 6

2.1.2 Mechanical behaviours of mollusc shells 10

2.1.3 Biomimetic nacre-like materials 12

2.2 Bone 14

2.2.1 Cortical bone 15

2.2.2 Trabecular bone 23

2.2.3 Fracture toughness of bone 26

2.3 Mechanical testing techniques 32

2.3.1 Tension and Compression Testing 32

2.3.2 Bending or Flexural Loading 33

2.3.3 Indentation 34

2.3.4 Resonance ultrasound spectroscopy (RUS) 36

2.4 Three-dimensional characterisation of materials and deformation 38

2.4.1 X-ray computed tomography 38

2.4.2 Digital volume correlation 43

2.5 Modelling of biomaterials 47

2.5.1 Image-based finite element modelling 47

2.5.2 Reverse engineering modelling 61

2.5.3 Image-based modelling of the effect of porosity on elastic modulus 66

2.6 Summary 70

3 Experimental and analysis methods 73

3.1 Experimental methods 74

3.1.1 X-ray tomography of the microstructures of limpet and cortical bone 74

3.1.2 In-situ mechanical tests on biomaterials 88

3.2 Analysis method 116

3.2.1 DVC analysis of rigid body movements 116

3.2.2 DVC analysis of deformation 121

3.2.3 Porosity Characterisation 122

3.2.4 Premise: Simulation of elastic modulus from porosity 122

4 Image-based finite element modelling of biomaterials 124

4.1 Mollusc Shell 125

4.1.1 FE mesh generation 125

4.1.2 Contact compression modelling with simple boundary conditions 128

4.1.3 Finite element model with DVC boundary conditions 132

4.1.4 Comparisons of FE models with different boundary conditions 134

4.2 Bone 138

4.2.1 FE Mesh Generation 138

4.2.2 Finite element modelling of compression by indentation 139

4.3 Discussion of image-based models 152
4.3.1 Mollusc shell 152
4.3.2 Bone 154
5 Structural and elastic properties of cortical bones 156
5.1 Background 157
5.2 Porosity of cortical bone 158
5.2.1 The influence of patients' conditions on bone porosity 164
5.3 Elastic moduli of cortical bones 166
5.4 Extraction of bone properties using PReMISe 168
5.4.1 The combination factor E/E_0 168
5.4.2 The intrinsic elastic modulus, E_0 174
5.4.3 Bone anisotropy 179
5.5 Discussion 182
5.5.1 Porosity 182
5.5.2 PReMISe analysis of E/E_0 and E_0 184
6 Fracture toughness of trabecular bone 191
6.1 Background 192
6.2 Crack segmentation 195
6.2.1 Crack segmentation (watershed and manual methods) 195
6.2.2 Crack segmentation (DVC) 201
6.2.3 Crack segmentation (phase congruency) 206
6.2.4 Development of crack length with loading 209

6.3 Evaluation of the J integral for a propagating crack in trabecular bone 211
6.3.1 Pre-processing of DVC data from 3D to 2D 212
6.3.2 The identification of crack tip 220
6.3.3 The calculation of J integral 223
6.3.4 The relation between J integral and applied load 227
6.3.5 The stress intensity factor of trabecular bone 228
6.4 Discussion 229
7 Conclusion 234
8 Future work 237
9 Bibliography 239
10 Appendix 261
10.1 Further investigation of microstructures of limpets 261
10.2 Complementary information for Chapter 5 264
10.3 . Complementary information of Chapter 6 285
10.3.1 DVC results of trabecular bone under different loadings 285
10.3.2 Measurements of notch plus crack lengths 292
10.3.3 J integral calculation 298

Chapter 1

1 Introduction

1.1 Motivation

The study of biological system as structures has started since early 20th century. The engineering and material aspects of biomaterials have been shunned by biologists for decades until 1990s when biomaterials were included in the research of materials science and engineering due to their outstanding mechanical properties considering their relatively weak basic chemical compositions [1].

Benefiting from complicated morphological geometries and hierarchal microstructures, biomaterials present a good combination of stiffness, strength and toughness, which are still unmatched by their engineering counterparts. As a consequence, biomaterials' mechanical behaviours, especially their resistance to crack initiation and propagation under bending or compression, have been extensively studied for a wide range of applications in biological, medical and engineering fields. Furthermore, factors that influence these mechanical properties have also been studied to improve the design of new biomimetic materials. Conventionally, the mechanical properties of biomaterials such as critical strain, compressive strength, hardness and fracture toughness are measured by compressive and indentation tests. Besides these conventional mechanical techniques, tomography-volume-image-based digital correlation and finite element models are now available to complement the conventional techniques for further analysis of strain and stress fields within the specimens, with the aim of reducing the uncertainties of properties measured by conventional experiments.

In this thesis, a mollusc (British common limpet) and human bone (cortical bone and trabecular bone), which both belong to the class of quasi-brittle materials and possess excellent structural mechanical properties are chosen for investigation. A method combining X-ray tomography,

Digital Volume Correlation (DVC) and Image-based modelling techniques is employed. Compared with conventional mechanical testing, this approach facilitates the three-dimensional understanding of mechanical response of biomaterials under loading and offers a possible way to look into mechanical properties of materials with complicated geometries. Synchrotron and laboratory X-ray tomography instruments are the main tools for 3D imaging, which provide microstructural information for finite element (FE) modelling. Digital volume correlation (DVC) has been employed in order to measure the 3D distribution of displacement and strain fields in specimens during in-situ mechanical tests during tomography. This is used to investigate deformation and additionally it provides boundary conditions for FE modelling. Different modelling techniques apart from finite element modelling have been used for the prediction of mechanical properties of biomaterials (e.g. elastic modulus and fracture toughness). The objective of this thesis is concerned with the development of methods to measure the mechanical properties of biomaterials, in situ, using 3D imaging, with the displacements measured by image correlation and analysed by image-based finite element modelling as well as other modelling techniques. The knowledge acquired from models will contribute to the design of biomimetic engineering materials, which are stiff but damage tolerant, and biocompatible materials, which are used in clinical fields. In addition, image-based modelling techniques allow the incorporation of hierarchical structures of biomaterials into models, which will facilitate the investigation of structure-related issues on mechanical properties.

1.2 Scope of the project

The scope of this project can be categorized into two parts: 1) Optimization of 3D imaging for in-situ testing using X-ray tomography; 2) Development and modification of modelling techniques to extract mechanical responses of biomaterials based on 3D imaging.

Due to low material contrast in limpet shells, different X-ray tomography techniques (e.g. normal absorption scan and phase contrast scan) and instruments have been tried to achieve the

reasonable contrast level which is required for DVC analysis. Optimized scanning parameters have been discovered for reasonable accuracy for 3D displacement field extraction in deformed limpets. Bones have porous structures that are more favourable for X-ray tomography but there are significant issues of maintaining image quality when conducting in-situ indentation tests in hydrated condition due to the influence of the saline water on X-ray. Containers used for keeping bone moisturised were carefully designed to reduce the negative effect of solution. All the used cortical bone specimens in this project were obtained from patients undergoing hip replacement surgery, during which procedure the diseased ball portion of the joint was removed together with damaged cartilages and the new replacement of the ball part of the thighbone was inserted to the hip bone via a replacement socket part.

After obtaining 3D images with good quality, image-based FE models have been built with the incorporation of the 3D morphological information that can be resolved by X-ray tomography for both the limpet shell and cortical bones. For the limpet shell, the elastic modulus of the limpet specimen and 3D strain distributions within deformed shell have been predicted from FE model, informed by the measured boundary conditions, and these are compared with experimental results for validation. For cortical bones, due to their unpredictable and unstable mechanical behaviours during in-situ testing and big variations in reported mechanical properties in literature, the information gained can be used in FE modelling as input parameters and boundary conditions are constrained. Therefore only limited information has been extracted from FE modelling for cortical bones. Indentation testing was employed, inspired by potential interest in a micro-indentation device for use in patients undergoing hip replacement surgery, in which there was a need to measure mechanical properties in vivo. Detailed knowledge obtained of bone properties will help improve orthopaedic implant design, by closer matching the orthopaedic implant being inserted to the patient's own bone properties. Also, in order to obtain more mechanical information of bones from 3D imaging, existing modelling techniques which are designed for quasi-brittle materials have been used on bone, as it falls into the same

material category. Further mechanical property information such as intrinsic elastic moduli of cortical bones in different loading directions and fracture toughness of trabecular bone have been obtained. The simulation results have also been compared with existing experimental results in literature.

The experimental work in this thesis was carried out in a collaboration with Diamond Light Source and Imperial College, London. Christina Reinhard and Nghia Vo of the Diamond Light Source helped the author in in-situ testing of the limpet shell using Synchrotron X-rays. Dr. Oliver Boughton (Imperial College) prepared cortical bone samples for laboratory X-ray tomography imaging and provided experimental results of measured elastic moduli of cortical bones using Resonance Ultrasound Spectroscopy (RUS) and conventional compression tests. Dr. Shaocheng Ma (Imperial College) conducted three-point bending tests on trabecular bones at the Diamond Light Source and provided the author with reconstructed tomographs for further investigation. Mr. Koen Ever (Oxford University) conducted the Scanning Electron Microscopy imaging of limpets for further investigation of limpet microstructures.

Chapter 2

2 Literature review

In this chapter, current background literature on biomaterials as well as bio-mimetic engineering materials, conventional mechanical testing techniques on biomaterials, modelling related techniques and different relevant modelling techniques are presented.

The Biomaterials section summarises microstructures and mechanical properties of mollusc shells and bones together with nacre-like biomimetic engineering counterparts. Conventional mechanical techniques which are widely used on mollusc shells and bones are introduced including tension/compression, bending, indentation and resonance ultrasound spectroscopy (RUS). Three-dimensional characterisation techniques including X-ray tomography and Digital Volume Correlation (DVC) are described together with their applications on biomaterials. Finally, a review of the literature of modelling techniques available for biomaterials as well as for quasi-brittle materials which have potential applications on biomaterials including limpet and bone is presented.

Quasi-brittle biomaterials have been intensively studied by researchers, because of the intrinsically excellent mechanical properties originating from their hierarchical microstructures. Unlike brittle materials, which exhibit elastic linearity before catastrophic fracture, quasi-brittle materials show measurable deformation due to the extension or formation of micro-flaws prior to facture [2]. Mollusc shell and bone are two representative categories of quasi-brittle biomaterials due to micro-cracks occurring within their microstructures which result in certain degree of deformation prior to fracture and they have been widely investigated for several reasons: 1) the design of biomimetic engineering counterparts and 2) the fulfilment of specific clinically determined requirements.

2.1 Mollusc Shells

Mollusc shells are generally composed of calcite, aragonites, proteins and certain concentrations of iron, potassium, sodium and strontium. In general, the mineral phase provides stiffness while the organic phase provides toughness to mollusc shells [3]. Detailed compositions of mollusc shells differ among species [4] [5]. Mollusc shells show efficient adaption and excellent mechanical behaviors as they are prone to impacts brought by waves, currents, hard objects (e.g. logs and boulders) and predatory creatures. It is known that for mollusc shells, the greater threats in nature are brought by the wave-borne hard objects other than the wave itself because the compression strength required for shells to resist the natural wave with maximum speed is far below their intrinsic strength [6].

2.1.1 Factors that influence mechanical behaviours of mollusc shells

The morphology and morphometry of mollusc shells are factors that have been believed to contribute to their compression strength [7]. For example, it was found that the conic shape of limpets have higher compression strength compared with other mollusc shells with spherical or spiral shape (e.g. most gastropod shells) [8–10]. Conic limpets with increasing conicity (higher shell height to length ratio), a centered apex and increasing thickness [6] [11] were observed to have higher compression strength regardless of their various microstructures among different limpet species. However, Cabral and Jorge [6] proposed that the different resistance of mollusc shells to crushing, which was mainly determined by their deformability, was probably due to the differences in the internal compositions and structure among different species of mollusc shells, other than their morphology and morphometry.

The hierarchical microstructure of mollusc shells, as another important factor which contributes to their exquisite mechanical behaviour [12] have also been intensively studied [13] [14] [15]. As the second largest animal group [16], mollusc shells generally present layered microstructures.

Depending on species, microstructures of mollusc shells fall into several categories including columnar and sheet nacre, exfoliated, prismatic, cross-lamellar structures, etc [13] [14] [15].

Nacre, as an example of mollusc shells, consists of hard aragonite lamellas which are glued by soft organic interfaces (*Figure 2.1.1*). It possesses 3000 times the work of fracture of monolithic calcite crystal and the referred work of fracture is measured as the area under stress-strain curve until fracture [17]. Compared with nacre which has two-dimensional structure with in-plane isotropy, the cross-lamellar structure is another layered structure existing in mollusc shells (e.g. Strombus gigas, Gastropods including limpets, bivalve) with three-dimensional anisotropy which attracts much interest from researchers [18] [19]. In mollusc shells with cross-lamellar structure, sub-order lamellae are observed (*Figure 2.1.2*). It is reported that mollusc shells with cross-lamellar structure possess higher fracture resistance [20] than those with nacreous structure [21]. These microstructures give different morphological responses under loading including channel cracking, barb-like interlocking, deflection and arrest of cracks by interfaces between lamellae, micro-cracking, mineral bridging, fibre bridging, etc (*Figure 2.1.3*) to prevent propagations of cracks, which result in excellent mechanical properties of mollusc shells [12].

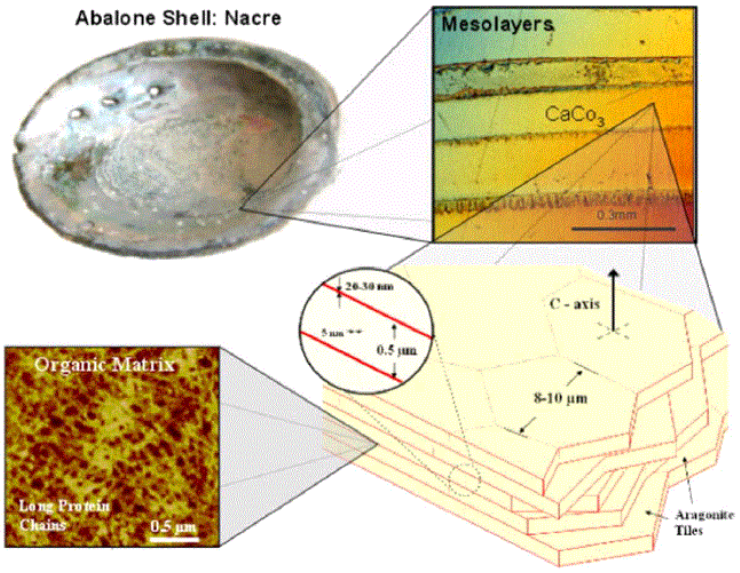
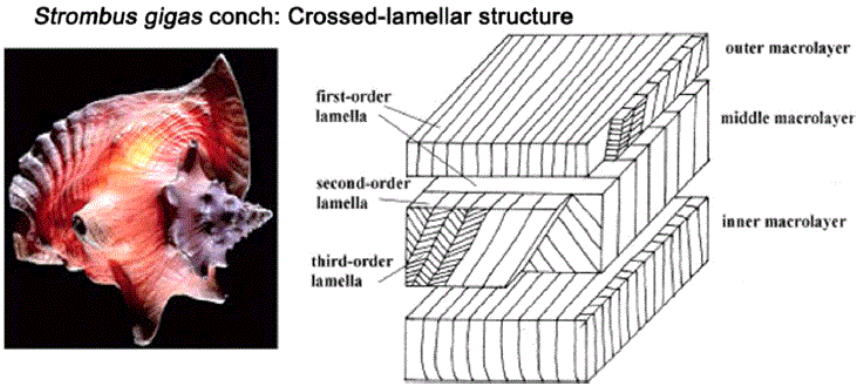
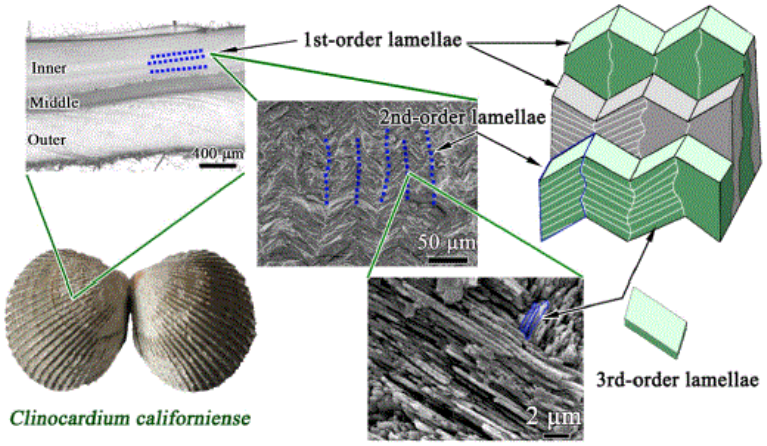


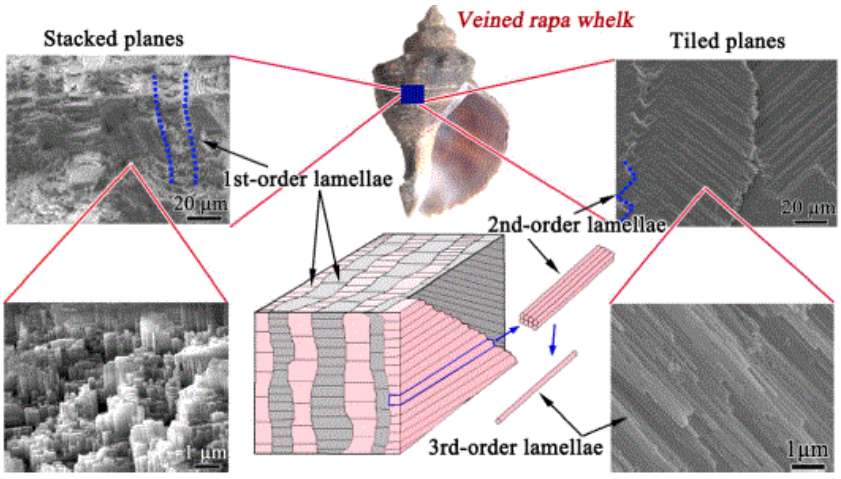
Figure 2.1.1.Hierarchical structure of nacre [1].



(a)



(b)



(c)

Figure 2.1.2. Three orders of lamellar structures present in cross-lamellar molluscs. (a) Strombus gigas; (b) Clinocardium californiense (bivalve); (c)Veined rapa whelk (gastropode) [19] [22] [23] [12].

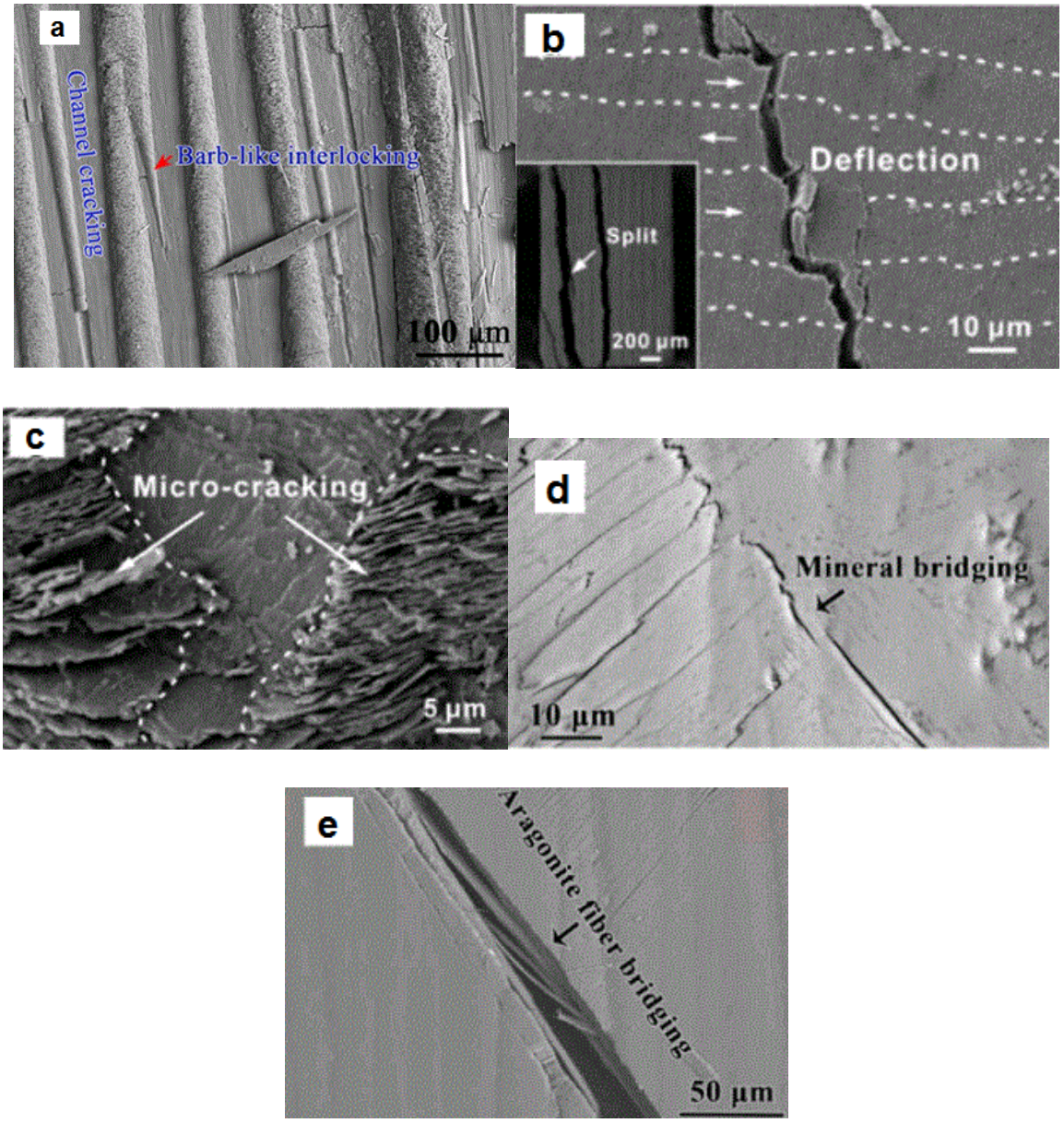


Figure 2.1.3. Microstructures which prohibit the propagation of cracks under loadings. (a) Chanel-cracking and Barb-like interlocking; (b) deflection of cracks by interfaces; (c) micro-cracking; (d) mineral bridging; (e) fibre bridging. White dashed lines indicate interfaces between lamellae [12].

In addition, the hydrated condition of mollusc shell also influences its mechanical property. The fracture resistance of nacre tested dry (stored in ambient environment) is approximately four times less than that tested wet (soaked in distilled water for 3 weeks) [21]. The compressive strength of wet mollusc shells is higher than dry specimens in three loading directions, which are parallel, perpendicular to growth lines on shell surface and perpendicular to shell surface [24] [25]. However, dry mollusc shells show higher hardness than wet ones [26]. The influence of

hydrated condition in bending strength of mollusc shells is highly dependent on shell species. For S.gigas shell, wet samples show 50 percent higher bending strength than dry ones [20] while for S. purpuratus, the bending strengths of wet and dry samples are comparable [25].

2.1.2 Mechanical behaviours of mollusc shells

Common British limpets (Patella vulgate) show intermediate percentages of four major compression behaviours, as shown in *Figure 2.1.4*. Typical cracks appearing in common British limpets under different conditions are also presented in *Figure 2.1.5*. For dry samples, the majority present cracking and fissuring of the anterior end while for wet samples, due to the existing living animals which increase lateral shear resistance, holes at the limpet apexes are observed [6].

In general, the elastic moduli of mollusc shells fall into the range of 40-70 GPa. The tensile strength is reported to be within 40-100 MPa while the compressive strength is up to 10 times the tensile strength [27] [28].

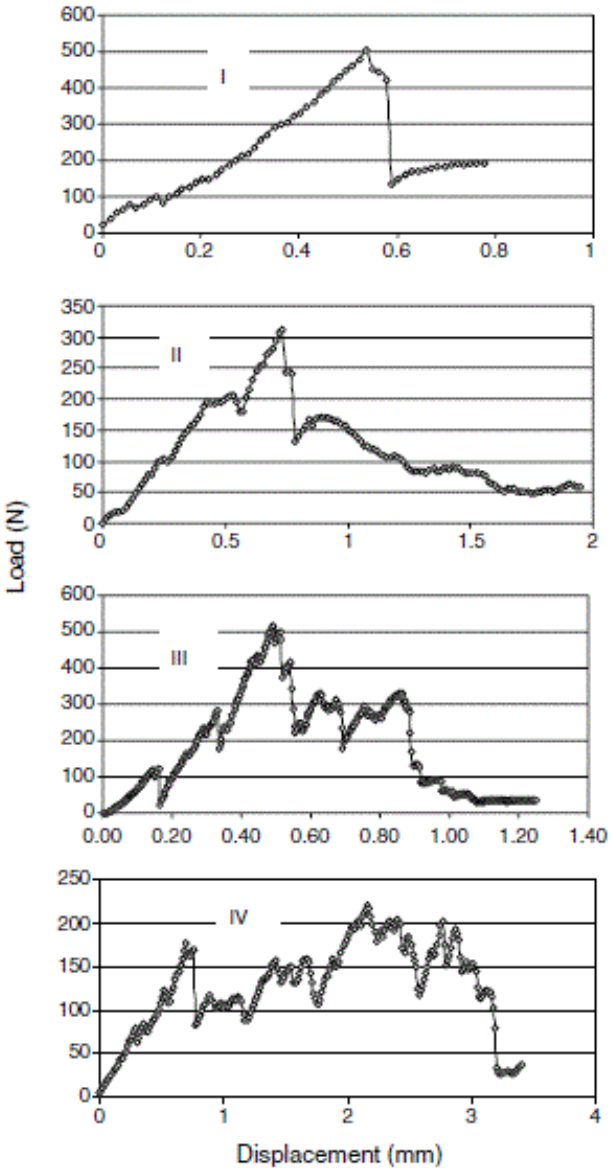


Figure 2.1.4. Four main types of compression patterns in load-displacement curves. The distribution of crack patterns per species differs [6].

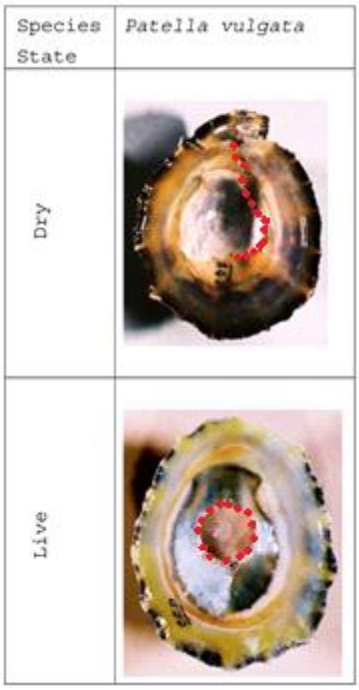


Figure 2.1.5. Typical cracks occurring on common British limpets under different conditions. Crack patterns are indicated by red dots in cracked dry and live shells [6].

2.1.3 Biomimetic nacre-like materials

Researchers investigate the mechanical properties of mollusc shells, especially nacre, in order to duplicate their excellent properties into the design of bio-mimetic materials. However, the replication of the intrinsic toughening mechanisms of biomaterials and the fabrication methods used to duplicate their complex nano- or micro- structures still remain as challenges [29].

Two major directions have been focused on for nacre-like materials' study and fabrication: 1) duplication of the microstructure by different processing techniques; 2) imitation of the toughening mechanisms of materials.

Various techniques have been employed to produce nacre-like materials. Among all the current techniques, layer-by-layer deposition [30] [31], solution casting [32], self-assembly [33] [34] and thin film deposition [35] show outstanding performance to fabricate relatively good-quality biomimetic materials. However, the final products produced by these processes are still not

feasible for practical applications. A newly-developed technique, freeze casting, has been believed to have potential to realize the practical applications of nacre-like materials [29].

Different toughening mechanisms have also been applied when researchers try to improve the toughness of nacre-like biomimetic materials. Based on the concept that weak interface between mineral and organic matrix contributes to excellent toughness of nacre, Clegg et al. [36] used thin silicon carbide (SiC) square tiles (50mm X 50mm X 200μm) which were doped with boron to mimic mineral bricks. Graphite was used to coat the tiles in order to obtain weak interfaces. The resulting laminates showed 5 times better toughness compared with monolithic SiC. However, no material was used in this method to mimic the soft organic phase present in nacre, which is believed to improve the total toughness. Tablet sliding, which is regarded as an important toughening mechanism in nacre, is also used for some scientists when they produce nacre-like materials. In 2003, Tang et al deposited nano-scale clay platelets and polyelectrolytes layer by layer to form 5μm artificial nacre. High strain has been obtained under tension due to the electrostatic interaction between clay layers over a long range of sliding distance [30]. In 2008, Bonderer et al. carefully designed the aspect ratio of alumina bricks in order to promote tablet sliding and used chitosan polymer as the mortar. The resulting materials show the characteristic structure and behaviours of nacre even with low ceramic content [37]. Biomimetic materials with close behaviours to natural nacre, were produced by Munch et al. in 2008. Layers of alumina/PMMA bricks and mortar were fabricated to make the composites. Freeze casting was used to produce the ceramic bricks from alumina powder and the alumina bricks were then sintered and infiltrated by PMMA. Excellent toughness and deformation under loading have been observed [38]. The reported mechanical properties of these nacre-like composites are shown in *Table 2.1.1*.

Table 2.1.1. Mechanical properties of different nacre-like biomimetic materials [30,36–38].

Materials	Strength/ MPa	Modulus/GPa	Toughness/MPa.$m^{1/2}$
SiC/graphite laminates (Clegg et al. [36])	633	450	15
Clay /polyelectrolytes laminates (Tang et al. [30])	123	11	-
Alumina/chitosan composite (Bonderer et al. [37])	300	10	-
Alumina/PMMA composite (Munch et al. [38])	200	-	30

2.2 Bone

The study of mechanical properties of bones has a significant impact in clinical applications such as age-related fracture, skeletal fragility diseases and bone or joint replacements [39] [40].

Bone, which has a good combination of strength, toughness and damage tolerance, is composed of two major nano-phases: collagen fibrils and plate-shaped hydroxyapatite (mainly $Ca_{10}(PO_4)_6(OH)_2$) nanocrystals which are arranged in a periodic and staggered array and preferentially orient along the c-axis of fibrils. Apart from hydroxyapatite, the mineral phase has traces of other minerals such as Mg, Na, HCO_3-, etc. Both collagen and mineral phases make roughly 80% of bone and provide bone with strength and toughness [41] [42] [43]. Water (e.g. living tissues) occupies the remaining part of bone which gives additional flexibility [43].

Bones fall into two categories considering the macro-scale structure: cortical bone and trabecular bone. The femur head which is located at the head of long femur bones is composed of dense cortical bone as outer layer and porous trabecular bone as interior as it shown in *Figure 2.2.1*. Two methods have been generally applied to distinguish these two types: (1) the degree

of porosity [44] or apparent density which has an approximate linear relation to porosity [45]. For cortical bone, the porosity ranges from 5-30% while for trabecular bone, the range can fall between 30-90% [44]. However, there is always an ambiguous line for the definition between very porous cortical bone and very compact trabecular bone [46]; (2) Difference in microstructure. Cortical bone has a structure consisting of lamellae with regular and cylinder-like shape while trabecular bone has a structure composed of lamellae with irregular shape [47]. Microstructures of both types of bones will be described in detail later.

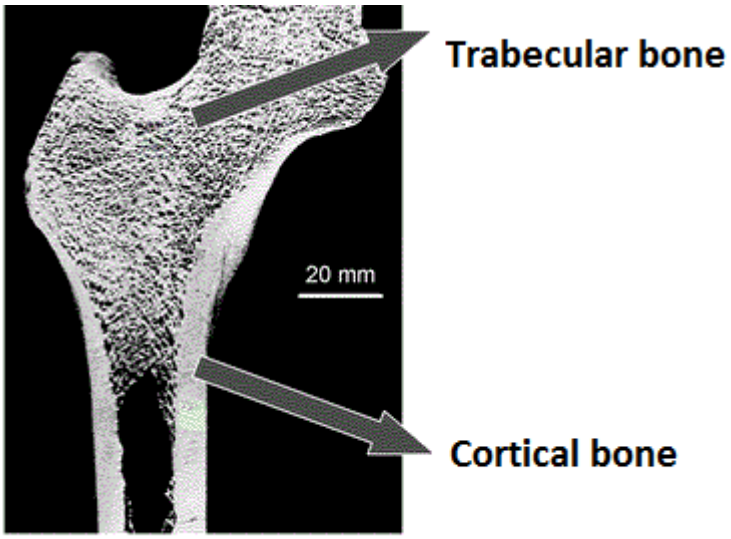
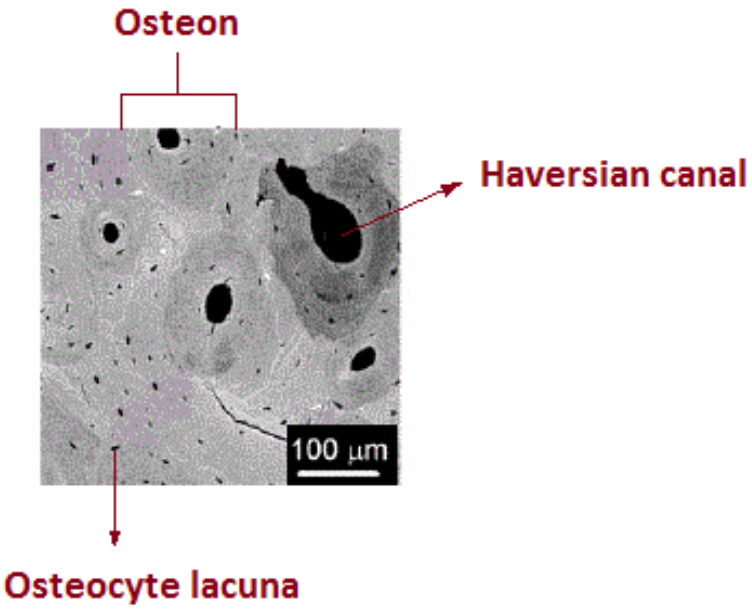


Figure 2.2.1. Locations of cortical bone and trabecular bone in femur head [48].

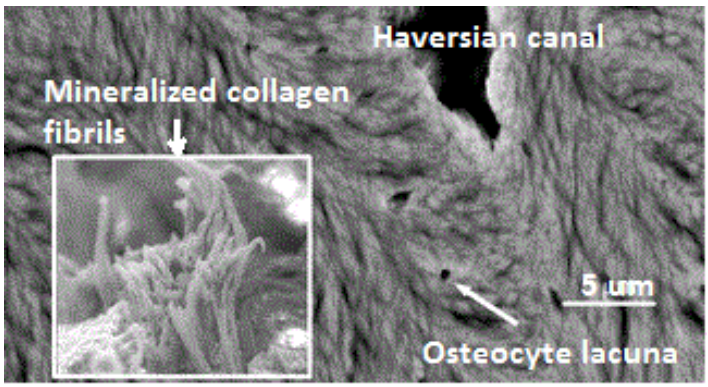
2.2.1 Cortical bone

With increasing incidence of skeletal fractures due to aging (osteoporosis and osteoarthritis) [49] [50], the structure-related issues on mechanical properties of bone are becoming more important [51]. Among different types of bones distributed within human body, cortical bone is considered to play a major part in physiological loading in lower limbs and to be the predominant sites for the non-vertical fracture which accounts for 80% of all factures and is the main reason for fracture-related morbidity and mortality among aged groups [52] [51] [53]. Therefore it is important for the investigation of elastic properties of cortical bones and their relations with age and gender.

2.2.1.1 Cortical bone microstructure



(a)



(b)

Figure 2.2.2. Microstructures of cortical bone. (a) Backscattered electron imaging (BEI) of cortical bone; (b) Scanning electron microscope (SEM) image of the lamellar and fibrillar material texture around an osteocyte lacuna [48].

Cortical bone has a microstructure that is composed of osteons or Haversian systems and interstitial areas between [54], shown in *Figure 2.2.2*. Osteons or Haversian systems measuring approximately 200-250 um [55] are lamellae of mineralized collagen fibrils which are arranged in concentric patterns, around blood vessels or canals [54] [47]. Apart from Haversian canals, Volkman's canals (average diameter: 5-10 um), osteocyte lacunae (average diameter: of the

order of 5 um) and canaliculi network (average diameter: of the order of 1 um) are also parts of the complicated pore network within cortical bones [56].

2.2.1.2 Cortical bone mechanical properties

Mechanical properties of cortical bones are measured at different length scales. Elastic properties of cortical bones at the macro-scale are highly dependent on their microstructures and compositions [51] and are referred to as apparent properties which include influences of both bone matrix and pores. The elastic properties of cortical bones at the microstructural scale are referred to as intrinsic properties and only the elastic properties of bone matrix components including osteonic lamellae and interstitial lamellae are considered. The present mechanical properties of bone matrix are influenced by factors such as the orientation of collagen fibres, mineralization degree and the arrangement of both phases [55,57–62]. The material density of cortical bone ranges from 1.7g/cm^3 to 2.1g/cm^3 [63].

2.2.1.2.1 Cortical Bone: apparent elastic modulus

The apparent elastic moduli of cortical bones measured by different experimental methods reported in literature are summarized in *Table 2.2.1*. Different experimental methods (e.g. conventional mechanical testing results in lower measured stiffness tensors of bone compared with ultrasound testing due to material's inelastic behaviour [56]) or different specimen microstructures can result in different values of elastic moduli measured. However, these data are useful to give a range of elastic moduli which can be used for the comparison with apparent elastic modulus of cortical bones predicted from models.

It is well established that the pore network is an important determinant on bone apparent elasticity [56,64–66] and the apparent elastic modulus of cortical bone decreases with increasing porosity [56] [65]. Small pores below 10 um were found to have a minor contribution to the apparent elastic modulus compared with Haversian canals in Sevostianov and Kachanov's [56]

model based on elastic potential of a solid containing cavities with different shapes, orientations and densities.

Blood, lymph, nerve and osteocytes etc are within different types of pores, which are considered to be soft with moduli ranging from the order of 1 kPa to 10 MPa compared with mineral contents which have moduli in the order of GPa. Thus the influence of these soft tissues within pores on apparent elastic moduli of cortical bones has been neglected [56]. However, Grimal et al. [67] considered that the Poisson's ratio instead of Young's modulus of the fluid within the pore, has a significant impact on apparent elastic properties of cortical bones, based on a FE model in the case that high loading rate is employed in experiment and thus fluid inside pores cannot be assumed to flow freely. Real geometries of pores within a representative volume element of bone were used in the proposed model.

Table 2.2.1. Summarized apparent elastic moduli of cortical bones measured by different experimental methods.

Reference	Methodology	Reported values of elastic moduli of cortical bones (GPa)		
X. N. Dong, X.E.Guo [68]	Tensile test	Transverse	Longitudinal	
		9.55±1.36	16.61±1.83	
X. Acuna et al. [69]	Compression test	Transverse	Radial	Longitudinal
		5.65±1.5	6.49±3.22	20.5±7.77
M. J. Mirzaali et al. [51]	Multiple tests	Tension	Compression	
		18.16±1.88	18.97±1.84	
O. Boughton et al. [70]	Compression test	Longitudinal		
		9.62±2.86		
Prof Quentin Grimal's group [70]	Resonance Ultrasound Spectroscopy (RUS) test	Transverse	Radial	Longitudinal
		9.41±2.23	9.48±2.39	17.70±3.08

2.2.1.2.2 Cortical bone: intrinsic elastic modulus

Nano-indentation measures the properties of a very local volume of material under specific conditions of strain rate and is considered as a valuable method to include the microstructure of bones into the measurement of mechanical properties and avoids influences of intrinsic defects and heterogeneity of microstructures [47].

Local elastic modulus of a specimen can be obtained via nano-indentation using Berkovish tip with measurements of applied load, contact depth, projected area of contact and specimen's Poisson's ratio [62]. The reported intrinsic elastic moduli of cortical bones from literature, which are measured using nano-indentation, are summarized in *Table 2.2.2*. The reported elastic moduli of interstitial lamellae is always higher than those of osteonic lamellae in one specific axis direction of the same specimen due to higher mineralization degree [51]. There was no significant variation for the intrinsic elastic moduli in longitudinal directions measured in dehydrated condition. Dehydrated bones are usually used for nano-indentation tests [55] [60] [61] except Zysset et al has measured intrinsic elasticity of cortical bone in hydrated condition and a lower value was obtained [62]. The lower elastic modulus reported by Zysset et al. [62] cannot be directly linked to the wet condition of tested bones because in Zysset et al.'s study, the cortical bones are from human femur while others' [55] [60] [61] are from human tibiae. However, it would seem more representative to measure the intrinsic mechanical properties in a moist environment, which is closer to the real condition of living bones, but this involves more experimental complication. Overall, this is a very localized test method and can only be used in highly polished, often embedded samples [71]. Thus, there is a need for an alternative approach that can extract the intrinsic elastic moduli of the bone matrix in hydrated, less-prepared bone samples.

Table 2.2.2. Summary of intrinsic elastic moduli of cortical bone components measured by nano-indentation.

Reference	Experiment details	Intrinsic elastic moduli (GPa)		
Z. Fan et al. [55]	Indenter: Berkovich tip Maximum load: 8 mN Loading/unloading rate: 400 uN/s Test condition: dehydrated condition	Osteonic lamellae	Transverse	16.6 ± 1.5
			Radial	17.0 ± 2.2
			Longitudinal	25.1 ± 2.1
			Matrix anisotropy (longitudinal : transverse)	1.51 ± 0.19
			Matrix anisotropy (longitudinal : radial)	1.48 ± 0.23
		Interstitial lamellae	Transverse	19.7 ± 1.5
			Radial	18.5 ± 1.1
			Longitudinal	27.1 ± 1.7
			Matrix anisotropy (longitudinal : transverse)	1.38 ± 0.14
			Matrix anisotropy (longitudinal : radial)	1.46 ± 0.13
P. K. Zysset et al. [62]	Indenter: Berkovich tip Maximum depth: 500nm Loading/unloading rate: 10 nm/s Test condition: wet condition	Longitudinal	20.1 ± 5.4	
Jae-Young Rho et al. [60]	Indenter: Berkovich tip Maximum load: 20 mN Loading/unloading rate: 1 mN/s Test condition: dehydrated condition	Osteonic lamellae	Longitudinal	22.4 ± 1.2
		Interstitial lamellae		25.7 ± 1.0
Jae-Young Rho et al. [61]	Indenter: Berkovich tip Maximum load: Around 13.5 mN Loading/unloading rate: 750 uN/s Test condition: dehydrated condition	Osteonic lamellae	Longitudinal	22.5 ± 1.3
		Interstitial lamellae		25.8 ± 0.7

2.2.1.3 Cortical bone anisotropy

Bone anisotropy have been clearly demonstrated, as shown in *Table 2.2.1* and *Table 2.2.2*. Elastic properties such as elastic moduli measured along the orientation direction of osteons, which is considered as longitudinal direction are higher than transverse and radial directions and

variations of elastic moduli in directions on the transverse/radial directions are small [55] [68] [69]. Two factors: porosity and matrix anisotropy, are normally considered to affect bone anisotropy [72]. A negative correlation of porosity to elastic bone anisotropy (the ratio of longitudinal to transverse apparent elastic modulus) has been reported by Dong and Guo [68], but that study did not discuss the role of the bone matrix in bone anisotropy. Others [55,67,73–75] have reported that the bone matrix is the main factor which contributes to overall bone anisotropy. Most studies [55,73–75] consider the orientation of collagen fibrils in bone matrix is the dominant factor to overall bone anisotropy. Compared with the soft collagen phase, mineral phase of collagen plays a more significant role in bone anisotropy [74]. The anisotropy ratio of the whole bone is reported to be 1.7-2.1 [47].

2.2.1.4 The influence of age and gender on microstructure and mechanical properties of cortical bones

Because an increasing tendency of bone fracture has been observed in aged populations, the relationship of microstructure and mechanical properties of cortical bone with age and gender is important. In particular, the study of the influences of age and gender on porosities of cortical bones is important because porosity is an important factor which influences mechanical properties of cortical bones [56,64–66].

Mirzaali et al. [51], Khosla [76] and Hoffler et al. [77] reported a positive trend between age and porosity (*Figure 2.2.3* (a) (b)). It is reported [76] [78] that women tend to lose more mineral content and thus have increased porosity in cortical bone compared with men in old age. However, for patients who suffer from osteoarthritis which is considered as an age-related disease, patients tend to have higher mineral density and thus less bone porosity unlike osteoporosis which leads to higher bone porosity [49] [50].

A relation between elastic moduli measured by tension, compression and torsion with donor age has also been reported shown in *Figure 2.2.3* (c) [51]. This finding is inconsistent with B. Martin

[79], who found a weak relation between elastic modulus and age in tensile results. However, as it is indicated in *Figure 2.2.3* and *Figure 2.2.4*, the number of samples used in Martin's observation [79] is much less than Mirzaali et al.' [51], which casts doubt on the accuracy of the results. When it comes to lamellar-scale elastic moduli of cortical bones which are measured using nano-indention, the independence of micro-scale elastic moduli on age and gender has been reported [51,77,80]. There is also no obvious relation between macro-scale elastic moduli of cortical bones and gender (*Figure 2.2.3* (c)) [51].

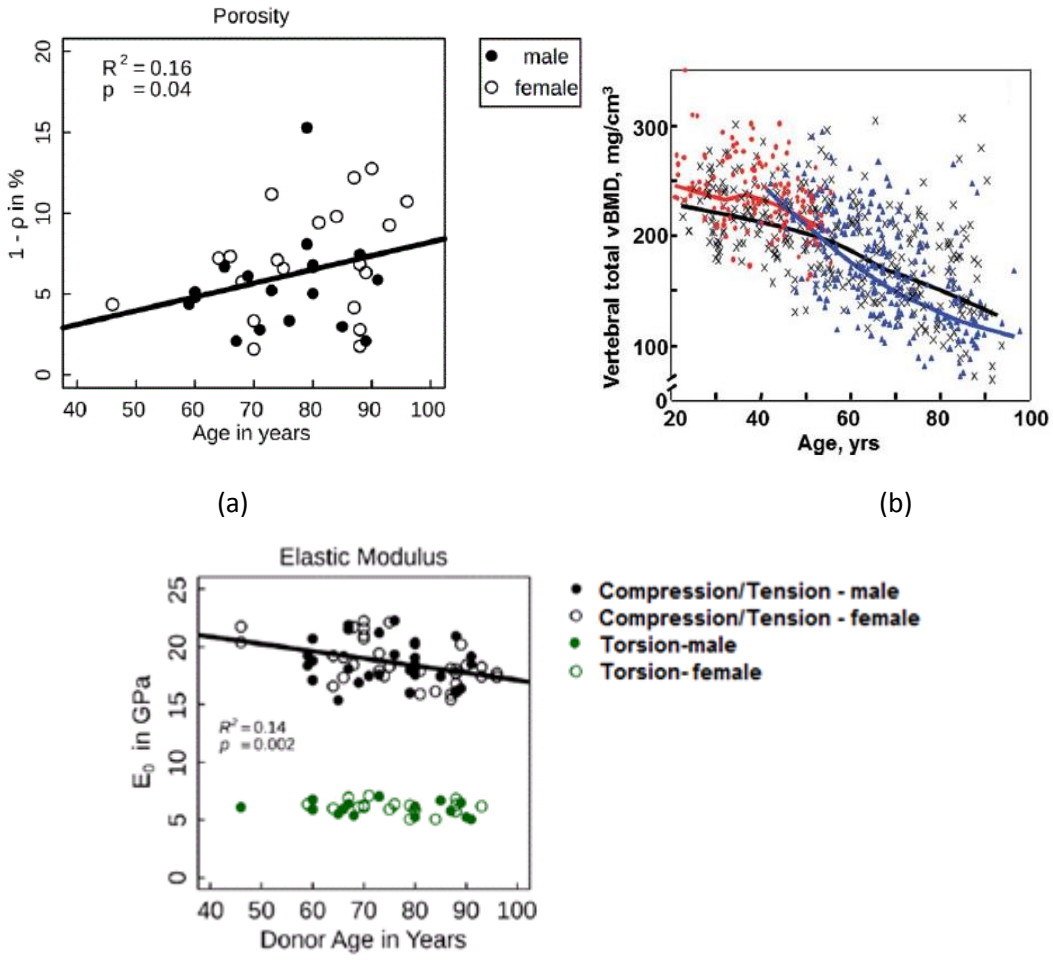


Figure 2.2.3. The relation between porosity and lamellar-scale elastic moduli vs age: (a) the relation between porosity and donor age (ρ represents mineral volume fraction and thus 1- ρ represents porosity). The conclusion was made using cortical bones from femurs of 19 male (46 to 99 years) and 20 female donors (59-91) [51] *; (b) volumetric bone mineral density (vBMD) versus age. Higher the value of vBMD, lower the value of porosity* [76]. *The conclusion was made using samples from 373 female (red: premenopausal female, blue: postmenopausal female, black: male) and 323 men; (c) the relation between elastic modulus measured using compression, tension and torsion versus donor age* [51].

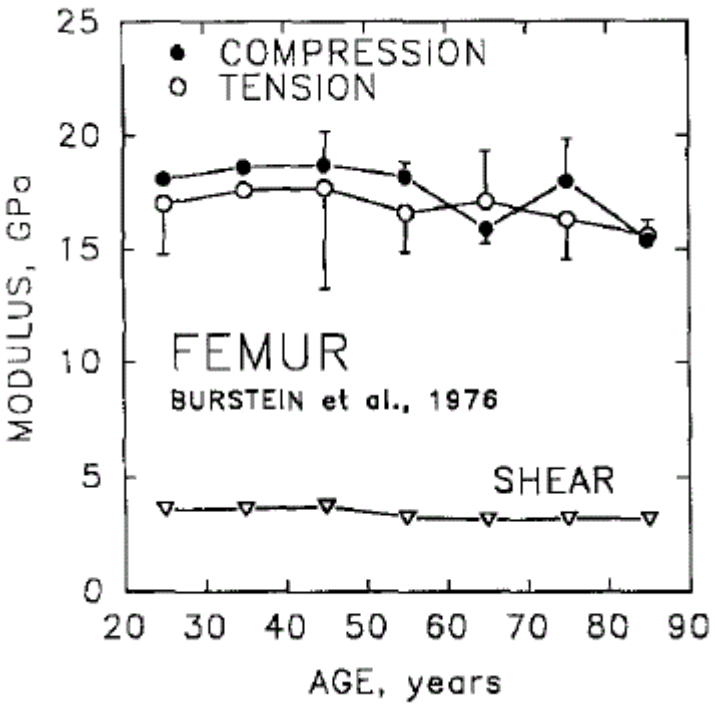


Figure 2.2.4. The relation between bulk elastic modulus and age [79].

2.2.2 Trabecular bone

Trabecular bone as a porous material is composed of trabecular struts and pores filled with marrow [81]. The structure of trabecular bone is shown in *Figure 2.2.5*. Reported range of apparent density of trabecular bone is from 0.09-1.553 g/cm^3 [82]. Together with cortical bone, trabecular bone contributes to the strength of bone [83].

Both apparent elastic modulus and intrinsic elastic modulus are used to describe the elasticity of trabecular bones in literature. Elastic modulus of trabecular bone has been measured by different experimental methods, which are summarised in *Table 2.2.3*.

Different reported elastic modulus values in literature may be due to the applied different testing methods (static and dynamic measurements [84]), intrinsic compression errors (frictions between samples and plates) [84–86], dehydration level [87] and different sample origins. Trabecular bone in dry condition tends to have higher intrinsic modulus than in wet condition due to the soft phase that is affected by moisture. Regardless of microstructural features such as

porosity, the reported intrinsic elastic moduli of trabecular bones are less than two times lower than cortical bone when measured using nano-indentation. Given the fact that the reported apparent elastic moduli of trabecular bones are more an order of magnitude lower than cortical bones, it indicates that the influence of the microstructural geometry on apparent elastic moduli of bones is higher than that of bone matrix.

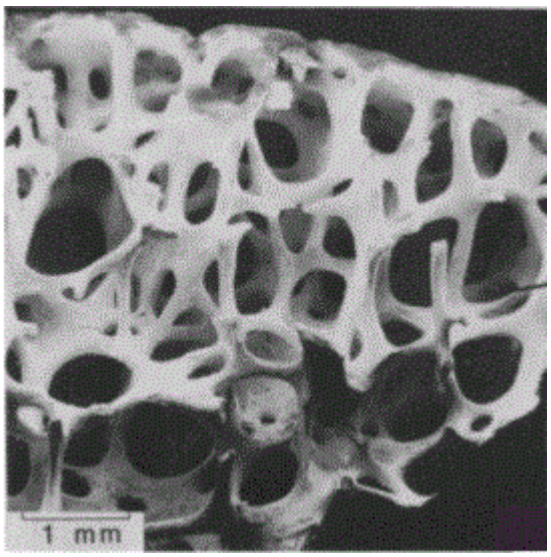


Figure 2.2.5.Scanning electron micrograph of trabecular bone from femoral head with rod-like structure [88].

Table 2.2.3. The summarized measured elastic moduli of trabecular bones.

Reference	Testing method	Reported elastic modulus		
R.B. Ashman and J. Y. Rho [81]	High frequency pulse transmission ultrasound technique (by tuning ultrasonic frequency to measure both apparent and intrinsic elastic modulus) (wet condition) Different femur specimens used in this study were from different donors with large variation in apparent density but much less variation in material density. It explains the observed different apparent elasticity and similar intrinsic elasticity among different femurs	Sample (n: sample number)	Apparent modulus (GPa)	Intrinsic modulus (GPa)
		human femur 1 (n=11)	0.959 ± 0.388	12.7 ± 2.00
		human femur 2 (n=21)	1.78 ± 0.857	13.1 ± 1.55
		human femur 3 (n=21)	2.17 ± 1.07	13.1 ± 1.05
Townsend et al. [89]	Single trabecular buckling (human medial tibia1)	Intrinsic modulus (GPa)		
		Wet bone	11.4 GPa	
		Dry bone	14.1 GPa	
T. M. Keaveny et al. [84]	Wet compression test (9 samples from human lumbar spine)	Apparent modulus (GPa)		
		0.165 ± 0.11		
F. Linde and I. Hvid [86]	Wet compression test (human tibia)	Multiple apparent elastic moduli depending on the boundary conditions applied to bone during compression (MPa)		
		0.262 -0.666		
O. Jirousek [87]	Nano-indentation (dry)	Intrinsic elastic modulus (GPa)		
		15.39 ± 1.4		
S. D. Ryan and J. L. Williams [90]	Tensile testing (bovine femoral bone)	Apparent modulus (GPa)		
		0.75± 0.39		
J. L. Kuhn et al. [91]	Wet three point bending test (human iliac crest)	Apparent modulus (GPa)		
		Age group of 63-year-old	4.16± 2.02	
		Age group of 23-year-old	3.03± 1.63	
Shaocheng Ma et al. [92]	Tensile testing on trabecular bones from human femoral head (hydrated)	Apparent modulus (GPa)		
		0.1 - 0.4		

2.2.3 Fracture toughness of bone

Due to the fact that bone is a brittle material with inherent micro-cracks and some degree of inelastic behaviour, fracture toughness can provide an engineering basis to describe the capability of bones to withstand fracture. The fracture toughness is a material parameter that is independent on specimen size and geometry and thus facilitates the comparisons of works on fracture data from different studies and researchers [93]. Two approaches have been used for the measurement of fracture resistance of bone in literature review [93–98].

2.2.3.1 Critical stress intensity factor

The stress intensity factor (K), especially the critical stress intensity factor (K_c), is a common way to measure fracture resistance in materials including bone [93–98]. K describes the magnitude of the stress field around the crack tip, and hence the elastic strain energy that is available for crack growth. For any linear-elastic material with a relatively small region of inelasticity at the crack tip, the size of which is more than an order of magnitude smaller than the length of in-plane crack (a) and the geometry of specimen, K can be calculated as $Q\,\sigma_{app}\,(\pi a)^{1/2}$, where Q is a geometry function of order unity and σ_{app} is applied stress [99]. K_c which describes fracture toughness of material, is a critical value for crack propagation [100].

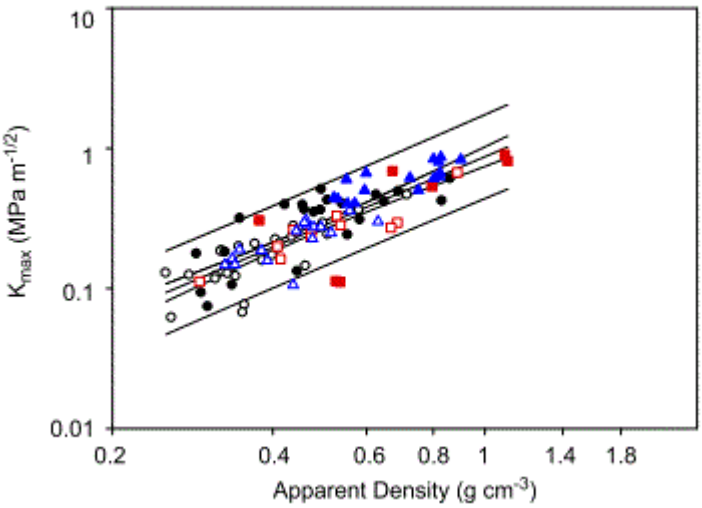
The reported critical stress intensity factors of cortical bones are summarized in *Table 2.2.4* [93,97,98,101] which shows that cortical bone has higher fracture toughness in the transverse direction compared with the longitudinal direction within individual sample. However, values of measured critical stress intensity highly depend on original conditions of samples.

Table 2.2.4. Literature data for the critical stress intensity factor of cortical bones.

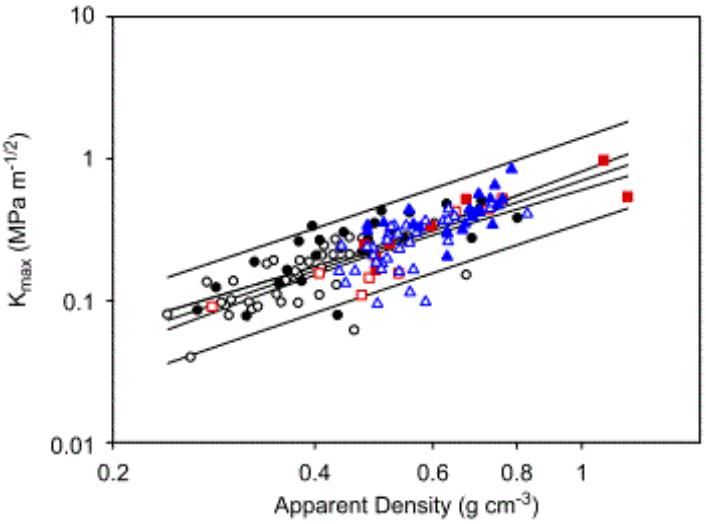
Reference	Experiment details		Measured Kc ($MPa.m^{1/2}$)		
	Samples	Methods			
R. O. Ritchie et al. [93]	14 rat femurs (wet) 15 mouse femurs (wet)	Three-point bending test	Rat	Mouse	
			2.16±0.67	2.89±0.34	
J. B. Phelps et al. [97]	18 female baboon femora	Tension	Longitudinal	Transverse	
			1.76±0.48	6.21±0.70	
T.L. Norman et al. [98]	15 human cortical bones from tibiae (wet)	Compact tension test	2mm sample thickness (longitudinal direction)	3mm sample thickness (longitudinal direction)	
			4.32±0.58	4.05±0.76	
R.K. Nalla, J.H. Kinney and R.O. Ritchie [101]	Hydrated human cortical bones from cadaveric	Double-notch four point bending test	Transverse direction	Anti-plane longitudinal direction	In-plane longitudinal direction
			5.33±0.41	2.21±0.18	3.53±0.13

Only one paper [102] reports values of fracture toughness of trabecular bone, and describes a strong relationship between K_{max} and apparent density (*Figure 2.2.6*) to a power function between 1 and 2 based on experiment results, which is in agreement with the hypothesis of Gibson and Ashley that the density of trabecular bone governs the fracture toughness of trabecular bone [103] [104]. K_{max} is the stress intensity factor at the point where the applied load reaches maximum and it was assumed to be the critical stress intensity factor for crack propagation. No effect of orientation on stress intensity factor of trabecular bone has been observed from this study.

Overall, cortical bone exhibits higher fracture toughness than trabecular bone, which is probably linked to higher density and lower porosity present in cortical bone.



(a)



(b)

Figure 2.2.6. Relations between K_{max} and apparent density.(a) samples manufactured parallel with trabecular structure; (b) samples manufactured perpendicular to trabecular structure [102].

2.2.3.2 Critical energy release rate (G_c and J integral)

The energy release rate is a more direct method to evaluate toughness of bones. The energy release rate approach which is directly related to the stress intensity factor, was proposed by Irwin [105] in 1956 as a way to measure the energy required to propagate a crack by a unit surface area. The critical value of energy release rate (G_c) describes the material's fracture

toughness, and it is independent on both loading condition and crack shape. It can be linked to the stress factor intensity for linear elastic material [100]:

$$G = \frac{K_I^2}{E'} + \frac{K_{II}^2}{E'} + \frac{K_{III}^2}{2\mu} \qquad \textit{Equation 2.2.1}$$

Where K_I, K_{II} and K_{III} represent the stress intensity factors in loading mode I (opening), mode II (shearing) and mode III (anti-plane shearing); μ is the shear modulus; E' is equal to E in plane stress while it is equal to $E/(1-\nu^2)$ in plane strain [100].

J integral was first introduced by Cherepanov [106] and Rice [107] in 1967 independently as a method to calculate the energy release rate of both elastic and non-linear elastic materials. Mechanical responses of linear elastic and non-linear elastic materials during crack propagation are shown in *Figure 2.2.7*. For linear elastic materials, energy release rate is measured as the released energy with an increment of crack growth while for non-linear elastic materials, absorbed energy caused by plastic deformation is added to the measurement [108]. The strain energy release rate calculated as *J* integral is equal to *G* under linear elastic conditions [93].

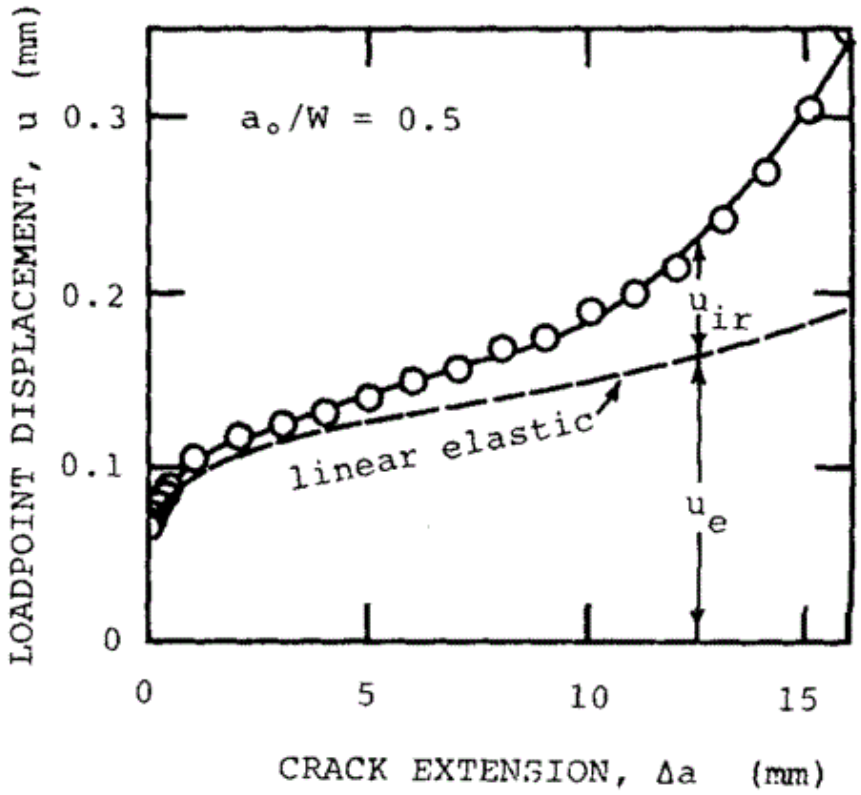


Figure 2.2.7. Relation between the load-point displacement (u) and the related crack extension (Δa) of a notched graphite specimen with notch (a_0)/ sample thickness (W) = 0.5. The dashed curve represents a linear elastic specimen and the line with circles represents a non-linear elastic specimen. U_{ir} represents the irreversible displacement caused by plastic deformation [109].

J integral, as a path-independent contour integral, describes the near crack deformation field. The value of J integral is constant for all paths that enclose the tip of a crack or a planar notch [107] and is zero for an enclosed contour due to its path independency [107]. A typical J integral contour which starts from one crack surface and ends to the other crack surface in a cracked body, is shown in *Figure 2.2.8*.

J integral is calculated as the integral of the potential energy along a contour which contains a crack, which represents the strain energy release rate per unit surface area:

$$J = \int_{\Gamma}[W(\epsilon)dy - T \cdot \frac{\partial u}{\partial x} ds] \qquad \textit{Equation 2.2.2} \text{ [107]}$$

Where W is the strain energy density, T represents the traction tensor on the contour Γ which is equal to $\sigma_{ij}\, n_j$ where n is normal to the path, u is the displacement vector while ds is the arch

length shown in *Figure 2.2.8* [107]. J integral has been then modified from line integral [107] into surface/area integral using Green's theorem [110] and volume integral [111], which allow the implementation of finite element analysis.

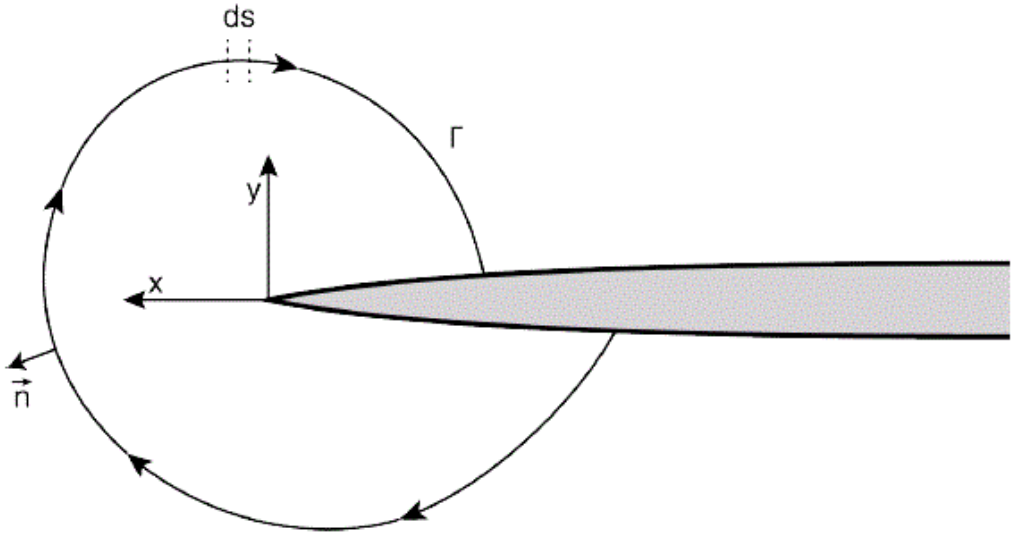


Figure 2.2.8.The typical contour Γ of J integral [108].

Only a few papers [98] [93] report the use of energy release rate to measure the fracture toughness of bones. In Timothy et al.' research, the reported value of average tensile energy release rate for female and male cortical bones from human tibia is 339±132 J.m^{-2} and the average shear energy release rate is 4200±2516 J.m^{-2}, which are calculated based on compliance methods:

$$G_c = \frac{P_Q^2}{2B}\frac{\partial C}{\partial a} \qquad \textit{Equation 2.2.3}$$

Where *B* is the specimen thickness, *C* is the inverse slope of the linear region of load-displacement curve, P_Q is the critical load which is determined as the intersection between a line with a slope of 0.95 (1/*C*) and the load-displacement curve at the onset of crack growth, and *a* is the crack length [98]. Ritchie et al. studied J integrals of rat femurs with sample number of 14

and mouse femur with sample number of 15 using three-point bending tests. The reported critical J integral is 15900±8170 J.m^{-2} for rat femurs and 10680±3050 J.m^{-2} for mouse femurs, which were not measured directly from load-displacement, but were calculated from the measured stress intensity factor $K_{c,eq}$ (*Table 2.2.4)* and elastic modulus $E' = E$ (plane-stress) using

$$K_{c,eq} = (J_c E')^{1/2} \qquad \textit{Equation 2.2.4} \text{ [93].}$$

The reported energy release rates in literature are not comparable due to different species of bones used by researchers, which have quite different structures and densities.

2.3 Mechanical testing techniques

A range of tests are used to obtain the mechanical properties of materials including biomaterials. Those that are relevant to this work are briefly summarised here.

2.3.1 Tension and Compression Testing

Tensile and compressive tests are two conventional methods to measure mechanical properties of various materials. In the field of biomaterials, compressive tests play a more important role because compression was usually the natural mode of force that a biomaterial was under [112]. However biomaterials are also tested under tension [113–116].

The relevance of compression testing has been shown by in-situ observations using X-ray tomography. Hussein et al. used stepwise compression (1 step = 1 mm) while scanning a human spine segment with adjacent inter-vertebral discs at each step until failure. By using digital volume correlation (DVC) to measure three-dimensional deformation field, relatively low strains were observed in the cortical shell of the vertebra near the middle plane and the cone-shaped deformation patterns of higher strains were developed in the interior trabecular bone (*Figure 2.3.1*). This pattern of deformation consistent with 'bi-concave fracture', which is commonly observed in patient X-rays [117] [118].

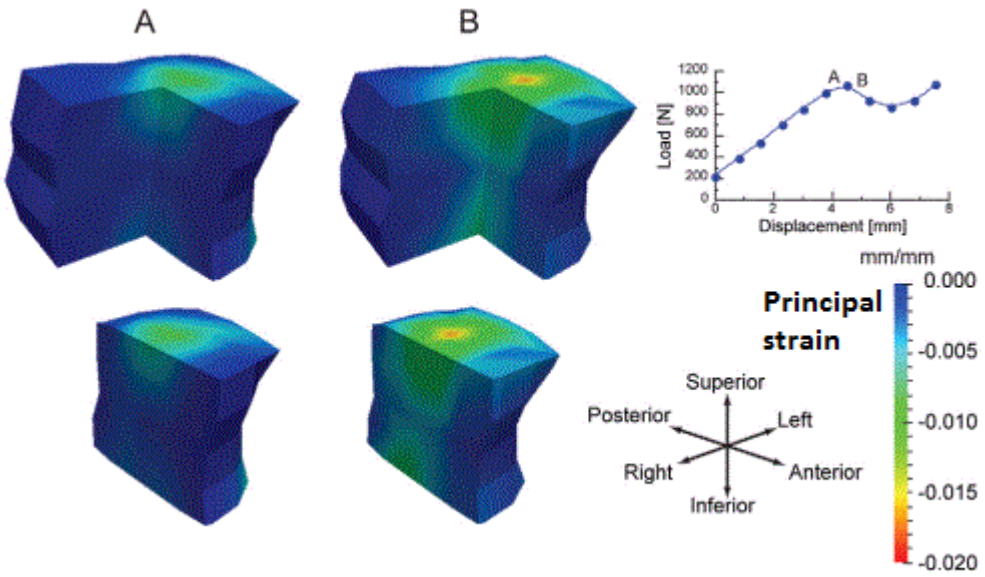


Figure 2.3.1.DVC results of incremental minimum principle strains with the anterior right quadrant of vertebrae removed (top view) and with the right half removed (bottom row) for viewing purposes. A and B correspond to two load-increment stages on the displacement-load curve [117].

2.3.2 Bending or Flexural Loading

Bending or flexural tests are also commonly done on biomaterials. Flexural loading is a common mode in biomechanics and the bending strength and stiffness of biomaterials such as bones could not be estimated by simple tensile tests [119]. Martin and Boardman reported three-point bending tests on cortical bones from bovine tibias and found that bending properties (e.g. elastic modulus) were influenced by the collagen fibre orientation, percentage of mineralization, density and porosity of the bones [120].

Bending tests are also employed to investigate the fatigue properties of biomaterials. Boyce et al have used four-point bending to induce fatigue damage to human cortical bones (from men 40-90 years old) in order to analyse morphologies and positions of developed damages under fatigue bending. In the tensile strained regions of specimens, extensive networks of fine and ultrastructural-level cracks were observed while in the compressive strain region, linear microcracks were formed in interstitial areas [121].

2.3.3 Indentation

Indentation test has been widely regarded as a simple and accurate way to determine the toughness of brittle materials [122].

Hertzian indentation is a common indentation method, which uses a hard sphere indenter and introduces a blunt contact to the material. The contact will be essentially elastic until the point of fracture. Hertzian cone crack is formed under blunt contact. Its evolution during loading and unloading is shown in *Figure 2.3.2*. When the spherical indenter contacts the surface, compressive stress distributes over the contact site while tensile stress is induced in a shallow skin region outside the contact area, which is shown in *Figure 2.3.2* (a). The magnitudes of both compressive and tensile stresses increase with increasing size of contact region. When the tensile field continues expanding and meets a suitable flaw, the flaw will then form a surface ring crack. The ring crack continues moving downwards and at the same time deviates outwards to avoid the compressive field with further loading and expanding contact. A fully-developed Hertzian cone crack spontaneously will then form when the ring crack becomes unstable [85]. The indentation hardness is calculated as following:

$$H_n = \frac{P_{max}}{\pi a_n^2}$$ *Equation 2.3.1* [123]

Where P_{max} is the maximum applied load while a_n is the radius of contact area at maximum load. Analysis of the cracks that are nucleated by Hertzian indentation has also been used to calculate fracture toughness (K_C) of brittle materials [124].

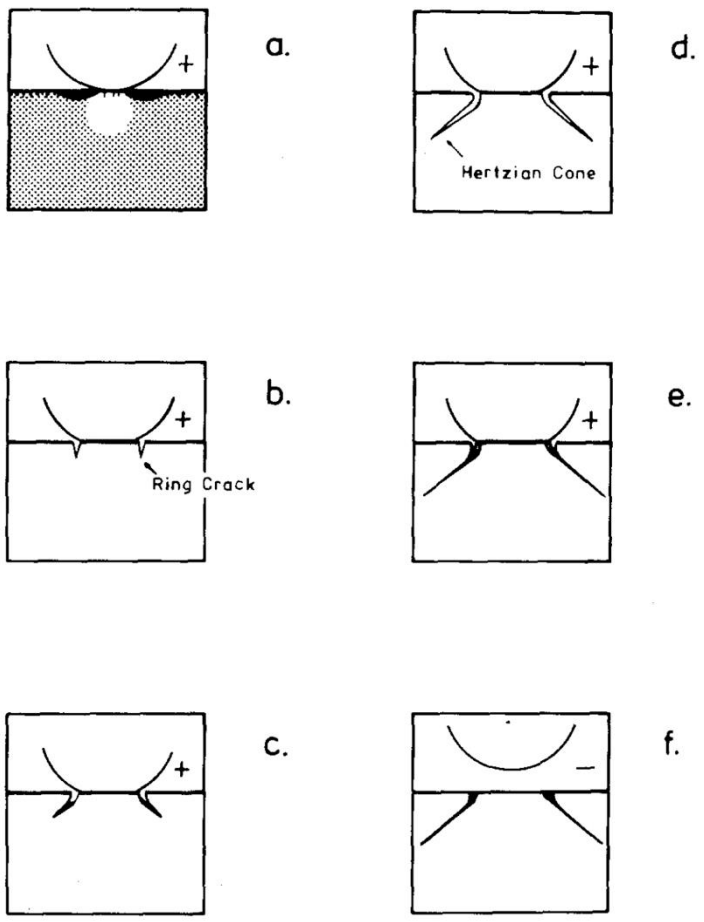


Figure 2.3.2. The evolution of Hertzian cone crack during blunt indenter loading (+) and unloading (-). The tensile filed is marked as black and the compressive filed is marked as unshaded region which are shown in Figure 2.3.2 a [122].

Compared to Vickers indentation, which induces a sharp contact, Hertzian indentation eliminates complications associated with the residual stress [125]. However, Hertzian indentation test has its own drawbacks: 1) Since Hertzian indentation is a surface characterization technique, the formation of Hertzian cone crack and processes of damage and deformation cannot be directly observed at the surface of an opaque material and therefore is not as amenable to the determination of fracture toughness of materials as destructive analysis [122]. 2) The stress intensity factors for cracks developed by Hertzian loads are difficult to be accurately estimated due to the steep gradient of stress fields in depth [125].

Biomaterials have fine microstructure, so nano-indentation techniques have been used for biomaterials, especially for measuring the elastic properties of different microstructural phases

within the specimen [61]. He, et al. used nano-indentation with both pointed and spherical-shaped indenters to measure the elastic modulus of human enamel and found that the organic component within the enamel lowered the total elastic modulus of the whole system, which is supported by Ge et al.'s AFM-based nano-indentation results [126]. The elastic modulus and hardness of different microstructural components within tibia cortical bone and nacre have also been measured using nano-indentation in literature [61] [127].

Generally the elastic modulus of biomaterials measured by nano-indentation tests were higher than those measured by macro-scale compression tests due to hierarchical microstructures of these materials and differences in measuring scales [128] [129].

2.3.4 Resonance ultrasound spectroscopy (RUS)

Unlike conventional static compression and tension tests, resonance ultrasound spectroscopy (RUS) is a dynamic method for the measurement of elastic modulus at small strains [130] [131]. Differences are present between the dynamic and static approaches. 1) The dynamic modulus is close to the value of initial tangent modulus while the static modulus is the chord modulus which is the tangent value between two chosen points on linear-elastic region of the stress-strain curve shown in *Figure 2.3.3* [132] [133], 2) RUS enables the measurement of elastic moduli in different directions of the same specimen while compression and tension tests only enable the measurement in one specific direction. Static compression testing is considered to be a less accurate method for the measurement of elastic modulus due to larger standard deviation compared with dynamic measurement technique [132]. The RUS method is also a favourable way to measure elastic moduli of samples with complicated geometry or in very small size which make conventional testing methods difficult [131].

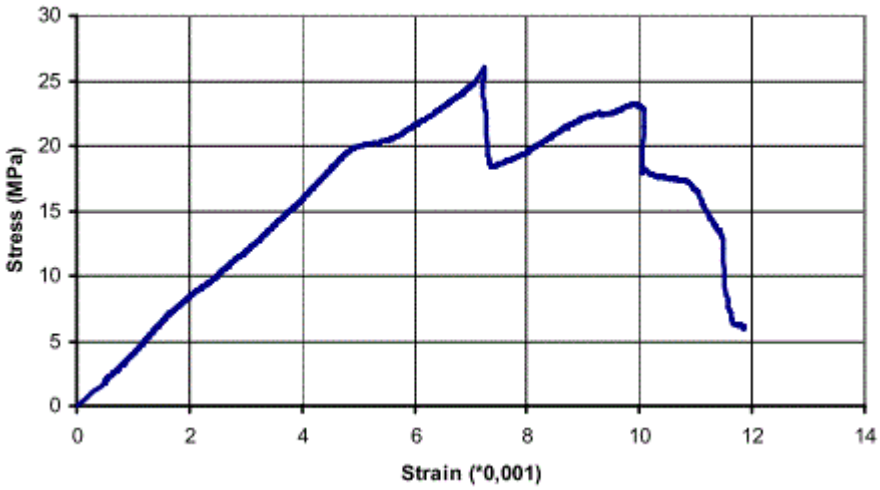


Figure 2.3.3. Stress-strain curve obtained from conventional compression test. Elastic modulus of the specimen is determined as the cord modulus of elasticity in one third of specimen's strength [132].

RUS elasticity measurement combines both experimental and numerical methods. The method is first introduced by Migliori et al in 1993 [134], for samples with simple geometries. The addition of Finite Element Method (FEM) by Plesek et al. [135] in 2004, enabled the analysis of sample with complicated geometries. The RUS method is outlined in *Figure 2.3.4* and will be explained in detail, as it provides critical data in this thesis.

The frequency response of the sample is measured, using two transducers, as a ratio between the excitation and receiving spectra [131] (the typical range of frequency spectra used for RUS is 10 kHz to 20 MHz [136]). The resonance frequencies (eigenfrequencies) are then obtained using peak detection based on the response frequency spectrum. At the same time, an equivalent FE model with the knowledge of the estimated elastic modulus of an ideal sample is used to generate numerical resonance frequencies (eigenfrequencies). A cost function *F*, which is shown in *equation 2.3.2*, is then introduced for the minimization of the relative error between experimental and numerical frequencies [131].

$$F = \sum_i \left| \frac{|f_i^{exp} - f_i^{num}|}{f_i^{exp}} \right|^2$$ *Equation 2.3.2* [131]

Where f_i^{exp} is the experimental resonance frequency and f_i^{num} is numerical resonance frequency [131]. The elastic modulus and Poisson's ratio of the sample are obtained by matching experimental and numerical frequencies [131].

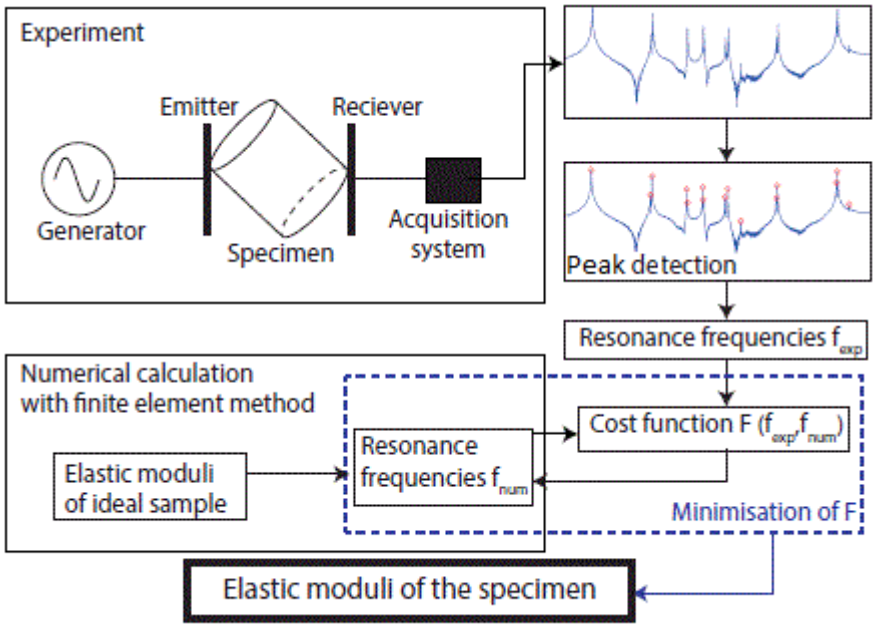


Figure 2.3.4. The schematic image of whole RUS procedures [131].

2.4 Three-dimensional characterisation of materials and deformation

2.4.1 X-ray computed tomography

X-ray computed tomography (CT) was first developed in 1970s [137]. It provides quantitative information about the spatial distribution of material density in 3D images. In the 1980s, X-ray micro-computed tomography (X-ray micro-CT) was developed with resolutions in a range of 5-50 μm [138][139]. Modern micro-CT microscopes are able to provide spatial resolution down to 1 um [140]. Micro-CT has been shown to give precise and correct structural properties when characterising biomaterials [141] [142]. However, high resolution (e.g 1 um) tomography of large volumes can be very costly and complex [143].

X-ray micro-CT generates 3D reconstructed images using X-ray projections (radiographs) obtained from multiple viewing directions. The spatial distribution of intensity (grey level) in the image map is determined by the energy of X-ray sources as well as the atomic compositions and local densities of the tested sample (linear attenuation coefficient), which influence the absorption of X-ray to the material. The relation between the absorption of X-rays and the materials can be described by Beer-Lambert's law:

$$\frac{I}{I_0} = e^{-\mu t}$$ *Equation 2.4.1* [144]

Where I is the intensity of transmitted x-rays, I_0 is the intensity of incident x-rays, μ is the linear attenuation coefficient of the materials and t is material's thickness through which x-rays have passed [144]. Typical linear attenuation coefficient vs energy plots are shown in *Figure 2.4.1* [145].

3D information of the microstructure of the scanned sample is directly or indirectly obtained after image thresholding of the reconstructed data [146] [147]. A schematic image of X-ray micro-computed CT is shown in *Figure 2.4.2*. Heterogeneous materials are especially suitable for the use of micro-CT because they have a structure that gives a wide distribution of grey levels [40][148][149]. Synchrotron radiation microtomography is a form of X-ray micro-CT with advantages of high intensity, collimation and monochromaticity of the X-ray radiation [150].

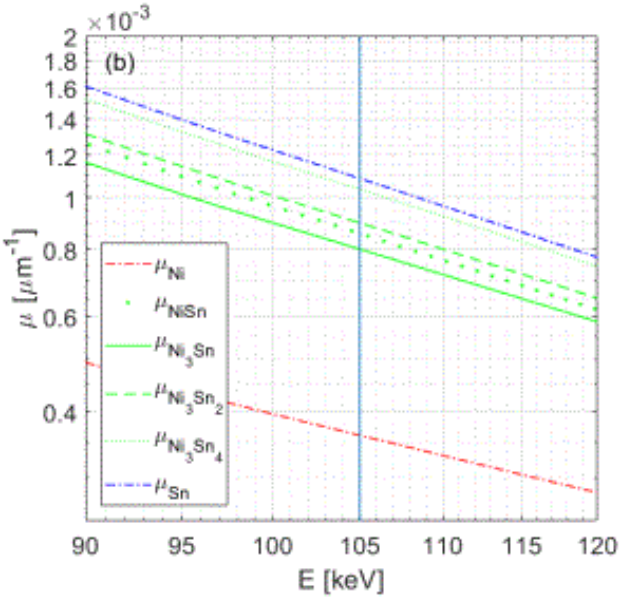


Figure 2.4.1. Linear attenuation coefficient vs energy plots of different phases in Ni-Sn sample. The blue line emphasized the energy (105keV) employed in Synchrotron test by Tekseth [145].

For specimens composed of materials with low attenuation contrast such as biological tissues, polymer or fibre composites [151] [152], phase contrast x-ray imaging is recommended instead of conventional x-ray absorption. In normal-absorption, differences in X-ray absorption of various phases are detected while for phase-absorption, the interference between diffracted and un-diffracted waves created due to the spatial variations of a phase of certain refractive index are used to provide contrast even at low absorption. Details can be enhanced within low-contrast materials (e.g. human breast tissues) by using phase-contrast scans (*Figure 2.4.3*) [152].

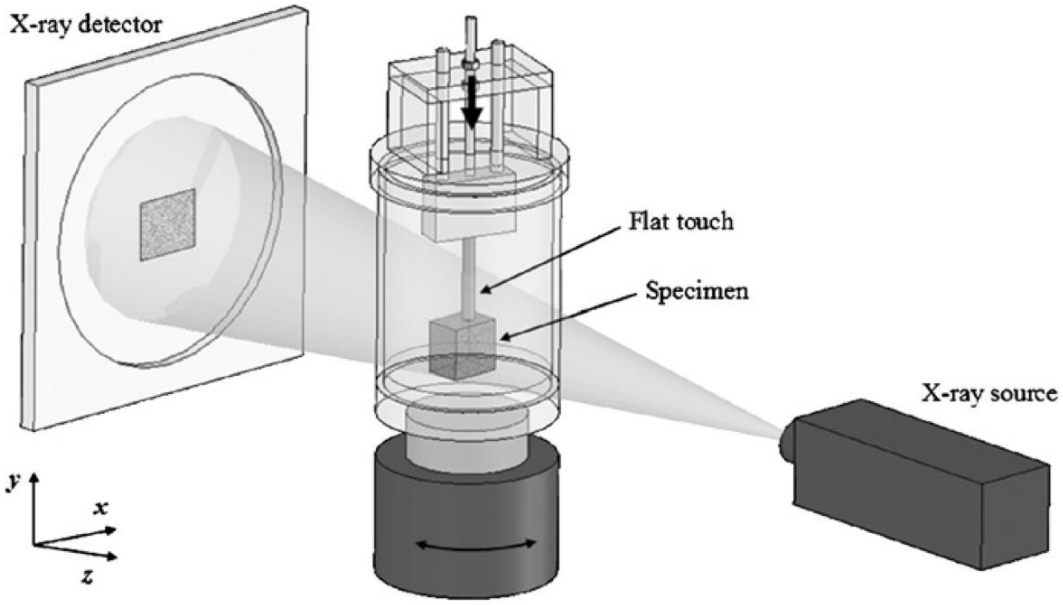


Figure 2.4.2. X-ray Micro-Computed Tomography [147].

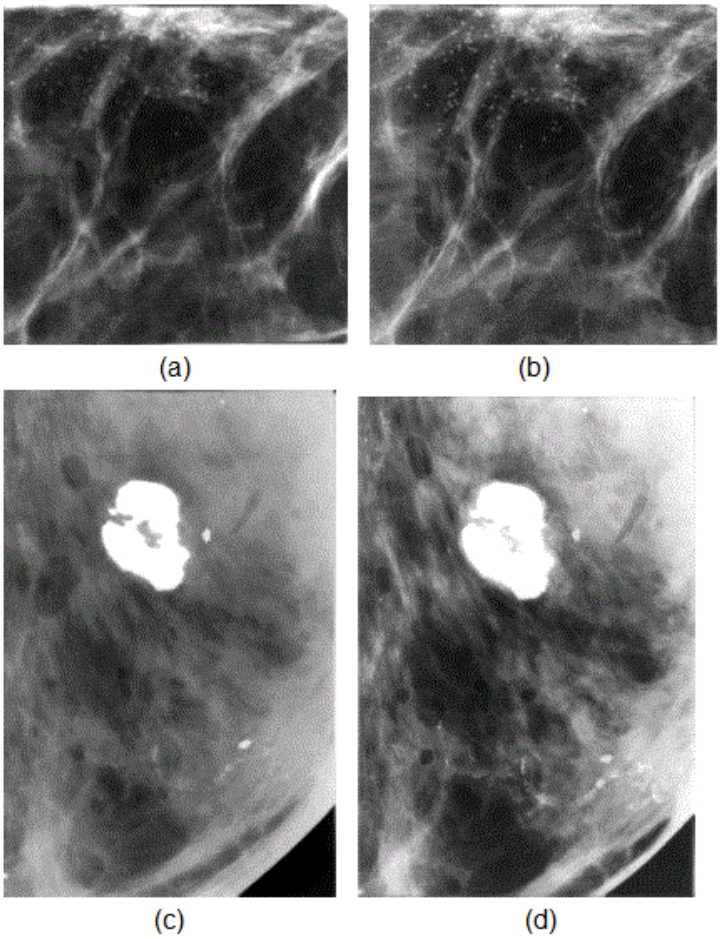


Figure 2.4.3. Comparisons between normal absorption CT scan and phase contrast CT scan of human breast tissues. (a) (c) normal absorption scan; (b) (d) phase contrast scan [152].

X-ray micro-CT has a wide range of applications in various materials including ceramics, polymers and biomaterials [153]. For biomaterials, micro-CT shows its advantages over traditional 2D histological analysis for following reasons: 1) as a non-destructive technique, micro-CT enables specimens to remain intact after analysis. Therefore future mechanical or histological testing is allowed on the same specimen [39,138,154]; 2) Micro-CT has higher efficiency and provides more quantitative information than 2D histological analysis [39].

Many micro-CT tests have been done on bones. For example, the structure of cancellous bone has been widely investigated and quantified by Müller and Ruegsegger [138,141,154,155]. Guldberg et al. used micro-CT to obtain information about the thickness, density and spacing of trabecular bones as well as the connectivity and anisotropy of the trabecular network of different structures. Different phases including newly formed bone, calcified cartilage within a growth plate or facture callus and the surrounding soft tissues were identified because of the signal contrast of micro-CT. Jones et al. used micro-CT to take multiple scans on the same sample bone, in vivo, in order to record the mineral formation and regenerative processes of the bone into different tissue-engineered scaffolds. The obtained information was then applied for the evaluation of the design and efficacy of these scaffolds [139]. In addition, micro-CT facilitates finite element analysis of mechanical properties of biomaterials (e.g. bone) with complicated morphology by providing information of real sample geometry

(

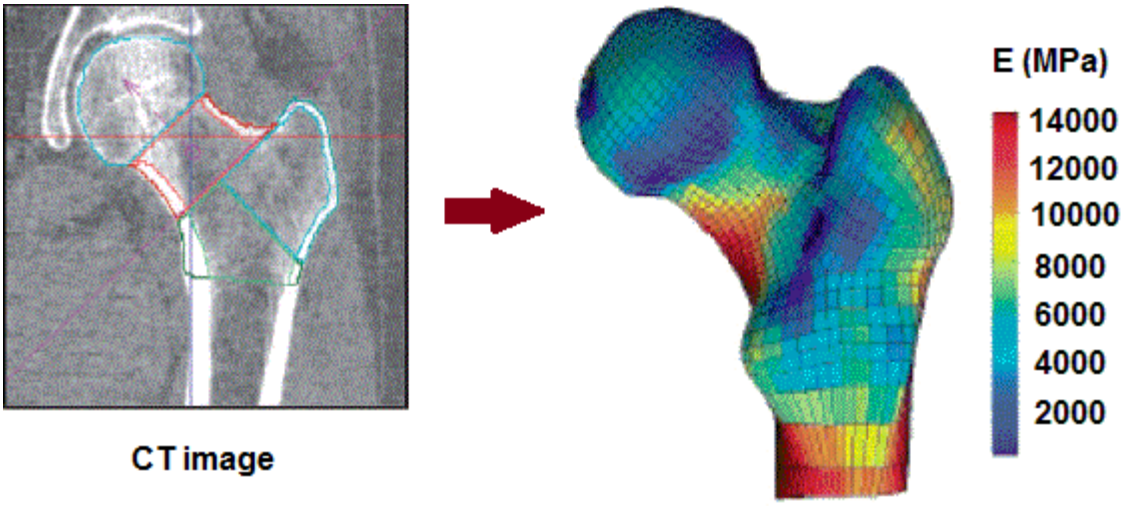


Figure 2.4.4) [140]. An example set of micro-CT images of a rat distal femoral are shown in *Figure 2.4.5* [39].

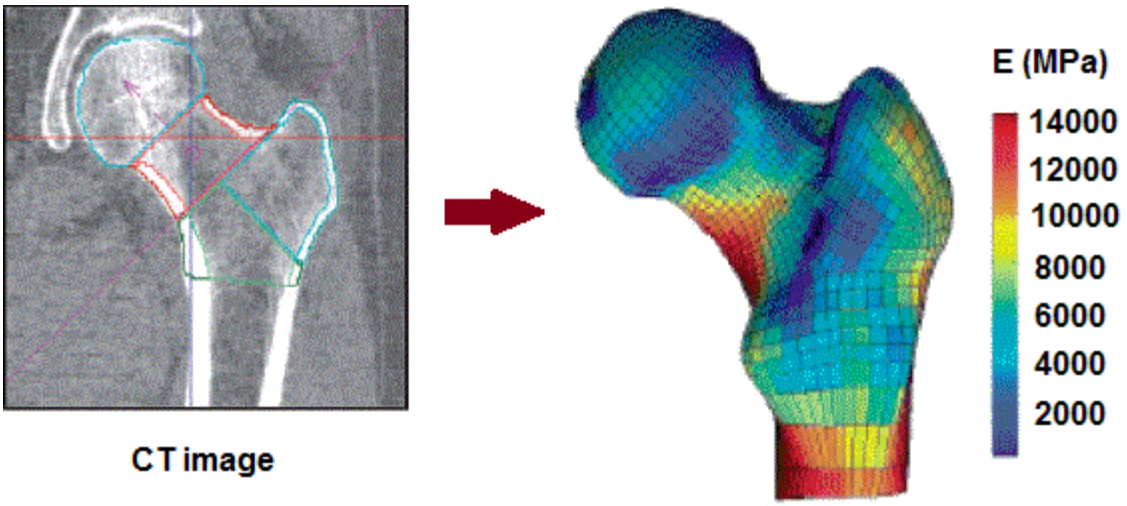


Figure 2.4.4 Distribution of Young's modulus within bone in the elements of mesh using CT data. No scale bar provided [140].

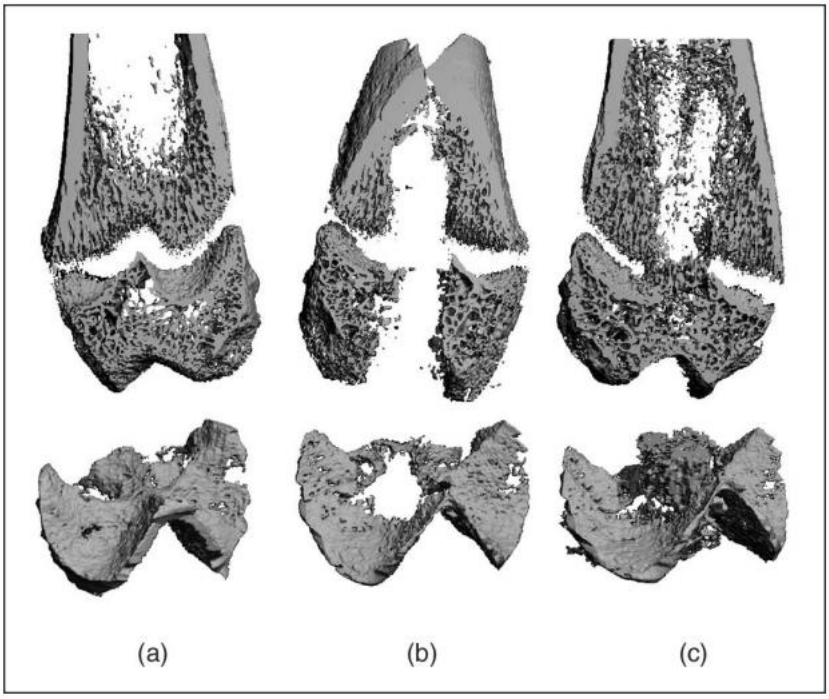


Figure 2.4.5 Micro-CT images of a rat distal femoral growth plate defect model *[39].*

2.4.2 Digital volume correlation

Digital volume correlation (DVC) was developed from digital image correlation (DIC), which has been in use since the 1980s. DIC allows one to measure displacements on the surface of specimens during mechanical tests while DVC allows measurement of 3D displacement fields within specimens and gives a better understanding of their distribution especially for non-plane loadings and specimens with complex geometries or heterogeneous structures [147,156,157]. Based on displacement fields, strains can be calculated using the gradients of displacement.

For study in the fields of medicine, biology and ceramics, DVC and X-ray micro tomography have been used together to extract 3D fields [147] [158]. The first paper in which Digital Volume Correlation was applied to computed tomography data was published by Bay in 1999 [148], reporting an investigation of mechanical damage in trabecular bone. Other techniques that provide volume images with 3D grey level distribution, such as confocal microscopy [159], micro-magnetic resonance confocal microscopy [160] and high resolution peripheral quantitative

computed tomography [161] are also able to work with DVC to measure 3D deformation of materials.

In general, DVC analysis is divided into three stages: 1) generation of 3D images of samples in unloaded and loaded states; 2) the measurement of the displacement field throughout the sample; 3) calculation of strain tensors based on the obtained displacement field [162]. DVC measures the displacement field between a reference specimen and the specimen after deformation. The data are evaluated on a 3D virtual grid. The cross-correlation of the grey levels in subsets of the volume, which surrounds a certain point of the grid in both reference and deformed states, is used to measure the displacement of each point in the grid. The 3D transformation Ø links the coordinates of the same point in both states. For a subset centered at the point of X_0 in the reference state and X is the coordinates of the same point in the deformed state, X_0 links to X via:

$$\emptyset(X) = X + U(X_0) + \frac{\partial U}{\partial X}(X_0)(X - X_0) \qquad \textit{Equation 2.4.2} \text{ [147]}$$

Here $U(X_0)$ in the equation gives the intensity (*u,v,w*) of the rigid body translation and $\frac{\partial U}{\partial X}(X_0)$ can be neglected in the case of small local strain [147]. Different objective functions such as the sum-of-squares correlation coefficient, cross-correlation and normalized cross-correlation can be applied to match the reference subset and corresponding deformed images [162]. The strain tensor can then be calculated based on all the components of the gradient of the transformation Ø, calculated from displacements of the centers of the subset with a least square estimation method or a second-order approximation [147,148,163].

The measurement uncertainty varies with different volume image sources. For example, displacement measurement uncertainty after DVC processing of a data set with a voxel resolution of 60 µm and a DVC subset size of 31×31×31 voxels was approximately 0.037 voxel for optical scanning tomography and 0.049 voxel for X-ray micro computed tomography [147] (a voxel is a three-dimensional pixel in the image). In addition, the quality of the tomography also

influences the measurement errors. Tomographs with high contrast between different phases or sufficiently high intensity of one specific phase within the material benefit the analysis of displacement field by DVC processing [164].

Apart from image resources, analysis methods employed in DVC analysis also influence the accuracy of results. Liu and Morgan [165] have evaluated the accuracy and precision of digital volume correlation in quantifying displacements and strains in trabecular bone. Compared with previous studies [40,148,166], different bone types including the bovine distal femur, bovine proximal tibia, rabbit distal femur, rabbit proximal tibia, rabbit vertebral body and human vertebral body and 2 samples/bone type were used, and three DVC methods including cross-correlation, normalized cross-correlation and maximum likelihood estimation were employed. The accuracy and precision of the displacement and strain were evaluated by the mean and standard deviation. It was found that DVC showed a variability in performance that was highly dependent on DVC methods. The maximum likelihood estimation method, which was considered as a global DVC algorithm [162], gave the best accuracy and precision when evaluating displacement and strain on all bone types. The dependence of DVC results on the analysis methods have been further demonstrated in the review by Roberts et al in 2014 [162]. Parameters such as DVC objective function, shape function, image subset size, image contrast and voxel size were all shown to affect the accuracy and precision of strain and displacement field. The optimization of these parameters requires significant computation effort. Therefore, Robert et al. gave a conclusion that regardless of the computational cost, a large subset size which enables it to be distinguished from other subsets (although smaller correlation subvolume size improves the displacement map spatial resolution but can introduces excessive noise in the displacement data [167]), a shape function which compasses the full set of affine transformation, a robust objective function and a high-order interpolation scheme were recommended for reduced displacement or strain errors [162].

In the commercial software Davis software, which is used in this project, Fast-Fourier-transform (FFT) and Direct-correlation (DC) are two embedded approaches for digital volume correlation. For both approaches, a piece-wise linear shape function and a normalized cross-correlation coefficient are used to evaluate the similarity between the reference and deformed grey level mappings. The difference lies on the use of a Fourier space for FFT and the direct coupling for DC. Multiple passes from bigger subvolume size to smaller final subvolume size are recommended in DVC calculation because the displacement field obtained from the previous step can be used to inform the next step and with the iterative interpolation and translation of grey level in the deformed image compared with reference one, the best correlation coefficient could be achieved. Previous studies had shown that the DC approach provided less error compared with FFT in the study of bones but with higher computation cost [168].

Apart the evaluation of deformation in biomaterials, Hussein et al.' study [117] shows the possibility using DVC to evaluate the initiation and propagation of cracks in whole bones under compression. The DVC method used in Hussein et al.'s work included two stages: 1) rigid body image registration, which removed the rigid-body motion; 2) maximum likelihood estimation.

2.5 Modelling of biomaterials

Modelling is used for the prediction of mechanical properties of biomaterials. It has several advantages: (1) to predict behaviours of materials under experimental conditions that are not currently experimentally feasible [169] (e.g. prediction of behavior in service); 2) to pre-run proposed experiment in order to testify and improve experimental protocols [169]; 3) to gain knowledge of materials by matching simulated and experimental results [170] [171]. The main relevant modelling techniques will be introduced in this section.

2.5.1 Image-based finite element modelling

In the project, image-based finite element models (FEM) will be used for the simulation of materials behaviours of biomaterials with the introduction of the real geometries and microstructures of specimens.

Image-based finite element models facilitate the generation of models based on materials, which have complex microstructures. Any digital imaging technique (e.g. magnetic resonance imaging, X-ray computed tomography), which provides a pixel or voxel map of finite resolution, can be used as the basis for finite element meshing. For example, after thresholding a grey level image into different material domains, meshes can be generated from individual voxels by assigning appropriate nodal connectivity and material properties. These meshes can then be imported into models to generate 3D finite element simulations of complex material systems [172] [173].

Results obtained from image-based FEM are highly influenced by the resolutions of images used for meshing. Increasing voxel size of the image leads to coarser meshes (*Figure 2.5.1*) and thus results in increasing loss of information about the microstructure such as connections of the microstructure within trabecular bones. As it is shown in *Figure 2.5.2*, underestimations of elastic modulus and average Von Mises tissue stress have been observed in FE models based on images with higher voxel sizes due to the loss of loading carrying bone mass during meshing [174].

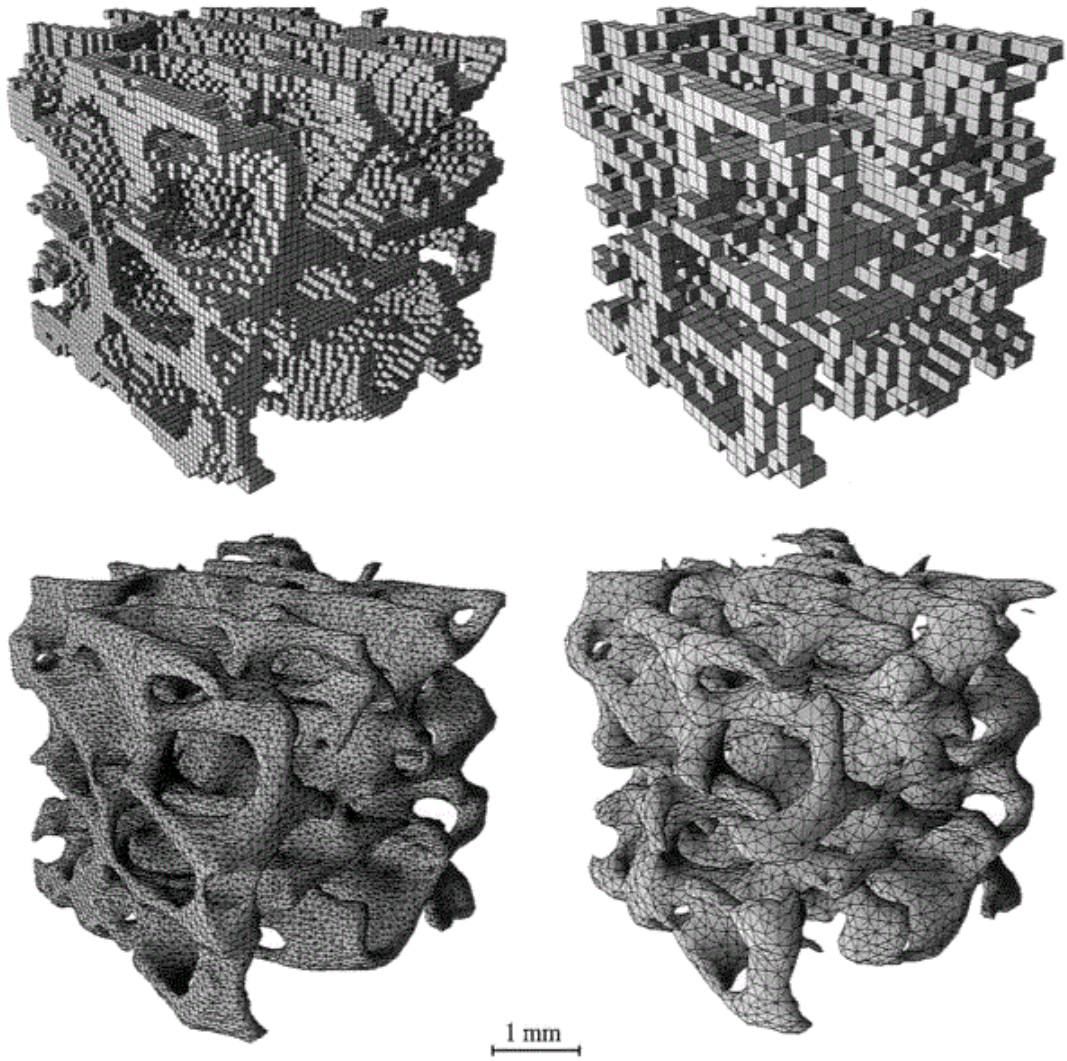


Figure 2.5.1. Finite element meshing of human femoral head at a voxel of 84 um (left) and 168 um (right) with hexahedron (top) and tetrahedron (bottom) meshes. Image with the voxel of 168 um results in much coarser meshes compared with image with the voxel of 84 um. The method which is employed to generate tetrahedron meshes, results in a smoother meshed bone surface and less loss of bone volume during thresholding. Finer meshes result in higher computation time [174].

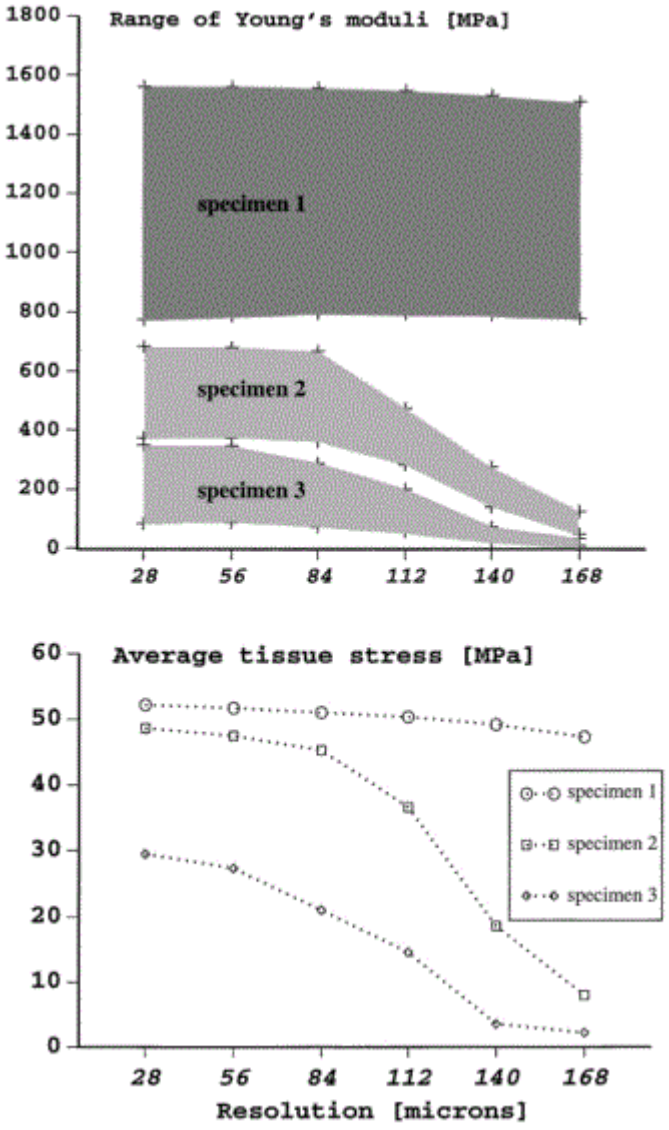


Figure 2.5.2. Mechanical properties calculated from finite element (FE) model based on plain voxel-conversion meshing technique versus voxel size. Top: predicted elastic modulus range versus voxel size of image used for meshing; Bottom: predicted average von Mises tissue stress versus voxel size of image used for meshing. The estimated elastic modulus and average Von Mises tissue stress decrease with increasing voxel size (coarser meshes) [174].

2.5.1.1 Modelling the mechanical properties of biomaterials

Various models, including finite element models, have been used for the prediction of the mechanical behaviours of natural materials such as bone and mollusc shells. These range from simple 2D analytical models that predict the basic properties, including stiffness [175] [113], strength [176] [177] and toughness [177–179], to more complex numerical models [180–182]

which incorporates deformation and crack propagation mechanisms into the 2D or 3D microstructures.

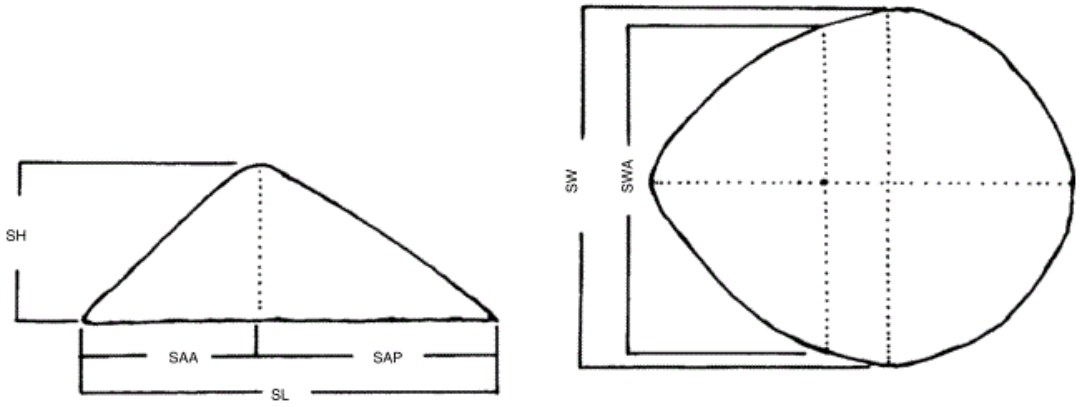
Models for the prediction of mechanical properties and material responses under loading of biomaterials are developed in order to solve the limitations of conventional mechanical tests and measurements. Limitations of mechanical test include: (1) Sample size: samples larger than 1 millimeter are a requirement for fully assessment of materials with heterogeneity in millimeter-scale [67]; (2) Sample preparation: due to requirements of specific sample geometries for standard tests, parallel surfaces must be obtained within small volumes of samples, which makes sample preparation difficult [67]. For example, larger specimen sizes of mollusc shells, for example, are difficult to prepare for compression tests due to their curved surfaces [12]; (3) Number of specimens required for different loading modes and loading directions in order to fully understand properties of heterogeneous materials [12]. It can result in additional difficulty in investigations of precious biomaterials such as human bones; (4) Limitations and errors resulted from conventional mechanical testing due to contact artifacts (e.g. damage at specimen ends, friction between specimen and compression platen, etc), which can be significant for small sample size [84], and the effects of off-axis loading on measurements [183]. To avoid these requires extensive care and work in experiment design, which can be aided using finite element analysis [82]. The use of finite element analysis also allows the simulation of displacement/strain/stress distributions in the 3D volume [82] and thus the prediction of fracture locations [184] under conditions that are difficult to realize in mechanical tests.

Some examples of image-based finite element models will be introduced in the following section.

2.5.1.1.1 Mollusc Shell

In the finite element models that were built by Cabral and Jorge [6] to simulate dried mollusc shells, a uniform and constant distribution of shell thickness was assumed and only the general

geometry of the shell was considered (*Figure 2.5.3*). For all simulations, shell material was considered the same, with an elastic modulus and Poisson coefficients of 1,000 MPa [185] and 0.2, respectively. The proposed simulations have fallen into two sets: the first set considered identical wall thickness for all species (average thickness based on thickness measurements of all specimens among four species) while the second set used different measured mean shell thickness for each species. The predicted forces with 1 mm deformation were compared with the real data obtained in the experiments (*Figure 2.5.4)* and it was found the simulated forces were lower than the observed values (*Table 2.5.1*). The difference between the models and experiments were possibly due to the use of the same approximated elastic modulus for the different shells. In addition, the relative rankings of compression resistance that were predicted were different from the experiment results. It was deduced that the external shell shape was not the only reason that contributed to the compression resistance of the shell. Other factors such as the internal microstructures and compositions of shells, which affect the shell properties. were proposed to also play a part in determining the mechanical behaviours of shells [6]. In addition, the changing of shell thickness from apex to margins may also contribute to the compression resistance of mollusc shells.



Species	SL	SW	SH	SAA	SAP	SWA	SH/SL	SAA/ SAP	SW SL
Patella intermedia	30	25.5 (25.4-25.7)	10.5 (10.3-10.8)	11.9 (11.7-12.1)	18.1 (17.9-18.3)	22.9 (22.8-23.1)	0.34 (0.33-0.35)	0.64 (0.62-0.65)	0.83 (0.81-0.85)
Patella rustica	30	25.3 (25.1-25.5)	13.1 (12.8-13.4)	12.4 (12.2-12.7)	17.6 (17.3-17.8)	23.4 (23.2-23.7)	0.44 (0.43-0.46)	0.72 (0.70-0.75)	0.86 (0.83-0.89)
Patella ulyssiponensis	30	23.3 (23.0-23.7)	9.3 (9.0-9.6)	12.3 (12.0-12.6)	17.7 (17.4-18.0)	20.1 (19.8-20.4)	0.24 (0.22-0.25)	0.54 (0.51-0.56)	0.60 (0.57-0.62)
Patella vulgata	30	24.1 (23.9-24.3)	10.9 (10.6-11.2)	12.1 (11.8-12.4)	17.9 (17.6-18.2)	21.7 (21.5-21.9)	0.30 (0.29-0.31)	0.57 (0.54-0.60)	0.67 (0.64-0.71)

Figure 2.5.3.Mean measured geometries of multiple samples of four shell species. The measured values were used to create 3D volumes of different shell species in FE models. SL is shell length, SW is shell width, SWA is shell width at the apex, SH is shell height, SAA is shell length from apex to anterior end, SAP is shell length from apex to posterior end [6].

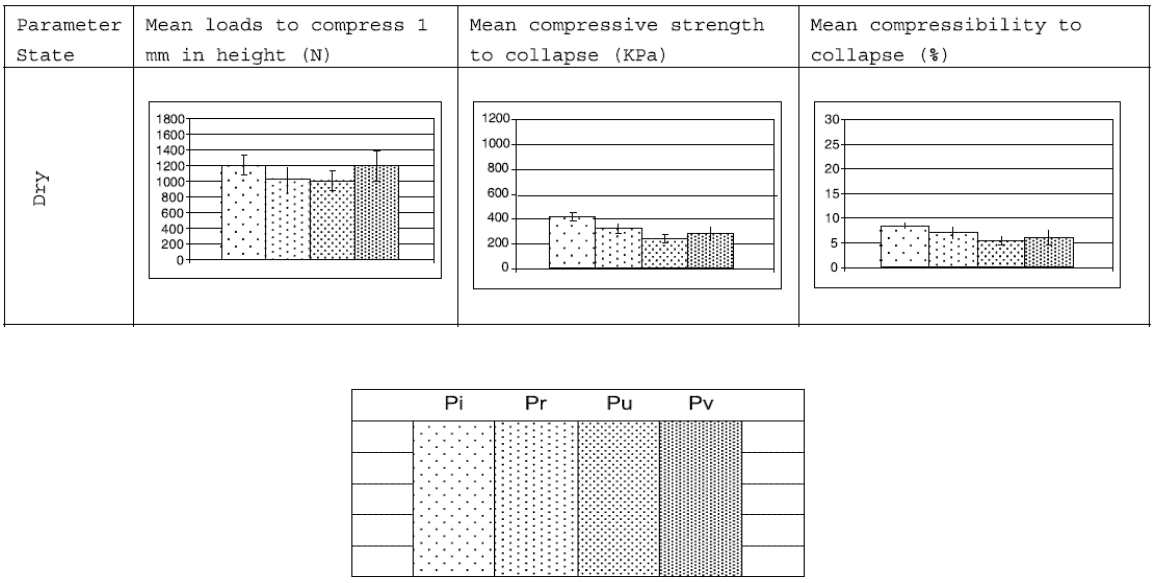


Figure 2.5.4. Experimental results for standardized 30-mm height shells. Pi, Pr, Pu and Pv are four species of shells: Pi----P. intermediate, Pr-----P. rustica, Pu----P. ulyssiponensis and Pv----P. vulgate [6].

Table 2.5.1. Simulated force to compress shell 1 mm in height [6].

Simulated force to compress 1mm in height (N)	First set of simulations	Second set of simulations
P. rustica	335 N	399 N
P. vulgata	286 N	302 N
P. intermedia	258 N	307 N
P. ulyssiponensis	258 N	230 N

Apart from predicting mechanical properties of seashells, linear-elastic contact FE models (*Figure 2.5.5*) based on geometries of mollusc shells have been developed by Shojaei et al. [184] for the prediction of fracture locations under compression by computing the distribution of principal stress within the 3D volume of shells. The shell material is assumed to be isotropic with an elastic modulus of 50 GPa and a Poisson's ratio of 0.31. In addition, the tensile and compressive strengths of the shell are assumed to be 40.3 MPa and 257.1 MPa. All these mechanical parameters used for modelling are from literatures [26] [186]. A fixed 2.88 mm displacement was applied to the shell in loading direction in the model with a loading rate of 0.15mm/min, simulating the

experiment. Simulated maximum stresses in stress concentration areas (*Figure 2.5.6*) which agree with the real fracture areas in experiments, eventually exceed the maximum and minimum stress criteria set in the model (compressive and tensile strengths) and the probability of failure increases [184]. The mechanical properties used in the reported model are assumed and therefore need further discussion in order to investigate the impact of these parameters on simulated stress field and thus testify the accuracy of the simulation.

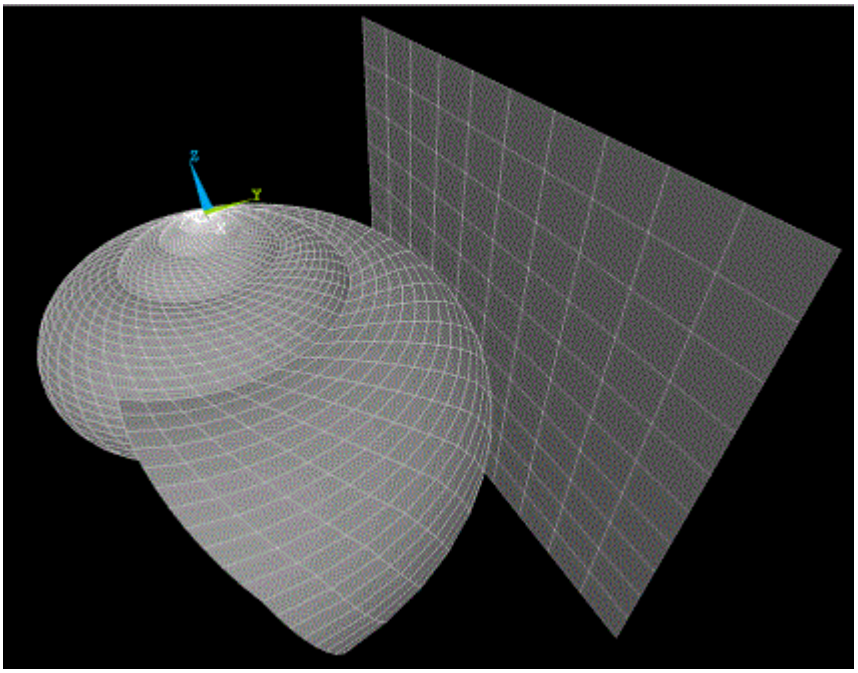


Figure 2.5.5. 3D volume of mollusc shell and loading plate in finite element model [184].



Figure 2.5.6. Results from experiments and simulations at the final step. Two failure areas of tested samples on the (a) aperture and (b) columella. Stress concentrations predicted in FE analysis: (c) the third principal stress field (the most negative stress) on the aperture; (d) the first principal stress field (the most positive stress) on the columella [184].

2.5.1.1.2 Bone

Various models including finite element models [187–190] have also been built to analyse bone at microstructure scale. One of the very early models was reported by McElhaney et al. [191], in which cranial bone samples with different microscopic structures (cortical bone plus trabecular bone) were assumed to share identical microscopic properties. The local density, which is assumed to proportionally relate to elastic modulus and ultimate strength, and internal geometry were the two parameters that were taken consideration into the model (*Figure 2.5.7*). Good correlations between the experimental and the predicted modulus and strength have been observed (*Figure 2.5.8*).

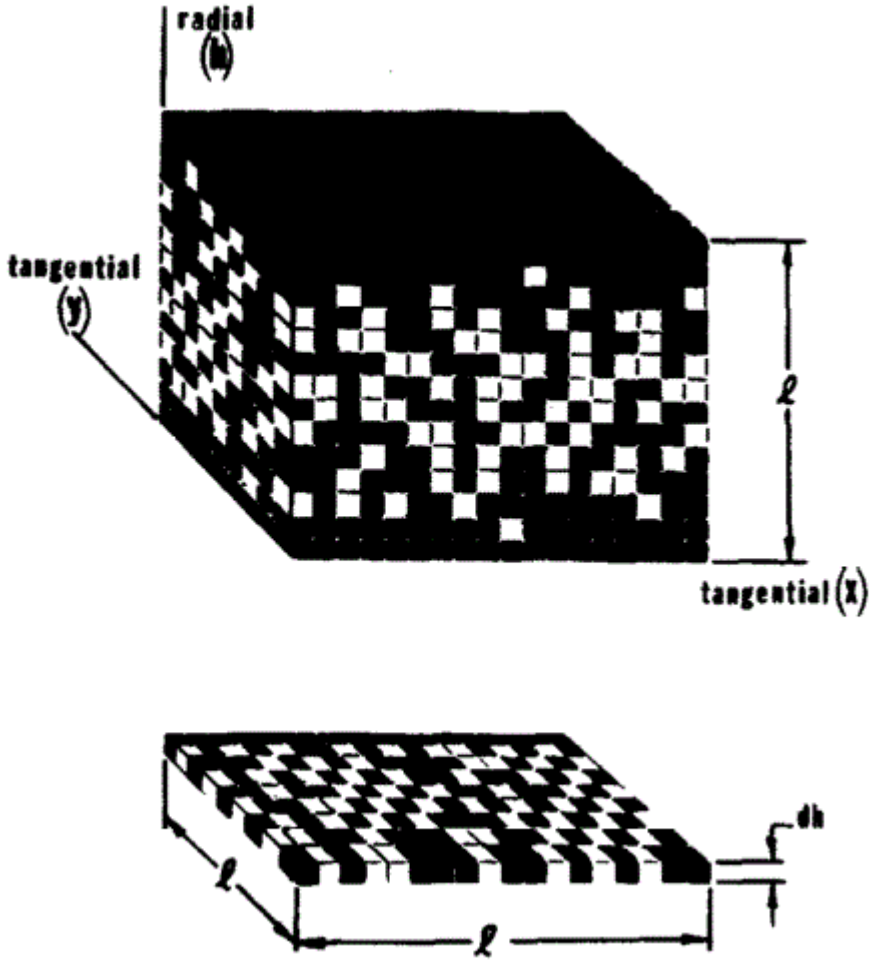


Figure 2.5.7. Porous block model of cranial bone. White blocks indicate pores while black blocks indicate bone matrix. Bone in the tangential direction has homogeneous distribution of pores while in radial direction an increase in porosity moving from outer face to inner region [191].

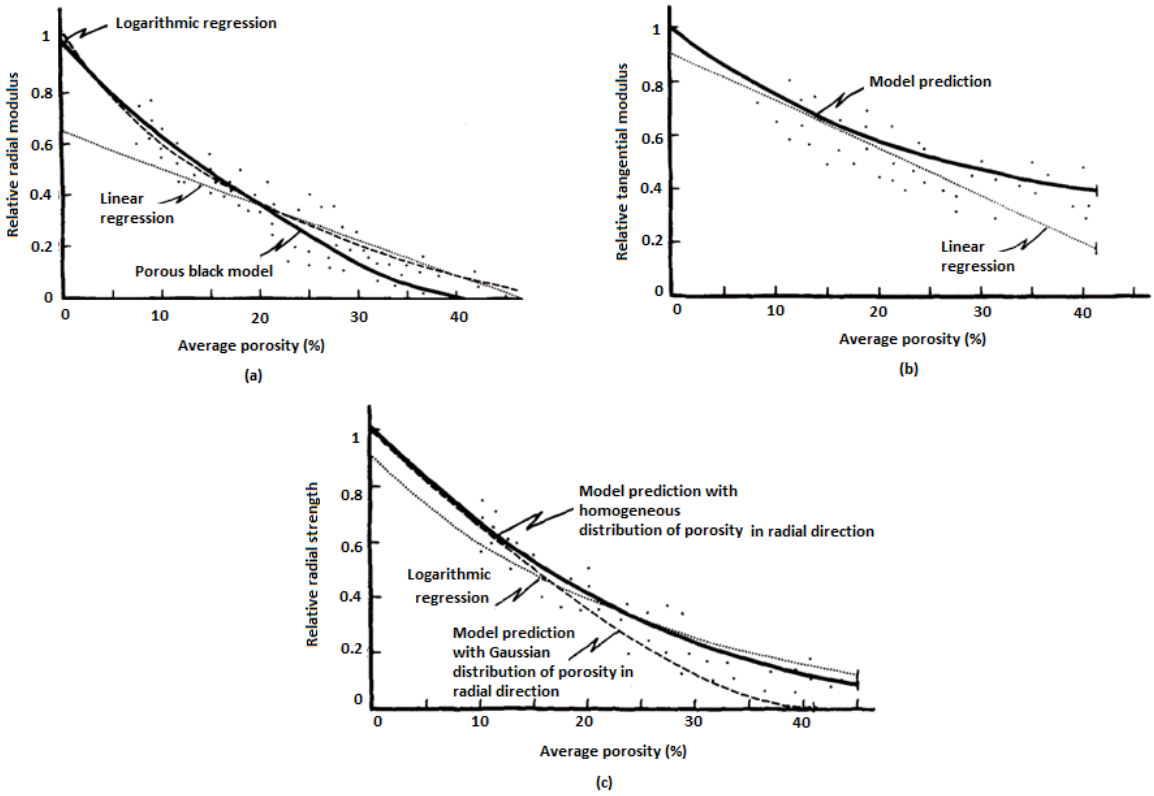


Figure 2.5.8. (a) (b) Comparisons between predicted normalized elastic moduli (E/E_0 normalized by $E_0=1.8x10^6$ psi) in radial and tangential direction & normalized strength (σ/σ_0, $\sigma_0=21,000$ psi) and experimental ones versus porosity. (c) Comparisons between normalized strength (σ/σ_0, $\sigma_0=21,000$ psi) and experimental ones versus porosity. Experimental results are fitted by either linear regression and logarithmic regression [191].

Instead of using sketched structure, a three dimensional FE model was built by Müller and Rüegsegger [155] using a real segmented trabecular bone structure (21x20x20 voxels) (*Figure 2.5.9*) from low resolution computed tomograph (CT) with a resolution of 250 um. A compression of 0.6% strain was applied, and the apparent Young's modulus (564 MPa) was calculated from the simulated stress and global applied strain, which falls into the range of experimentally measured apparent moduli of trabecular bones in literature [81,84,86,90].

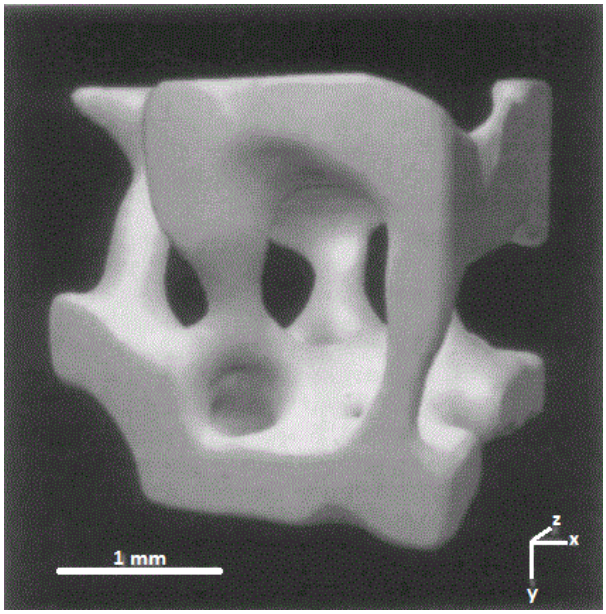


Figure 2.5.9. Three dimensional visualization of bone structure representing 21x20x20 voxels [155].

Grimal et al [67] developed a numerical model which used data from scanning acoustic microscopy to introduce the real geometry of cortical bone including the shape, number and sizes of pores into the modelling. In addition, the model also considers the anisotropy of bone matrix, which was not mentioned by Müller and Rüegsegger's model [155] in order to further increase the accuracy and reliability of the results. The whole model is based on a finite element homogenization procedure. The predicted mechanical properties of cortical bones have been reported to have a good agreement with experimental results (*Figure 2.5.10*). However, this model requires high computation cost when it comes to systematic parametric studies.

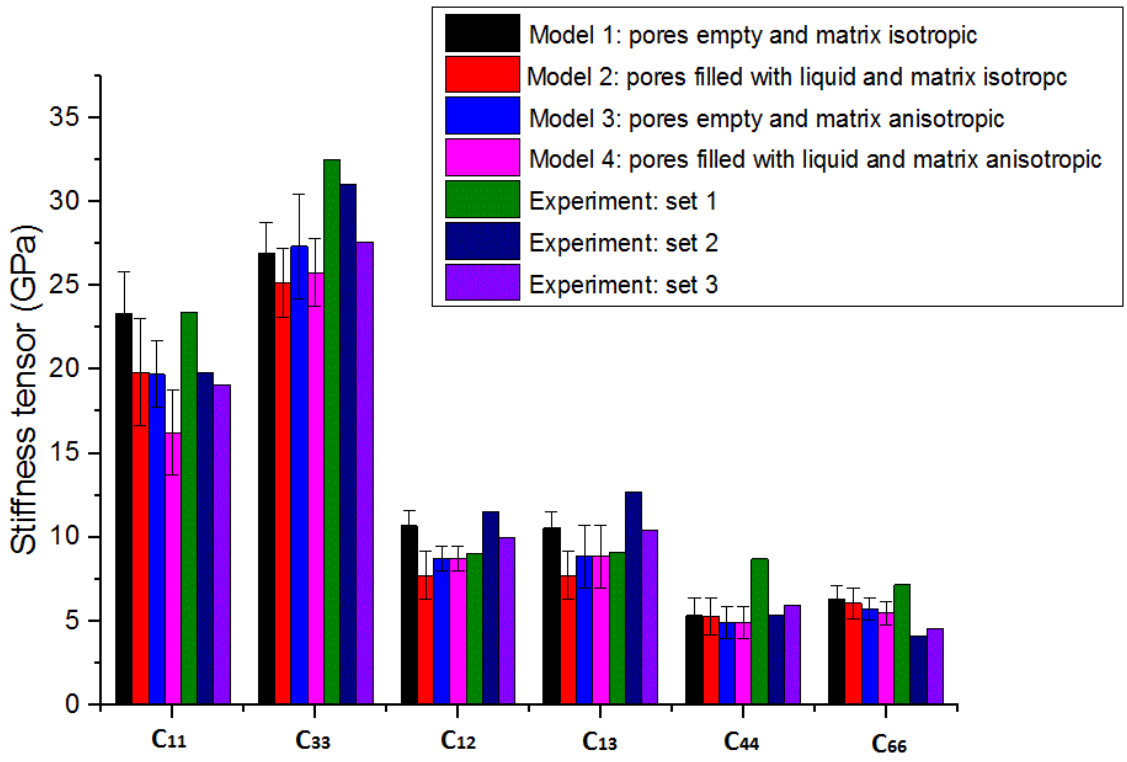
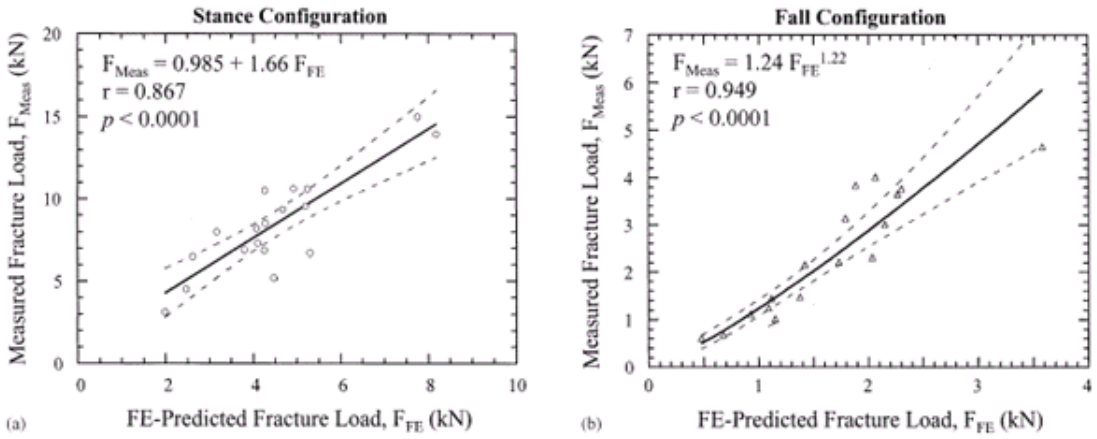


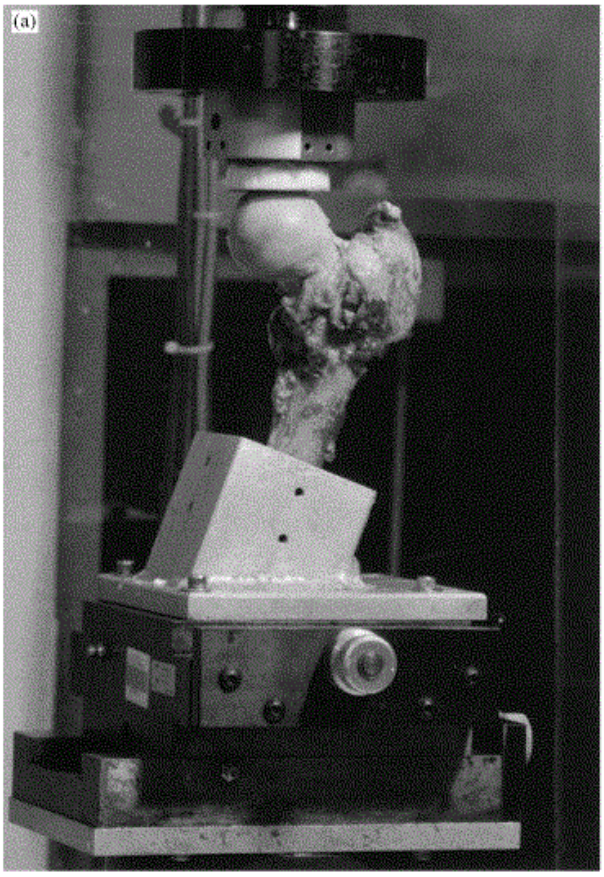
Figure 2.5.10. Comparisons between predicted stiffness tensors based on models with different assumptions of pore content and bone matrix property and experimental results [67].

Further improvement has been made in a combined CT/FE approach proposed by Keyak et al [192] to predict femoral fracture load under stance and fall loading conditions (*Figure 2.5.11*). Instead of using same materials throughout the specimen, heterogeneous material properties were assigned to different elements in this model. Simple loading boundary conditions, based on experiments, were applied to the meshed geometry of a femoral obtained from CT. The obtained results had a relatively good agreement with measured values in both loading configurations


Stance Configuration
$F_{Meas} = 0.985 + 1.66\ F_{FE}$
r = 0.867
$p < 0.0001$
Measured Fracture Load, F_{Meas} (kN)
FE-Predicted Fracture Load, F_{FE} (kN)
(a)
Fall Configuration
$F_{Meas} = 1.24\ F_{FE}^{1.22}$
r = 0.949
$p < 0.0001$
Measured Fracture Load, F_{Meas} (kN)
FE-Predicted Fracture Load, F_{FE} (kN)
(b)

(

Figure 2.5.12).


(a)

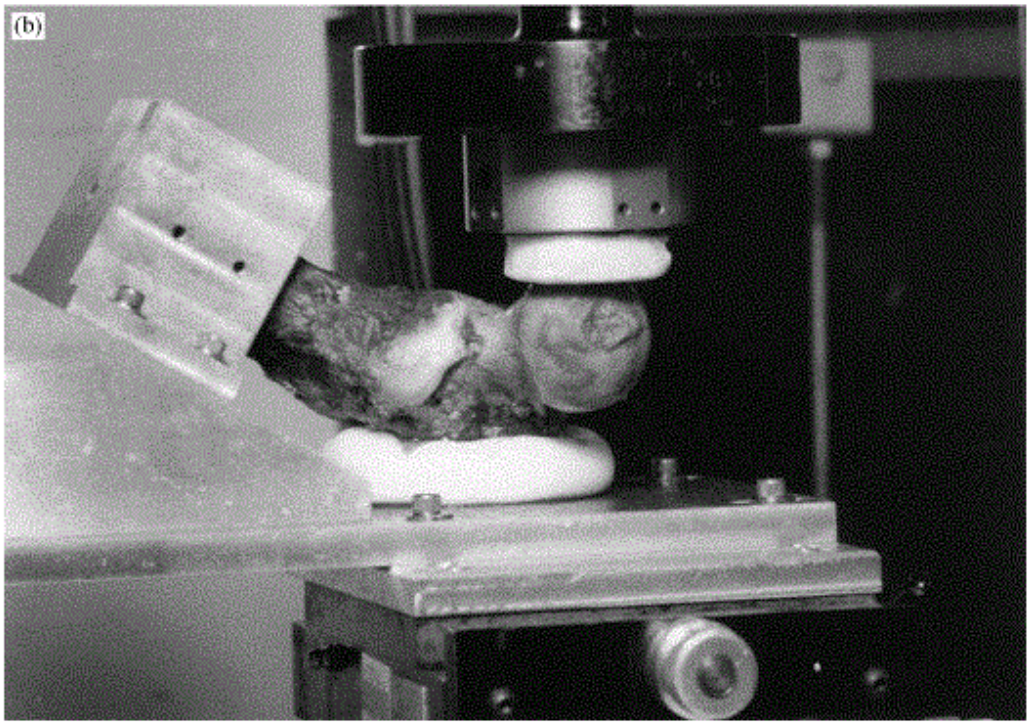


Figure 2.5.11. a) stance; (b) fall loading configurations [192].

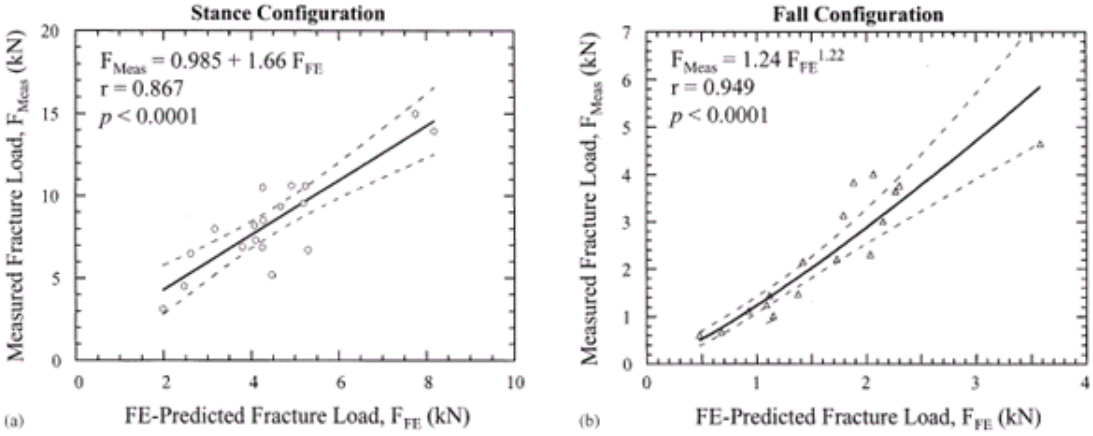


Figure 2.5.12.Measured fracture load versus simulated facture load for different loading configurations. (a) Stance; (b) fall. Dashed lines indicate the bounds of the 95% confidence intervals for the regression equations [192].

Virtual field method which extracts mechanical properties of materials (e.g. stiffness tensor) from full-field displacement measured by imaging complex-configured mechanical tests, has also been successfully applied to biomaterials such as wood or biological tissues to extract anisotropic moduli based on computed strain field [193].

Apart from prediction of mechanical properties, finite element models of biomaterials have also facilitated the design of biomimetic materials. Jaecques et al used micro CT-based finite element modelling to quantify the stress and strain fields in bone tissue and in tissue constructs in order to optimize the design of bone scaffolds [194]. Bessho et al also used a CT-based finite element model to estimate the strength, maximum strains and fracture site of the proximal femur under compression in order to design preventive strategies for elderly people who suffered from osteoporosis. The region of fracture of femur predicted by the simulations was found to be approximately the same as the experimental result [195].

2.5.2 Reverse engineering modelling

Reverse engineering modelling can provide a powerful approach to validate, modify and improve established models by matching experimental results with simulated ones. Importantly, it can also be used to extract material properties from experiments that have complex loading and geometry.

Reverse Engineering Modelling is a process that consists of several steps including data capture and pre-processing, segmentation of data point clouds which classify different regions, meshing and surface fitting to create a model and the development of the geometric model based on the specific application [196] [197]. Applications of reverse engineering modelling on materials have been introduced as following.

A mixed numerical-experiment method (*Figure 2.5.13*) of reverse engineering model has been used by Geers et al. [198] on fibre reinforced polypropylene plates with different fibre lengths and orientations. Displacement fields collected from Digital Image Correlation analysis of non-deformed and deformed images of the pre-notched material were used as the input for the finite element model. An optimized set of materials properties (θ) was determined which gave the closest agreement of simulation output (*h)* to the experimental measurement (*m*) (*Figure 2.5.14*).

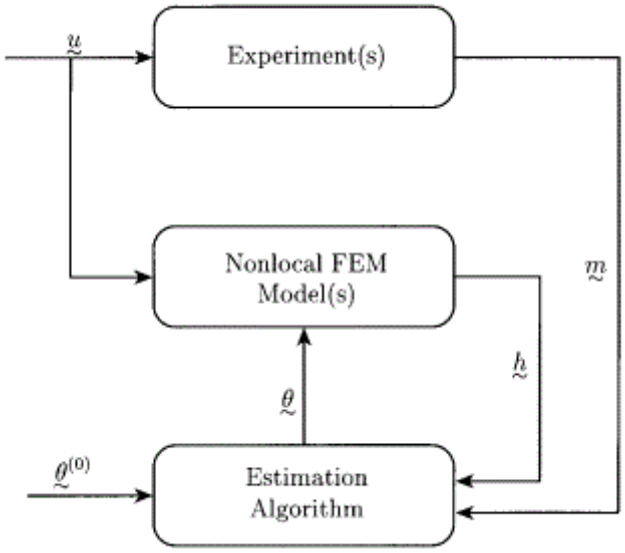
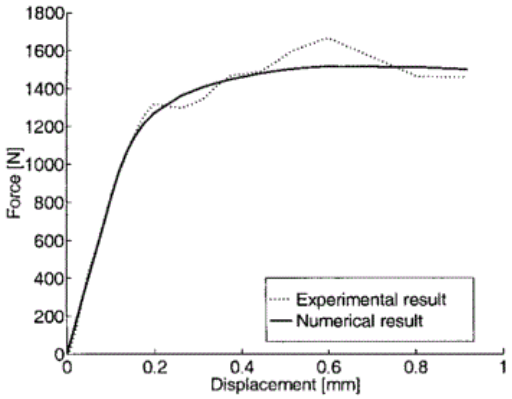
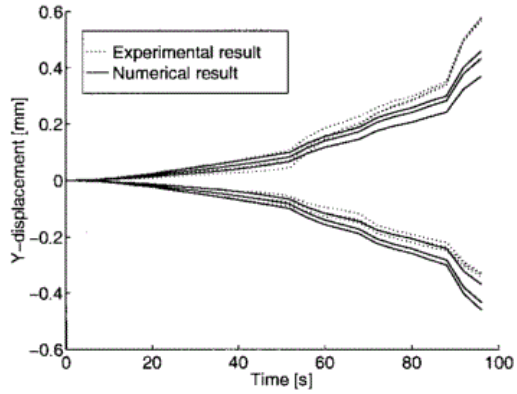


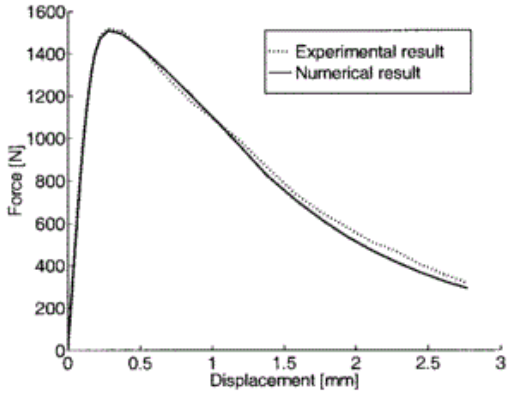
Figure 2.5.13.Mixed numerical-experiment method. u is the input for both experiment and numerical analysis, m is the measurement set collected from experiment, ɵ is stored unknown materials properties in model ($ɵ^{(0)}$ is the first estimation of these materials parameters), h is the response from the model which is a function of m and ɵ [198].



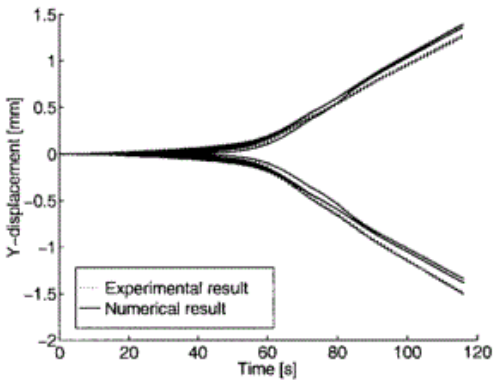
(a) Forces in GMT–SM.



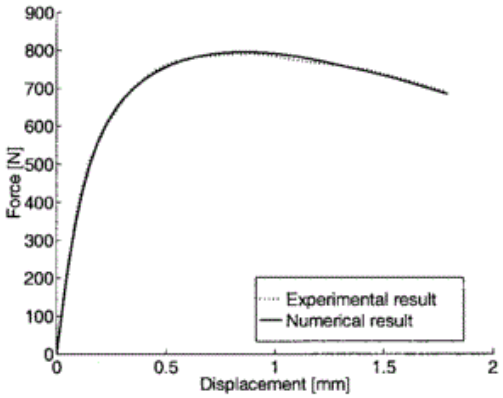
(b) Displacements in GMT–SM.



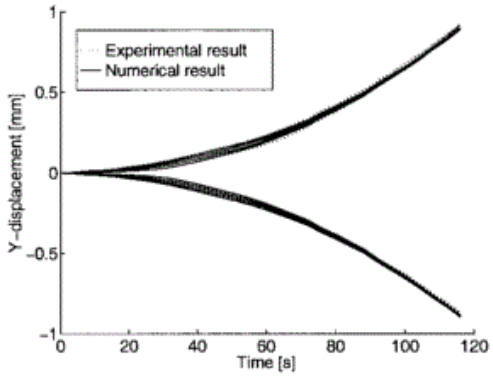
(c) Forces in GMT–PM.



(d) Displacements in GMT–PM.



(e) Forces in SFRTP.



(f) Displacements in SFRTP.

Figure 2.5.14. Computed force and displacement versus experimental ones of different fibre reinforced polypropylene composites. (a)(b) Glass mat thermoplastics (GMT-SM), the glass mat of which are melt impregnated on a belt press; (c)(d) Glass mat thermoplastics (GMT-PM) which are manufactured using paper making process; (e)(f) Short glass-fibre reinforced thermoplastics (SFRTP) using injection moulding. Displacements used for (a),(c),(e) on horizontal axes are measured from DIC analysis [198].

Lin, Li and Fok [199] developed a finite element model, based on reverse engineering and experimental strain mapping, to predict the distribution of elastic modulus in inhomogeneous materials such as graphite. With predefined Poisson's ratio, iterative steps are used for tuning the Young's modulus of individual elements using three types of modulus distributions (homogeneous, linear and random distributed) until the simulated strain field matched with the experimental one. As a result, the distribution of material properties throughout the sample can be predicted. The used Poisson's ratio is 0.16 in this model and the strain distribution from experiment which is used for matching with simulation, was obtained under a load of 3.955 kN. This method has been successfully employed to predict the distribution of elastic moduli within graphite disc under compression (*Figure 2.5.15*). The proposed model by Lin, Li and Fok [199] has advantage over other models for engineering analysis which tend to consider materials as homogeneous, isotropic and linear elastic. However, in reality, many materials are heterogeneous, anisotropic and non-linear elastic.

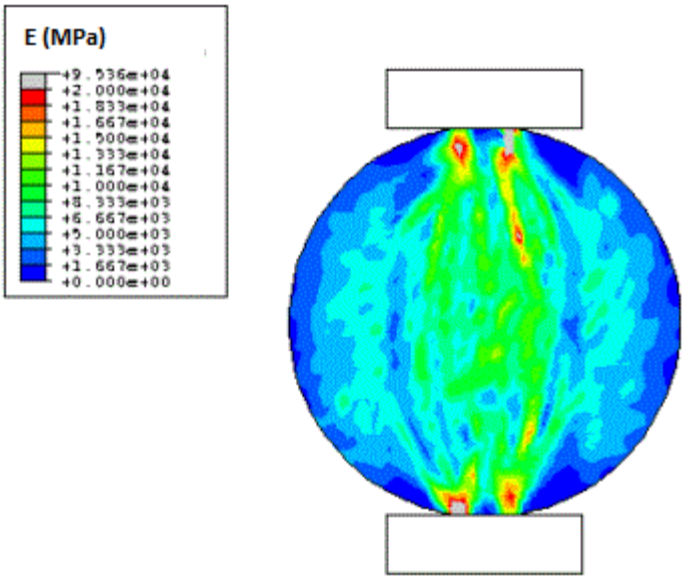


Figure 2.5.15. The distribution of elastic moduli within graphite disc under compression [199].

Three-dimensional finite element models based on reverse engineering techniques on biomaterials have also been presented. In Aghili et al.'s work [170], the stress/strain fields within human femurs have been predicted. Models are developed based on the real geometries of the half and whole human femurs and analysed by applying single (apply total load to one node), expanded (apply total load on all surface nodes of femur head) and partial expanded (apply total load at 50 nodes on the femur head surface) loads onto the sample. With the good agreement of the simulated displacement field with the experimental one, the accuracy of the chosen material properties and the simplifying assumption that the model considered the bone materials as isotropic, can be verified [170]. In Yosibash's work [171], instead of considering bone material as a continuum, different apparent elastic moduli were assigned to different regions (trabecular, cortical, etc) of proximal femur. These were based on the relation between elastic modulus and apparent density, and were implemented in a finite element model with the real geometry of the femur obtained from CT. By tuning the relation between elastic modulus and apparent density in the model, the relation which achieves the closest simulated forces compared to experimental results was selected with 1mm displacement applied. After that, the selected

relation between elastic modulus and apparent density was used for the comparison between simulated displacements and experimental ones at different loading angles related to the long axis of femur (*Figure 2.5.16*), achieving a good agreement.

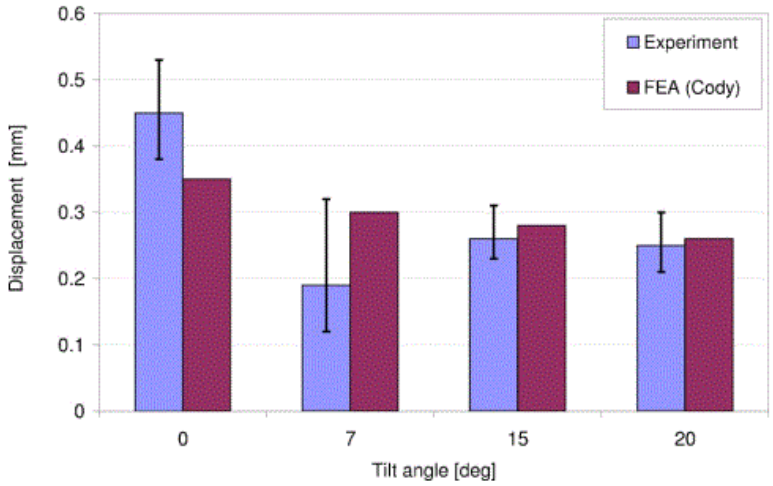


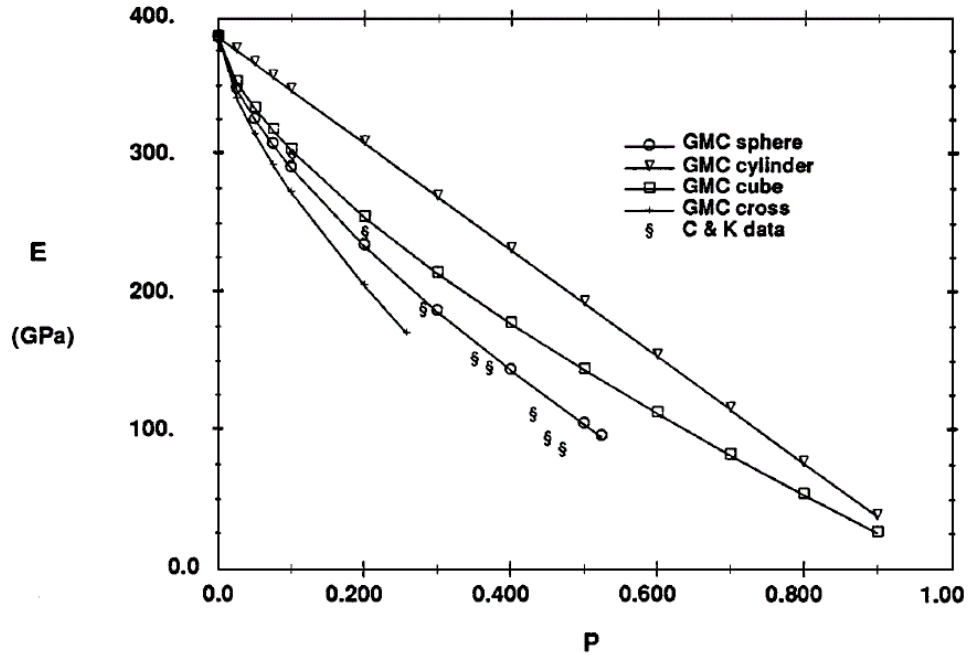
Figure 2.5.16. Finite element analysis of displacements compared with experimental ones (femur head under a compression of 1500N at different loading angles). The error bars indicate the minimum and maximum measurements of displacements during experiment [171].

2.5.3 Image-based modelling of the effect of porosity on elastic modulus

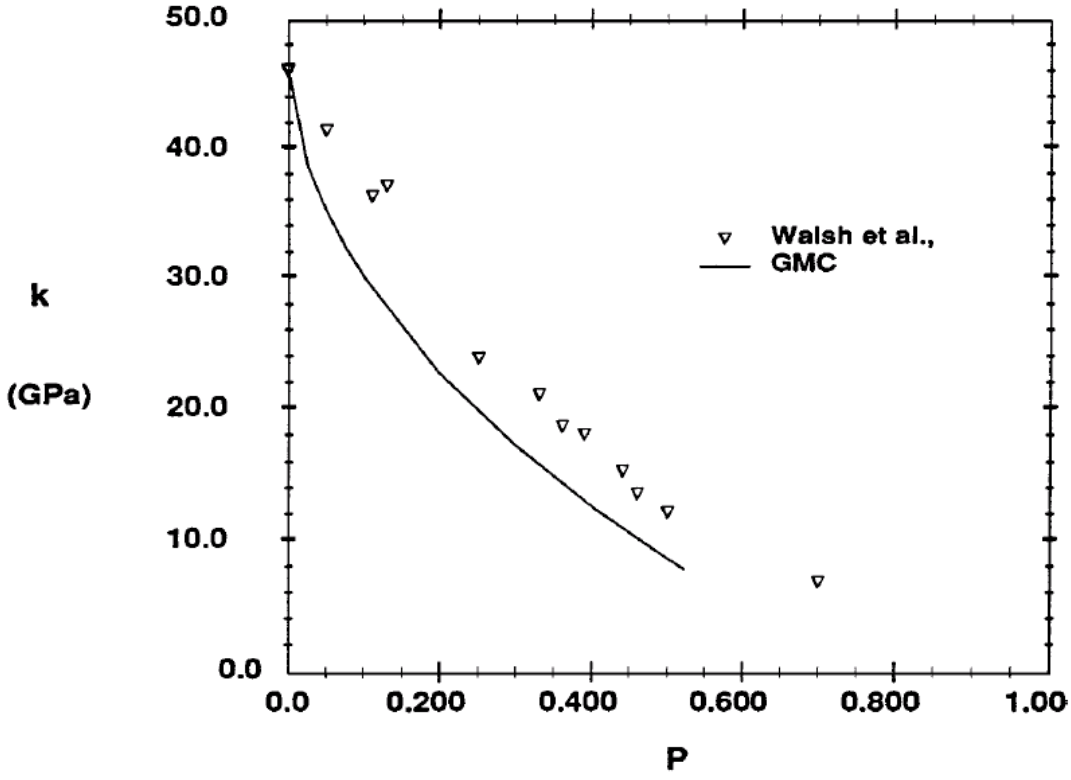
Image-based models may also be applied at the microscale, and because it is proposed that porosity is a determinant of the bone apparent elastic modulus [64] [56] [65] [66], models relating porosity with elasticity of porous materials have been reviewed, as they may have application for porous biomaterials including bones.

Various models have shown that an arrangement of spherical pores with increasing pore fraction will decrease the elastic modulus [200] [201]. And apart from porosity, the pore shape [202] is also an important factor which influences the elastic modulus of porous materials. Models based on the generalized methods of cells (GMC) have been used to simulate elastic modulus of porous alumina and glass and compared with experimental results [203] [204]. Both simulated data in an assumption of sphere pores which are expected for sintered ceramic powder,

achieved a relatively good agreement with experimental data (*Figure 2.5.17*). The GMC simulation of cube-shaped pores [202] also shows an excellent agreement with minimum solid area model proposed by Rice [205], who explained the effect of pore geometry and packing arrangement on elasticity of porous material using the relation between pore geometry with minimal solid areas, over the full range of porosity.



(a)



(b)

Figure 2.5.17. Comparison between simulated elastic modulus based on GMC and experimental result. (a)Alumina with different pore shapes; (b) Glass with spherical pores [202].

Because bone is a porous material, models based on the relation between pore network and elastic modulus of bone have also been established by researchers. Sevostianov and Kachanov [56] proposed a model which simulates the influence of three types of pores (Haversian canals, Volkman's canals and canaliculi) on elastic moduli in different directions. They found that for transverse directions, the predicted elastic modulus is insensitive to partial porosities denoted by different pore types while in longitudinal direction, elastic modulus is dependent on the partial porosity contributed by Haversian canals. The predicted stiffness tensors are in relatively good agreement with ultrasound experimental results [206] [207] . The advantage of the model is that it takes the size, shape and orientation of pores into consideration based on the theory proposed by Kachanov, Tsukrov and Shafiro [208]. However, the model doesn't treat the bone matrix as an anisotropic material. This is important, because nano-indentation tests on bone matrix components [56] show that it is anisotropic, and so its influence cannot be ignored. This was also noted in Grimal et al.'s model [67]. In addition, models that are based on the basic shape of pores and a rather simple geometric approximations of cortical bone do not reflect the real structure of the material [56].

2.5.3.1 PReMISe

The PReMISe model, which is based on the generalized methods of cells (GMC), was developed in 2017 by Vertyagina to study the significant effect of pores on elastic modulus of quasi-brittle porous materials. A limited number of cellular automata (CA) cells in the model have been assigned with different states in order to represent hierarchical microstructures within the material (e.g. cells representing pores have been assigned with null properties) and follow the rule of evolution such as fracture damage. It has been proved successful in predicting the properties of nuclear graphite, which had been exposed to radiolytic oxidation, and obtained a good agreement with experimental results even for samples with highs level of oxidation and high porosity. Compared with other models [200] [209] [201], PReMISe, as a multi-scale model, solves issues by considering the detailed microstructure of the material, the real geometry of

pores and the wide distribution of pore sizes [210]. It uses a cubic voxel description of the microstructure and is well suited to be applied to CT data.

PReMISe employs Phani's general relationship for the calculation of elastic modulus for porous materials based on the provided pore network:

$$\frac{E}{E_0} = (1 - aP)^n \qquad \textit{Equation 2.5.1}$$

where E_0 is the Young's modulus of pore free material, *E* is the apparent elastic modulus of the material, *a* is in the range from 1 to 3.85 which is a packing geometry factor (a is set to be 1 in all the simulation of elastic modulus in PReMISe which satisfies zero modulus when porosity reaches 100%) while *n* is extracted based on the pore geometries as below:

$$n = (\frac{A_{surf}}{A_{total}})^{-k} \qquad \textit{Equation 2.5.2}$$

where *k* is ½, a topological factor which is decided by the cubic cell shape in the model, A_{surf} is the sum of the free surface area of matrix cells around the pore which have no free surface parallel to the loading direction, A_{total} is the sum of the free surface area of all the matrix cells around the pore. A_{surf} and A_{total} are schematically demonstrated in *Figure 2.5.18*.

For Phani's relationship, at the same value of *a*, the theoretical value of *n* is equal to 2.14 for a distribution of closed spherical pores while *n* is equal to 4.12 for interconnected irregular pores. Unlike Phani's rule, *n* is not constant in PReMISe and it is calculated directly from pore microstructure via *Equation 2.5.2*. Simulations of E/E_0 for spherical, ellipsoidal and arbitrary pores in PReMISe agree well with Phani's curves for spherical and irregular pores over a wide range of porosity *(Figure 2.5.19*) [210]. This shows it may be a useful tool to simulate the elastic properties of porous bone that contains an arbitrary distribution of pores.

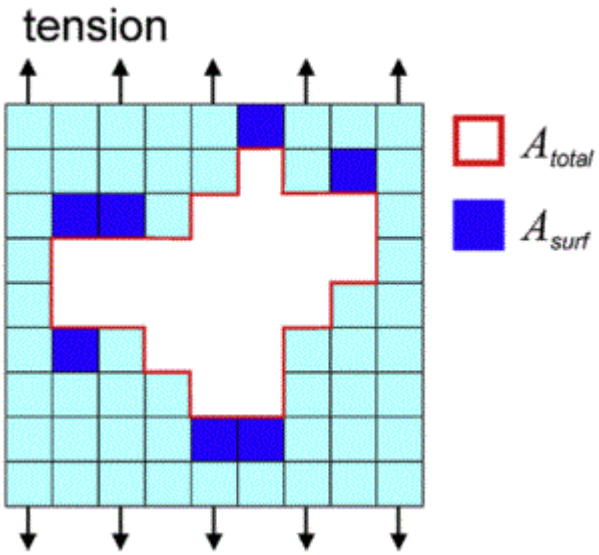


Figure 2.5.18.Schematic pore geometry in a cubic lattice in PReMISe model [210].

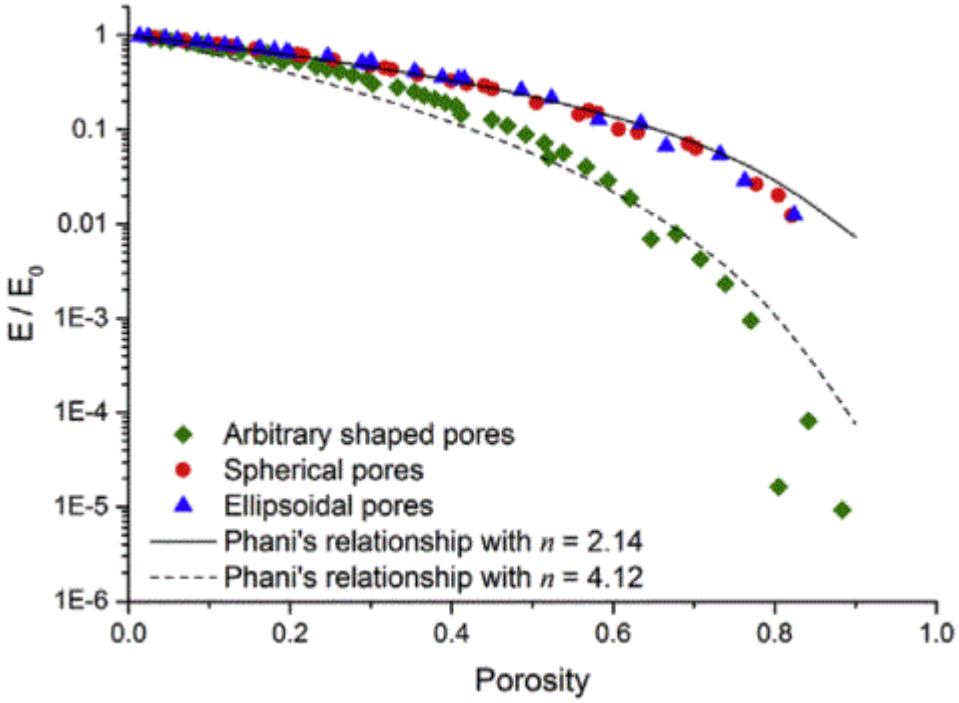


Figure 2.5.19. Comparisons between PReMISe simulations of pores with different shapes and Phani's relationship [210].

2.6 Summary

This literature review can be mainly divided into four main sections: biomaterials, techniques for the extraction of mechanical properties of biomaterials, image-based techniques which provide information for modelling and examples of the different model approaches for the prediction of

mechanical properties of biomaterials or their extraction from experimental data by reverse modelling.

The biomaterial section consists two parts: mollusc shells and bone. The chemical compositions, microstructures and mechanical properties of different mollusc shell species have been noted and the factors (shape, microstructure, hydrated condition, etc) which influence shells' mechanical properties have been summarised. The obtained knowledge can be useful for the design of biomimetic materials. With regard to bone, the morphologies at the macro-scale and micro-scale of cortical and trabecular bones have also been described, with the reported mechanical properties including apparent and intrinsic elastic moduli in different loading directions. Fracture toughness data for bones have been summarized and various experimental methods used for fracture toughness measurement have been compared. Important factors which influence bone properties such as porosity, age and gender have been looked into, as these provide useful information for modelling.

The common experimental techniques which have been employed for mechanical property measurement have been summarised. Modelling, for the extraction of mechanical properties from biomaterials, has been developed in order to address the limitations of mechanical testing, so the techniques which are commonly used to facilitate modelling of biomaterials have been introduced. In particular, X-ray tomography provides real geometric information for modelling and has been introduced together with its applications in biomaterials. The principal of digital volume correlation (DVC) has been explained together with its application with X-ray tomography in biomaterials to provide information of displacements in 3D volumes under loading, from which strain and stress fields can be derived. The obtained information can thus be used for either comparing with simulated results for validation or used as boundary conditions in models for further investigation of other materials' properties.

Different modelling techniques especially the finite element method that have been applied to biomaterials have been reviewed, in the context of both clinical application and biomimetic materials' design. Models which emphasize the relation between pore-network in elastic materials and their properties have been looked into which may have potential use to link pores to elastic properties of porous biomaterials such as bones.

The challenge addressed in the current study is to investigate and extend the application of such models to give reliable predictions of mechanical properties of biomaterials with complicated and hierarchical microstructures. Two different biomaterials have been selected, one with a complex external geometry (mollusc shell, i.e. common British limpet) and one with a complex inner geometry (porous bone).

Chapter 3

3 Experimental and analysis methods

This chapter is divided into two sections that separately describe the experimental methods and analysis methods. In the first section on experimental methods, the scanning techniques used for obtaining 3D microstructures of mollusc shells and bones are introduced together with examples of the obtained X-ray tomograph results. In-situ tests, which include compression testing of limpets and Hertzian indentation on bones are presented in detail, and tomography results of deformed specimens along with the recorded mechanical behaviours upon loading are presented.

In the second section on analysis methods, a set of complementary techniques related to experiment development and modelling are presented. This section includes DVC analysis of rigid body movement to testify the suitability of displacement field extraction based on in-situ tests and also the porosity measurement using the Avizo software. These porosity data are later used to build the relationship between porosity and simulated elastic moduli of cortical bones from PReMISe and so a description is provided of the pre-processing of tomographs of cortical bones that was necessary to use PReMISe software for elastic modulus prediction.

3.1 Experimental methods

3.1.1 X-ray tomography of the microstructures of limpet and cortical bone

3.1.1.1 Limpets

Common British limpets, which were collected from a UK beach, were chosen for the investigation of their mechanical properties due to their efficient adaption and excellent mechanical behaviour in circumstances where they are prone to impacts brought by waves, currents, hard objects (e.g. logs and boulders) and predatory creatures. Limpets are also selected as they have good accessibility compared with other materials such as human bone. Preliminary observations were made using laboratory and synchrotron X-rays as part of the process of experiment design for subsequent in situ mechanical tests. It is useful, at this stage, to describe the methods and the nature of the data obtained.

3.1.1.1.1 Laboratory X-ray tomography (normal absorption and phase contrast)

Limpets shells were first studied both as-whole and in a small 2 mm x 2 mm x 2 mm fragment, which was removed, using an abrasive cutter, from the wall of a limpet to examine the interaction between specimen size and data quality using Oxford's ZEISS Xradia 510 Versa High-Resolution 3D X-ray Tomography microscope. A typical limpet shell is shown in *Figure 3.1.1*. This particular limpet is approximately 25 mm in length, 20 mm in width and with a shell thickness of about 2 mm.

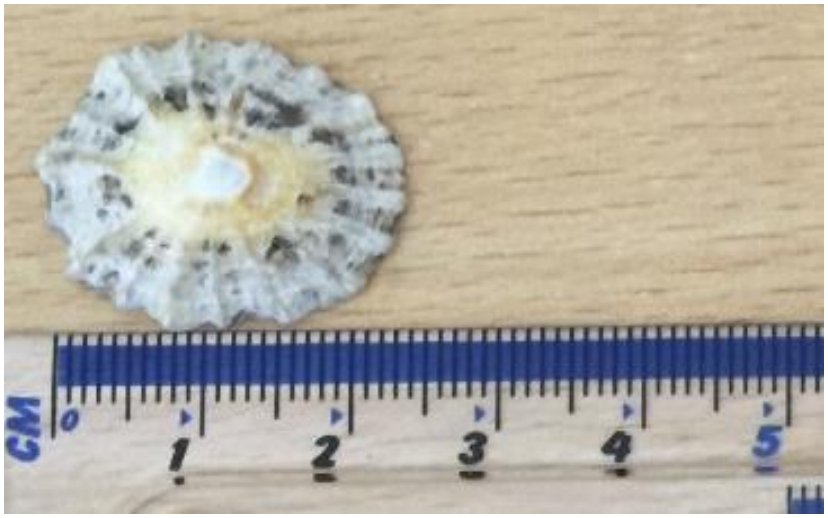


Figure 3.1.1. A limpet shell.

Calcium carbonate and protein are two main components of mollusc seashells [7]. In order to identify good condition to obtain contrast between these two phases in X-ray imaging, linear attenuation coefficients of both components versus photon energy have been calculated for the selection of optimum scan voltages [211]. Linear attenuation coefficients of absorbing materials under ideal narrow-beam conditions satisfy:

$$\frac{ln\left(\frac{I_0}{I(x)}\right)}{x} = \mu \qquad \textit{Equation 3.1.1}$$

Where μ (cm^{-1}) is the linear attenuation coefficient, I_0 is the initial photon intensity and $I(x)$ is the photon intensity after passing an absorber with thickness of *x* [212]. From the curves (*Figure 3.1.2*), the attenuation coefficients of both components are close to each other and thus phase contrast scan would be favoured, rather than simple attenuation contrast (normal absorption) [213].

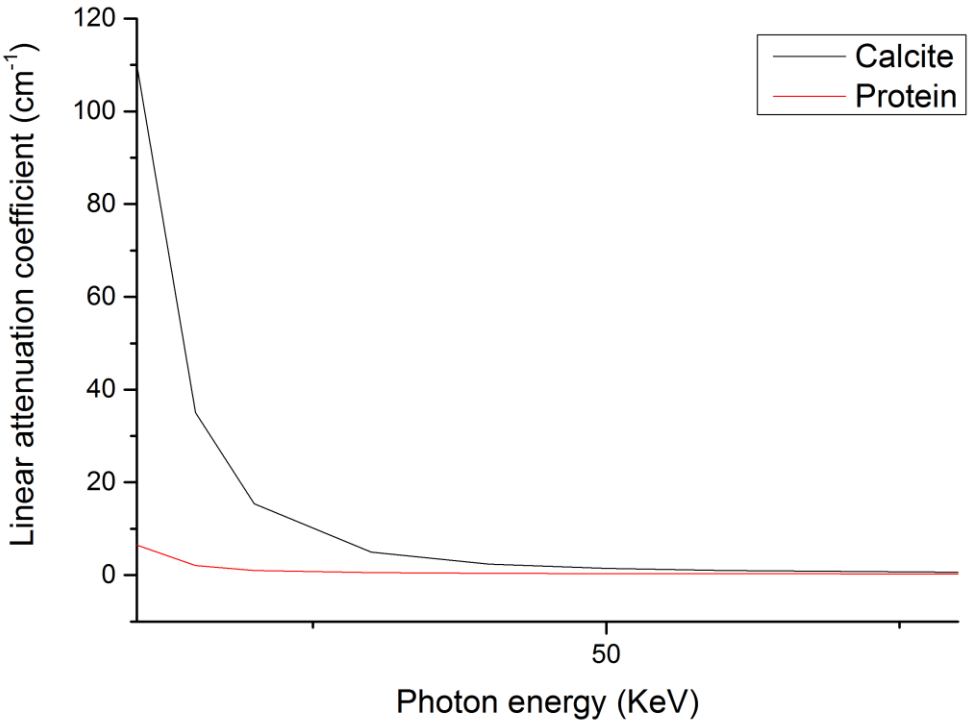


Figure 3.1.2. Attenuation coefficients of calcite and protein versus electron voltage in the limpet [211].

In these whole limpet trials, the parameters were selected in order to achieve good-quality imaging with reasonable resolution and good contrast but with shorter scan time. Although lower photon energy is favoured for better absorption or attenuation contrast, it is not feasible for such a long scan time. Therefore, the applied voltage was selected to be 50 KV which gave an acceptable level of absorption contrast, sufficient transmission rate of radiograph (>30%) [213] but with much shorter scan time. The objective lens has been selected to be 0.4 in order to ensure the whole limpet is in the field of view, with image binning set to be 2 (i.e. radiograph of ~1000 x 1000 pixels from a 2000 x 2000 pixel detector). Phase contrast scan has been adopted here because it can enhance the interface between different phases with similar linear attenuation coefficients by detecting the interference pattern caused by diffracted and un-diffracted waves in a material with a certain refractive index instead of absorption for different phases in normal absorption scan. It can be introduced with longer source-detector distance, but

this will result in much smaller field of view and increased scan time. Therefore as a compromise, the source to sample distance was set at 62.4 mm and the distance between sample and detector was set to 117.5 mm. No filter is required for phase contrast scan in order to keep low energy photons which enhances the contrast between phases. The resolution of the radiographs was 23.6 um. Because the counts of the tomograph need to be ideally above 5000, which is determined by the detector (DW936N-BV-558 manufactured by Andor) [214], the exposure time was 6 seconds to achieve sufficient counts in each radiograph. A 360° scan was used with 3201 projections, so the overall scan time was 6 hours 54 minutes (with an additional 30 minutes' warm-up to ensure constant ambient temperature and the stability of source during the scan). Obtained tomographs of the whole shell (*Figure 3.1.3* (b) (c)) were reconstructed into a stack of 16-bit tiff files using the instrument software. The same reconstruction approach was used for all laboratory tomographs in this project. Compared with a similar limpet scanned using normal absorption (*Figure 3.1.3* (d)) with similar resolution (24.5 um), enhance contrast has been observed between layers in phase contrast images.

Although no detailed microstructure such as lamellae described in literature [12] is revealed, layered structures of the limpet can be identified. Laminography may be a better solution for specimen with high aspect ratio such as limpet and it gives possibility for revealing detailed microstructure information. However, the laboratory X-ray tomography that was currently used in this project is not suitable for such application. All the tomographs present in the project have been pre-processed in Image-J. The brightness and contrast of tomographs have been optimized by adjusting the range of grey level.

.

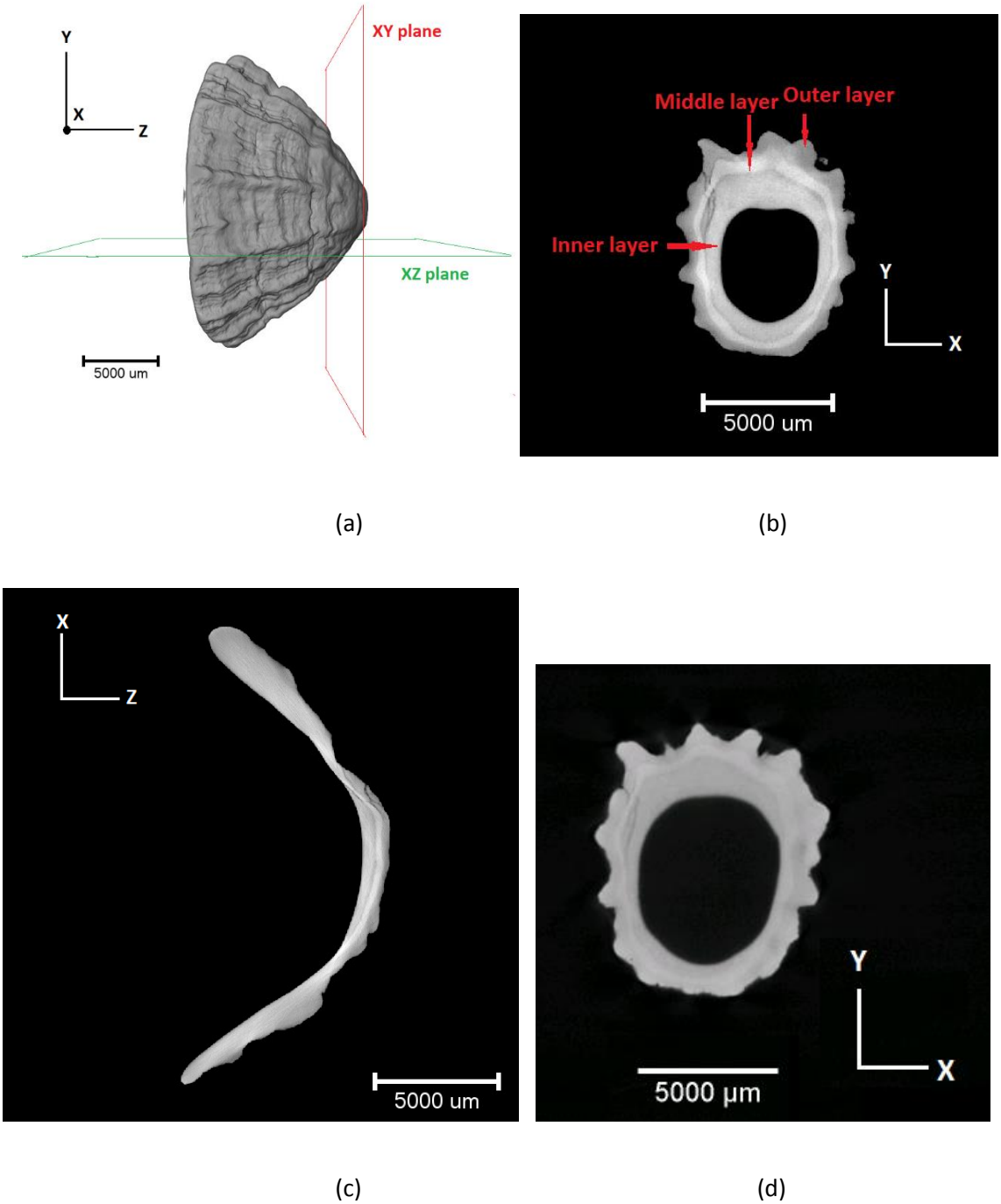
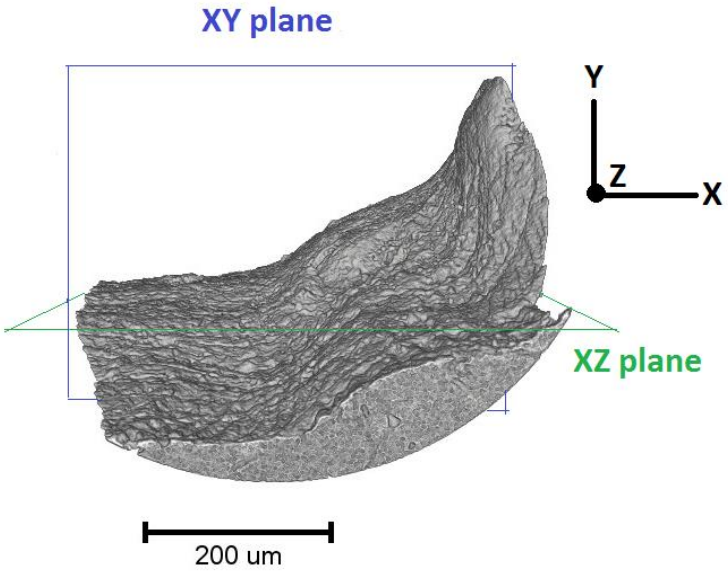
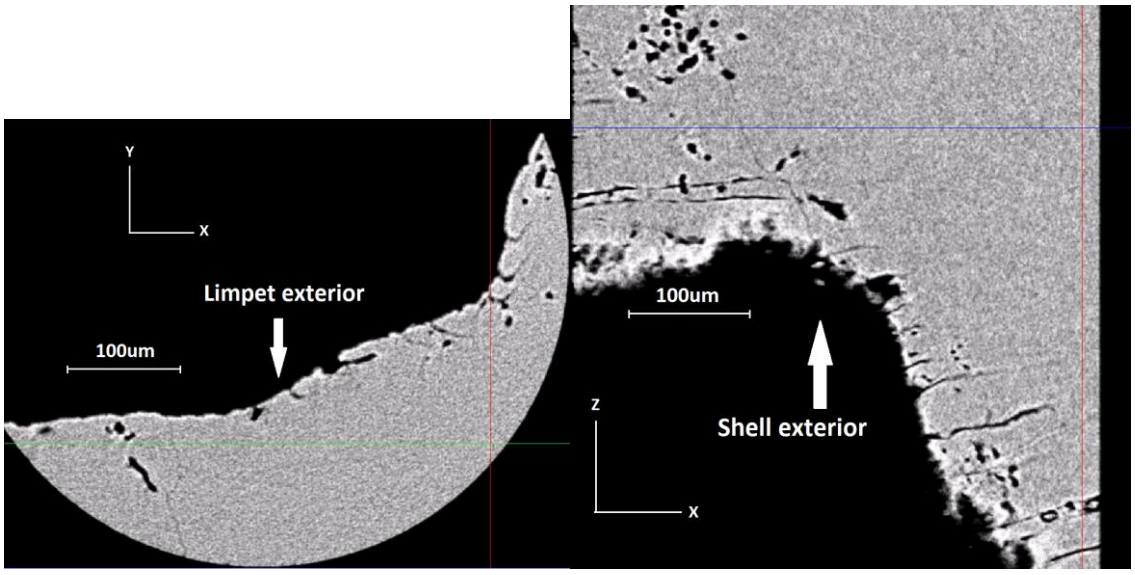


Figure 3.1.3. a) 3D volume of the limpet with dashed lines indicating the selected orthoslices for tomography scan; Orthoslices of the whole shell: b) XY plane and c) XZ plane are taken by Oxford's ZEISS Xradia 510 Versa High-Resolution 3D X-ray Tomography. Phase contrast scan is employed with voltage 50W and scan time 6h54min. No filter is applied. The voxel size is 23.6um. Layered structure has been observed which may be due to changes in material densities among layers. However, no further microstructural features have been observed. (d) XY plane of a similar shell scanned using normal absorption. The resolution is 24.5 um. Contrast between different layers are weaker than phase contrast.

Compared with the whole limpet, a 2mm x 2mm x 2mm small fragment is more suitable for phase contrast scanning as it allows greater flexibility in the source, sample and detector positions. Optimum conditions were obtained at an energy of 65 KeV to obtain a transmission rate larger than 30%, which is recommended for phase contrast scans [213]. To achieve a resolution below 1 um, but with a scan time less than 25 hours, the objective lens was chosen as x20 with x4 binning (i.e. the radiograph image size is ~994 x 952 pixels). Tomographs with most optimum phase contrast was achieved with a source-sample distance of 31.5 mm and a detector-sample distance is 55 mm. The exposure time was 35 seconds and a 360^{o} scan was required with 1601 projections. The overall scan time was 17 hours 13 minutes with additional 45 minutes' warming time. However, even with these optimal settings, no detailed microstructure could be resolved except some cracks at the edges of the limpet surface. Example orthoslices of the small fragment of the limpet wall obtained by phase contrast scans are shown in *Figure 3.1.4*.



(a)



(b) (c)

Figure 3.1.4. (a) 3D volume of a small segment from limpet wall with selected orthoslice planes; orthoslices: (b) XY plane and (c) XZ plane based on phase contrast scan, no filter, the voltage is 65kV and the scan time is 17h13min. The voxel size is 0.59 um.

3.1.1.1.2 Synchrotron X-ray tomography

X-ray tomographs of British limpets had been obtained at the Diamond Light Source in Harwell before the start of the project during experiment EE1504-1, and these were also processed for comparison with the laboratory tomographs. The monochromatic beam energy was 53.2keV,

and three scans have been taken with pixel sizes: 7.9um, 3.2um and 1.3um. The field of view decrease with the pixel size, and correspond roughly to the whole limpet, ¾ limpet and the top section of the same limpet, respectively. The visualisation of the reconstructed whole-shell, with ortho-slices of whole limpet, ¾ limpet and limpet top in Avizo are shown in *Figure 3.1.6*.

The original tomographs were smoothed with a Gaussian Blur 3D filter with 2 pixel radius to reduce image noise. In order to reduce the computational cost in Avizo and later in Abaqus, the original 32-bit synchrotron data were down-sampled to 8-bit and cropped by ImageJ. The Avizo software was used to segment and render the 3D volume of the limpet (*Figure 3.1.5)* and obtain ortho-slices of the limpet. As it can be seen from *Figure 3.1.6* (a), three layers observed in synchrotron tomograph with a resolution of 7.9um, which is in agreement with the observation of laboratory tomograph (*Figure 3.1.3* (b)). The ortho-slice obtained from tomograph (*Figure 3.1.6* (c)) with 1.3um pixel size reveals more details of microstructure than those with 3.2um pixel size (*Figure 3.1.3* (b)). Numbers of mineral stacks can been see in tomograph of limpet top (*Figure 3.1.6* (c)) which is consistent to the observation of microstructures in other gastropods [23]. Comparison of the tomographs obtained by laboratory and synchrotron tomography indicates the necessity for using a monochromatic tomography instrument such as a synchrotron to image the microstructure of limpets, in order to obtain good contrast of the microstructure.

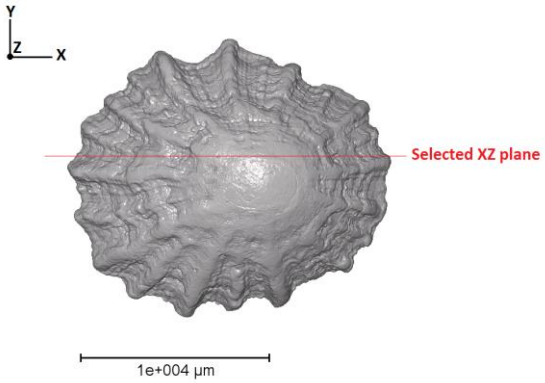
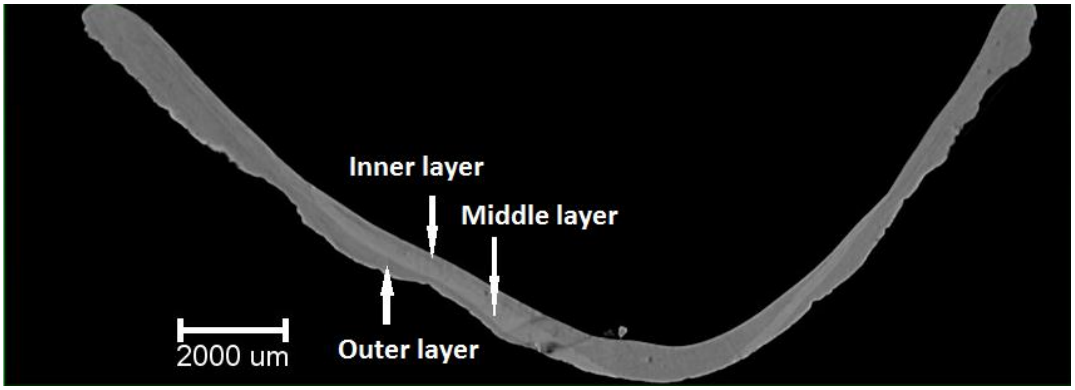
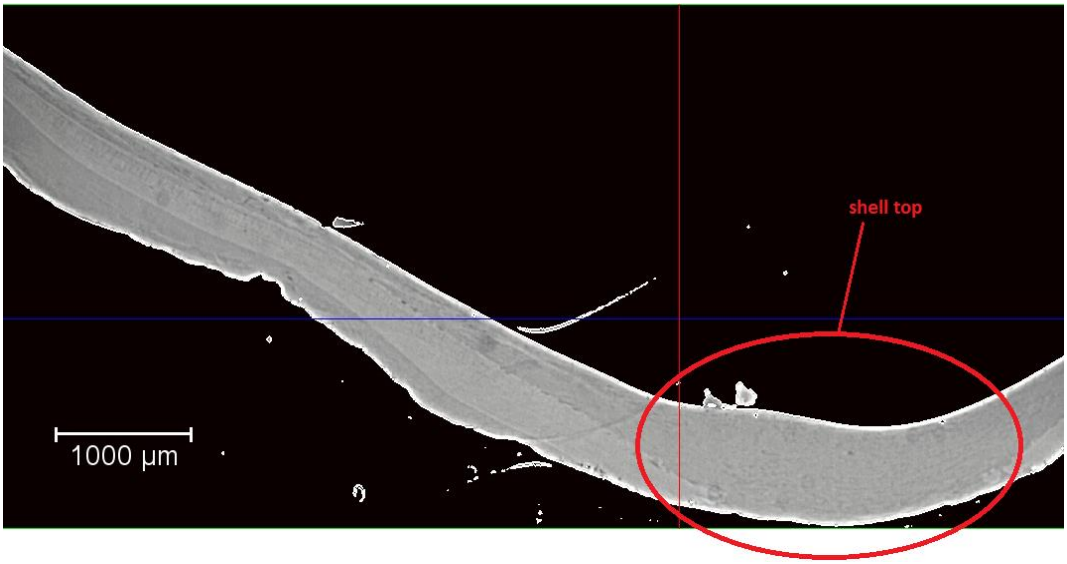


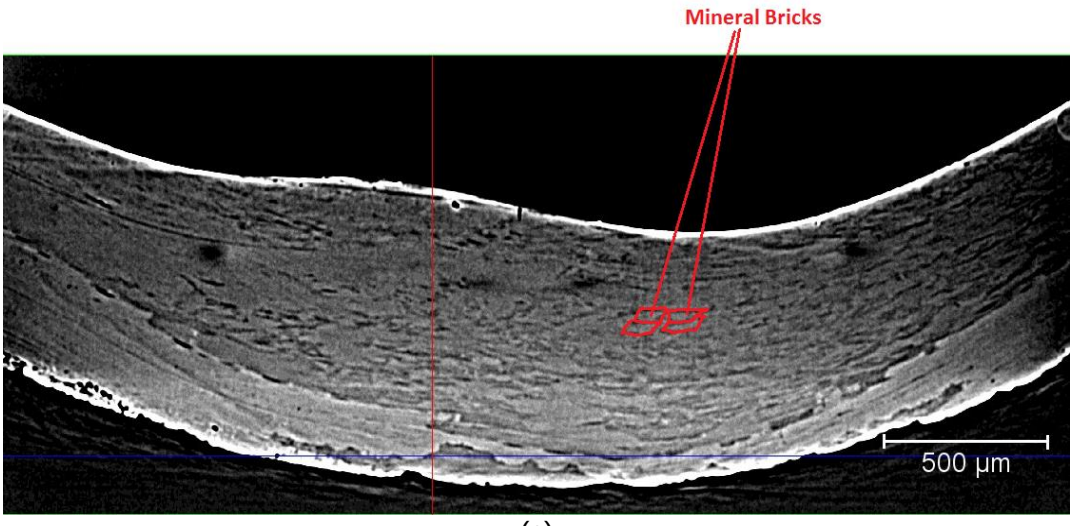
Figure 3.1.5. 3D volume of whole shell using tomograph with a resolution of 7.9um. Orthoslices shown in Figure 3.1.6 are selected on the selected XZ plane emphasized by red line.



(a)



(b)



(c)

Figure 3.1.6. Ortho-slices on XZ plane obtained from: a) whole limpet tomographs with a resolution of 7.9um, b) ¾ limpet tomographs with a resolution of 3.2um and c) limpet top tomographs with a resolution of 1.3um. All the images are processed from original data using ImageJ and Avizo. The regions within redlines indicate the mineral stacks within the microstructure of the limpet.

3.1.1.2 Bone

Compared with limpets, human bone specimens are very precious and difficult to obtain. Samples available to this project were cortical bones with different porosities, which were provided by patients undergoing elective total hip replacement. The samples had been cut, with cross-sectional area of approximately 3 mm x 3 mm in the laboratory of Imperial College, London by Dr Oliver Boughton. The sample collection had full ethical approval (Imperial Tissue Bank number R13004a) and all the patients had given their consent to the provision of samples.

3.1.1.2.1 Preparation of cortical bone specimens

All the cortical bones were cut from the medial, calcar area of the femoral neck, which is demonstrated in *Figure 3.1.7* (a), using a water-cooled bandsaw. The resultant cortical bone sample which is shown in *Figure 3.1.7* (d), has the longitudinal direction which is parallel to direction of the osteons and is cut by the diamond wafering blade using different sample grips in order to gradually reduce the size of the sample, which are shown in *Figure 3.1.7* (b) and (c). In total, 18 cortical bones with a size of approximately 3 mm x 3 mm x 6 mm were cut from the same region of the femoral necks to avoid the influence of inhomogeneity of cortical bones [62,66,215]. The samples were stored at -20°C during transfer to Oxford, and also between scanning sessions.

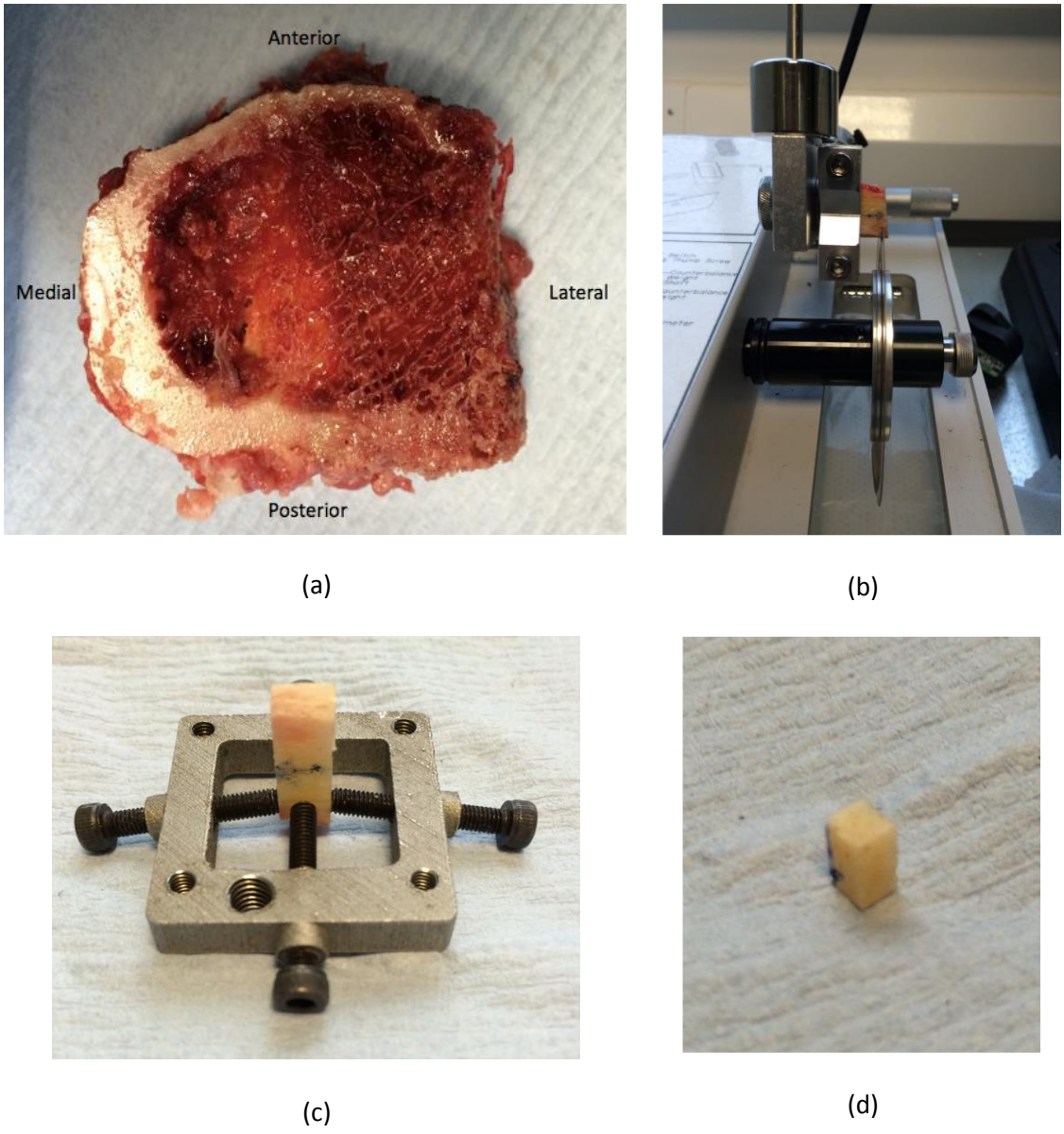


Figure 3.1.7. Preparation of cortical bones. (a) Cortical bones scanned in the experiment were sectioned from the medial, calcar areas in femoral neck; (b) A conventional clamp used for the diamond wafering blade to make the first reduction of bone height to 9mm in Imperial College, London; (c) A custom-designed clamp by Imperial College, London was used to achieve the required height for the experiments; (d) The resultant cuboid cortical bone with a size of 3x3x6 mm. The longitudinal direction is parallel to the direction of osteon.

3.1.1.2.2 Laboratory X-ray tomography (normal absorption)

In order to keep the bone moisturized, each sample was attached to the bottom of a long tube, using super glue (ethyl 2 cyano-acrylate), which was filled with phosphate buffered saline solution. The X-ray transparent container (polyamide, produced by an EOS 3D printer) was sealed by a plastic film (manufactured by KUREHA) via transparent glue (ethyl 2 cyano-acrylate) and O-ring to prevent the evaporation of water during scan, which is schematically shown in

Figure 3.1.8. A bone sample within the container before the scan inside the tomography chamber is shown in *Figure 3.1.9*. Due to the similar size and resolution required for this batch of bones, similar scanning conditions were applied to all.

The beam energy used was 50 kV, for transmission of 20-35%, with a maximum power of 4 W. Image binning was x2 with objective of 0.4x as the intended resolution was between 5 um - 10 um. The filter LE1, which is a low energy filter and is made of SiO_2, is chosen according to filter selection table in the manual of ZEISS Xradia 510 Versa High-Resolution 3D X-ray Tomography microscope for normal absorption scan [216]. The filter provides a clearer image by absorbing low-energy photons that scatter and result in beam hardening [217]. To achieve sufficient counts, the exposure time was 6 seconds with 1601 projections over a 360° rotation. The whole scan duration was ~ 5 hours with 30 minutes' warming-up. Because the sample size has slight differences between samples, distances between sample-source and sample-detector slightly changed from sample to sample which resulted in slight differences in resolution (sample-source distance: around 18 mm; sample-detector distance: around 160 mm). The resolutions of 18 bone samples varied slightly between 6-7 um, with a field of view around 7 mm x 7 mm. These parameters provided good quality images, with good contrast between different phases and clear visualisation of microstructures of the cortical bones. An example radiograph of cortical bone specimen is shown in *Figure 3.1.10* and orthoslices of the obtained tomograph of the microstructure, including the pore network within the bone volume, are demonstrated in *Figure 3.1.11*.

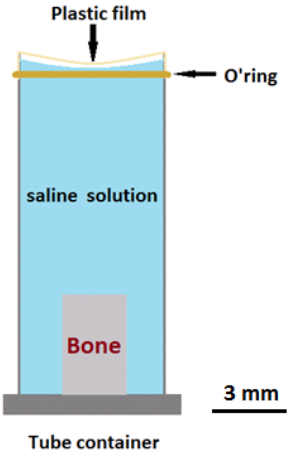


Figure 3.1.8. Schematic image of tube container used for the scanning of cortical bone.

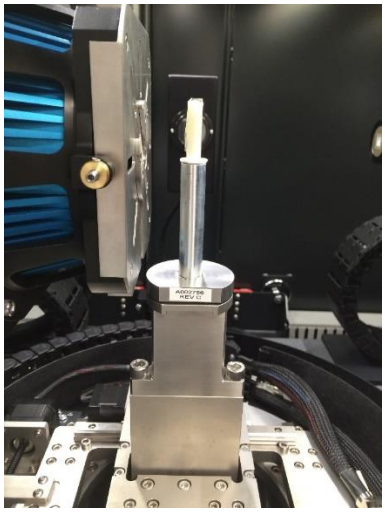


Figure 3.1.9. The sealed container with bone and phosphate buffered saline solution inside Xradia tomography chamber.

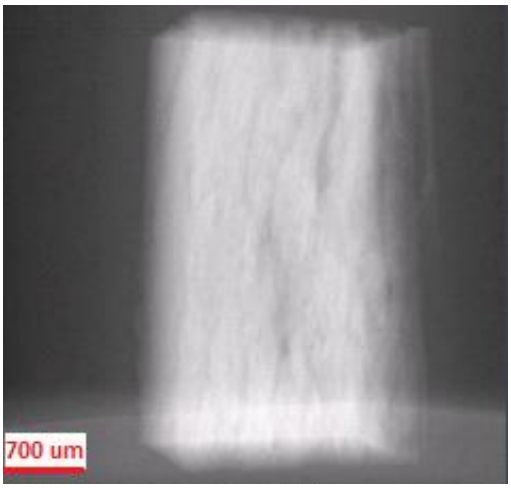
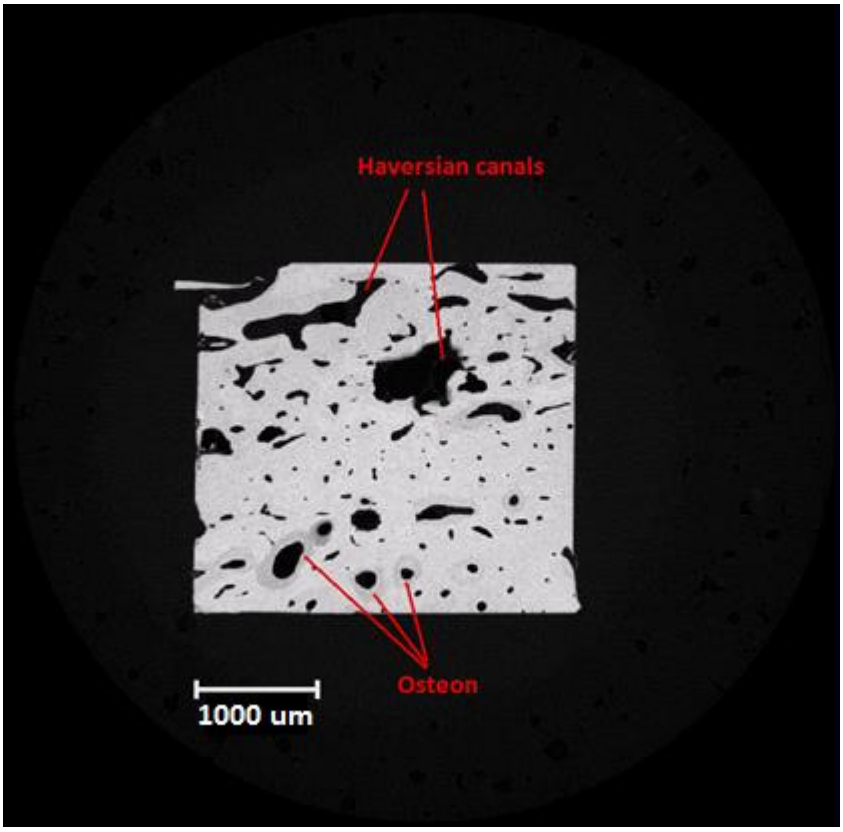
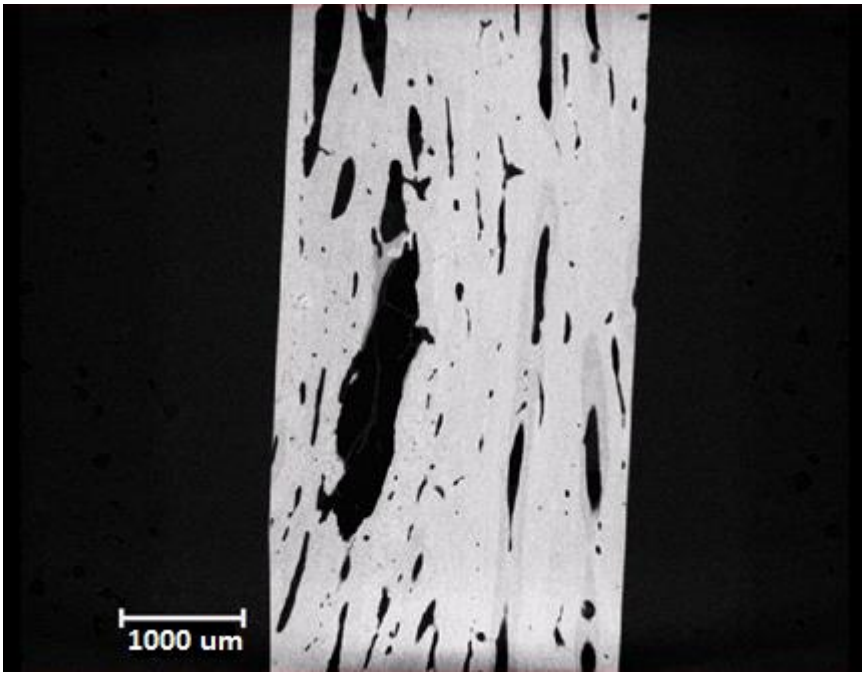


Figure 3.1.10. Radiograph of cortical bone (THR72).



(a)



(b)

Figure 3.1.11. Reconstructed tomograph of cortical bone (THR72) with a resolution of 6.9 um. (a) orthoslice on XY plane. Black pores are Haversian canals inside the bone volume while the grey matter which surrounds Haversian canal is Osteon which has very complicated lamellae structures which are not revealed by the tomograph due to the resolution limit. (b) Orthoslice on XZ plane.

3.1.2 In-situ mechanical tests on biomaterials

3.1.2.1 In-situ compression tests on limpets

Because laboratory scans of microstructures of limpets failed to achieve sufficient contrast for DVC analysis and scan time was very long for scans with high resolutions, synchrotron tomography was used for in situ loading tests on limpets. The tested limpets were either in dry state as collected or in wet condition, having been kept in brine at room temperature. The wet limpets were collected within a few hours of their contents being eaten by seagulls from the surface of rocks which were below the high tide mark on a British beach, and were stored in brine immediately after collection.

3.1.2.1.1 In -situ synchrotron x-ray tomography

In the first in situ synchrotron experiment (part of EE12585-2), a Shimadzu 5 kN load frame was used (*Figure 3.1.12*) to compress a complete dry limpet shell. The bottom of the shell was ground using SiC paper (3000 grit) to achieve a smooth, flat, surface and to avoid stress concentrations. Boards of high density polyethylene were attached to the upper and lower compressive plates shown in *Figure 3.1.13* to further avoid stress concentrations. The applied monochromatic energy beam was 80 keV and PCO.4000 CCD camera (2560x2169 pixels, 16-bit depth) was used to take radiographs with module 2 optics, the resolution of which is 7.9 um. The exposure time per radiograph was set to be 0.05 sec and 2500 projections were obtained over an angular range from -74.4 to +71.8 degrees because two columns of the testing machine make the full 180^{o} scan impossible and it results in the loss of data. The distance between specimen and detector was chosen by beamline scientist to be 1 m for optimum phase contrast from the coherent beam. Each scan took approximately 2 minutes. The data was reconstructed using I12's tomography reconstruction code which contained the function for suppression of limited angle tomography artefacts. The limpet was preloaded at a very small load (<5 N) and

progressively loaded using displacement control with interval load of around 75N until fracture. Relaxation of load was observed during each scan, but was less than 6% of the applied load.



Figure 3.1.12. Shimadzu loading cell mounted in Beamline I12.

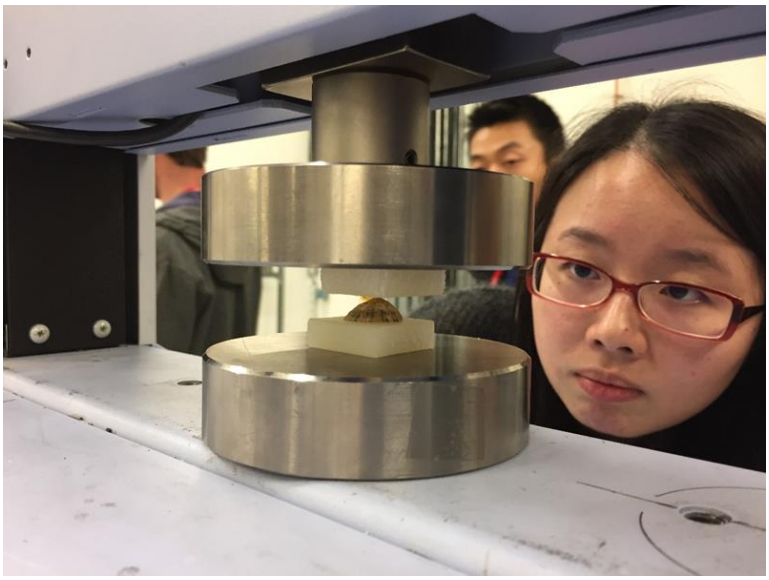


Figure 3.1.13. Set-up of compression test before scan.

The second in-situ synchrotron experiment of compression tests on limpets were conducted for two reasons: 1) to study the influence of hydrated conditions on limpet mechanical responses; 2)

to test the possibility to obtain a stable and straight crack from a notch, in order to quantify the fracture toughness. These experiments were conducted in experiment EE 16115-1 on beamline I12 at Diamond Light Source. The author has written the proposal for the second in-situ synchrotron experiment. Two pre-notched dry limpets, two complete dry limpets and one wet limpet were prepared (*Figure 3.1.14*) before the experiment. For pre-notched specimens, short notches with an approximate width of 0.5mm and depth between 3-5mm were introduced using an abrasive cutter to some dry limpets shown in *Figure 3.1.15* (a).

The limpets were tested under compression using a Deben CT5000 loading rig (*Figure 3.1.15* (b)), which is designed for in-situ mechanical tests such as tensile, compression and indentation tests during X-ray tomography. Specimens were scanned with a monochromatic beam energy of 53 keV using module 2 optics (7.9 µm pixel) over a 360^{o} rotation with projections at intervals of 0.1 ^{o} with an exposure time of 0.005 sec. Wide field mode with an offset rotation axis was employed in order to capture the full volume of the limpet. The distance between specimen and detector was chosen by beamline scientist to be 1 m for the same reason as the first synchrotron experiment.

Scans which focused on the region of interest (e.g. notch tip) were taken using the module 3 (3.2um resolution) and module 4 (1.3um resolution) optics with exposure times of 0.05 sec and 0.5 sec, respectively after each module 2 scan of the same limpet. A full 180° scan was employed with projections at intervals of 0.1 ^{o}. It took approximately 30 minutes for each sample to collect three sets of data at different resolutions.

For pre-notched limpets, scans were taken under static load, applied in displacement control. The limpets, which had flat ground surfaces at their bottom, were progressively loaded from the preload, which was nominally 5 N, until the limpet fractured. The Deben Rig was controlled using the Deben Microtest V6. 270 software in compression mode. Displacement control was used for compressing the limpet and the rate of the increment of displacement was varied according to

the change in load to avoid rapid build-up of load. Scans of limpets under periodic unloads between each load were also taken. Load relaxation (up to 13N at high load) was observed in this experiment before and after each scan. For complete limpets, similar loading approaches have been applied. However, the applied maximum load was controlled to be lower than the fracture one. In all tests, except of one test (pre-notched limpet 1, in which a polytetrafluoroethylene compression plate was used), the tests were conducted between the metal platens of Deben rig. The same scan parameters were used for all loaded states of each sample.

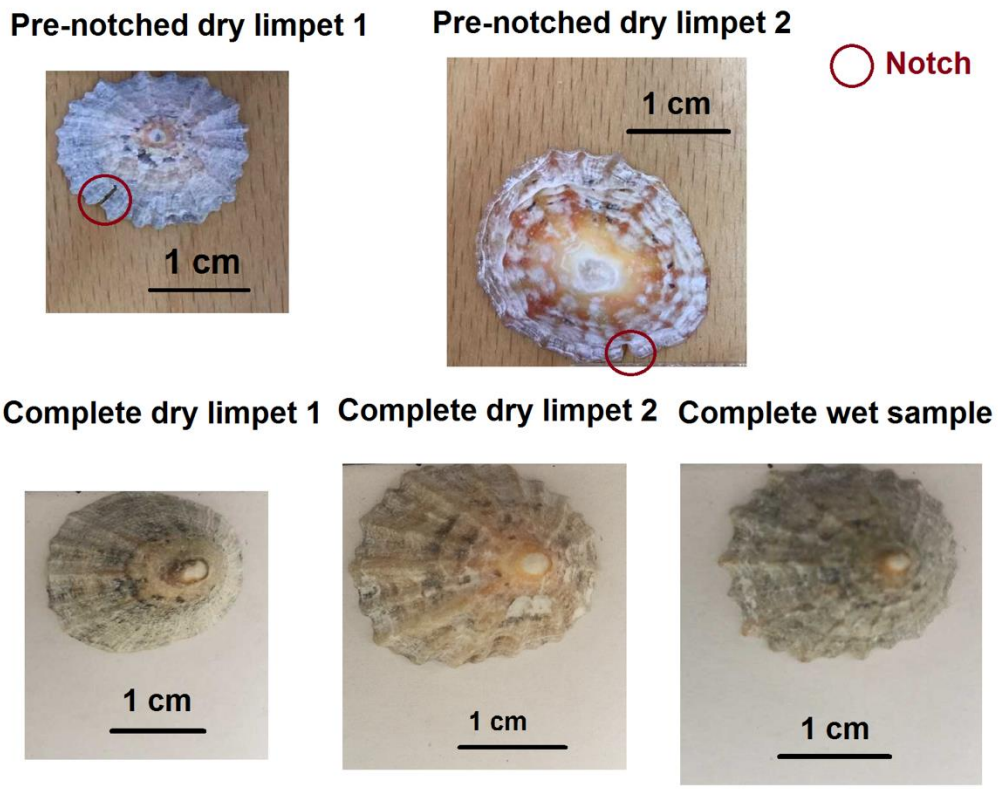
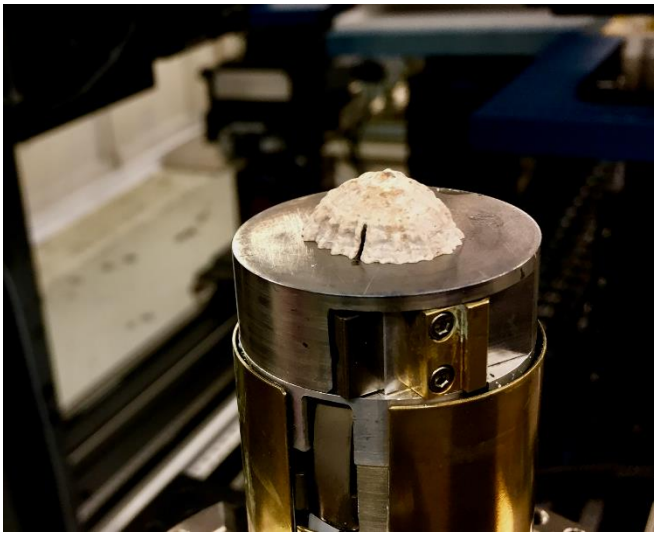
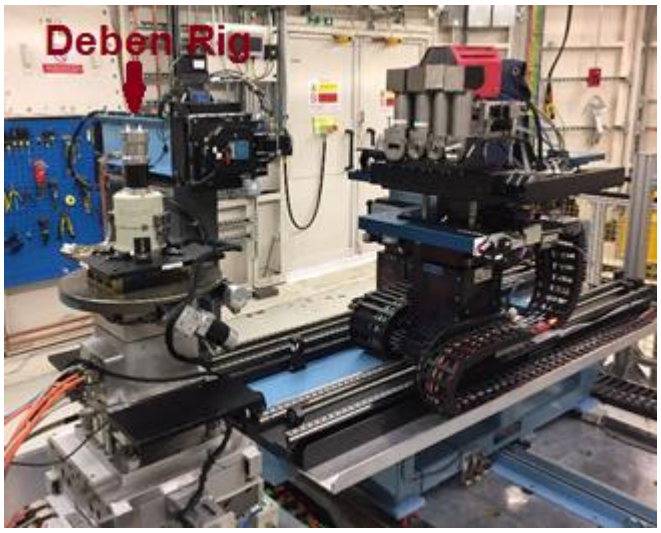


Figure 3.1.14. Tested limpet specimens.



(a)



(b)

Figure 3.1.15: Experimental settings: a) Pre-notched limpet which was positioned on the lower compressive jaw of the Deben rig; b) Installation of Deben rig on the beamline and the specimen/detector distance is around 1 m.

3.1.2.1.2 General fracture behaviour of limpets

For complete dry limpet used in the first synchrotron test, the typical crack pattern (cracking and fissuring of anterior end) which is reported by literature for this particular mollusc species in dry condition [12] is observed (*Figure 3.1.16*). For pre-notched limpets (used in the second synchrotron experiment), the fracture did not always initiate at the notches and cracks with complicated growth patterns were observed (*Figure 3.1.17*). In two specimens, a crack did

develop from the notch tip, but in one the main failure was due to a long crack from the anterior end (*Figure 3.1.17*).

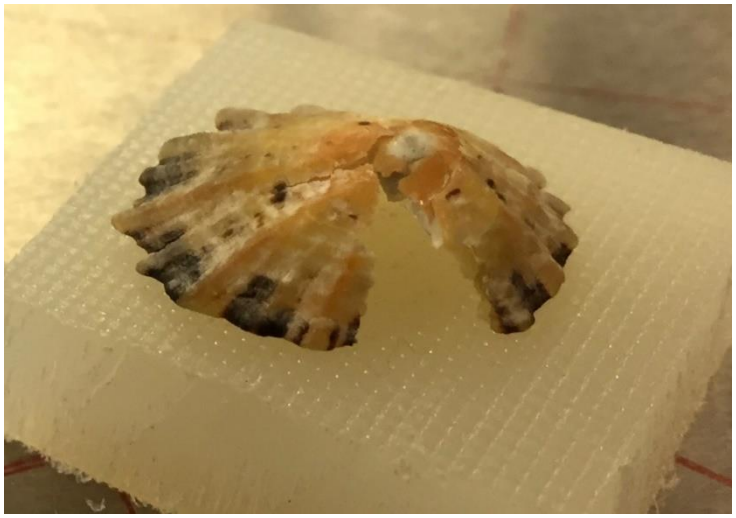
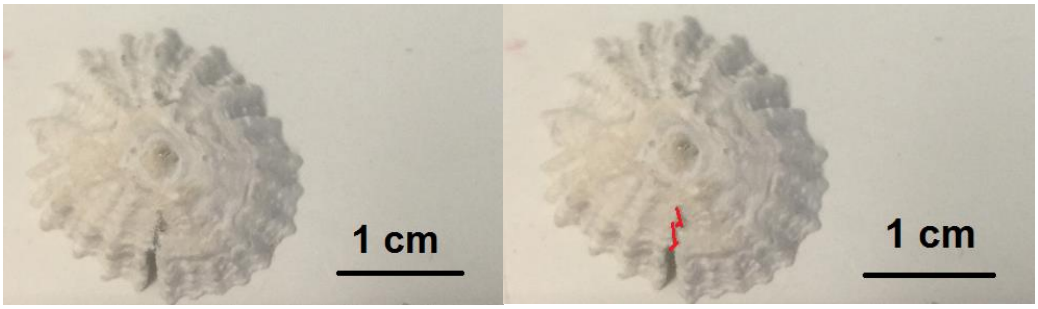
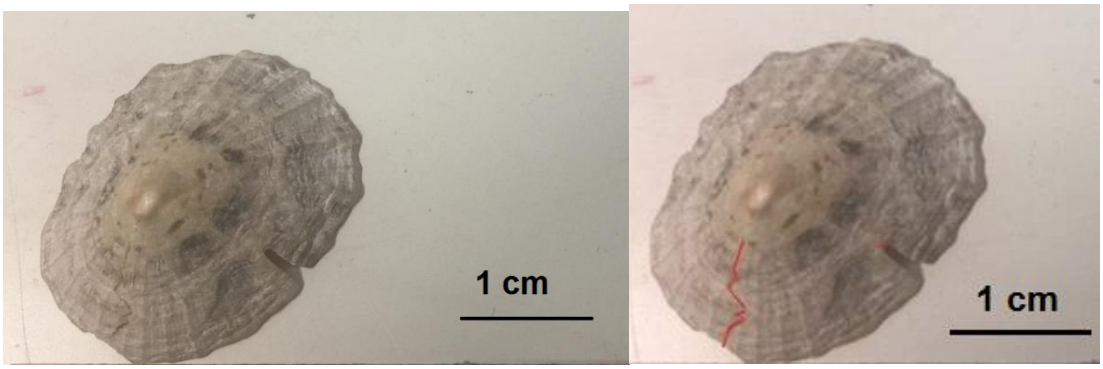


Figure 3.1.16.The limpet after fracture in the first synchrotron test.



(a)



(b)

Figure 3.1.17. Two pre-notched limpets after fracture in the second synchrotron tests. The general patterns of cracks are emphasized in red. (a) Pre-notched limpet 1: left: original fractured limpet; right: the same limpet with red line emphasizing the crack; (b) Pre-notched limpet 2: left: original fractured limpet; right: the same limpet with red line emphasizing the crack. All the observed cracks are not continuous and fully open, which are shielded by mineral fragments and cannot be easily identified by eyes.

3.1.2.1.3 Load-displacement data

The obtained displacement-load curve of the complete dry shell, tested in the first synchrotron experiment without unloading steps, is shown in *Figure 3.1.18*. The displacements were obtained by measuring the change in height of limpet in the radiographs, relative to the pre-loaded image. The error is estimated to be within a pixel (7.9 um). The experimental load was recorded by Shimadzu loading cell and the error bars represent the drop of load during the scan.

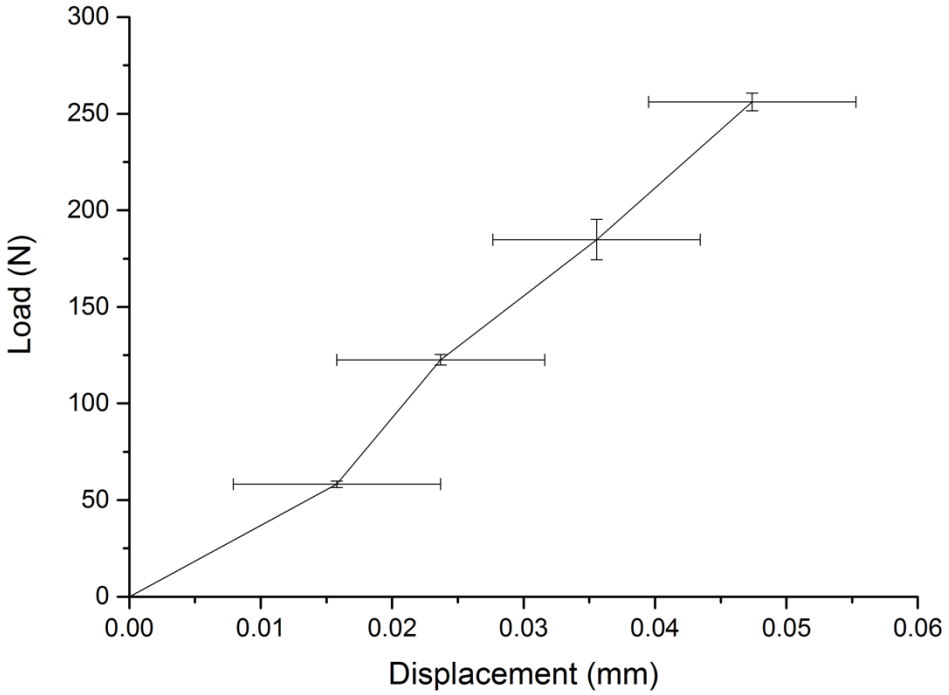
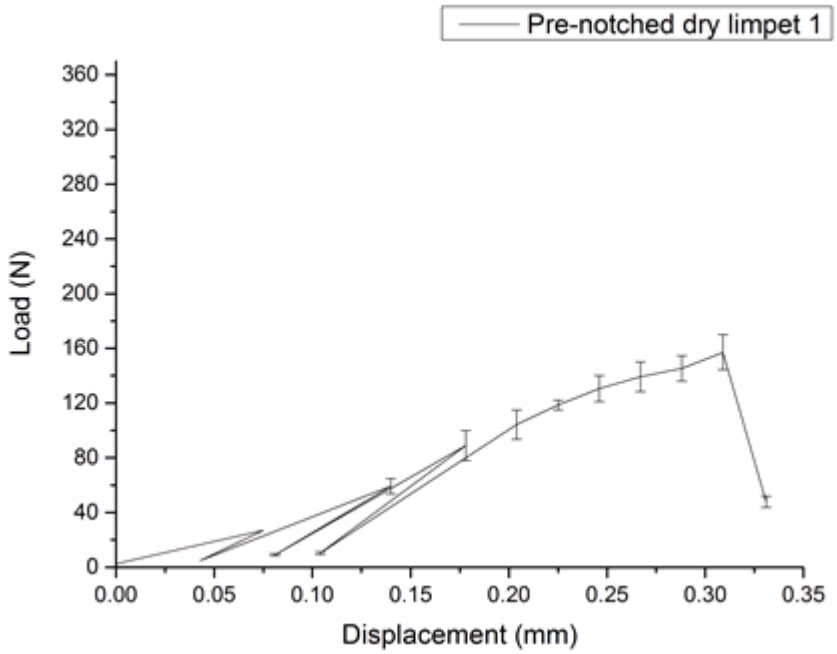


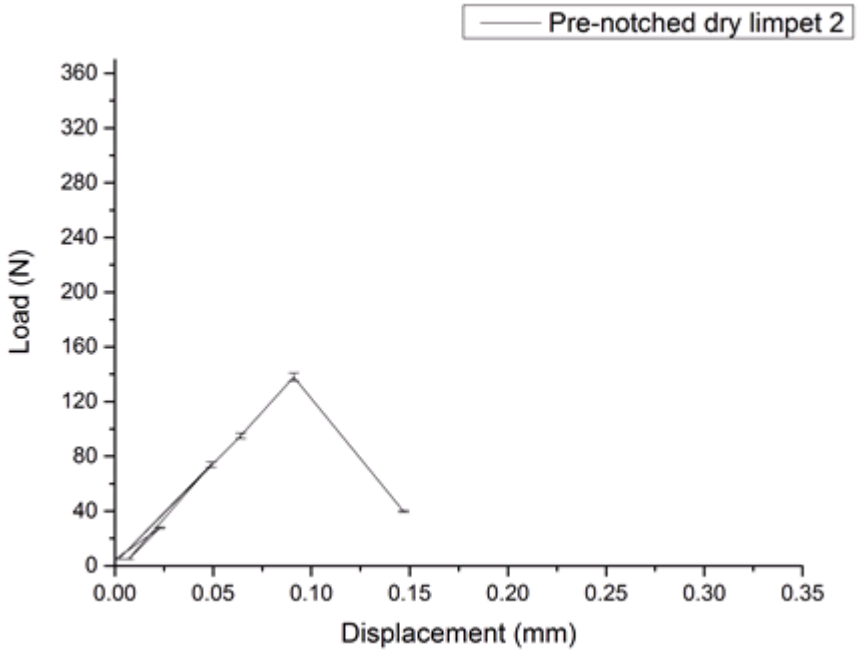
Figure 3.1.18. Experimental load-displacement curve of a complete dry shell.

In the second synchrotron experiment, due to the limited field of view at the limpet top and bottom areas, the applied displacements could not be reliably measured from radiographs. The displacement–load curves were obtained directly from the readings of Deben rig. The data are presented using same scales in order for clearer comparisons between samples. Direct comparisons are difficult, due to differences in the size and shape of the limpets. However, if one compares the two pre-notched limpets (*Figure 3.1.19* (a) and (b)), although the fracture loads were similar, the one compressed with plastic anvils reached a larger displacement change

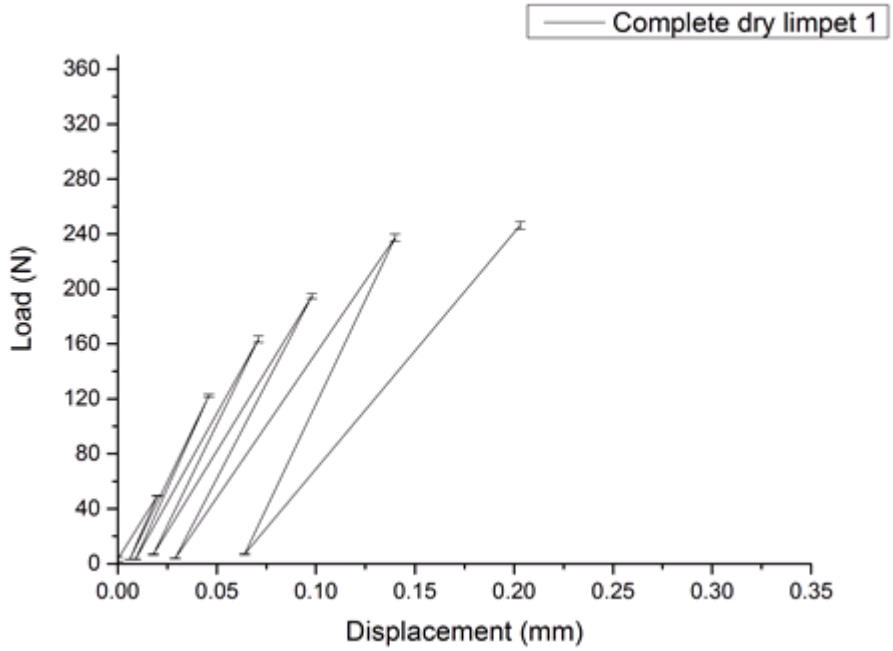
and this most likely indicates the influence of the compression materials used. The wet limpet (*Figure 3.1.19* (e)) shows higher stiffness compared with two dry limpets ((*Figure 3.1.19* (c) and (d)). This behaviour is consistent with literature [24] [25].



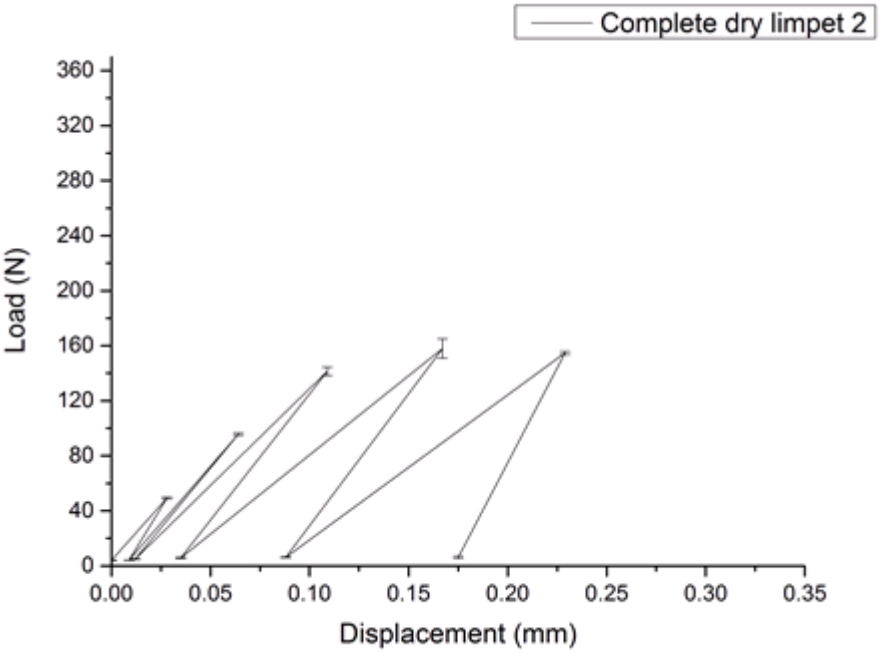
(a)



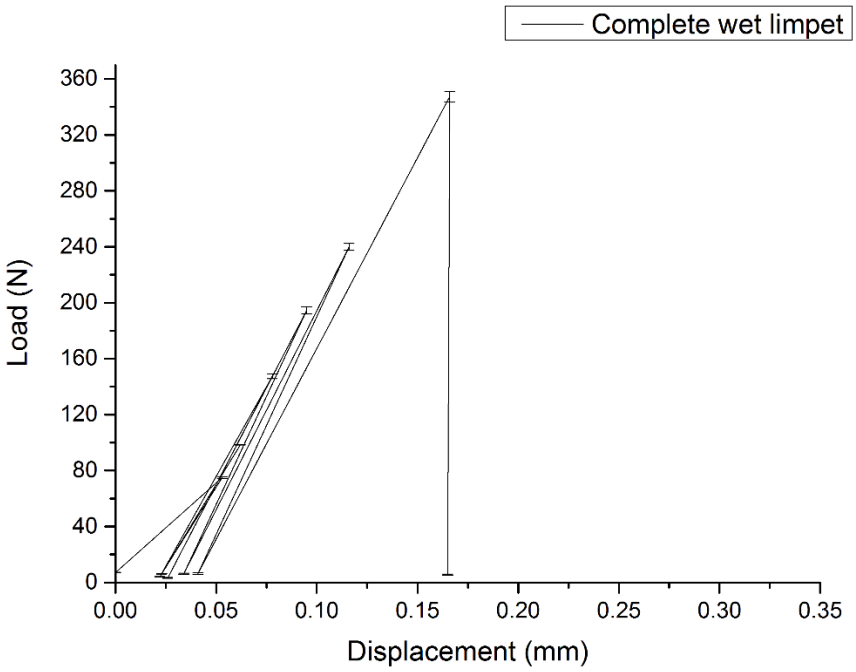
(b)


Complete dry limpet 1
Load (N)
Displacement (mm)
0
40
80
120
160
200
240
280
320
360
0.00
0.05
0.10
0.15
0.20
0.25
0.30
0.35

(c)


Complete dry limpet 2
Load (N)
Displacement (mm)
0
40
80
120
160
200
240
280
320
360
0.00
0.05
0.10
0.15
0.20
0.25
0.30
0.35

(d)



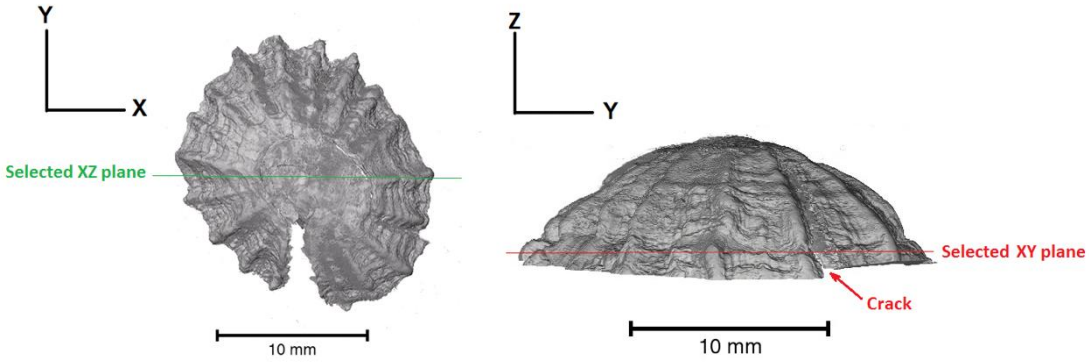
(e)

Figure 3.1.19. Recorded experimental displacement-load curves of compression tests by Deben rig on different limpet specimens with periodic unloading steps. (a) Pre-notched dry limpet 1; (b) Pre-notched dry limpet 2; (c) Complete dry limpet 1; (d) Complete dry limpet 2; (e) Complete wet limpet. Note: Other than pre-notched limpet 1, (in which a polytetrafluoroethylene plate was used), other tests were conducted between metal platens.

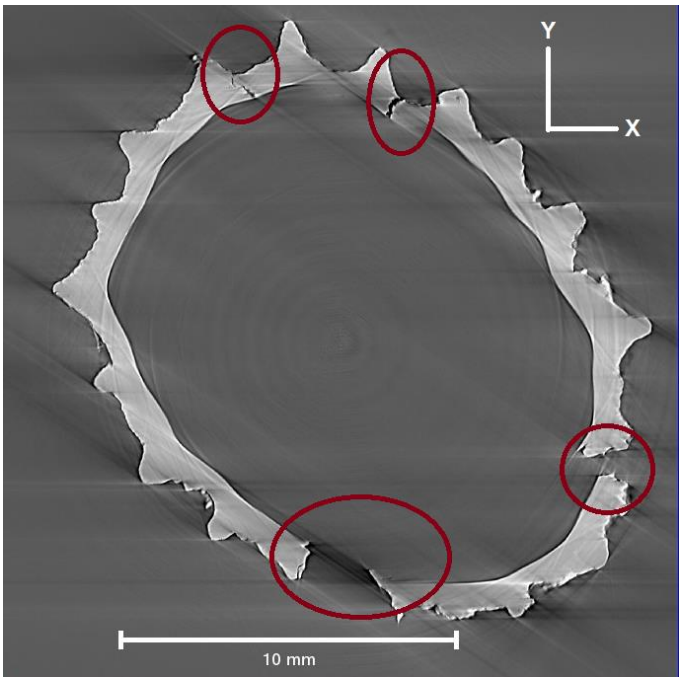
3.1.2.1.4 Visualisation of Tomographs

Reconstruction scripts were provided by beamline scientists: Christina Reinhard and Nghia Vo to obtain tomographs with good quality from synchrotron tests. Before reconstructing radiographs into 32-bit tiff or raw files, images were aligned by adjusting rotation centre until sharp features were achieved and filters were applied to suppress artefacts such as beam hardening. All these functions were included in the provided scripts.

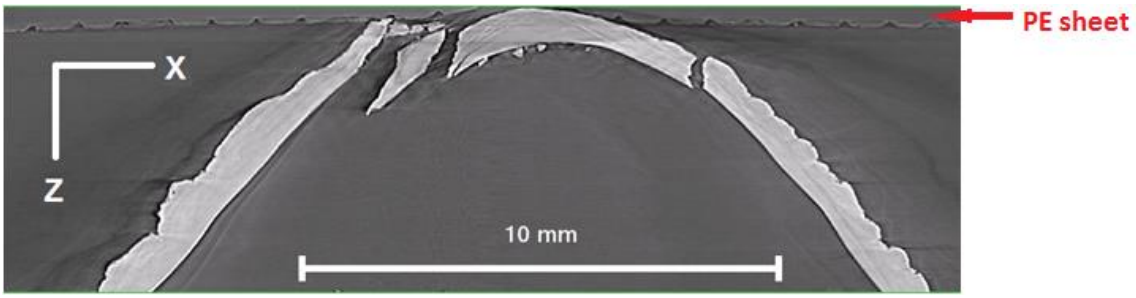
Reconstructed tomographs of the fractured specimen from the first synchrotron in situ test is shown in *Figure 3.1.20*. Multiple cracks can be observed, developing from limpet anterior and a catastrophic fracture of the limpet apex is also clear (*Figure 3.1.20* (b) and (c)).



(a)



(b)



(c)

Figure 3.1.20. Reconstructed tomographs of fracture limpets in module 2 (7.9 um) used in first synchrotron test. Artefacts (e.g. streaks) are resulted from limited angle tomography. (a) 3D volume of fractured limpet indicating positions where orthoslices (b) and (c) are sectioned from; (b) XY plane orthoslice, cracking areas are marked in red circles; (c) XZ plane orthoslice.

For the second synchrotron test, it was found that successful reconstructions could not be done of the wide angle tomographs (module 2). A 3D visualisation of the intact limpet could be obtained, and this is shown in *Figure 3.1.21*. The reconstructions of the higher resolution tomographs of pre-notched limpet 1, which focused on the notch tip (*Figure 3.1.22 and Figure 3.1.23*), were successful.

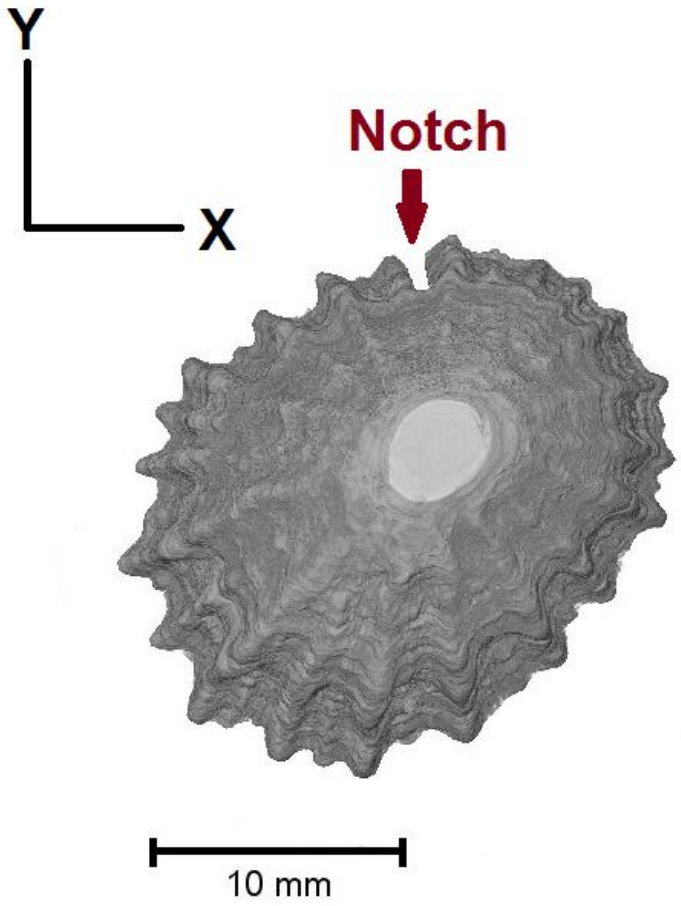
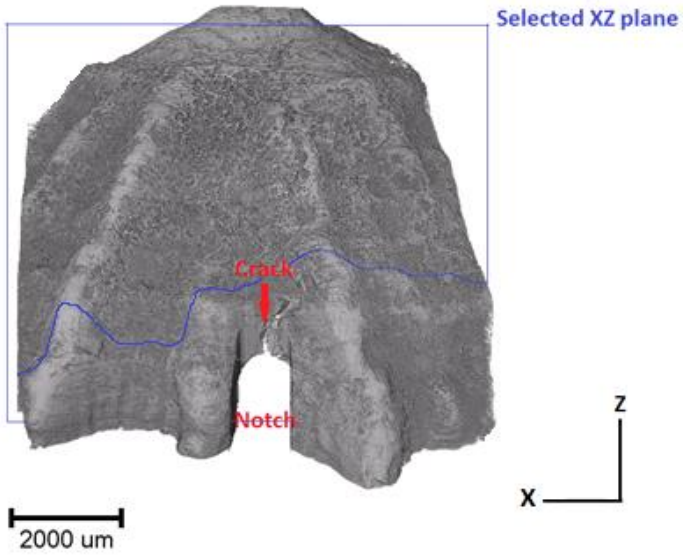
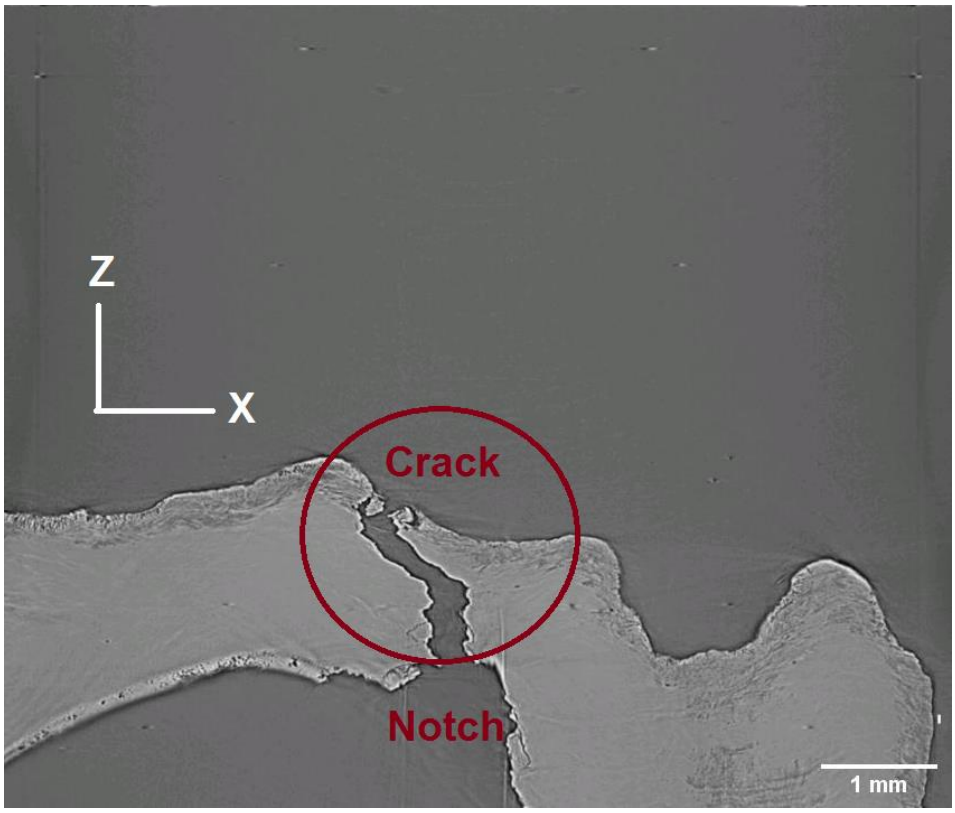


Figure 3.1.21. 3D volume of pre-notched dry limpet 1.

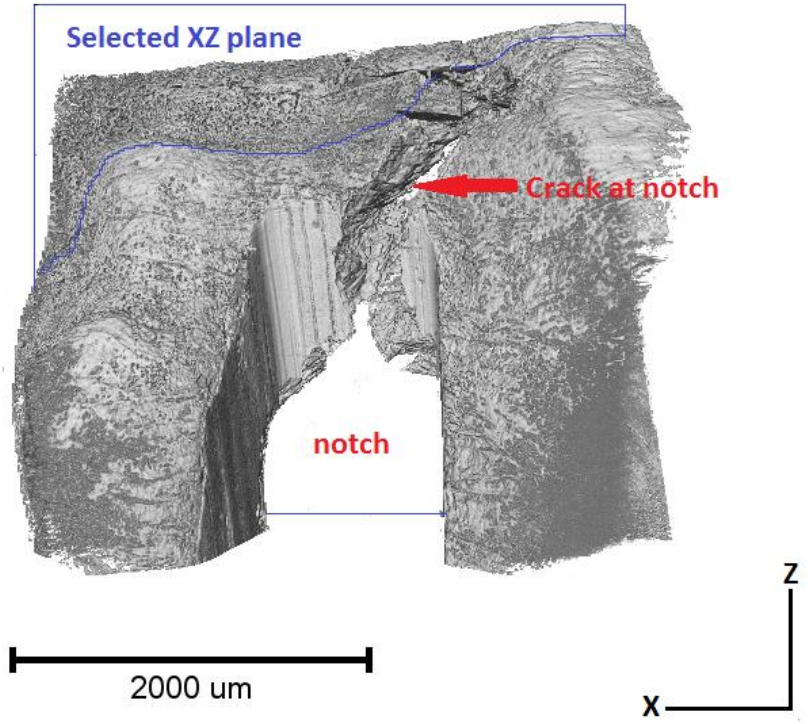


(a)

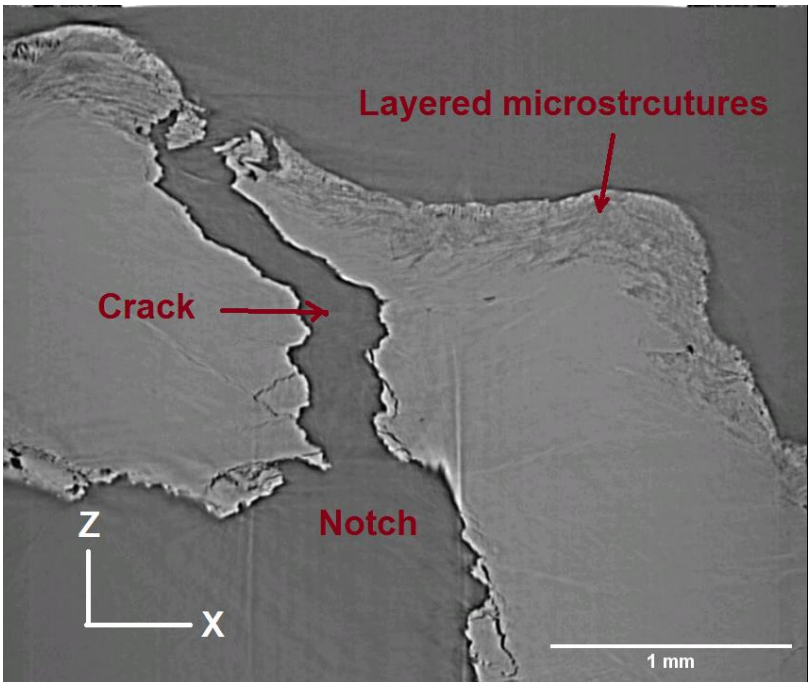


(b)

Figure 3.1.22. Module 3 tomograph of the notch region of fractured pre-notched limpet 1 (resolution: 3.2 um): (a) 3D volume with selected plane for orthoslice (blue square); (b) orthoslice on selected XZ plane.



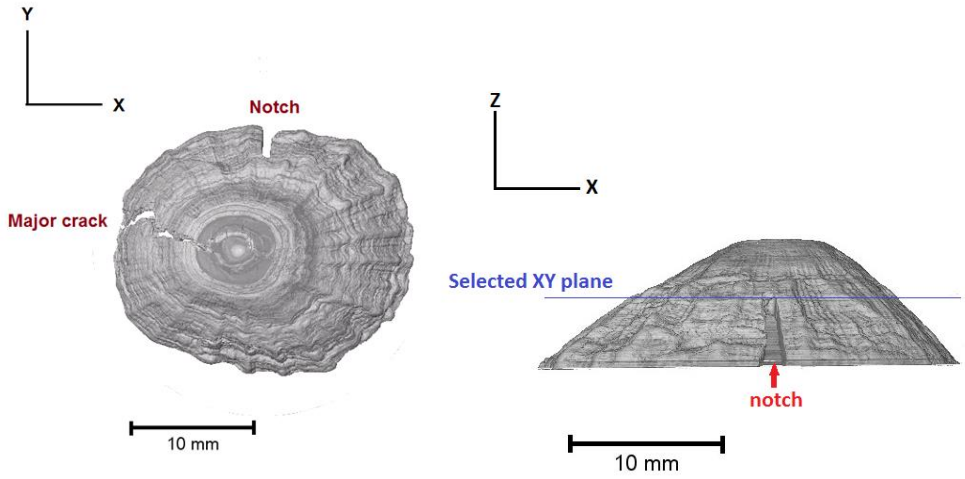
(a)



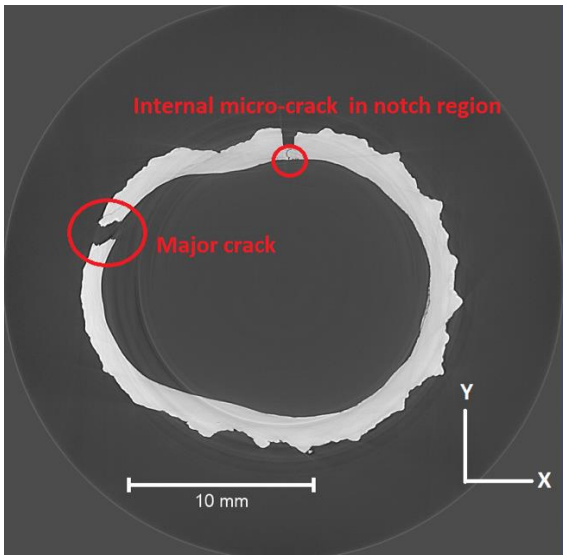
(b)

Figure 3.1.23.module 4 tomograph of the notch region of fractured pre-notched limpet 1 (resolution: 1.3 um): (a) 3D volume with selected plane for orthoslice (blue square); (b) orthoslice on selected XZ plane.

In the 3D visualisation of whole pre-notched limpet 2 (*Figure 3.1.24* (a): *module 2 tomograph*), a major crack with complicated geometry developed from limpet anterior area is observed. The reconstructed tomographs of pre-notched dry limpet 2, which focus on the cracking areas are shown in *Figure 3.1.25 (module 3 tomograph) and Figure 3.1.26 (module 4 tomograph)*.

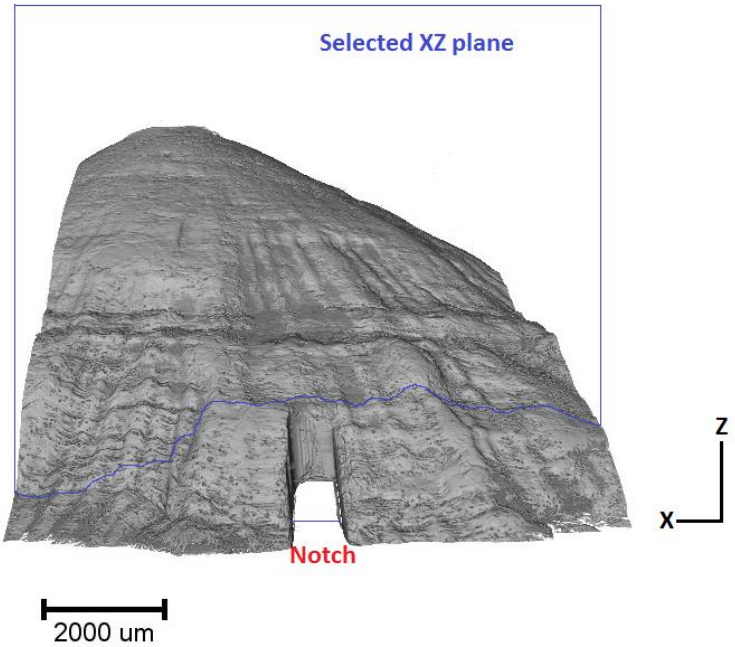


(a)

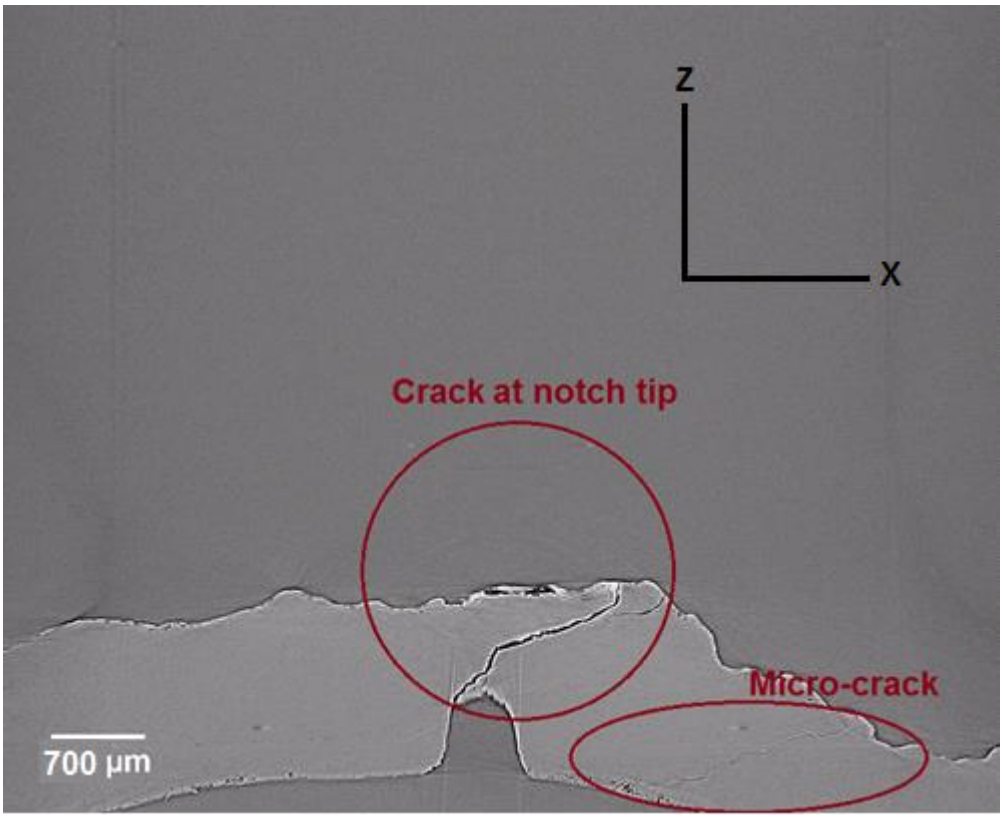


(b)

Figure 3.1.24. Reconstructed tomographs of pre-notched dry limpet 2 after fracture. (a) 3D volume of fracture pre-notch limpet 2 and selected XY plane for orthoslice (blue line); (b) Module 2 tomograph (7.9um) on selected XY plane.

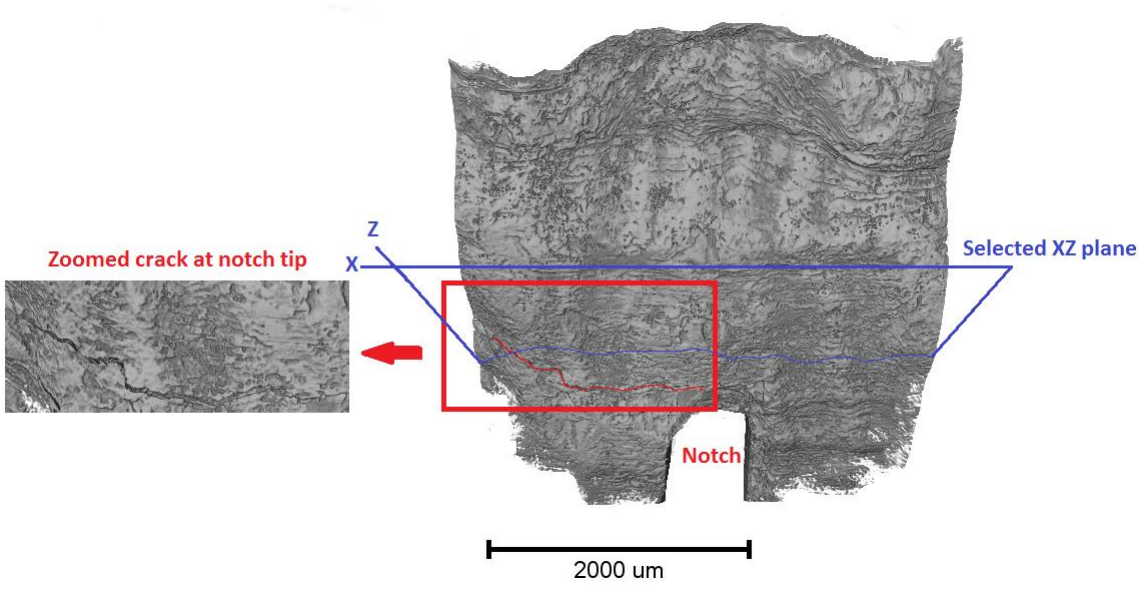


(a)

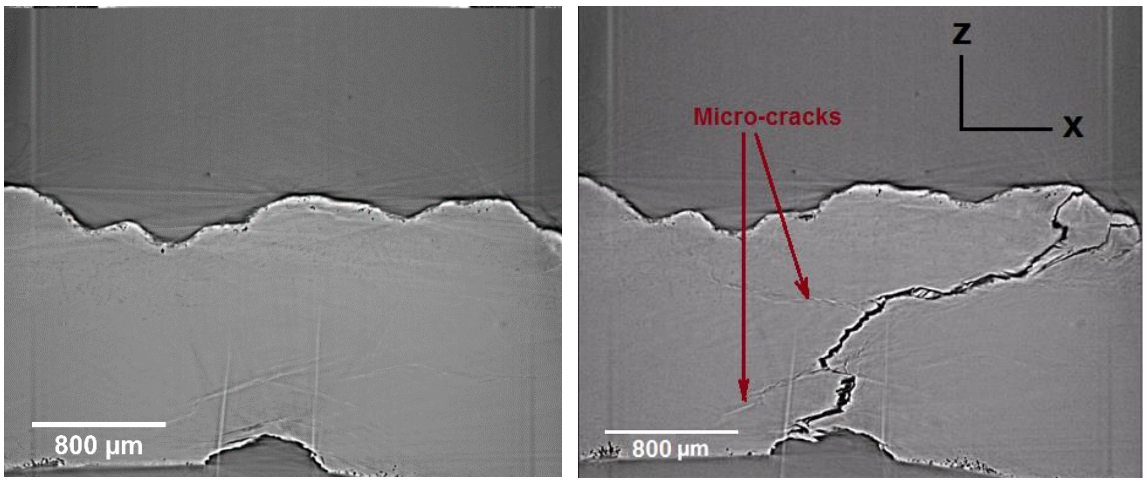


(b)

Figure 3.1.25. Reconstructed tomographs of pre-notched dry limpet 2 after fracture. (a) 3D volume of module 3 tomograph and selected XZ plane for orthoslice (blue square); (b) Module 3 tomograph (3.2um) on selected XZ plane.



(a)



(b) (c)

Figure 3.1.26. Reconstructed tomographs of pre-notched dry limpet 2 after fracture. (a) 3D volume of module 4 tomograph and selected XZ plane for orthoslice (blue square), crack at notch tip is highlighted in red; (b) and (c): Module 4 tomograph (1.3 um) on selected XZ plane at its preload and fracture states, respectively.

In module 3 tomograph (*Figure 3.1.25* (b)), a crack is observed that is initiated from the notch, similarly to that seen in *Figure 3.1.17* (b). Micro-cracking which is perpendicular to the notch plane can be observed in the high resolution model 4 tomograph at limpet's fracture state (*Figure 3.1.26* (c)). No such feature is observed in *Figure 3.1.26* (b) at limpet's preload state, which confirms micro-cracks observed in its fracture state are not the results of artefacts or pre-existing flaws.

No significant change in shell exterior surface has been observed for complete dry and wet limpets after tests. However, different behaviours under compression have been observed for complete dry limpets and wet limpets according to experimental recorded displacement-load curves (*Figure 3.1.19* (c) (d) and (e)). Damages seem to be built up within dry limpets at relatively low load while elastic deformation has been observed within wet limpet until the last loading step at which point the applied load is around 340 N. Therefore, reconstruction tomographs of complete dry limpet 2 (*(f*) Preload step (g) Last-load step

Figure 3.1.27) and complete wet limpet (*(f)* Preload step (g) Last-load step

Figure 3.1.28) have been selected for the investigation of possible internal change before and after loading (preload state and last-load step). Based on the experience obtained from first synchrotron test (*Figure 3.1.16*) that limpet tends to fracture at limpet apex and bottom, two orthoslices on XY planes selected from top and bottom regions, respectively, have been selected (*(f*) Preload step (g) Last-load step

Figure 3.1.27 *(a)* and *(f)* Preload step (g) Last-load step

Figure 3.1.28 (a)). Fracture has been observed at the interior side of the apex of dry limpet in its last-load step (*(f*) Preload step (g) Last-load step

Figure 3.1.27 (c)) while no change has been observed in the dry limpet bottom (*(f*) Preload step (g) Last-load step

Figure 3.1.27 (d) and (e)). No obvious crack or damage has been observed in wet limpet by comparing tomographs in its preload and last-loading steps (*(f)* Preload step (g) Last-load step

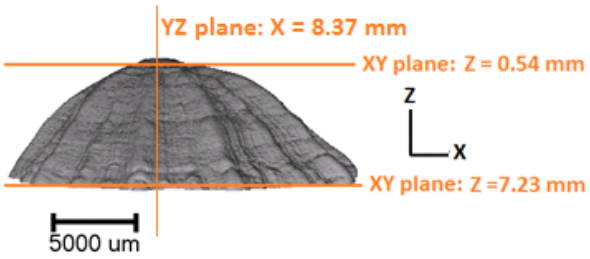
Figure 3.1.28). YZ planes have also been checked for complete dry limpet 2 and wet limpet to study whether structural damage occurs in orthogonal planes. Cracks have only been found at

shell apex in dry specimen (*(f*) Preload step (g) Last-load step

Figure 3.1.27 (f) and (g)) and no crack has been found in wet specimen (*(f)* Preload step (g) Last-load step

Figure 3.1.28).

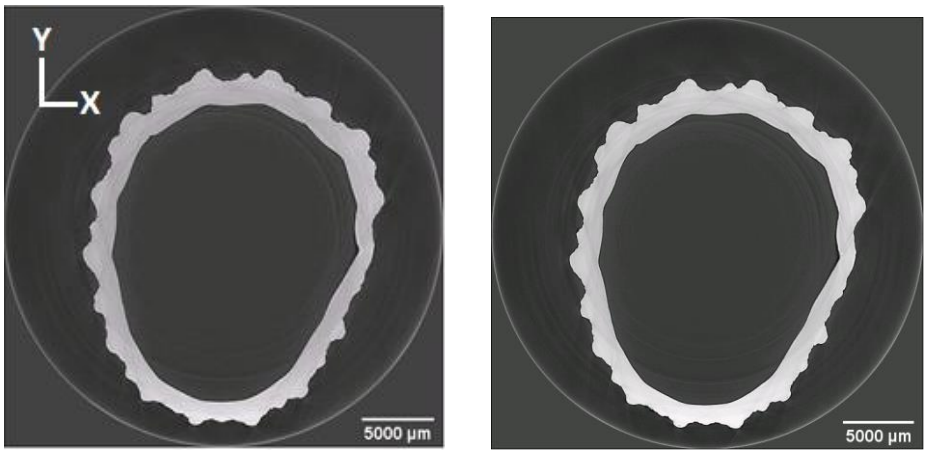
Overall, given the information from limpet tomographs, for pre-notched limpets, fracture behaviours differ among samples because pre-notched limpets 1 fractures at notch tip while pre-notched limpet 2 tends to grow a big crack from thin area in limpet margin and only a very small crack develops at notch tip. For complete limpets, the hydration condition of limpet influences the mechanical behaviour of the specimen. Wet specimen presents more resilience to compression compared with dry limpet.



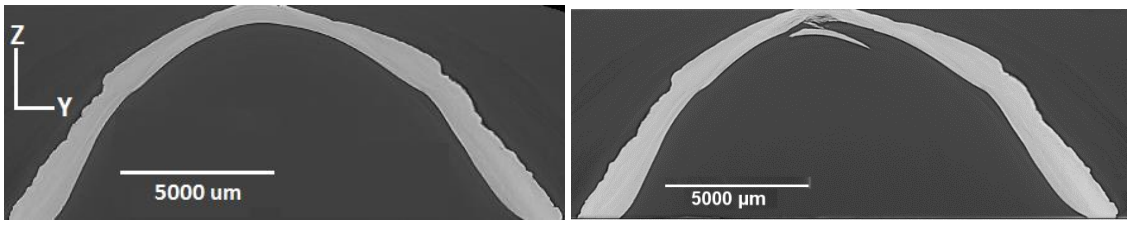
(a)



(b) Preload step (c) Last-load step

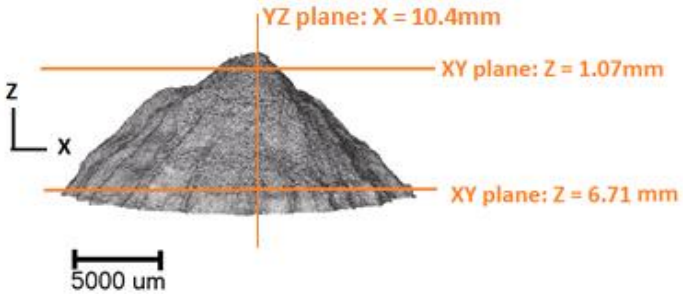


(d) Preload step (e) Last-load step

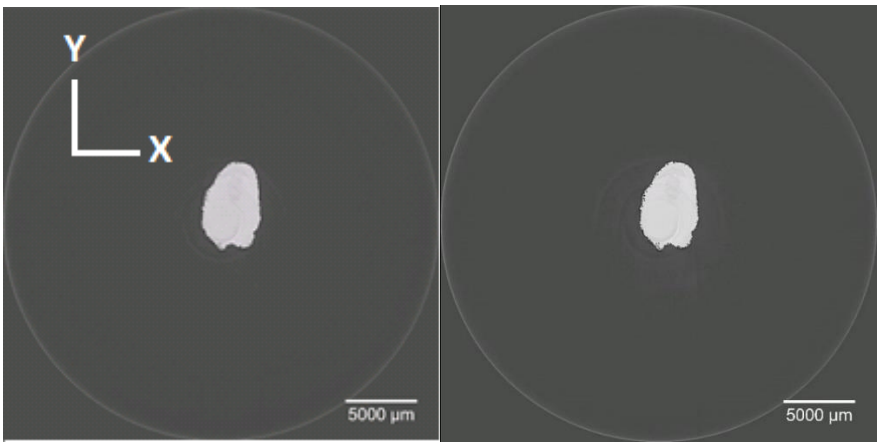


(f) Preload step (g) Last-load step

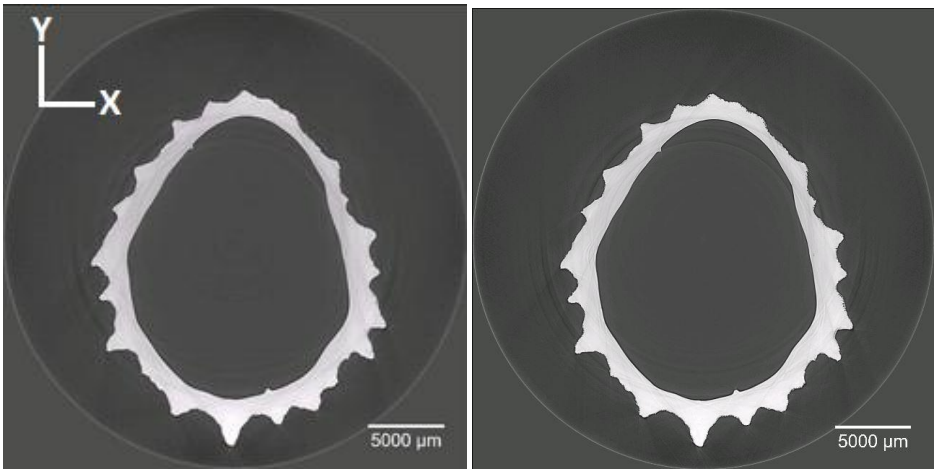
Figure 3.1.27.Reconstructed tomographs of complete dry limpet 2. (a) 3D volume of limpet and selected XY planes from limpet top and bottom; Orthoslice from limpet top: (b) preload, (c) last-load; Orthoslice from limpet bottom: XY plane: (d) preload, (e) last-load, YZ plane: (d) preload, (e) last-load.



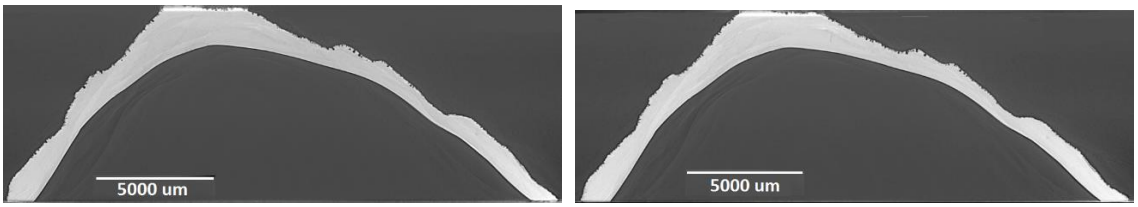
(a)



(b) Preload step (c) Last-load step



(d) Preload step (e) Last-load step



(f) Preload step (g) Last-load step

Figure 3.1.28. Reconstructed tomographs of complete wet limpet. (a) 3D volume of limpet and selected XY planes from limpet top and bottom; Orthoslice from limpet top: (b) preload, (c) last-load; Orthoslice from limpet bottom: XY plane: (d) preload, (e) last-load, YZ plane: (d) preload, (e) last-load.

3.1.2.2 In situ tomography of indentation tests on cortical bone

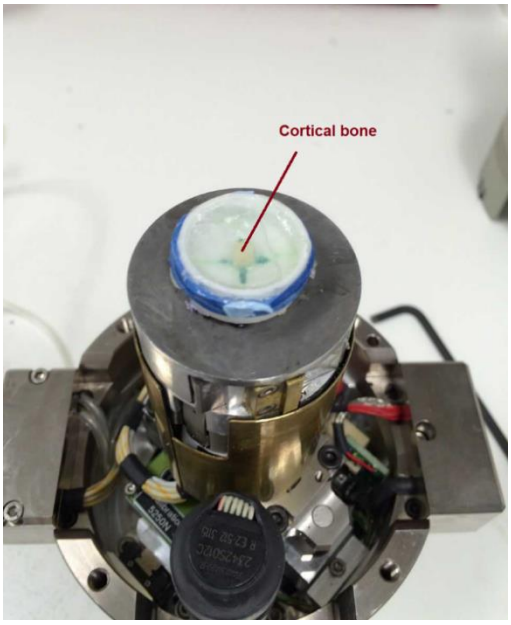
In-situ Hertzian indentation tests were conducted during X-ray tomography to obtain 3D microstructural information of bone samples before and after loadings.

3.1.2.2.1 Cortical bone sample preparation and design of sample chamber

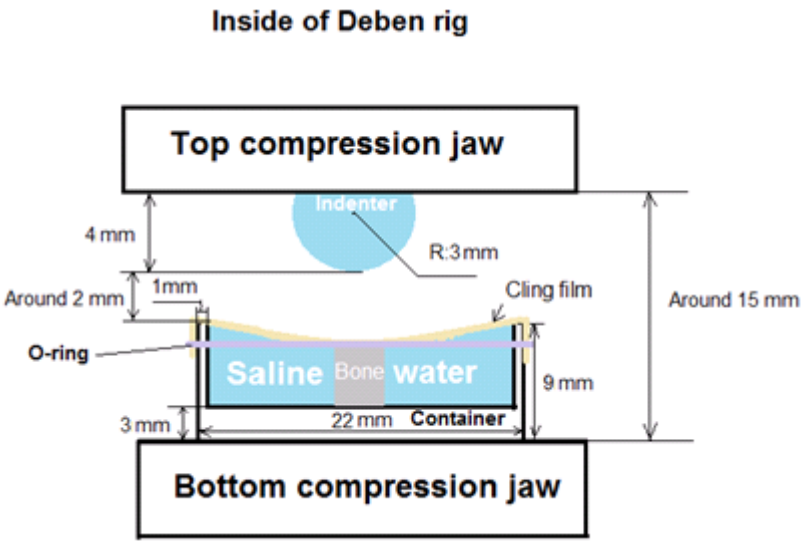
For the in-situ tests, sections of cortical bone were cut into smaller sizes compared with those used for microstructural information which are approximately 3 mm x 3 mm x 4 mm. This allowed higher resolution tomographs in a reasonable time, while keeping the whole bone volume in the field of view.

The container to hold the phosphate saline solution and keep the bone moisturised was modified for the in-situ tests with consideration for the intrinsic travel limit of the top and bottom compression jaws of the Deben rig, which is around 15 mm without the application of indenter and sample. The sealed container with cortical bone glued to the bottom is shown in *Figure 3.1.29* (a) and a schematic image of the arrangement of specimen and indenter inside of Deben rig before scan is shown in *Figure 3.1.29* (b). The design is based in knowledge of the size of indenter tip (a sapphire ball with a dimeter of 6 mm), approximately 4 mm of the indenter tip protruded from the top jaw, which left less than 11 mm space for both indenter moving space and container height. The indenter was mounted in the middle of top compression jaw using Pritt stick glue. For high resolution scans, a longer scan time is required, which results in a greater loss of liquid by evaporation. The container needs to be taller than the bone sample, in order to ensure the whole sample is immersed in the liquid, and it should have a reasonable base size to hold enough solution to compensate the possible loss of solution during the scan. However, the base diameter could not be too large considering the fact that long path of X-rays through saline solution to reach the sample may cause the loss of image sharpness, particularly with convection movement of the fluid . Therefore it is sensible to have the container with reasonable base size but high wall to hold as much solution as possible.

As a consequence, the container was designed to have an inner diameter of 20 mm, excluding the 1 mm wall thickness, and a height of 9 mm including the 3 mm base thickness, which still allowed the indenter to have room for movement before touching the bone. The same material and production method for the container have been applied as before. In order to minimize solution evaporation, the same sealing method has been used as for tomography of microstructures. But in this case, cling film was sealed loosely to avoid additional stress induced by the stretching of plastic film during the indentation. In order to make a comparison with wet samples, dry samples were also prepared (*Figure 3.1.30*). Dry samples were also glued to the centre of the container bottoms but no saline solution and sealing were applied to the container, which had the same dimensions as those used for wet specimens.



(a)



(b)

Figure 3.1.29. (a) Cortical bone in wet condition which is placed in a sealed container with loosed applied film; (b) schematic image of the arrangement of sample and indenter inside of Deben rig.

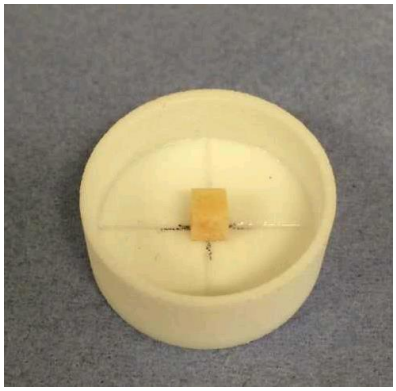


Figure 3.1.30. The prepared dry bone.

3.1.2.2.2 Testing method

The in-situ Hertzian indentation test composes of preloading, loading and unloading steps. For the preloading step, the bone was held under a load below 5 N to keep contact between indenter and bone. Due to relaxation of the bone under indentation, displacement control loading was used, and the load was gradually increased with increasing displacement at a rate of 0.1 mm/min. The behaviour of the bone under the indentation was observed using X-ray tomography, with two or three loading steps generally applied to generate sufficient displacement fields which can be measured using DVC. Typically, the displacement applied on top of cortical bones for each loading step was ~0.15 mm and the load at the final step was up to 300 N. For the unloading step, the load was decreased to its original preload (5 N) and the tomographs were recorded to examine whether permanent deformation had occurred during indentation.

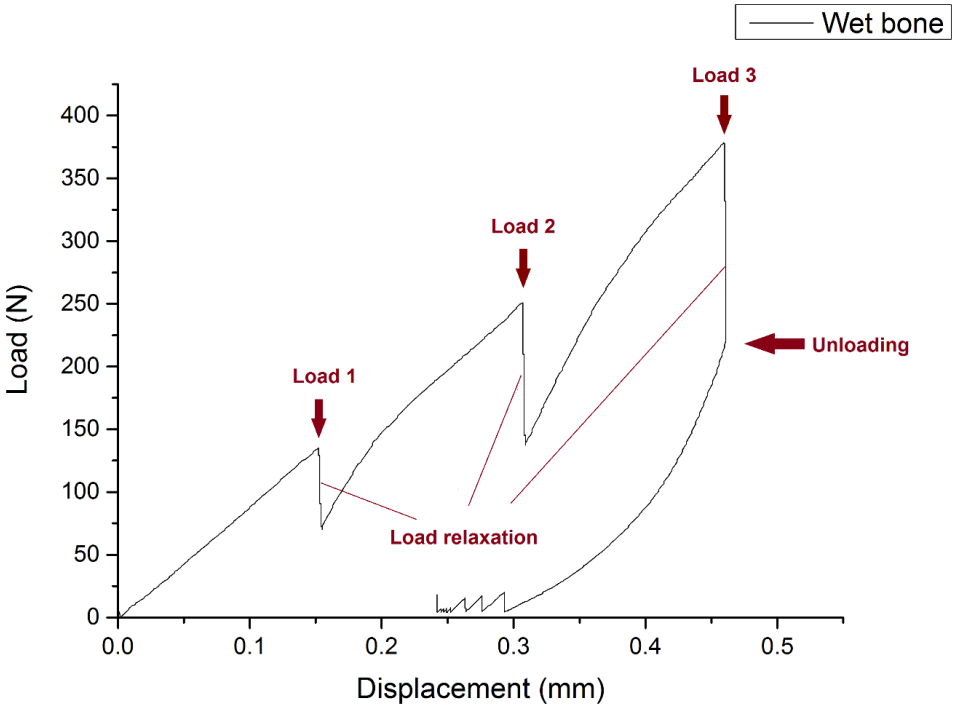
The selection of scanning parameters (applied voltage, exposure time, bin number, objective and projection number) followed the same process as the normal absorption scanning. No filter was required in this case because the X-transparent carbon tube of the Deben rig intrinsically acts as filter for low-energy X-rays. The in-situ indentation tests required a resolution of approximate 2 um and full field of view of the specimen, so the objective was selected as x4 with no binning. The applied voltage was 80 kV and 1601 projects were collected over the 360^{o} scan. Due to the different conditions of each sample (e.g. size) and saline solution (e.g. density), exposure time varied from 30 sec to 50 sec per projection to achieve a balance between sufficient count rates (5000-10000) for the radiograph and a reasonable scanning time. These were maintained for the multiple scans of the same sample under the different loading conditions. A half-hour warming-up step was applied before each scan and depending on the exposure time, the time for each scan varied from 19 hours to 24 hours. No automatic reference image could be taken during the scans due to the size of Deben rig, which cannot be moved out of the field of view completely. Hence, manual reference images were taken by the removal of the sample from the rig before

the in situ experiments, using the same scan parameters. After the reference scan, the container with sample inside was roughly placed in the centre of the bottom compression jaw, the position of which could be adjusted, according to live radiographs, to ensure that the indenter would touch the top of the bone. Radiographs at 0 and 90° taken with a 0.4 objective were used to adjust the position of sample because with the x4 objective, it was not possible to observe both the indenter and the sample in the same field of view.

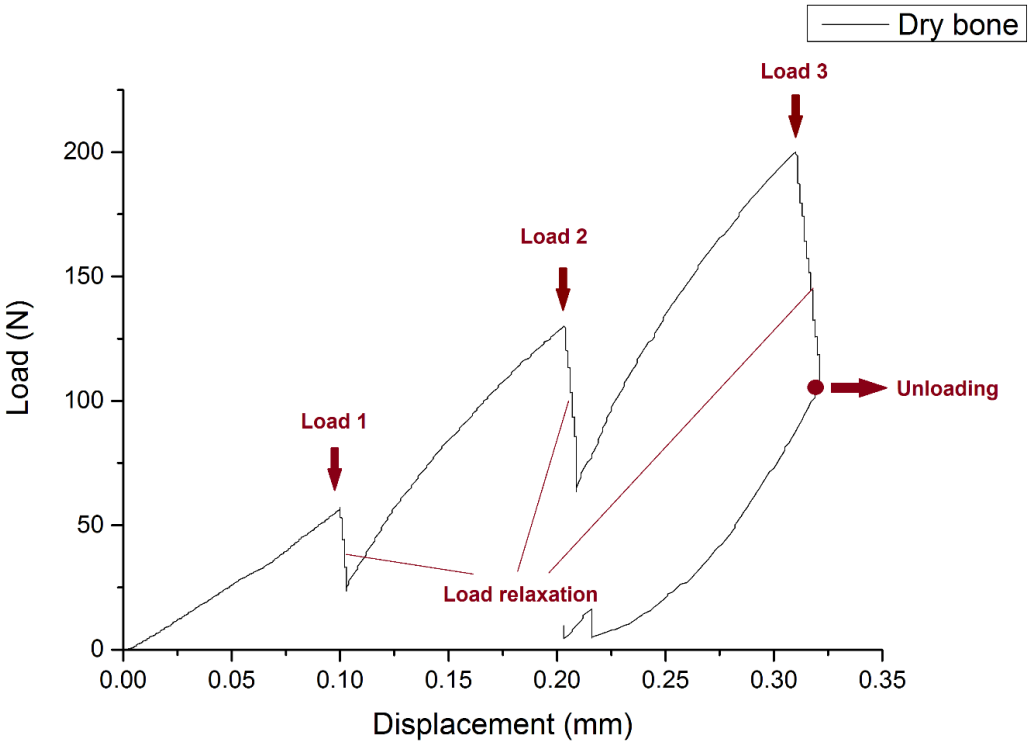
Examples of recorded load-displacement curves of one wet specimen and one dry specimen directly from the Deben rig are shown in *Figure 3.1.31*. The significant load relaxation during the tomography scans is apparent. A typical radiograph with indenter touching the bone is shown in *Figure 3.1.32*.

3.1.2.2.3 Tomograph results

Comparisons between tomographs of dry and wet bones are shown in *Figure 3.1.33*. Except the increased noise present for cortical bones under hydrated condition, bones overall has a microstructure which provides good trackable features and thus achieve a good spatial resolution for DVC analysis [148].



(a)



(b)

Figure 3.1.31. Recorded displacement-load curves of tested bones. (a) Wet bone; (b) Dry bone.

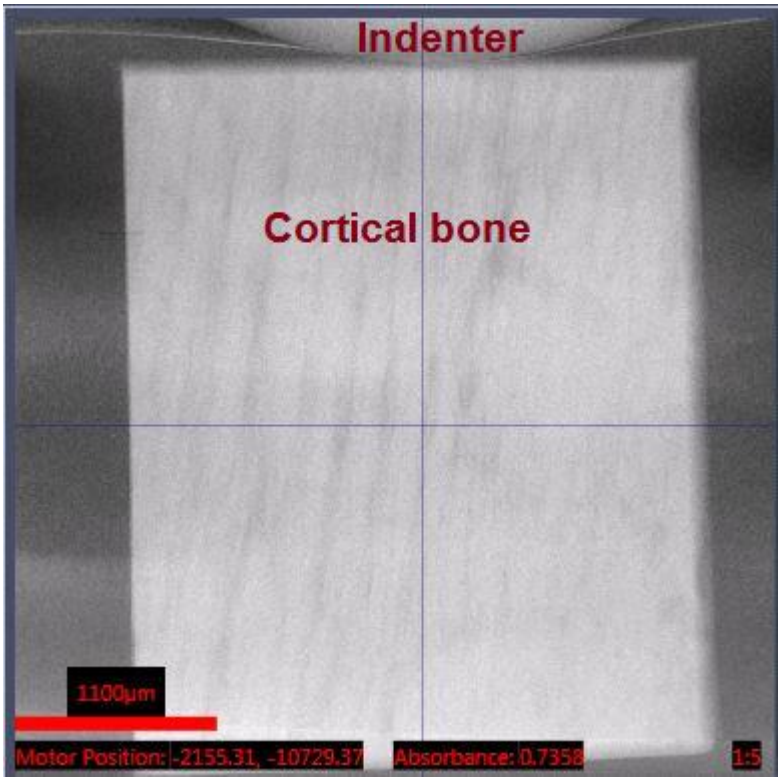
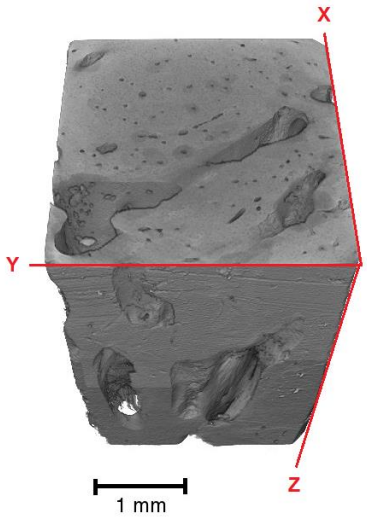
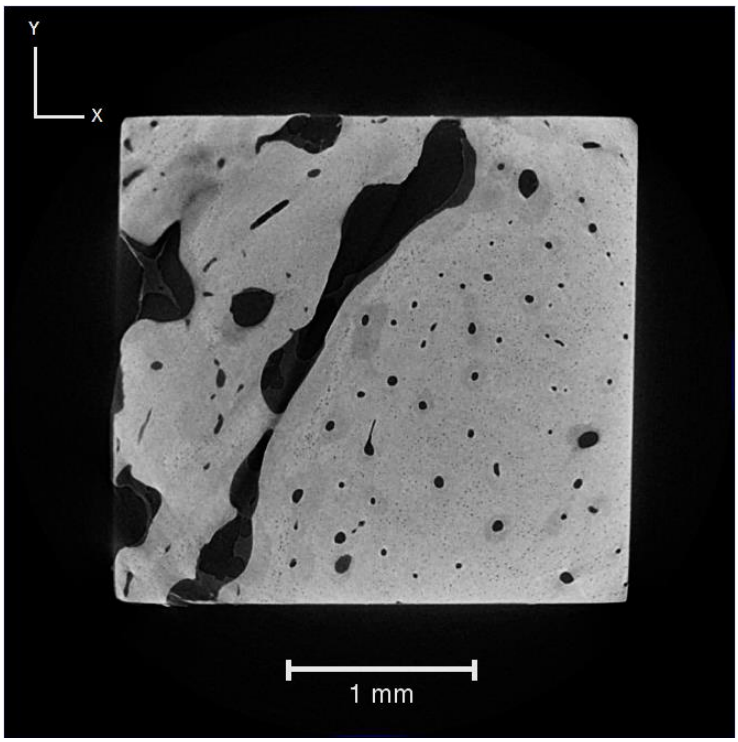
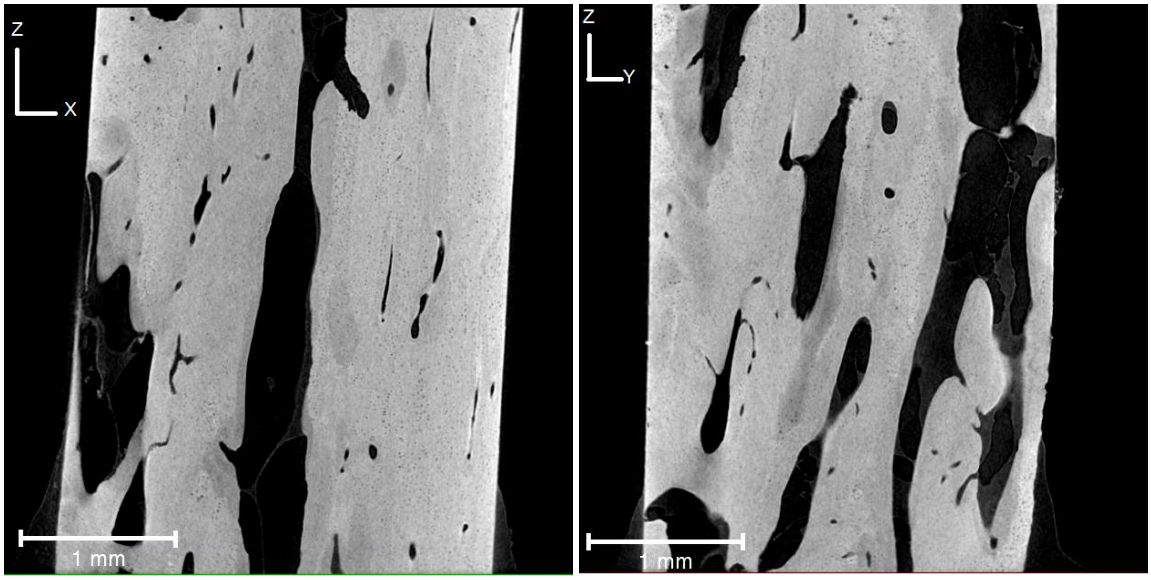


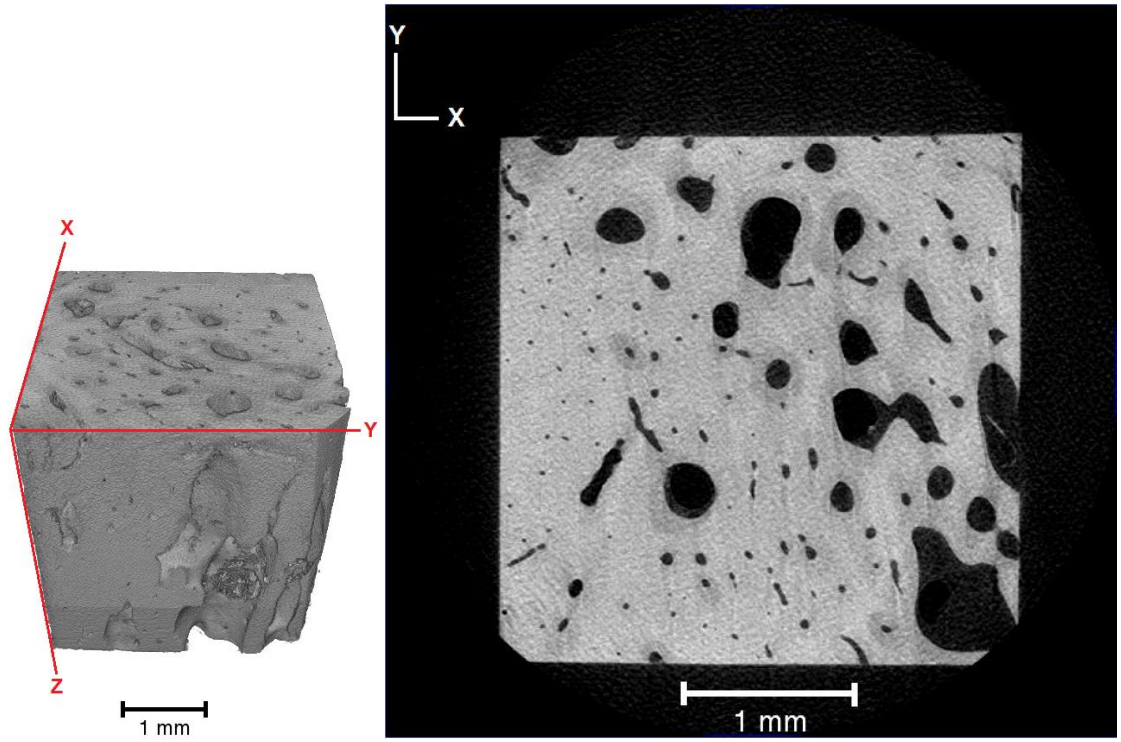
Figure 3.1.32. Radiograph of cortical bone in its preload state.

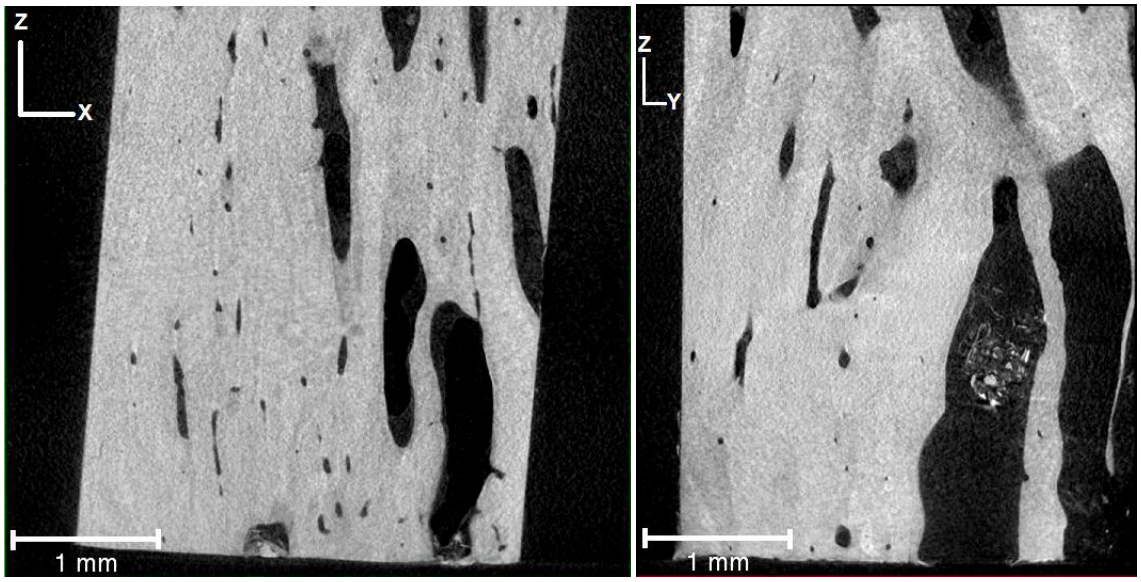






(a)





(b)

Figure 3.1.33. Comparisons between tomographs of cortical bones under different hydrated conditions: (a) 3D volume of a dry bone specimen and its tomographs in XY, XZ and YZ planes. Resolution is 2 um. The applied voltage is 80KeV, Bin: x1, objective: x4, no filter applied, exposure time: 30 seconds, 360^o scan, 1601 projections, scan time: 14hours 50miniutes. (b) 3D volume of a wet bone specimen and its tomographs in XY, XZ and YZ planes. Resolution is 2.2 um. The applied voltage was 80KeV, Bin: x1, objective: x4, no filter applied, exposure time: 40 seconds, 360^o scan, 1601 projections, scan time: 19hours24miniutes. Both scans have a half hour's warming up scan in order to stabilize the load and at the same time keep source warm.

3.2 Analysis method

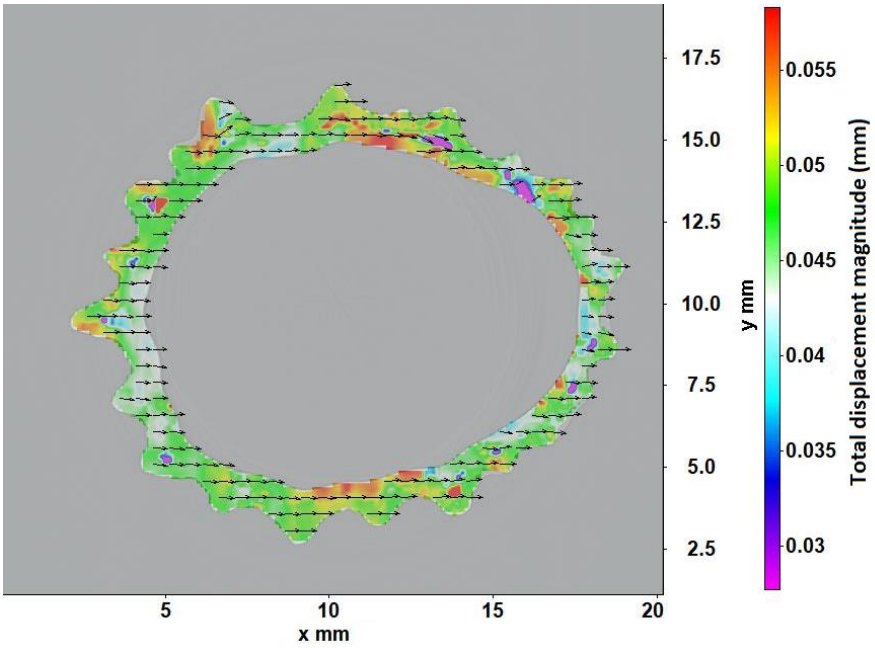
3.2.1 DVC analysis of rigid body movements

DVC analysis has been applied on tomographs of un-deformed and deformed specimens in order to extract displacement distribution throughout the 3D volume. Lavision Davis software (version 8.4.0) has been used.

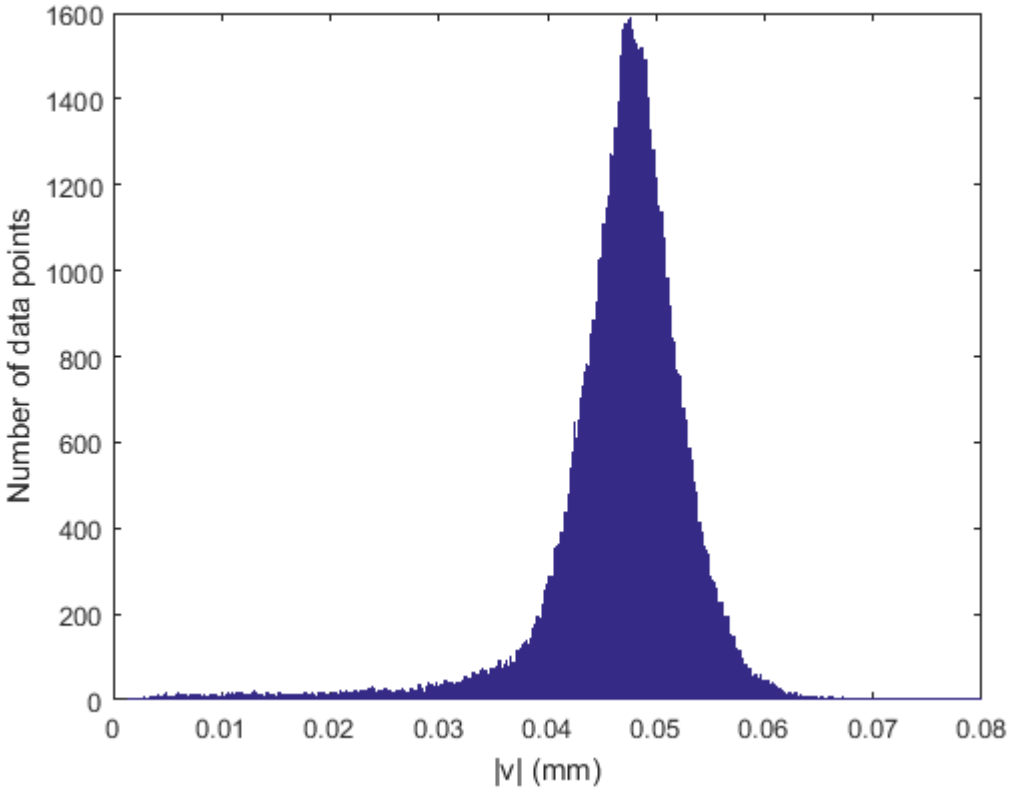
DVC analysis of rigid body movement was used to evaluate the accuracy of DVC and suitability for DVC to extract deformation information later on deformed samples. Tomographs with the same scan parameters of original specimen and specimen which has been moved in a single direction with a known distance were prepared before analysis.

3.2.1.1 Mollusc Shell

DVC analysis was done on module 2 synchrotron tomographs (resolution: 7.9 um) of a limpet sample with and without a nominal 50 um rigid body movement in x direction. An algorithmic mask has been applied in DVC software on both sets of tomographs by selecting the minimum grey level threshold (110) in order to remove background noise and segment regions of interest of the limpet. The selected DVC parameters are shown in *Table 3.2.1*. The resultant distribution of total displacement magnitudes in the limpet has been studied instead of x-displacement field since the movement axes may not be perfectly aligned. The distribution of total displacement magnitudes on one selected XY plane is shown in *Figure 3.2.1* (a) and the distribution of total displacement magnitudes throughout the 3D volume of data points is shown in *Figure 3.2.1* (b). The obtained mean total displacement magnitude in 3D volume is 0.047 mm with approximately 0.007 mm standard deviation ($\pm$15%), which is relatively accurate. Therefore it indicates that synchrotron tomographs of limpets have sufficient level of contrast for DVC analysis and thus the extraction of displacement and strain from deformed limpets is possible.



(a)



(b)

Figure 3.2.1. The distribution of total displacement magnitudes on one selected XY plane using synchrotron tomographs (resolution: 7.9 um): (a) Colour mapping of total displacement magnitudes on XY plane. Vectors indicate xy displacement on this plane; (b) Plot of distribution of total displacement magnitudes in 3D volume data points. The majority of the data points are around 0.047 mm. Large deviations were observed which result from noises in data.

Table 3.2.1. Optimum DVC settings for rigid body movement on complete limpets.

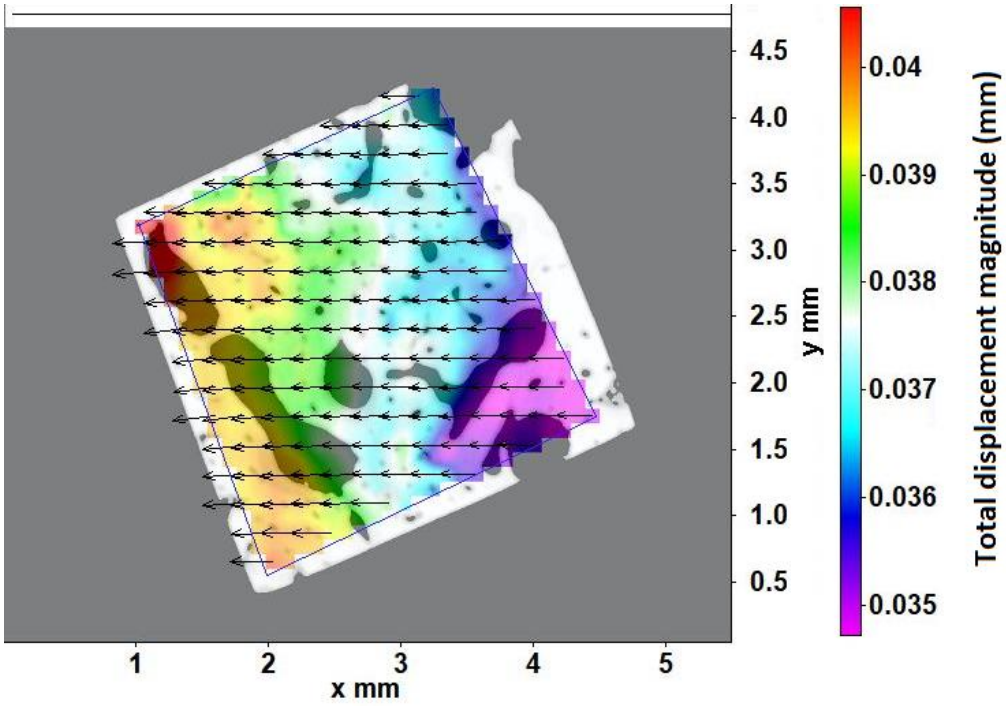
Multi-step process	Subset size	256x256x256 pixel^3	128x128x128 pixel^3	64x64x64 pixel^3
	Overlap of subset	50%	50%	75%
	Passes	2	2	1
Required valid voxel per window		50%		
Delete vector if the correlation coefficient		0.6		

3.2.1.2 Bone

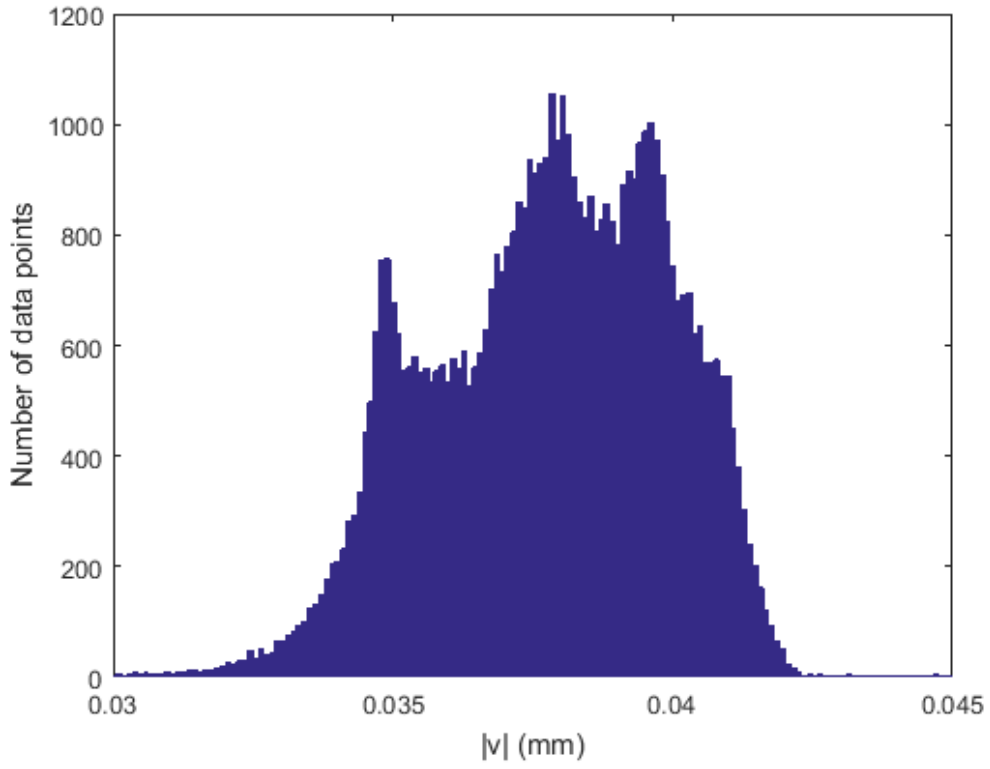
A similar procedure has been done on one bone specimen in laboratory tomography with nominal 50 um movement in the x direction to study the suitability to use DVC analysis for deformed bone samples. The selected DVC parameters are shown in *Table 3.2.2*. as the same reason indicated for limpet study, the total displacement magnitudes of bone have been investigated. Total displacement magnitudes on one selected XY plane are demonstrated in *Figure 3.2.2* (a) together with the histogram of total displacement values in 3D volume of data points in bone (*Figure 3.2.2* (b)). Data points which are around edges of the sample and considered inaccurate have been removed in post-processing using geometric mask (blue square in *Figure 3.2.2* (a)). The mean value of total displacement magnitude in 3D volume bone is 0.0378 mm with 0.0023 mm standard deviation ($\pm$ 6%). Although the precision of DVC result on bone is slightly lower than limpet, limpet is very thin so DVC only captures the information of the edges of the specimen whereas for bone there is a distribution of relatively accurate displacement inside the material due to its pore network, which is favourable for DVC analysis.

Table 3.2.2. Optimum DVC settings for rigid body movement on bone specimen.

Multi-step process	Subset size	256x256x256 pixel^3	128x128x128 pixel^3	64x64x64 pixel^3
	Overlap of subset	50%	50%	75%
	Passes	2	2	1
Required valid voxel per window		70%		
Delete vector if the correlation coefficient		0.3		



(a)



(b)

Figure 3.2.2. Total displacement magnitude on one selected XY plane using laboratory tomographs (resolution: 6.9 um): (a) Colour mapping of total displacement magnitude on XY plane. Vectors indicate xy displacement vector on this plane; (b) Plot of distribution of total displacement magnitude in 3D volume data points. The majority of the data points are around 0.0378 mm.

3.2.2 DVC analysis of deformation

The method to get displacement and strain fields by correlation of undeformed and deformed tomographs of a sample from DVC analysis is similar to the one for rigid body movement. However, parameters for analysis have been changed based on the obtained tomographs and the optimum DVC setting is a multistep process involving 3 stages with decreasing subset size (*Table 3.2.3 Table 3.2.4 Table 3.2.5*).

Table 3.2.3. Optimum DVC settings for compression tests on complete limpets (FFT).

DVC parameters					
Multi-step process	Subset size	256x256x256 $pixel^3$	128x128x128 $pixel^3$	64x64x64 $pixel^3$	32x32x32 $pixel^3$
	Overlap of subset	50%	50%	50%	75%
	Passes	2	2	2	1
Required valid voxel per window		50%			
Delete vector if the correlation coefficient		0.6			

Table 3.2.4. Optimum parameters used for displacement and stress/strain on pre-notched limpets (direct correlation).

DVC parameters				
Multi-step process	Subset size	256x256x256 $pixel^3$	128x128x128 $pixel^3$	64x64x64 $pixel^3$
	Subset shape	round	round	round
	Overlap of subset	50%	50%	75%
	Binning	4x4x4	2x2x2	no
	Passes	2	2	1
Required valid voxel per window		30%		
Delete vector if the correlation coefficient		0.7		

Table 3.2.5. Optimum DVC parameters for indented cortical bones (direct correlation).

DVC parameters				
Multi-step process	Subset size	256x256x256 $pixel^3$	128x128x128 $pixel^3$	64x64x64 $pixel^3$
	Subset shape	round	round	round
	Overlap of subset	50%	50%	75%
	Binning	4x4x4	2x2x2	no
	Passes	2	2	1
Required valid voxel per window		70%		
Delete vector if the correlation coefficient		0.6		

3.2.3 Porosity Characterisation

Based on the reconstructed tomographs of 3D volumes of cortical bones, porosity of each sample can be calculated using ImageJ and Avizo. In ImageJ, features of samples present in tomographs have been enhanced using adjustment of contrast/brightness. Gaussian blur 3D filter is then applied to smooth out the noise in the background. Both steps are used to help pore segmentation in Avizo. After importing the raw file from ImageJ into Avizo, segmentation of pores from the bone matrix has been done in the Avizo using the function 'magic wand'. This function is used to select the range of grey level which distinguishes the bone matrix from pores and helps generate a new material phase which only contains the information of pores. The volume of this can then be calculated using the software function 'label analysis'.

3.2.4 PReMISe: Simulation of elastic modulus from porosity

The way to use PReMISe to obtain relations of porosity and E/E_0 (E stands for apparent elastic modulus and E_0 stands for intrinsic elastic modulus) in different loading directions for cortical bones is introduced in this section.

According to the PReMISe software requirement, the stack of reconstructed .tiff files of one particular bone sample needs to be transformed into 100 pixel x 100 pixel x 100 pixel .bmp file stack before imported into the software. In order to achieve that, the sequence of .tiff images requires pre-processing in ImageJ. In ImageJ, the brightness and contrast of .tiff images are adjusted to enhance the microstructural features. Rotation of image is applied for better cropping. The maximum volume limit of the bone was cropped with same lengths in transverse and radical directions with less than 15% reduction in volume compared with the original one. Along the longitudinal direction (z axis in *Figure 3.1.33*), each individual bone has been divided into several parts in order to create a several cubic volumes of bone with equal axis lengths depending on specimens' heights. After that, each cubic volume is resized into 100x100x100 $pixel^3$ using *Image-Adjust-Size* option with the bicubic interpolation algorithm in ImageJ. Avizo

was then used to convert final binary .raw data, which was obtained using Make Binary in ImageJ, into .bmp stack. In order to investigate the apparent elastic modulus in different loading directions (in the project, the loading is applied along the axes of the sample), each cube is rotated into three different orthogonal directions and then analyzed using PReMISe.

Chapter 4

4 Image-based finite element modelling of biomaterials

This chapter is divided into two sections. In the first section, two models with the geometry of limpet obtained from X-ray tomography have been built. The first model was built with loading boundary condition provided by the in-situ experiment in order to extract elastic modulus of limpet by matching simulated loads with experiment ones. The second model was built with 3D displacement field obtained from DVC analysis as boundary conditions to provide strain distribution of deformed specimen. The obtained strain fields from both approaches have been compared.

In the second section, a FE model of cortical bone with real porosity network in indentation area obtained from 3D imaging under indentation has been created. The variables in the model which influence the output strain field within the deform specimen have been discussed and compared with experimental strain field obtained from DVC analysis.

4.1 Mollusc Shell

The objective of the analysis was to take the real bulk geometry of a limpet into consideration to extract the elastic modulus. No detailed microstructure of limpet has been included in the model because limpet presents very complicated lamellar microstructure which is difficult to duplicate (Appendix: *Section 10.1* : Further investigation of microstructures of limpets). Abaqus 6.14-2 was used for finite element analysis.

4.1.1 FE mesh generation

Due to the complicated geometry of limpet, Simpleware software was employed to create a meshing before the creation of FE model in Abaqus. This was based on CT tomographs of the complete dry limpet from the first synchrotron experiment.

Before meshing, ImageJ software was employed for image pre-processing. 3D volume of the limpet has been reduced in size by a factor of 10 from 2560x2560x899 pixel^3 to 256x256x90 pixel^3 using option: image-adjust-size in order to reduce element number. There is no significant change in the geometry of limpet before and after resizing (*Figure 4.1.1*). The resized images were then imported into Simpleware software for meshing.

In Simpleware, the *threshold* option was used to create a new mask which contains the result of segmentation of the limpet for meshing and the selection of the grey-level range for the individual phase was checked visually. A region growing algorithm was then applied by using *Flood fill* tool on the mask to satisfy connectivity preservation. Parameters were chosen and modified to control the final size, shape and number of elements. For meshing, *smart mask smoothing* was chosen to create a smooth distribution of elements across the sample surface. The meshing was set to be based on the greyscale values of tomographs. The type of elements was set to be all tetrahedral (linear) for fast meshing. The minimum edge length (mm) of element was set to be 0.1 mm based on small feature sizes of limpet while the maximum edge length (mm) was set to be 1 mm in order to generate large elements where no delicate feature

is present. The allowance of maximum error was set to be 0.0079 mm. Internal change rate of volume mesh generation (1 (slow) to 100(fast)) was set to be 6, which allows finer mesh generation. The aim of element was expected to be around 50000-300,000 to ensure features of limpet contour can be kept and represented by elements. After the selection of meshing parameters, *full model* option was chosen for meshing. After checking element quality, an .inp file which contains information of node coordinates and mesh numbers was able to be generated and saved, which was used in Abaqus later [218] . The limpet before and after meshing are shown in *Figure 4.1.2*.

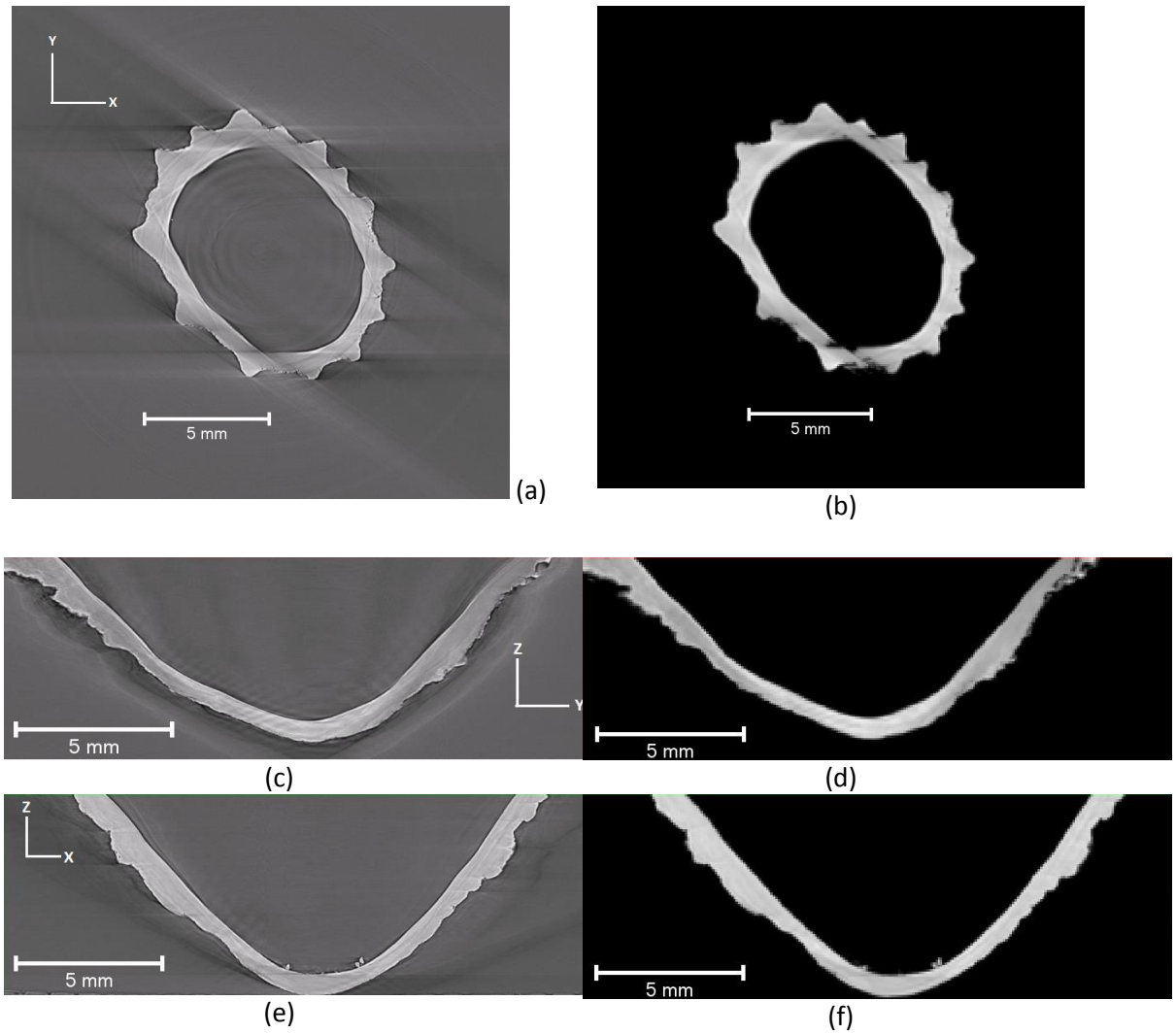


Figure 4.1.1.Orthoslices of limpet before (a) (c) (e) and after resizing (b) (d) (f). Orthoslice on (a) XY plane original; (b) XY plane after size reduction; (c) YZ plane original; (d) YZ plane after size reduction; (e) XZ plane original; (f) XZ plane after size reduction.

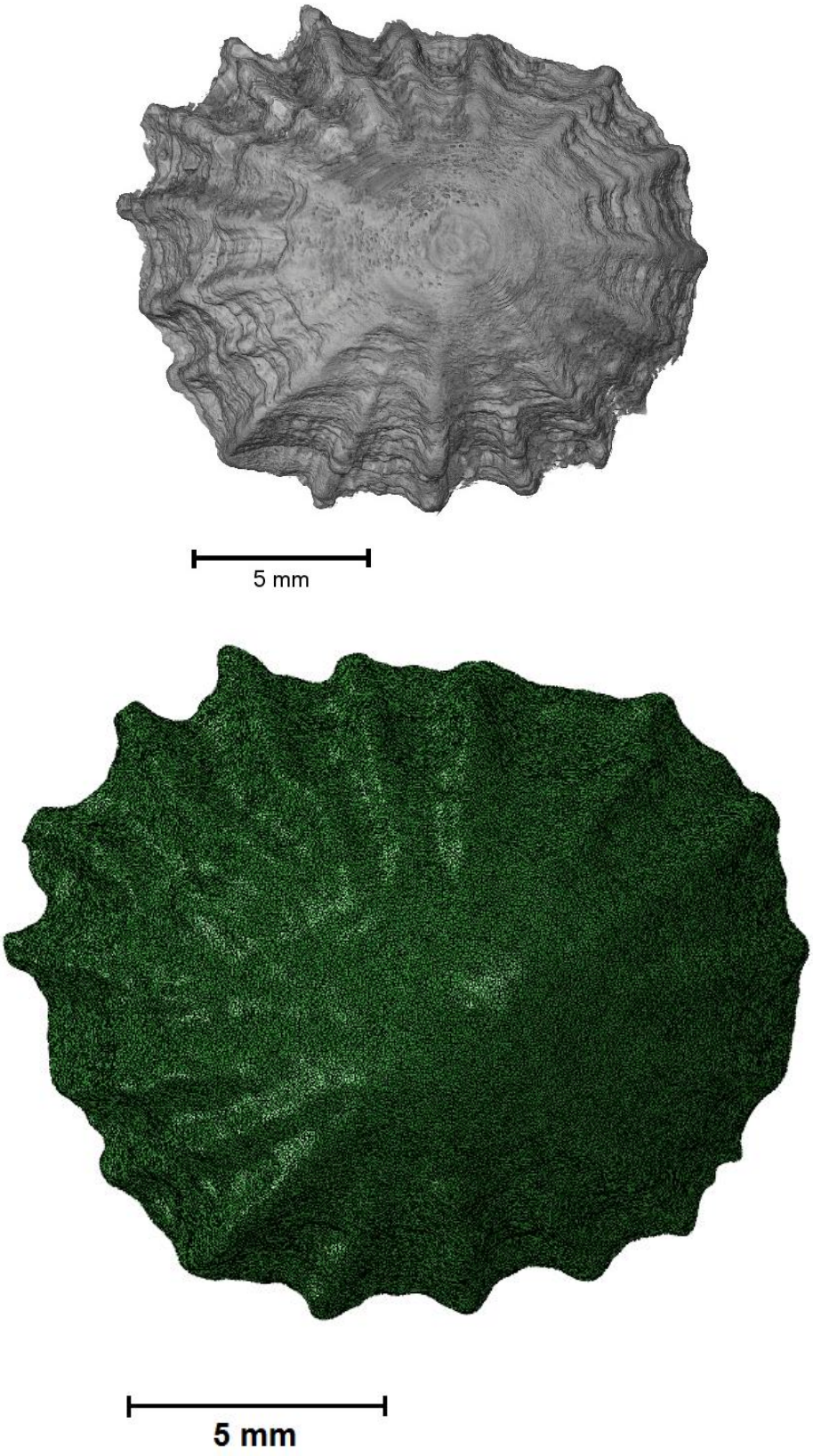


Figure 4.1.2. a) 3D volume of limpet; b) Meshed limpet with 382275 elements.

4.1.2 Contact compression modelling with simple boundary conditions

After importing the .inp file of meshed limpet from Simpleware into Abaqus, two high density polyethylene (HDPE) sheets with a size of 12 x 12 x 1 mm^3 and 20 x 20 x 1 mm^3 were created and meshed with 16237 elements and 44132 elements, respectively to represent the compression sheets used in the experiment. Node to node rigid body translations were applied to the PE sheets to position just in contact with the top and bottom of the limpet (*Figure 4.1.3*). Young's modulus and Poisson's ratio of PE were set to be 800 MPa [219] and 0.46 [220]. Linear elastic behaviour of limpet was assumed and at the same time the limpet material was simplified as continuum. The Poisson's ratio of limpet was assumed to be 0.3. The elastic modulus of limpet was set to be the only variable in the model, which was tuned to minimize the difference between simulated displacement and experimental measured one (<1%).

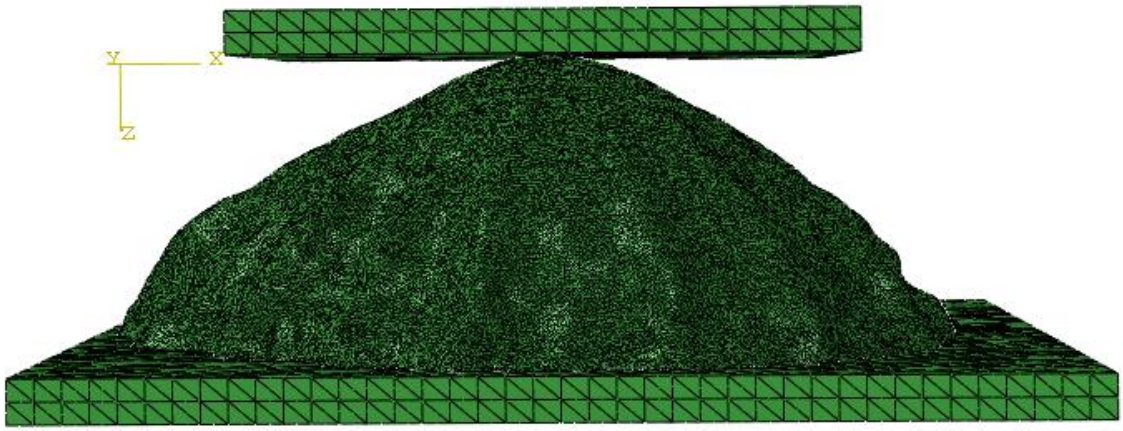


Figure 4.1.3. Positions of limpets and two PE sheets.

Meshes in the contact area around limpet apex and bottom were selected as master surfaces while meshes in the contact area on the bottom surface of top sheet and the top surface of the bottom sheet were selected as slave surfaces (under the options of surface to surface contact definition) because limpet has higher elastic modulus than HDPE sheet. Frictionless tangential behaviour was assumed and small sliding was allowed between contacted surfaces. The top sheet was able to move in negative z direction by allowing the bottom of the sheet to apply

experimental load onto the top of shell. No rotation on the XY plane was allowed by fixing one side of the sheet in x and y directions because in the experiment the top sheet has been fixed to the top jaw. The bottom sheet was allowed to expand in x and y directions under compression but movement in z direction was prohibited.

All the nodes with z coordinate equal to 0 mm were selected as the set of the limpet top while all the nodes with z coordinate equal to 7.031 mm were chosen as the set of limpet bottom, using Matlab, and later inserted into the .inp file to create sets in Abaqus. By applying the experimental recorded load via the top sheet to limpet, the simulated displacement across the whole limpet in the z direction was calculated as the difference between averaged values of the z-displacements of nodes at limpet top and bottom. By iterative adjustments of elastic modulus of the limpet, the expected elasticity of limpet was obtained when the difference between simulated and experimental displacement reaches minimum. The experimental displacement and load curve is shown in *Figure 3.1.18*; the displacement was measured from the change in height of limpet in the radiographs. The obtained elastic moduli of limpet at different loads are shown in *Figure 4.1.4*. Except for the first data point at which the limpet was compressed at 58 N, the remaining three data points vary slightly around 20 GPa (average 20.28$\pm$0.17 GPa).

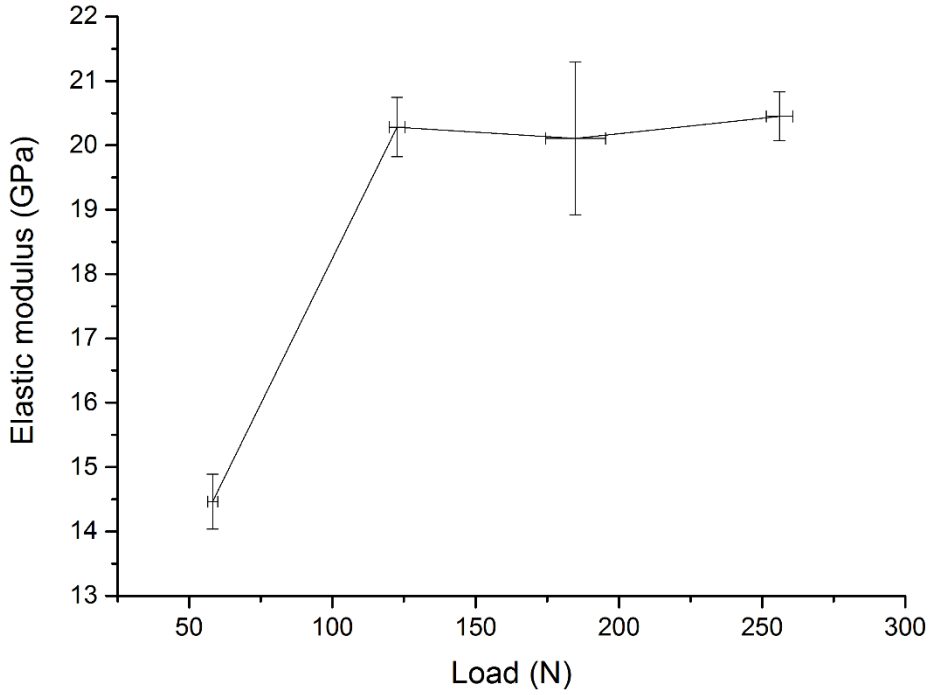
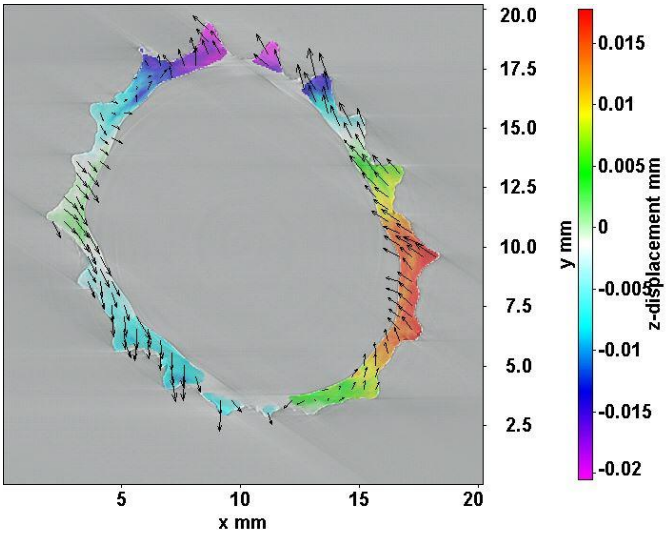
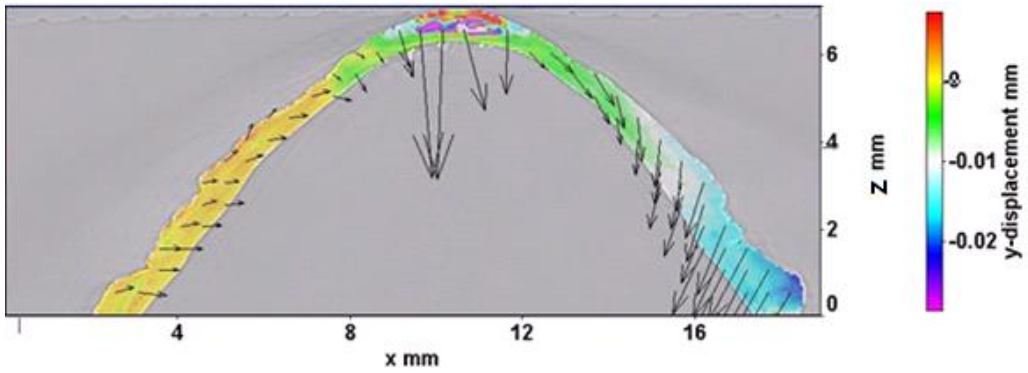


Figure 4.1.4. Simulated elastic modulus of limpet vs load.

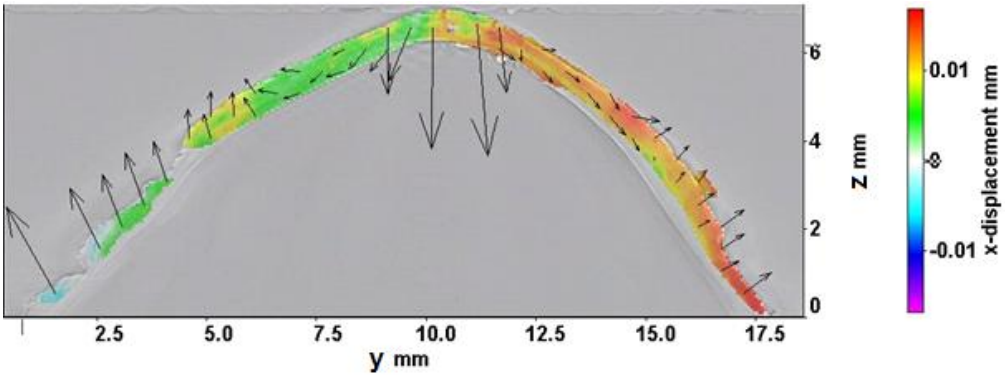
The lower value of simulated elastic modulus at low load (*Figure 4.1.4*) may be due to several reasons: 1) misalignment and movement of limpet under lower load; 2) a region of non-uniform loading, which may result from some small non-structural cracks at the limpet apex due to loading. There is evidence of rotation (*Figure 4.1.5* (a)), translation (*Figure 4.1.5* (b)) and tilting (*Figure 4.1.5* (c)) for the limpet under compressive loading of 58 N observed from DVC results. The displacements due to this would have a larger effect on the average displacement at low loads, and would support the first reason.



(a)



(b)



(c)

Figure 4.1.5. DVC results of displacement fields based on 32x32x32 pixel^3 subset with 75% overlap. (a) Vector arrows of XY displacements on the selected XY plane with colour mapping of z displacements and XY vectors indicate the rotation of the specimen on XY plane. (b) Vector arrows of XZ displacements on the selected XZ plane with colour mapping of y displacements. XZ vectors on the left side of the wall show x direction translation. (c) Vector arrows of YZ displacements on the selected YZ plane with colour mapping of x displacements. Except the top which show YZ displacements downwards which indicate that the limpet apex underwent compressions, vectors on limpet wall show upward YZ displacements which indicate the tilting of the limpet.

4.1.3 Finite element model with DVC boundary conditions

The analysis above used boundary conditions measured directly from experiment (load). An image-based FE model using the rotation-corrected displacement field, with removal of rigid body movement, as boundary conditions was built for comparison.

The output x, y and z displacement fields (ux, uy and uz) from DVC analysis were imported into Matlab together with x, y and z coordinates for rotation correction and rigid body movement removal using shoemake_3D code written by Dr. S. Barhli [108]. In the code, the rigid body movement can be removed by subtracting average values of non-zero ux, uy and uz from original ux, uy and uz. For rotation correction, Euler angle and rotation matrix were refined and obtained by iterative computations to achieve pure theoretical rotation. Rotation centre was calculated as (average value of x, average value of y, average value of z) for coordinates (x, y, z) at which *ux*+*uy*+*uz* is not equal to zero. Based on obtained rotation centre, Euler angle and rotation matrix, a rotation correction can be achieved by subtracting displacements due to pure rotation from the original data. The corrected displacements from DVC analysis were then interpolated to fit into FE model nodes in similar positions as boundary conditions using the SN_FE_reinj code, also written by Dr. S. Barhli. The interpolation matrix was calculated in the code by correlating three known coordinates in DVC to three points in the similar positions in FE model with known coordinates (*Figure 4.1.6*). The DVC data used for FE model was processed in 64x64x64 with 75% overlap for limpet under a load of 256 N instead of 32x32x32 pixel for less noisy result [167] (*Figure 4.1.7* (b)). Meshed limpet with 49510 elements was selected for the FE model which has element size in the same magnitude to the subsize of data point exported from DVC data (0.002 mm^3).

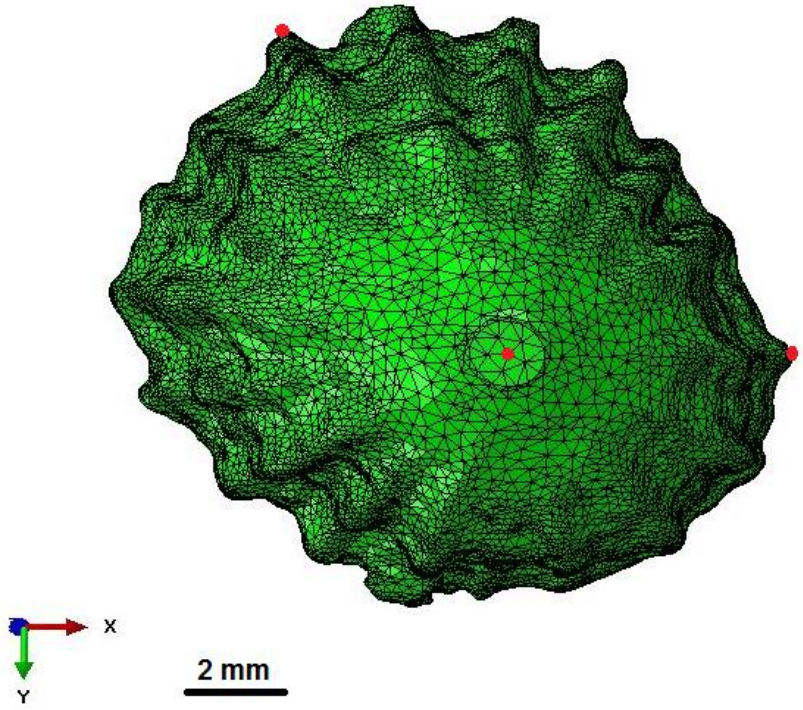
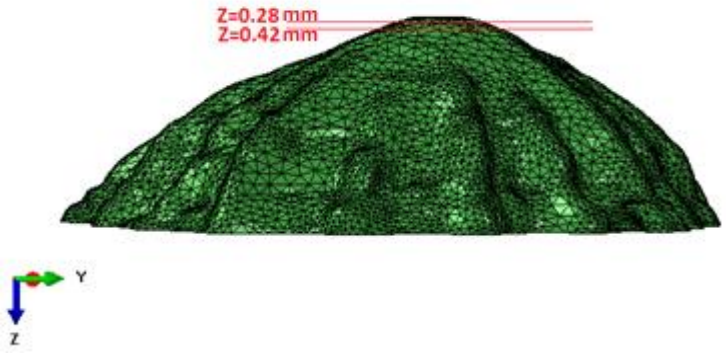
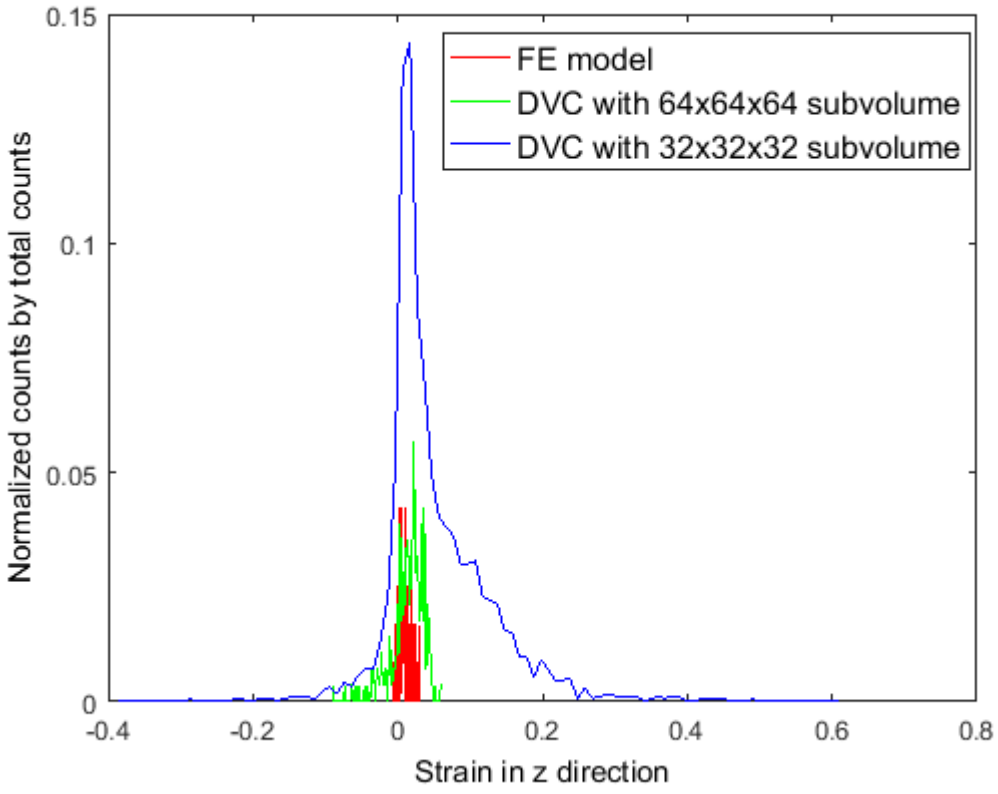


Figure 4.1.6. Three selected points in meshed limpet with 49510 elements in FE model for correlation to DVC data points in similar positions.

The obtained strains are compared with strains directly obtained from DVC in the same region of limpet. Due to differences between coordinates of FE nodes and DVC data points in similar positions, data on XY planes between Z=0.28 mm and Z=0.42 mm (*Figure 4.1.7* (a)) instead of one XY plane are selected for comparison. FE model with the corrected displacement field as boundary conditions gives much narrower strain distribution than that from DVC while DVC data processed in 64 x 64 x 64 pixel^3 subvolume gives narrower distribution of strain than that processed in 32 x 32 x 32 pixel^3 subvolume (*Figure 4.1.7* (b)). For three sets of data, the majority of the data points fall in a similar range of strain values.



(a)



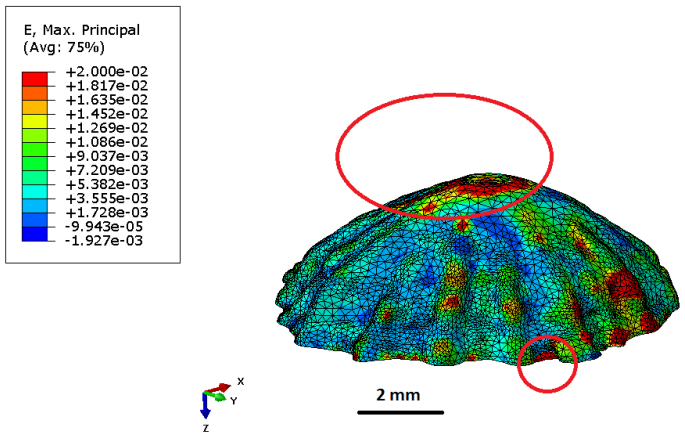
(b)

Figure 4.1.7. (a) Selected region in limpet for strain output. XY plane where z is equal to 0 mm represents limpet top.; (b) Histogram of simulated strain in z direction vs DVC strain results using different subvolumes.

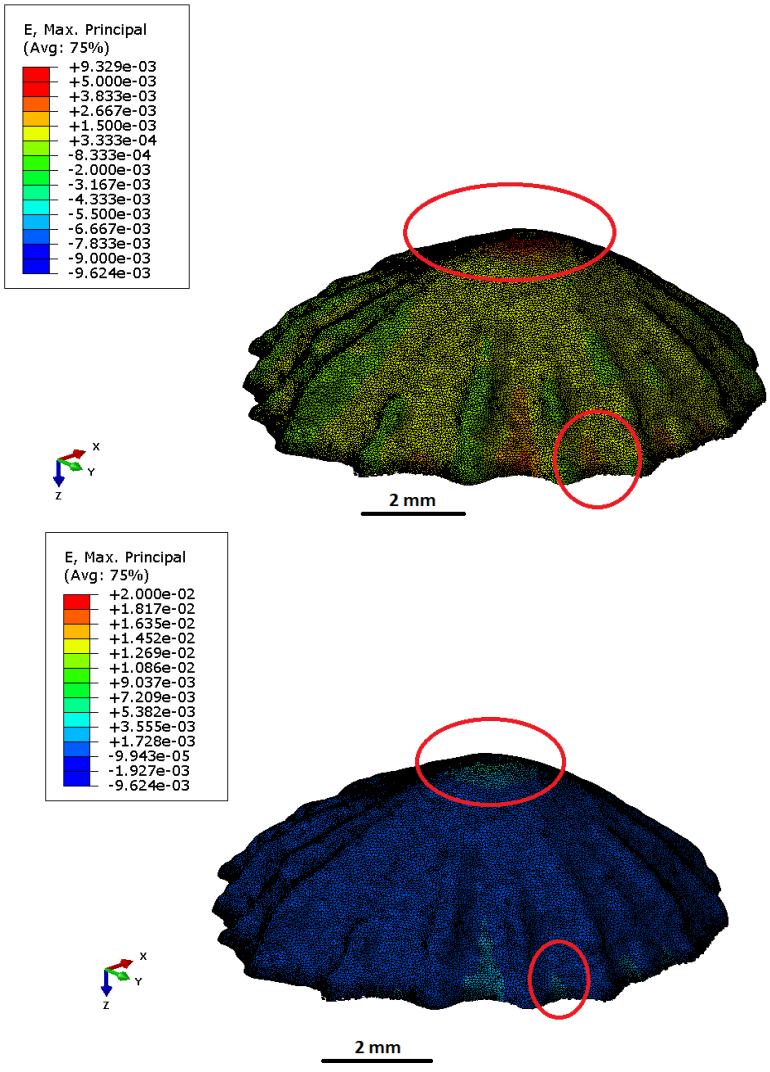
4.1.4 Comparisons of FE models with different boundary conditions

The strain results of contact compression modelling with simple boundary conditions (from *section 4.1.2*) are compared to FE model with DVC displacement fields as boundary conditions for the same loading condition. The actual load (256 N) and best fit elastic modulus (20451 MPa) (*Figure 4.1.4*) were used as input parameters for the contact compression model.

Both models present strain concentration areas where fractures may occur. Distributions of Max. Principle strain in 3D volume of limpet for both models are shown in *Figure 4.1.8*. Strain concentration areas where the actual major fractures in the experiment occur (*Figure 3.1.16*) (emphasized by red circles) observed in FE model with DVC boundary conditions (*Figure 4.1.8* (a)) are also observed in contact compression model (*Figure 4.1.8* (b)). The Maximum. Principle strains in strain concentrated areas in FE model with DVC displacements as boundary conditions are much higher than contact compression FE model. In addition, in contact compression model, strain tends to be concentrated in thin areas of the limpet margins (weak areas in limpet bottom) with similar possibility while in FE model with DVC displacements as boundary conditions, some particular regions in limpet bottom have much higher strain compared to other areas. The obtained strain field from FE model with DVC displacements as boundary conditions is close to experimental result due to the use of corrected experimental displacement field in the model.

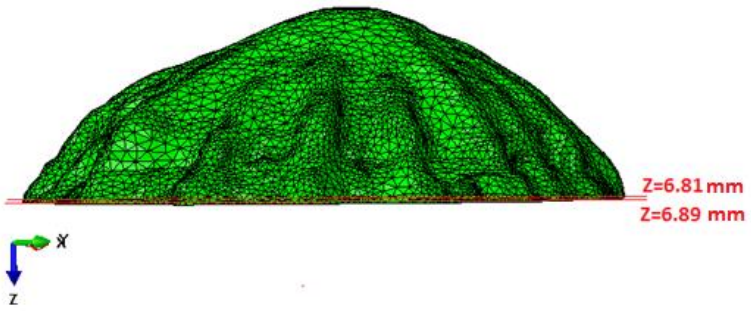


(a)

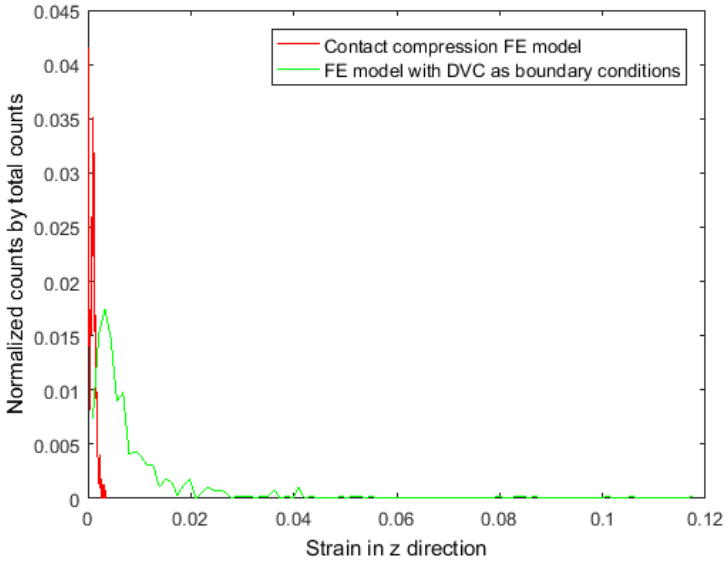


(b)

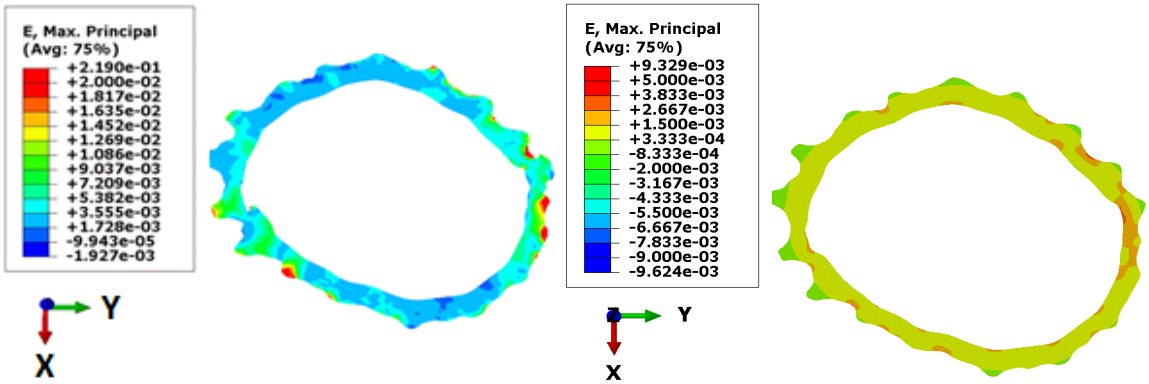
Figure 4.1.8. Simulated Max. Principle strain field in 3D volume of limpet. (a) Model with DVC displacement fields as boundary conditions; (b) Contact compression model with simple boundary conditions: top: the scale bar of strain has been modified to emphasize the strain concentration areas, Bottom: The scale bar of strain has been tuned to be the same as the one used for FE model with DVC as boundary conditions for comparison.



(a)



(b)



(c) (d)

Figure 4.1.9. Comparisons in Max. Principle strain in the selected region of limpet for contact compression model and model with DVC as boundary conditions. Z=0 mm is shell top.(a) 3D volume and selected region for data comparison; (b) Histogram of Max. Principle strain distributions for two FE models; (c) Max. Principle strain distribution on selected XY plane (Z=6.8 mm) for FE model with DVC displacements as boundary conditions; (d) Max. Principle strain distribution on selected XY plane (Z=6.8 mm) for contact compression FE model.

For further investigation of strain distribution in strain concentration area, values of Max. Principle strains on XY planes within the range of z=6.81 to 6.89 mm of limpet (*Figure 4.1.9* (a)), which are near the limpet bottom have been compared using histogram (*Figure 4.1.9* (b)). From *Figure 4.1.9* (b), the majority of the data points fall into a similar range of Max. Principle strain for both models but higher Max. Principal strains have been observed in FE model with DVC displacements as boundary conditions. As it is seen in *Figure 4.1.9* (c) *and* (d), less variation in strain mapping has been observed in contact compression FE model while relatively noisy data is present in model with DVC displacement boundary conditions on selected XY plane close to limpet bottom.

4.2 Bone

A two-phase finite element analysis of bone (bone matrix and pores) with real distribution and geometries of pores around indentation area has been built to study the mechanical behaviour of cortical bone under indentation.

4.2.1 FE Mesh Generation

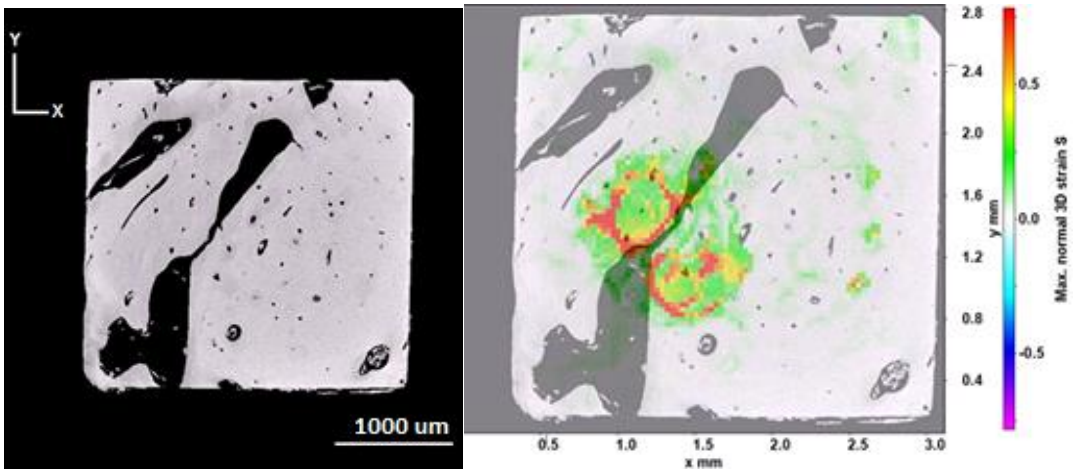
A bone specimen (THR61b) with a porosity of 14.03%, which has been indented in dry condition, was chosen for modelling.

In order to reduce the element number, the detailed features of pores have been kept around the indentation area while only very large pores were remained outside the indentation area (*Figure 4.2.1* (c)). The XY cross-sectional size of the area where features were kept, was determined by the Max. Principle strain concentration area present in DVC result of the maximum applied displacement (0.317 mm) (*Figure 4.2.1* (b)). The depth of the selected area where detailed features are kept is shown in *Figure 4.2.1* (e) in 3D volume. Before importing into Simpleware, the data has been resized from 1959x1956x1896 pixel^3 to 196x196x190 pixel^3 to further control the element number to be around 300,000 (*Figure 4.2.1* (d)). Small pores (less than 10 um) were neglected for meshing due to limited resolution of tomographs (*Figure 4.2.2*)

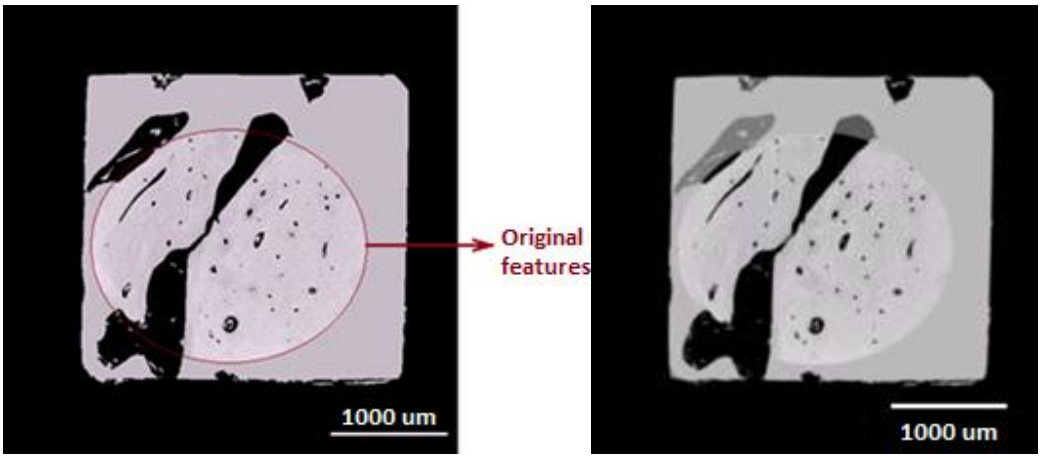
and they are expected to have negligible effect on simulated results with an estimated error of less than 10%. Detailed information has been explained in *Section 5.5.2.2*. The same meshing method has been used for bone as for limpet except the meshing parameters used in Simpleware varied. All tetrahedral elements (linear) have been created with minimum edge length (0.1 mm), maximum edge length (0.5 mm) and maximum error of 0.002 mm. The internal change rate of volume mesh generation was set to be 45, which allows relatively fine mesh generation but with reasonable element number. The resultant element number is 381347 and the meshed volume is shown in *Figure 4.2.3*.

4.2.2 Finite element modelling of compression by indentation

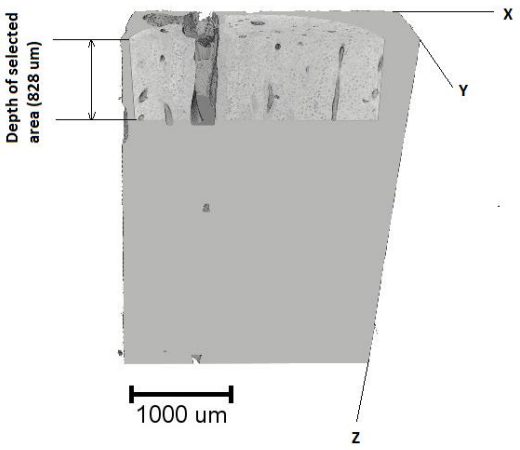
Two parts were created in the model. One was the meshed bone sample with selected element number and the other was a half-sphere indenter with the diameter which is the same as the one used in experiment (6 mm). Because the indenter in the experiment was made of sapphire, elastic modulus and Poisson's ratio were set to be 349 GPa and 0.29 [221]. The bone and the indenter were touching (*Figure 4.2.4*) and the contact between them was assumed to be hard and frictionless. The contact position was chosen to be in the centre of the area where indentation occurred, based on the DVC result (*Figure 4.2.7* (a)). The indenter was set to move down in negative z direction and compress the bone for a certain displacement (0.204 mm), which is the difference between the recorded absolute positions of the indenter in preloading step and first loading step in the experiment. The bottom of bone has been fixed and there is no expansion allowed in x and y directions for the indenter since the used indenter is much stiffer than bone specimen.



(a) (b)



(c) (d)



(e)

Figure 4.2.1.Pre-processing of tomographs before meshing. (a) Original tomograph; (b) DVC result of max. normal strain on selected XY plane using direct correlation using 64x64x64 pixel3subset with 75% under a displacement of 0.317 mm; (c) tomograph with simplified pore network(resolution:1.99um); (d) resized tomograph with simplified pore network (resolution:19.9um);(e) The depth of selected area in z direction in 3D partial volume of specimen.

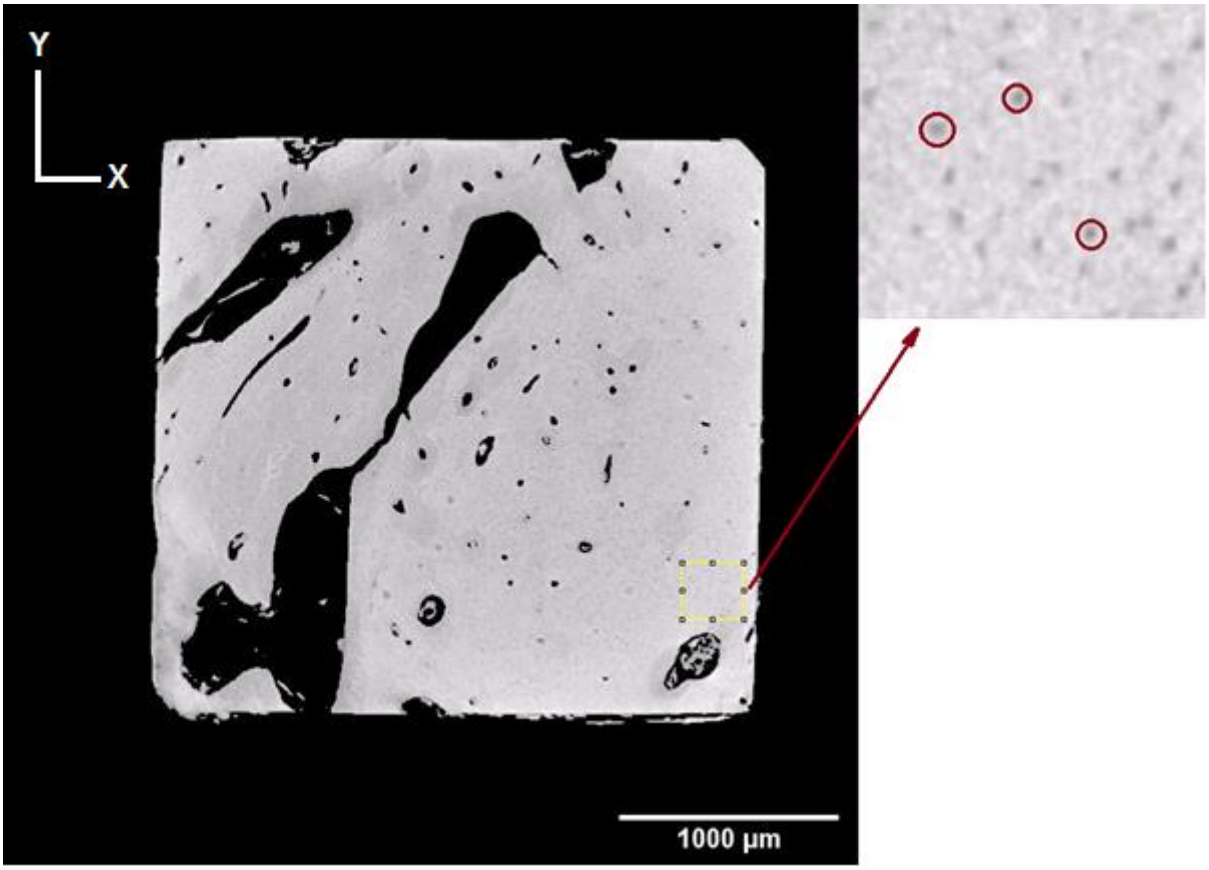


Figure 4.2.2. Amplified area in bone matrix where small pores marked in red circles are observed but not considered for meshing.

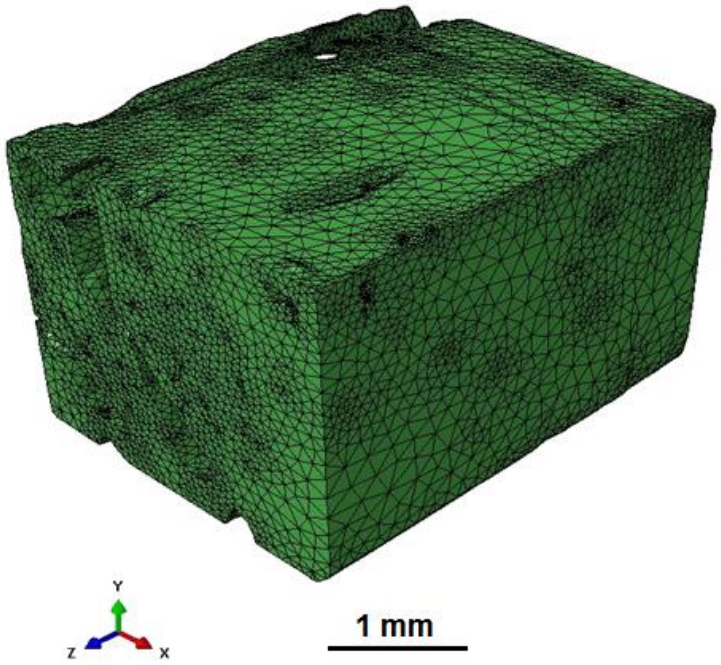


Figure 4.2.3. Meshed bone with 381347 elements.

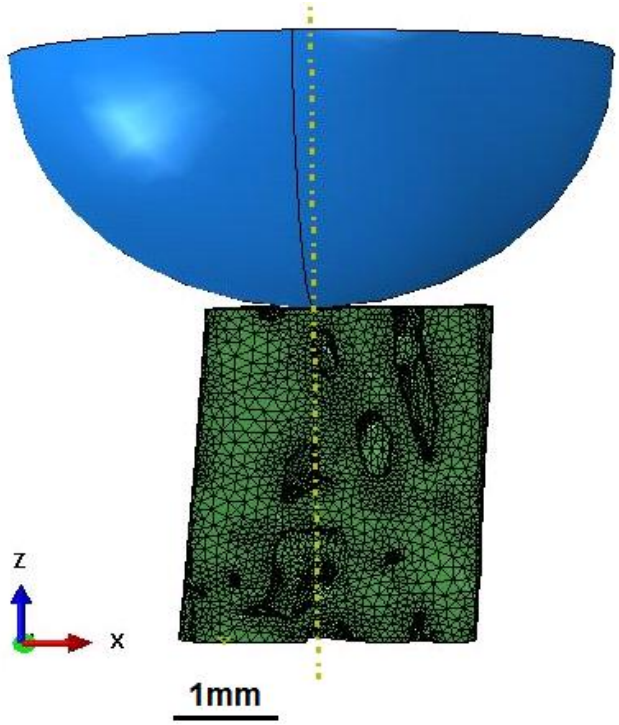


Figure 4.2.4. Indenter touching bone before the indentation occurs in the model.

According to the compressive stress-strain curve of one of cortical samples provided by Dr. Oliver Boughton from Imperial College, London, bone exhibits non-linear elastic behaviour under loading (*Figure 4.2.5*). However, there is a conflict about the mechanical behaviour of cortical bone under loading in literature for modelling [222] [223].

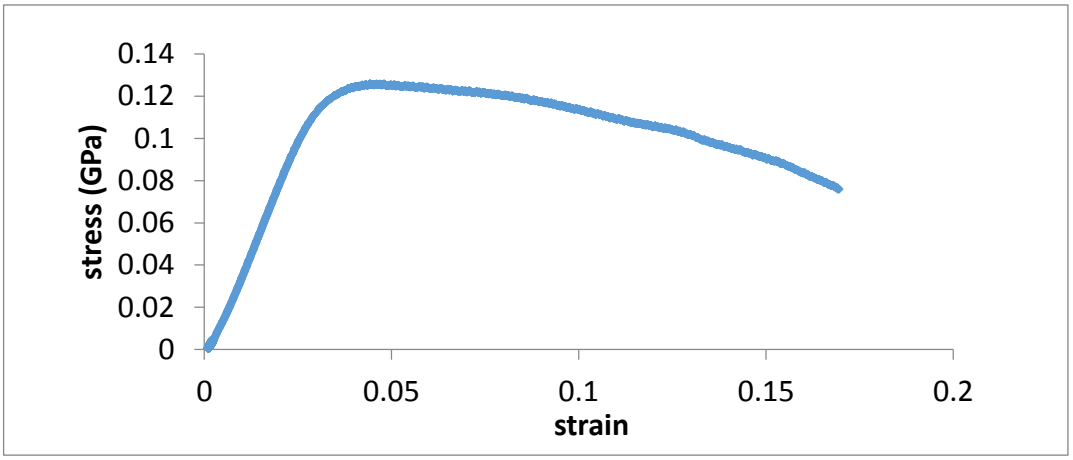


Figure 4.2.5. The experimental compressive stress-strain curve of cortical bone (data provided by Dr. Oliver Boughton from Imperial College, London)

Therefore, in material property definition, bone has been considered as either elastic or elastic-plastic. For elastic model, the selected elastic modulus of bone matrix was 26 GPa which is randomly picked within the range of calculated bone matrix moduli in *Section 5.4.2*. The Poisson's ratio was assumed to be 0.3. For the non-linear elastic model, the same definition of the elastic properties was used, and the strain and stress deviated from linearity were defined. No strain softening and hardening behaviour of bone material was assumed.

4.2.2.1 Effect of assumed deviation stress from linearity on strain distribution

Different deviation stresses from linearity have been selected and used to predict the strain distributions. The stress-strain curves used as input in the non-linear elastic model are shown in *Figure 4.2.6*. The resultant nodal strains in z direction within selected region from non-linear elastic model were compared with those obtained from DVC analysis and linear elastic model (*Figure 4.2.8*).

A vertical line parallel to z direction right beneath the indenter shown in the DVC result with a raw tomograph as background, (*Figure 4.2.7* (a) (c)) was selected for strain plotting. A vertical line in the similar position has also be selected in the FE model (*Figure 4.2.7* (b)). However, limited data points can be exported along the selected line (*Figure 4.2.7* (c)) due to the element edge length in the model, strains in a confined region around the selected line (± element edge length) were exported. The range of x coordinates of nodes was selected to be between 1.85 mm and 1.65 mm while y coordinates of nodes range from 2.02 mm to 2.23 mm. In DVC dataset, data points within a similar region of bone have also been selected but with different x and y coordinates' ranges due to different coordinate system used in Abaqus and Davis softwares. Data points with x ranging from 1.33 mm to 1.26 mm and y ranging from 1.24 mm to 1.31 mm were selected from DVC analysis, which are used for comparison.

The obtained profiles of strains in z direction with different deviation stresses from linearity from non-linear elastic model are compared together with elastic model (*Figure 4.2.8*). Z=0 represents

the bottom plane of bone while Z= 3.76 represents the XY plane where the indenter and sample are in contact. As it is seen from *Figure 4.2.8* (a), for non-linear elastic model, strain dramatically drops to zero from the point where maximum strain magnitudes have been reached. With increasing input deviation stresses from linearity from 10 MPa to 124 MPa, no significant change has been found in the magnitudes of strains located in indentation area (*Figure 4.2.8* (a)). For linear elastic model, the maximum compressive strains are observed in a similar position within indentation area to those predicted from non-linear elastic model. However, compressive strain in linear elastic model gradually reduces from maximum values with distance away from indentation region, approaching to zero but not zero.

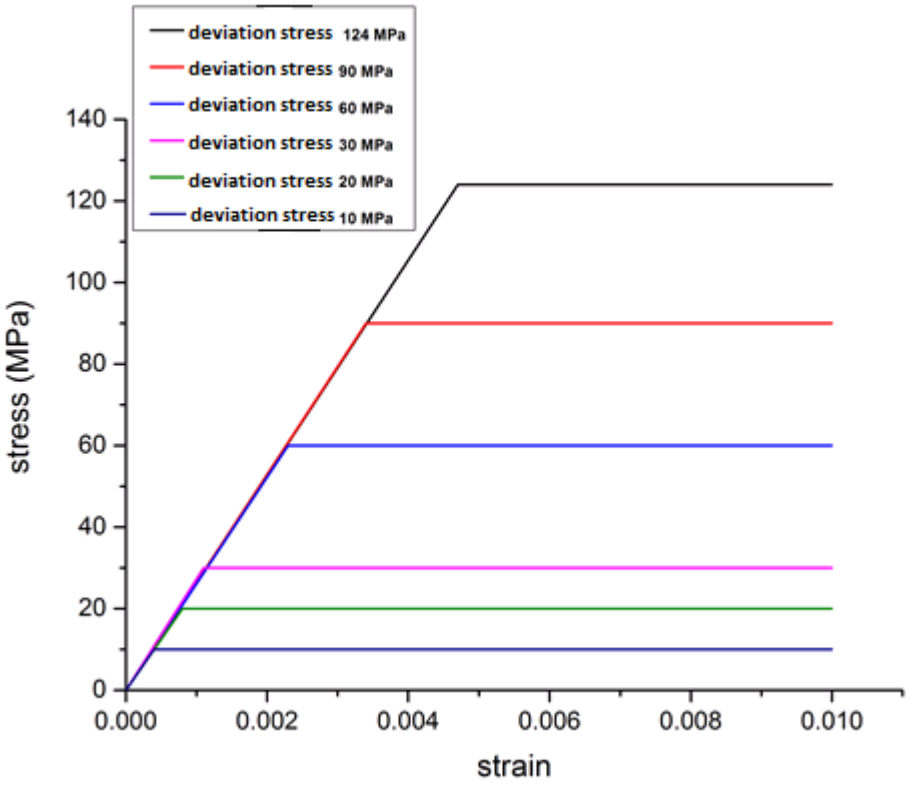


Figure 4.2.6. The input stress-strain curves for bone in modelling (zero strain hardening, with linear elastic modulus of 26 GPa).

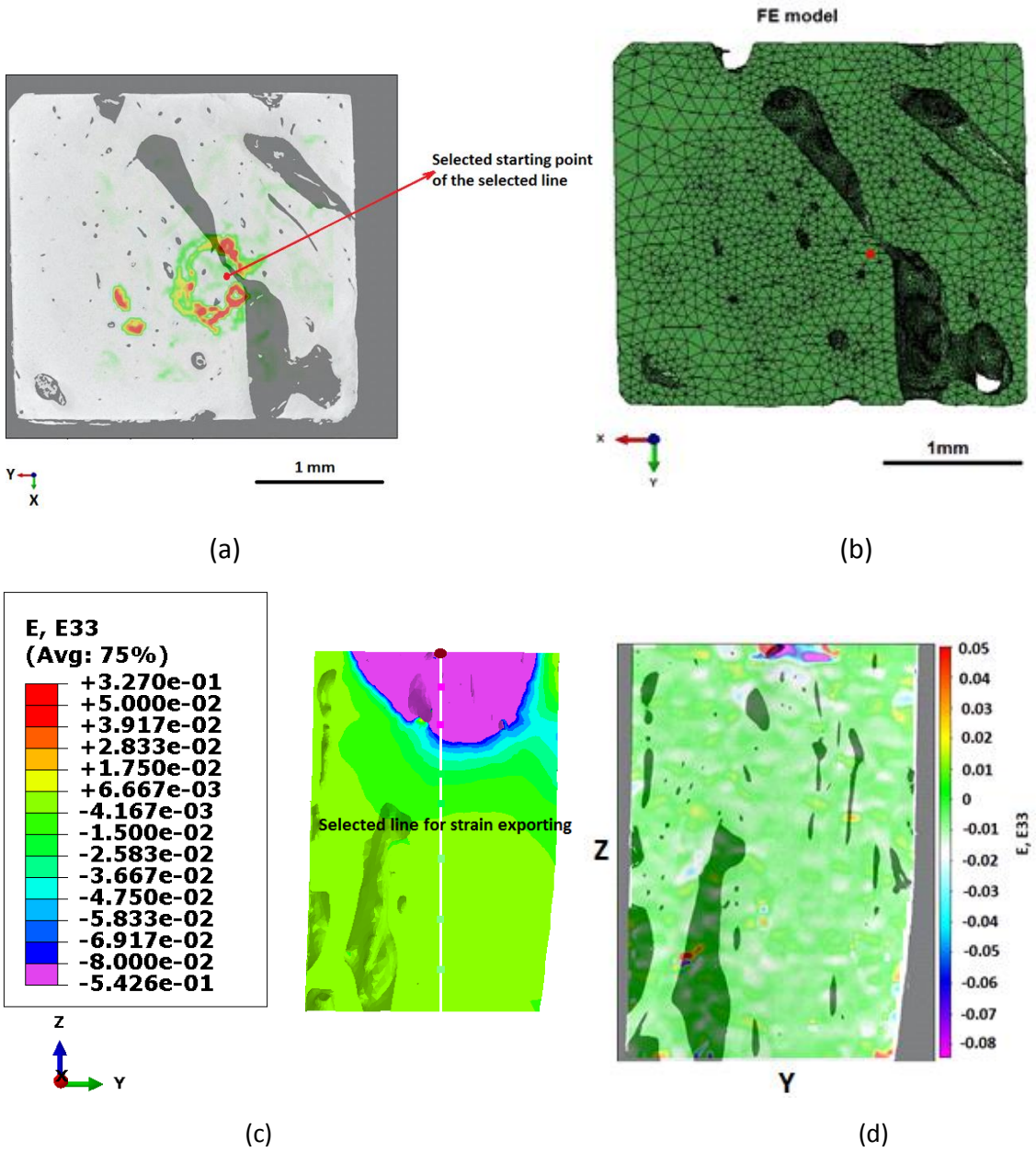


Figure 4.2.7. (a) DVC result together with tomograph under a displacement of 0.204 mm. The red spot is the starting point of the selected line around where strains were exported; (b) Similar x,y positions selected for strain line profile in FE model; (c) Simulated distribution of strain in z direction with the assumption that material's deviation stress from linearity is 90 MPa and strains in the region around white dashed line were used to compared with DVC results, (d) DVC result of strain field in z direction on the same YZ plane.

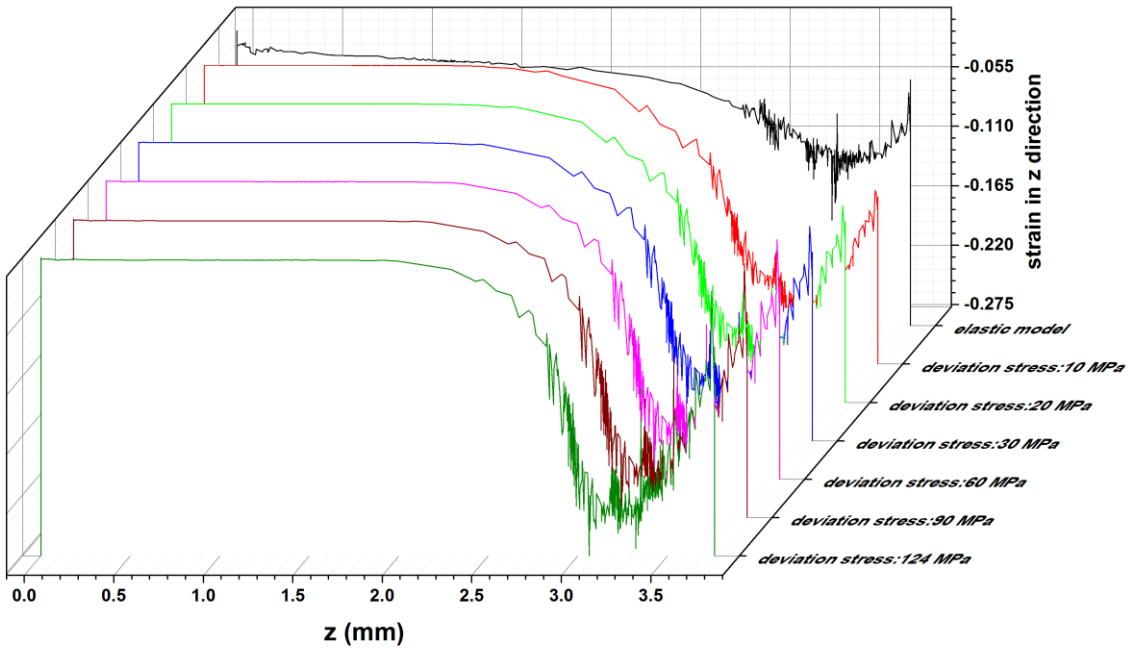
In addition, the simulated strains in models are also compared with DVC analysis (*Figure 4.2.8* (b)). The maximum strains (absolute value) observed in elastic model are close to the values obtained from DVC result. However, the magnitude of maximum strain observed in DVC analysis is much smaller than those observed in non-linear elastic models, which is also demonstrated in *Figure 4.2.7* (c) and (d) that within the same range of strain scale, the strain concentration area

in simulation is much larger than that in DVC result with higher strain values. The reason for higher predicted strain is that FE model doesn't allow crushing where the material yields and flows with constant volume while in real material, indenter has been accommodated by local crushing and bone volume decreases with crushing [224]. The trend of simulated strain along z direction away from maximum strain concentration area in non-linear elastic model is similar to that from DVC result because in both DVC result and non-linear elastic model, strain dramatically reduces to zero once away from the indentation-influenced area and it indicates the non-linear elastic behaviour of cortical bone under indentation.

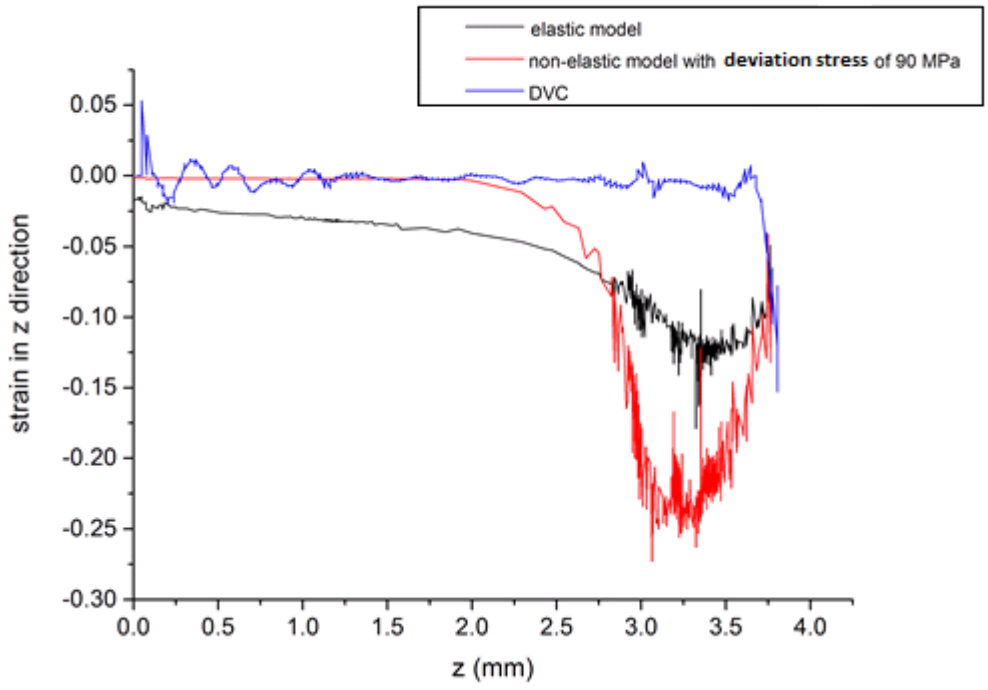
4.2.2.2 Contact area (simulation and experiment)

Because of the difference between magnitudes of simulated strain and experimental strain, one question arises what factors result in it. One of possible factors which may influence the simulated result is the contact area between bone and indenter under loading.

The sum of the nodal contact area (*Figure 4.2.9*) has been used to represent the simulated contact area for both non-linear elastic and linear elastic FE models. For the non-linear elastic model, the simulated contact areas with different assumed deviation stresses from linearity under a displacement of 0.204 mm are shown in *Figure 4.2.10*. The simulated contact area increases with increasing input deviation stress from linearity, accompanying with almost similar maximum strain. The obtained contact area ranges from 4.1 mm^2 to 6.5 mm^2 depending on the input deviation stress from linearity. For elastic model, the obtained simulated contact area is 3.74 mm^2.



(a)



(b)

Figure 4.2.8. Simulated results of line profiles of strains in z direction. (a) Comparisons of strains with different input deviation stresses from linearity together with elastic model; (b) Comparisons between strains obtained from simulations and DVC analysis.

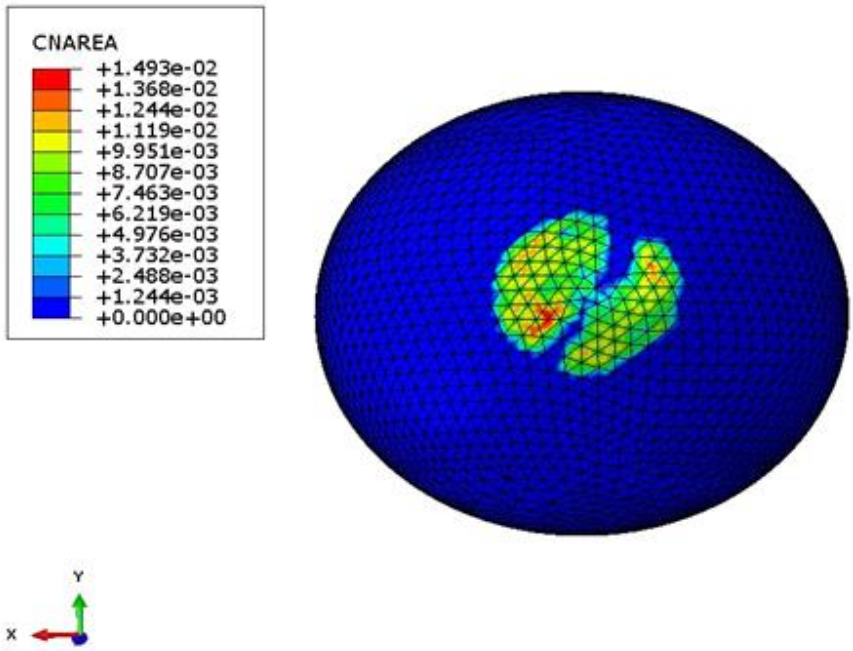


Figure 4.2.9. Contact area shown in indenter in simulation. CNAREA represents contact nodal area.

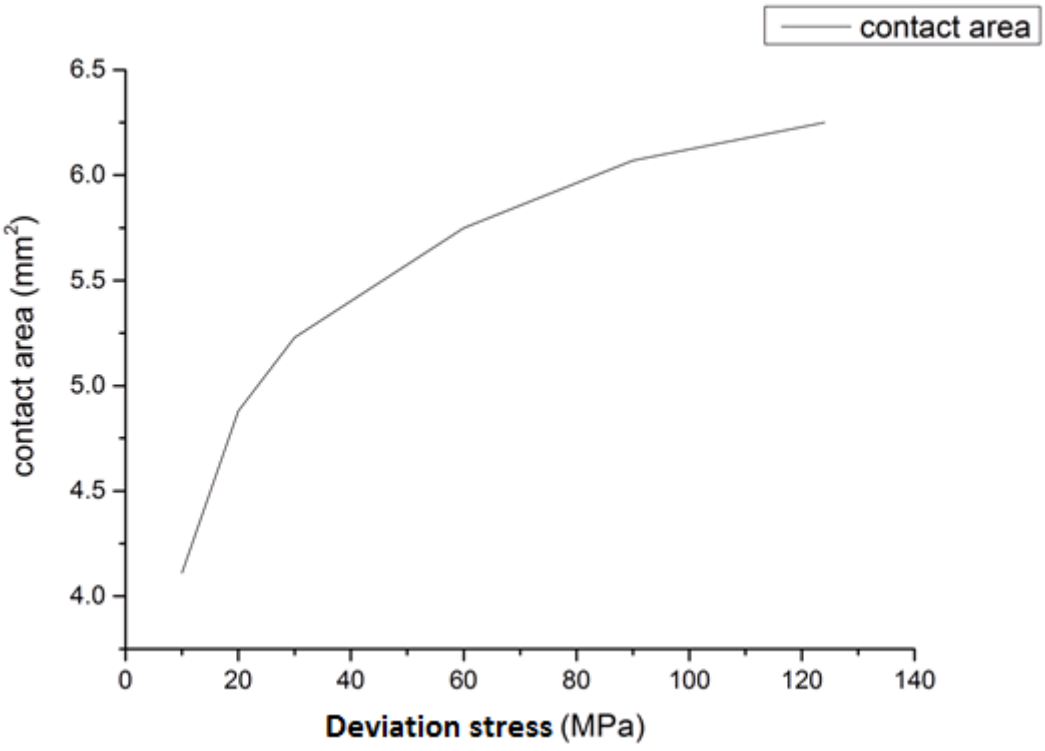
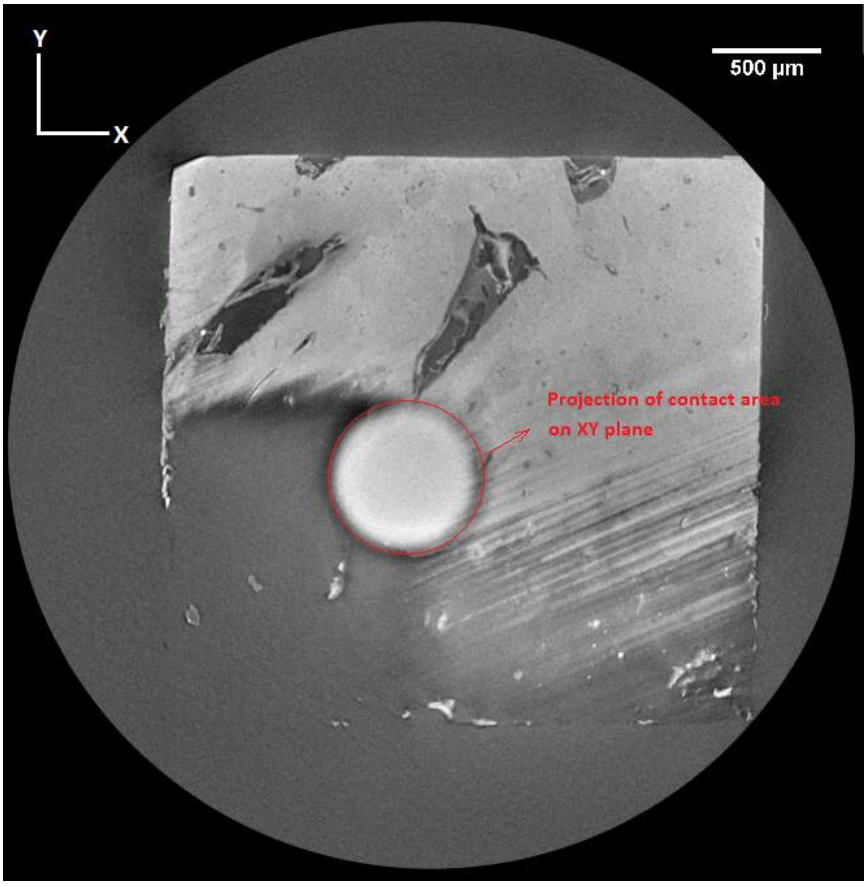


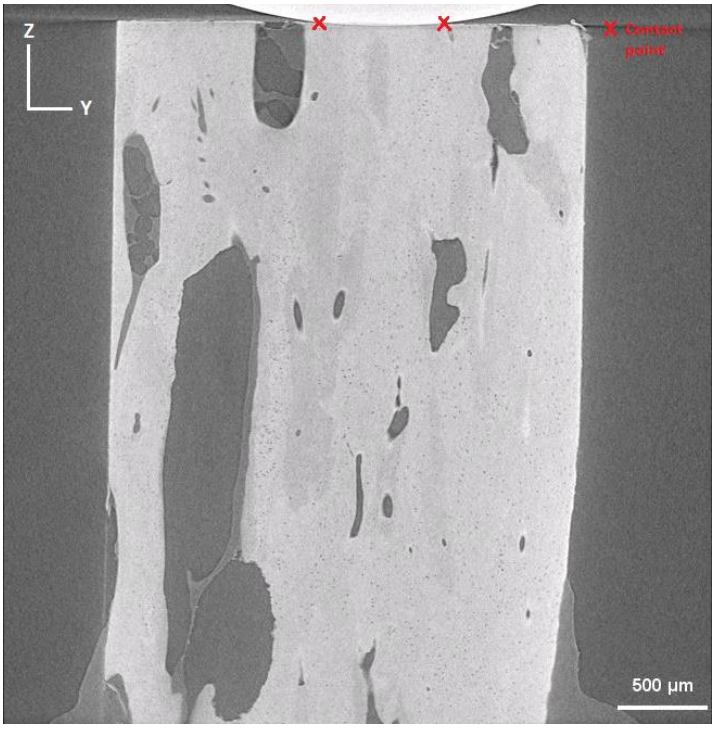
Figure 4.2.10. Obtained contact areas obtained from simulations with different deviation stresses from linearity.

For comparison, contact areas between indenter and bone generated during experiment under different loadings are also calculated. The experimental contact area was estimated from measurement in tomograph of specimen under a displacement of 0.204 mm (*Figure 4.2.11*). With the knowledge of the indenter radius (r = 3 mm) and the averaged measured approximate diameter of the projection of contact area on XY plane (L), the dome surface contact area can be calculated as $2\pi r(r - \sqrt{r^2 - \left(\frac{L}{2}\right)^2})$.

Contact areas for the specimen under different loadings for both simulations and experiment are summarized in *Table 4.2.1*. The displacements used in the simulations are the same as applied displacements in the experiment on the bone. The chosen deviation stress from linearity for non-linear elastic model is 90 MPa in this case. Contact area increases with increasing loading for both simulations and experiments in a similar pattern (*Figure 4.2.12*). However, the obtained contact areas from simulations are much larger than experimental values. Non-linear elastic model gives larger predicted contact area than linear elastic model under a specific displacement.



(a)



(b)

Figure 4.2.11. Tomograph showing contact area between bone and indenter under a displacement of 0.204mm (load 1). (b) Tomograph on YZ plane. The distance between two contact points marked in red crosses in this selected tomograph is approximate to L.

In order to study the factor which results in the larger contact areas in FE model compared with experiment measurements, reaction force of the indenter has been calculated in non-linear elastic model with the setting of 0.204 mm movement of the indenter onto the bone. The obtained force of the indenter in z direction is 351 N in non-linear elastic model which is much higher than the recorded peak load (57N) in the experiment with the indenter moving with the same distance onto the bone and it explains the larger simulated contact. In addition, it further explains the smaller strain concentration area observed from DVC result compared with simulated one (*Figure 4.2.7* (b) and (c)) and lower strain (*Figure 4.2.8* (b)) compared with the simulated one.

Table 4.2.1. Contact area measured from simulations and experiment.

Applied displacement (mm)	Non-linear elastic model	Linear elastic model	Experiment result	
	Contact area (mm^2)	Contact area (mm^2)	L (mm)	Contact area (mm^2)
0.204	6.07	3.14	0.65 $\pm$ 0.01	0.33 $\pm$ 0.01
0.210	6.22	3.83	0.81 $\pm$ 0.01	0.52 $\pm$ 0.01
0.317	7.59	5.59	0.96 $\pm$ 0.04	0.73 $\pm$ 0.06

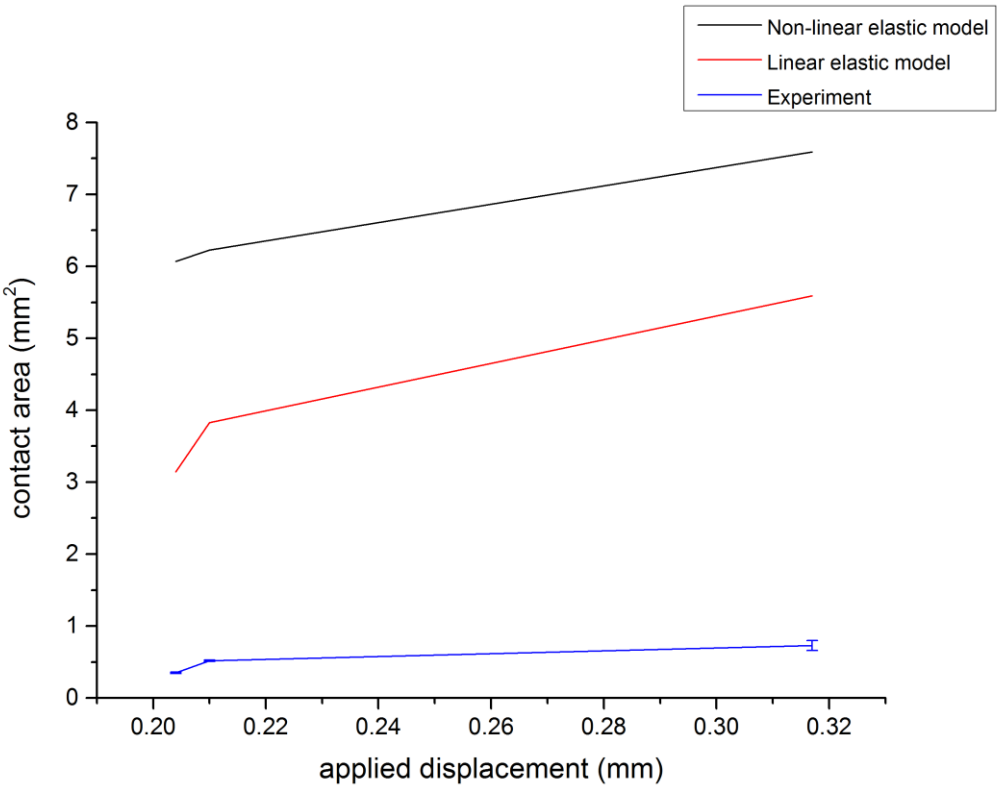


Figure 4.2.12. Contact area versus displacement for both simulations and experiment.

4.3 Discussion of image-based models

4.3.1 Mollusc shell

4.3.1.1 FE model with simple boundary conditions

Generally, the compression contact model of limpet under compression with simple boundary conditions (experimental loads) gives a good prediction of elastic modulus as well as strain distribution under a certain loading. Although the obtained limpet elastic modulus (approximately 20 GPa) predicted by FE model in the thesis is lower than the values reported in literature review [186], it is still within the same magnitude. Several reasons may contribute to lower values compared with literature : 1) difference in species (Anodonta, Ensis and Nautilus used in literature while Patella vulgate used in this project); 2) the difference in specimen preparation: in literature, samples have been prepared into standard tensile sample geometry while in the project, the whole limpet has been compressed and the obtained elastic modulus

has a close relation to the real geometry of limpet; 3) difference in testing methods: tensile in literature review and compression in project; 4) the calculated elastic modulus of limpet in literature review was affected by location where the specimen has been cut while in the project, such influence is avoided.

For this model, only the bulk geometry of the limpet specimen rather than more detailed microstructures given by SEM (Appendix: *Section 10.1*) was used. Considering the reasonable elastic modulus prediction, the millimeter scale geometry can be a very important factor which affects bulk elastic properties of limpet, which is consistent with literature [7]. Although Cabral and Jorge [6] argue that the influence of limpet morphology and morphometry on crushing resistance is not important based on their simulations of different mollusc species. However, no real geometries of mollusc shells and only sketched shapes of shells with measured sample sizes from experiment and the assumption of same thickness throughout the volume were employed in their models which may also influence the simulations. Some other models [3] [225] [226] have been developed to study the mechanical properties of mollusc shells in literature based on their lamellae structure, limitations existing for these models: 1) due to variations on microstructures among species and individuals [12], assumptions are always made on the structures used for modelling and the published models can not reflect the real microstructures of mollusc shells; 2) no bulk mechanical properties can be predicted due to the scale of the models which are much smaller than the real specimen.

4.3.1.2 FE model with DVC boundary conditions

Compared with DVC results, FE calculation of strains using the corrected displacement field presents a smoother and cleaner strain field than the DVC software. The regions of high strain are consistent with the areas where fracture occur and it indicates that the results are not influenced by the pre-processing step on displacement field from DVC. In current stage, element size similar to the subset of DVC data points is chosen in order to reduce computation time.

However, in the future, the element size of the model can be tuned to see whether it will influence the interpolation of DVC displacement field into FE nodes.

4.3.1.3 Comparisons between strains from models and DVC analysis

The strain distribution calculated using the FE model with DVC as boundary conditions is closer to the experiment result. Differences between strains obtained from the FE model with simple boundary conditions and DVC analysis are the result of four possible reasons: (1) The compressing sheets are sketched to be parallel with each other and the limpet bottom in the model with simple boundary conditions and it allows the load to be uniformly transferred from platen to shell, thus resulting in more uniformly distributed strain in the limpet. However, in the experiment which provides raw data for DVC analysis, the bottom of shell may not be flat and parallel to the compressing platens, which results in non-uniform distribution of load transfer within contact area. In addition, out-plane movement of limpet has occurred during compression. These situations are not considered in the model. (2) In the model, the contact between platen and limpet has been defined as hard and frictionless which is not the case in the real experiment. Due to the softness of the plastic platens, the rigid limpet specimen can crush into platen first before deformed by the load, which results in larger contact area generated compared with model, thus leading to different strain values. (3) The contact compression model is a linear elastic model while in real case, non-linear elastic behaviour is expected due to micro-cracking observed (*Figure 3.1.26* (b)) which results in larger deformation (thus larger strain) when the applied stress is beyond yield stress. (4) Higher Max. Principle strains obtained from DVC analysis can be a result of noises in DVC result itself (*Figure 4.1.9* (c)). (5) Different element sizes.

4.3.2 Bone

Compared with limpet, FE model based on bone tomographs is able to take more consideration into real microstructure of pore network rather than bulk geometry of sample. However, in

current stage, due to the uncertainty of bone mechanical behaviours, assumptions have been made in elastic modulus, the shape of stress-strain curve of bone materials etc in order to discuss the influence of one variable on the overall mechanical properties of bone.

The simulated strain distribution has been compared with experimental results and the trend of strain in z direction indicates that bone material behaves like a non-linear elastic material which is consistent with experimental result provided by Dr. Oliver Boughton, Imperial College, London (*Figure 4.2.5*).

The definition of contact in simulation, which is frictionless and hard, can explain the observations that the strain concentration areas from non-linear elastic model and experiment are slightly different. The higher maximum strain observed in simulation and the larger contact area observed from model compared with experimental measurements are due to neglecting crushing at contact in simulation and it has been testified by the obtained reaction force of indenter in the simulation, which is much higher than measured load in the experiment with indenter moving onto bone with same displacement. In addition, cortical bone exhibits certain degree of toughness even in dry condition and hard contact defined in simulation ignores this fact, which contributes to higher degree of strain concentration.

Overall, the prosed FE model of cortical bone doesn't act as a predictive model because the input stress-strain behavior of bone material has certain difference with the real physics of the material. However, it is a good starting point to provide a certain level of understanding of mechanical behaviors of cortical bone under indentation.

The calculation of elastic properties is not possible from FE model because there is no significant strain measured in the volume of materials that is away from the indentation and in addition, the load relaxation during the scan would also increase modelling error. Therefore it leads to the study in the following chapters using different modelling approaches to obtain elastic modulus and fracture toughness of bones.

Chapter 5

5 Structural and elastic properties of cortical bones

In this chapter, structural information including the porosities and elastic moduli of cortical bones are two main topics. Porosities of cortical bone specimens before and after pre-processing on data have been measured and compared. Effects of porosity on the experimental apparent elastic modulus and then the intrinsic elastic modulus of cortical bone have been investigated, where the intrinsic moduli are obtained using an approach combining modelling and experiment. Factors which influence the modelling results are discussed. In addition, the influences of patients' conditions (e.g. age and gender) on obtained structural and elastic properties of cortical bones have been studied.

5.1 Background

Eighteen cortical bones from patients with different ages and genders who underwent hip replacement surgeries due to osteoarthritis have been investigated. With the knowledge that osteon is a cylinder shown in *Figure 5.1.1* (b), which is roughly parallel to the long axis of bone [47], the z direction of the bone samples in this chapter, which were cut along the long axis of bone, is considered as parallel to the orientation of osteon and described as the longitudinal direction while x and y directions which are perpendicular to the longitudinal direction and mentioned as transverse/radial directions [56] (here equivalent).

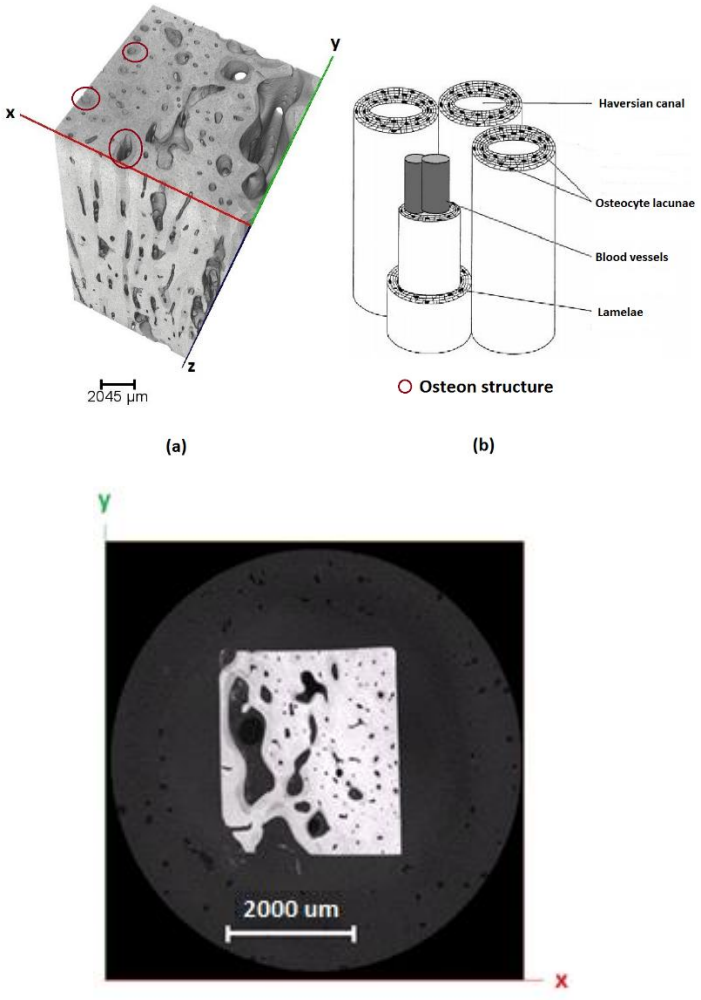


Figure 5.1.1. (a) The 3D visualization of a cortical bone sample with a porosity of 14.3% and the orientation of x,y and z axes in correlation with osteons. Several osteons have been selected which are shown in red circles. (b) The detailed structural information of osteon in literature [56]*,(c) x and y directions relative to tomograph (resolution: 6.9 um)..*

5.2 Porosity of cortical bone

The data prepared for PReMIse was first employed to calculate porosities of the eighteen specimens. To do this, as described in *Chapter 3*, the original volume of the cortical bone tomograph has been divided into two cubes. The obtained porosities for each part and the averaged porosity for each individual specimen are listed in *Table 5.2.1*. Because each part has the same volume, the overall porosity of each bone specimen was obtained by averaging the porosities of all parts, using the arithmetic mean:

$$P_{overall} = \frac{P_{part1}+P_{part2}+\cdots P_{partn}}{n} \qquad \textit{Equation 5.2.1}$$

Where *P* stands for porosity, *n* represents how many parts the whole bone has been divided into (here 2).

From *Figure 5.2.1*, it is clearly shown that sectional porosities calculated from different parts of each individual bone follow a linear relation with the average porosity. Therefore, the averaging method employed is suitable for the calculation of overall porosity.

Table 5.2.1. Porosity of each part of cortical bones and the averaged porosity for each individual bone sample.

Sample name	Porosity/% Part 1	Porosity/% Part 2	Averaged Porosity/%
THR111	2.19	1.81	2.00
THR110	1.36	3.43	2.40
THR106b	3.48	3.26	3.37
THR63	3.56	4.72	4.14
THR103a	3.58	6.35	4.97
THR108a	6.35	7.49	6.92
THR79	6.80	8.48	7.64
THR107	8.36	6.96	7.66
THR69	7.66	10.55	9.11
THR91c	7.93	10.61	9.27
THR82	9.30	13.63	11.47
THR75	6.31	16.65	11.48
THR76	8.20	15.14	11.67
THR104	12.22	11.25	11.74
THR74a	13.15	14.64	13.9
THR04b	11.58	16.63	14.11
THR72	16.93	14.56	15.75
THR83	22.11	21.09	21.60

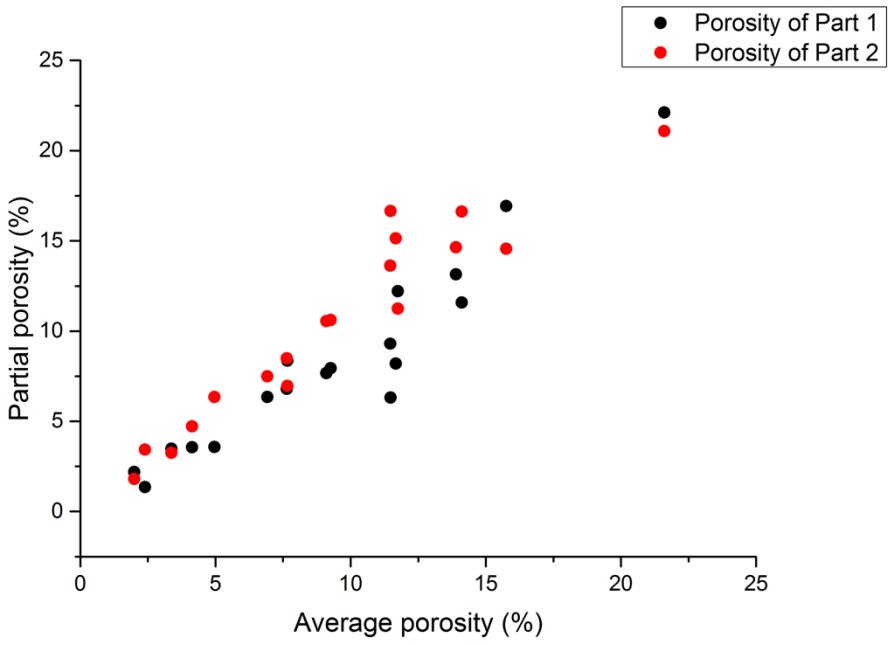


Figure 5.2.1. Sectional porosity versus averaged porosity.

The influence of pre-image processing employed for the use of PReMISe for porosity calculation such as binning on pore network is investigated. The influence of binning in porosity is shown using data before and after binning which is shown in *Table 5.2.2* and plotted in *Figure 5.2.2*. Porosities before binning were calculated using Avizo (i.e. with data at 6.9 µm/voxel, compared with 25.4 µm/voxel in the binned data). The slope of linear fitting of the curve present in *Figure 5.2.2* is 0.97 and R-square is 1 which indicates there is no significant change in the porosity for data before and after binning.

Changes in the distribution and geometry of pores before and after binning are studied as well. A typical cortical bone from the eighteen specimens has been taken as an example, in which there is a slight reduction in total porosity from 21.63% to 21.60% after binning. The distribution of pore volumes between data before and after binning is shown in *Figure 5.2.3*. Because the pores present inside the bone are interconnected, and so are very difficult to separate for the pore distribution calculation, manual adjustments are required in Avizo to ensure individual large pores present in horizontal planes and vertical planes are separated from small pores and are not split into small or medium-size pores. The volumes of pores within the bone have been found to have a very wide spread and therefore log10 (volume) has been used as x axis in order to make the histogram clear (*Figure 5.2.3*). As it is shown in *Figure 5.2.3*, compared with the almost constant volume fraction of large pores (1E+09-1E+12 um^3) against total volume of pores from 0.996 to 0.976 after binning, the change in small pores is minor which is believed to have negligible effect on later elastic moduli prediction [56]. In addition, there is no significant difference in the general geometry and orientation of pore network before and after binning as it is shown in *Figure 5.2.4* (a) and (c).

Table 5.2.2. Porosity measured before and after binning.

Sample name	Porosity before binning (%)	Porosity after binning (%)
THR111	3.09	2.00
THR110	2.40	2.40
THR106b	4.48	3.37
THR63	4.33	4.14
THR103a	4.41	4.97
THR108a	6.84	6.92
THR79	7.09	7.64
THR107	8.20	7.66
THR69	8.31	9.11
THR91c	8.80	9.27
THR82	14.46	11.47
THR75	13.89	11.48
THR76	10.70	11.67
THR104	13.00	11.74
THR74a	13.24	13.90
THR04b	14.29	14.11
THR72	14.66	15.75
THR83	21.63	21.60

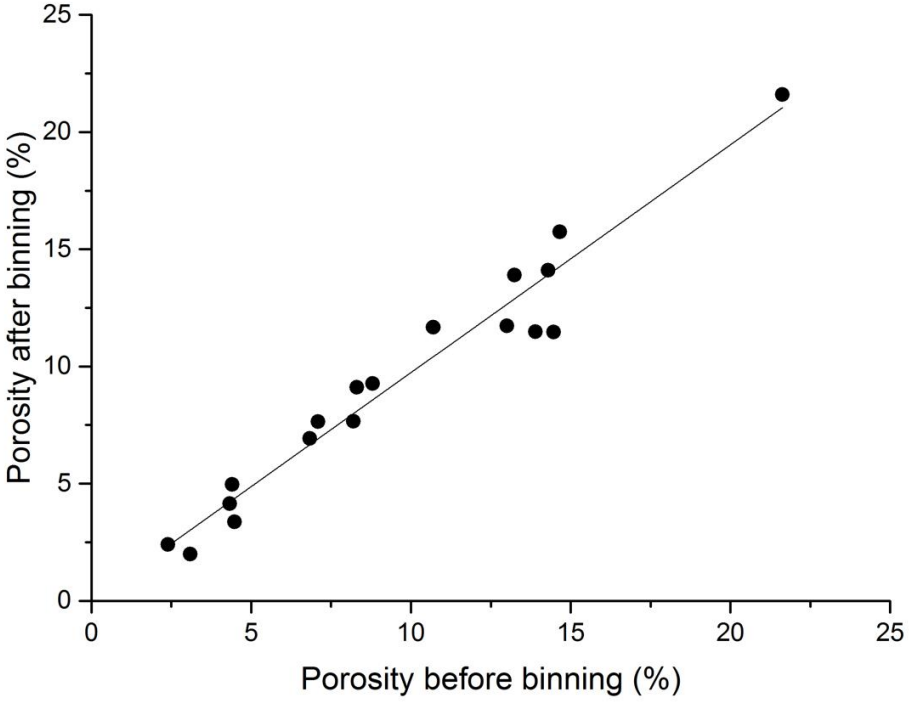
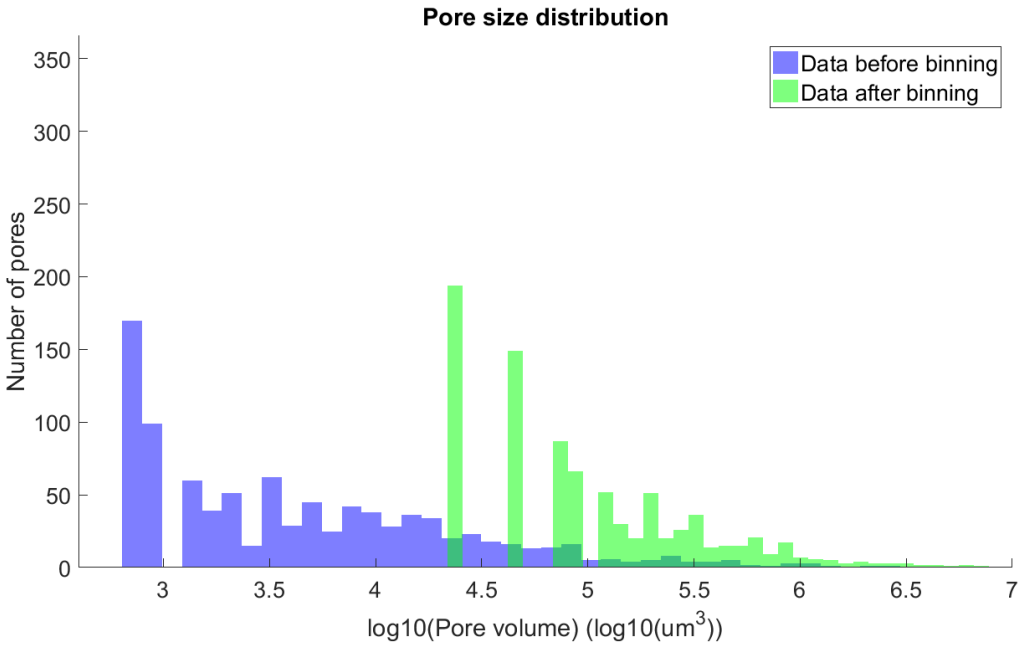
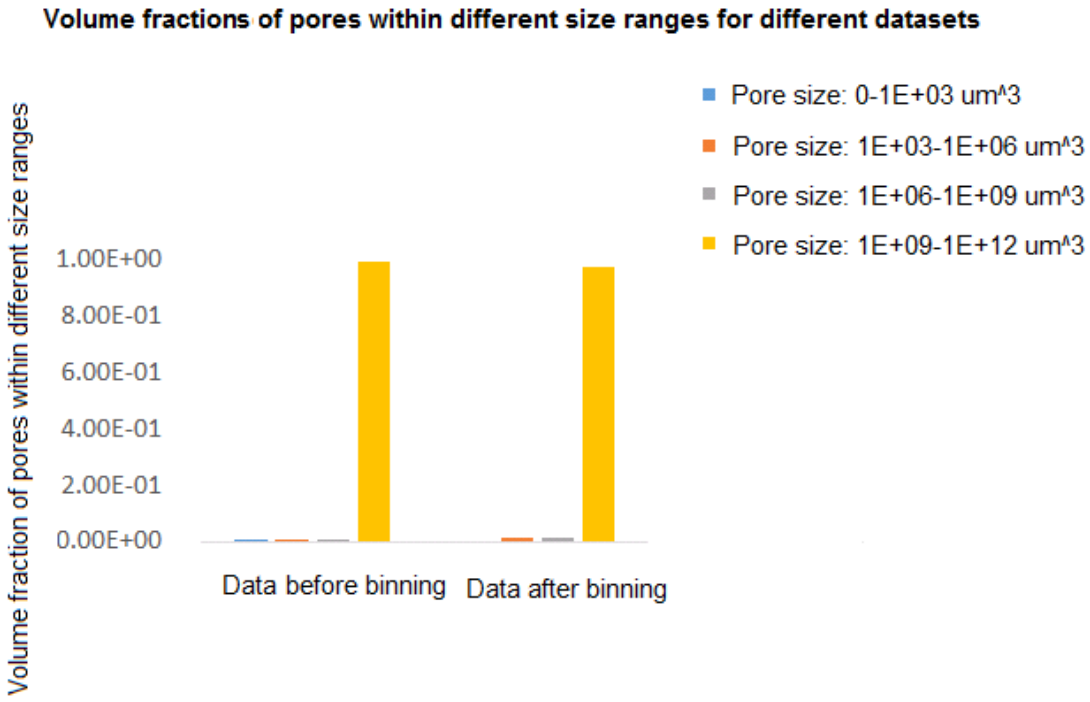


Figure 5.2.2. Porosity before and after binning.

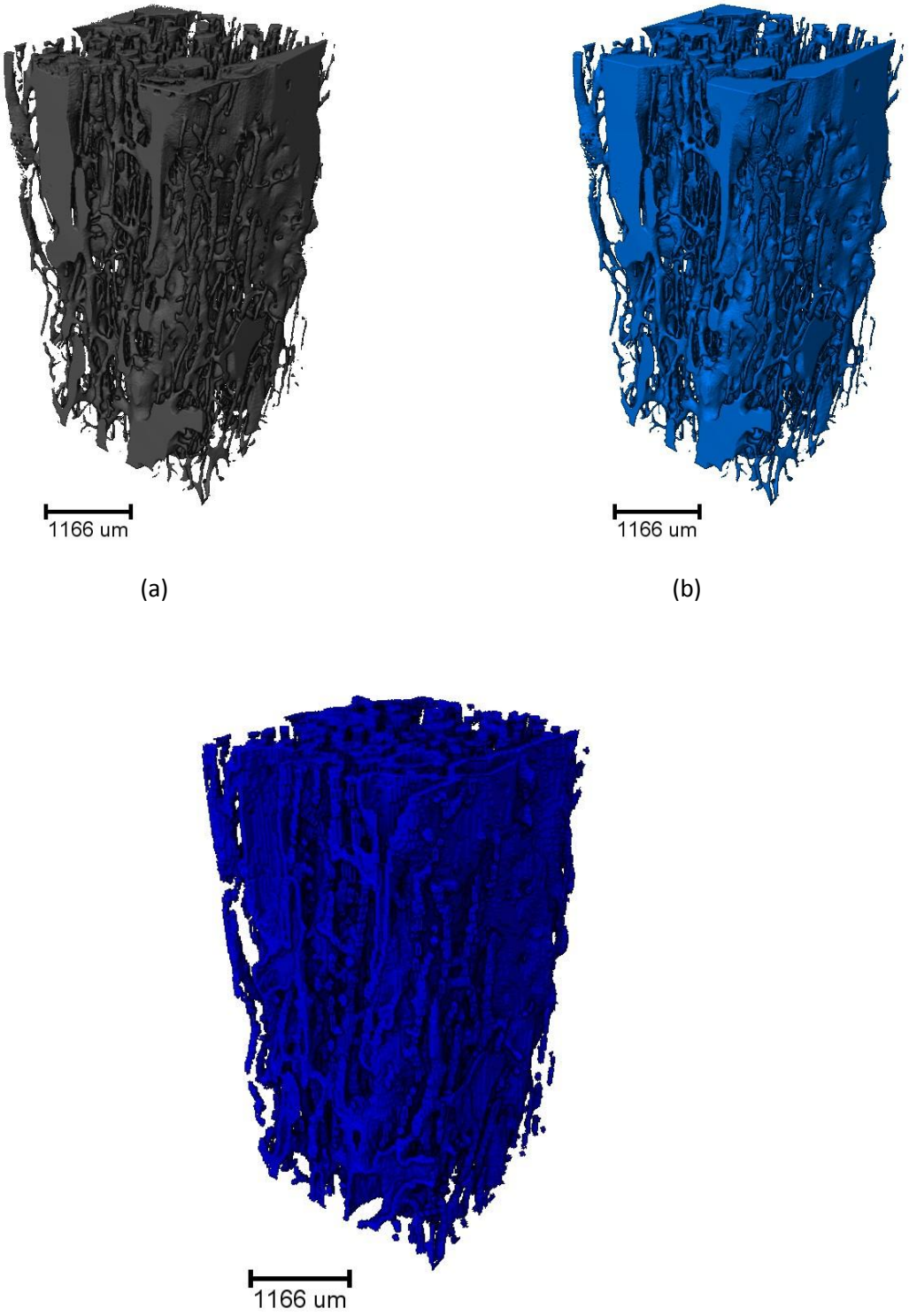


(a)



(b)

Figure 5.2.3. Pore distribution within bone volume: (a) pore size distribution; (b) Volume fractions of pores within different size ranges.



(a) (b)

(c)

Figure 5.2.4. Comparisons between pore networks from original cropped data and data after image pre-processing. Pore network of (a) original data; (b) data after thresholding and (c) data after thresholding and binning.

5.2.1 The influence of patients' conditions on bone porosity

With the knowledge of conditions of patients (*Table 5.2.3*), the relations between bone porosities and patients' ages and gender have been investigated. The relation of bone porosities with patients' gender and age has been plotted against porosity in *Figure 5.2.5*. As it is seen from *Figure 5.2.5*, the majority of bone samples from male group distribute in the age range from 45-65 years old while the majority from female group distribute in the age range from 65-82 years old. The comparison between both gender groups becomes very difficult due to the limited sample number for both groups which are within the same age range. In general, it seems there is no significant difference in porosity in relation of gender. However, in the overlapping age range for both groups from 60-65 years old, it appears that male patients have cortical bones with much lower porosity compared with female patients, which is consistent with literatures [78] [76] that women tends to lose more mineral content and thus increase porosity in cortical bone compared with men in elderly age.

No direct relation of porosity to age can be observed as well from *Figure 5.2.5*, although in literature [78] [76] the porosity of cortical bone was reported to decrease with increasing age. It can be the result of osteoarthritis that these patients suffer from because osteoarthritis can lead to decrease in porosity depending on the degree of the disease which is not necessarily related to age [49] [50].

Table 5.2.3. The conditions of patients who donated cortical bones for the study.

Bone specimen serial number	Sex	Age at time of surgery
THR111	Female	81
THR110	Male	60
THR106b	Male	62
THR63	Male	63
THR103a	Male	62
THR108a	Female	68
THR79	Female	67
THR107	Female	69
THR69	Female	75
THR91c	Male	50
THR82	Female	74
THR75	Female	79
THR76	Female	75
THR104	Female	59
THR74a	Female	62
THR04b	Male	79
THR72	Male	48
THR83	Female	68

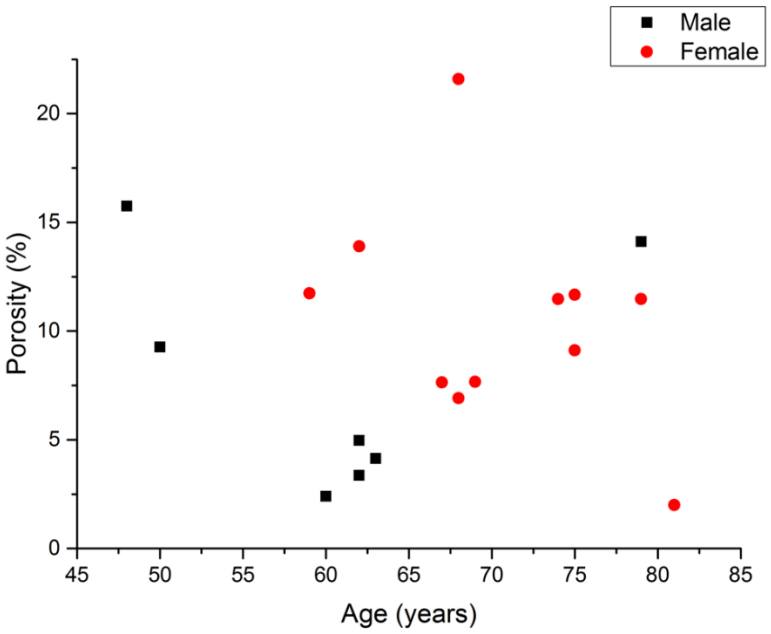


Figure 5.2.5. The relation between bone porosities and patients' ages and gender. Comparisons of porosities in two gender groups in the age span from 45-82 years old.

5.3 Elastic moduli of cortical bones

The elastic moduli of the same batch of cortical bones were measured by both Resonant Ultrasound Spectroscopy (RUS) tests and compression tests in the wet condition, after X-ray tomography scanning, by Prof Quentin Grimal's group in Paris and Dr. Oliver Boughton from Imperial College, London, respectively. The experimental results are summarised in *Table 5.3.1*. The author takes no credit for these experimental results.

The measured elastic moduli from both methods are plotted against calculated porosity in *Figure 5.3.1*. This shows the measured elastic modulus generally decreases with increasing porosity regardless of the measurement methods, as reported by various studies [65,227–229]. For RUS tests, elastic modulus measured in longitudinal direction of cortical bones are much larger than transverse and radial directions, which show that cortical bone has anisotropic properties.

In addition, the compression tests in the longitudinal direction of cortical bone give a much lower elastic modulus compared with RUS results (*Figure 5.3.1*), although literature data for compressive elastic modulus [43] [51] [69] in longitudinal direction are closer to RUS tests. However, it is difficult to compare measured compressive elastic moduli among different bone specimens used in literature and this project. The only issue which can be discussed in this case is why lower values of elastic moduli have been observed for compression tests compared to RUS tests for the same batch of samples used in the project. Several possible reasons can explain that: 1) technical problems such as friction and the load transfer issue occurred during compression tests between compression plate and the bone specimen which result in the underestimation of Young's modulus [85] [86] [84], 2) difference in the ways for elastic modulus determination between dynamic measurement and static measurement. The modulus obtained from dynamic tests such as RUS is the initial tangent modulus while from static way the modulus

measured is the chord modulus which is the tangent value between two specific points on the stress-strain curve [132] [133].

The results from the RUS tests are used in an analysis to obtain the intrinsic elastic moduli of cortical bone in this study due to several factors: 1) it provides information of elastic moduli in different directions for the investigation of bone anisotropy while the compression tests as a destructive method, only give information of elastic modulus in one specific direction, 2) the measured values from RUS tests are closer to what have been reported in literatures [51] [68] [69], 3) the compression test is considered to be a less accurate method for the measurement of elastic modulus due to larger standard deviation compared with dynamic measurement technique [132].

Table 5.3.1. The results of apparent elastic moduli measured in different axis directions using Resonant Ultrasound Spectroscopy (RUS) by Prof Quentin Grimal's group together with elastic moduli in longitudinal direction measured by compression test by Dr. Oliver Boughton [70].

Sample name	E1 from RUS test (GPa) transverse direction	E2 from RUS test (GPa) Radial direction	E3 from RUS test (GPa) Longitudinal direction	E3 from compression test (GPa) Longitudinal direction	Percentage of difference between E3 measured from RUS and compression ($E3_{RUS}$-$E3_{Compression}$)/ $E3_{RUS}$
THR111	9.91	11.05	20.38	13.9	31.8%
THR110	9.58	8.67	19.01	10.7	43.7%
THR106b	10.92	12.32	18.60	9.3	50.0%
THR63	9.31	8.10	22.19	13.8	37.8%
THR103a	12.53	12.56	18.64	9.5	49.0%
THR108a	11.27	12.27	19.55	8.7	55.5%
THR79	11.94	12.12	18.46	11.2	39.3%
THR107	11.40	10.76	17.48	9.2	47.4%
THR69	12.11	11.61	19.00	13.9	26.8%
THR91c	9.30	9.23	18.64	9.5	49.0%
THR82	6.53	6.76	12.56	6.1	51.4%
THR75	6.42	5.42	18.59	11.3	39.2%
THR76	8.07	9.33	13.23	11.1	16.1%
THR104	6.70	5.63	17.65	8.4	52.4%
THR74a	10.14	10.45	16.19	9.9	38.9%
THR04b	9.31	8.22	15.40	11.0	28.6%
THR72	7.36	5.98	17.50	8.0	54.3%
THR83	4.75	8.13	10.44	7.4	29.1%

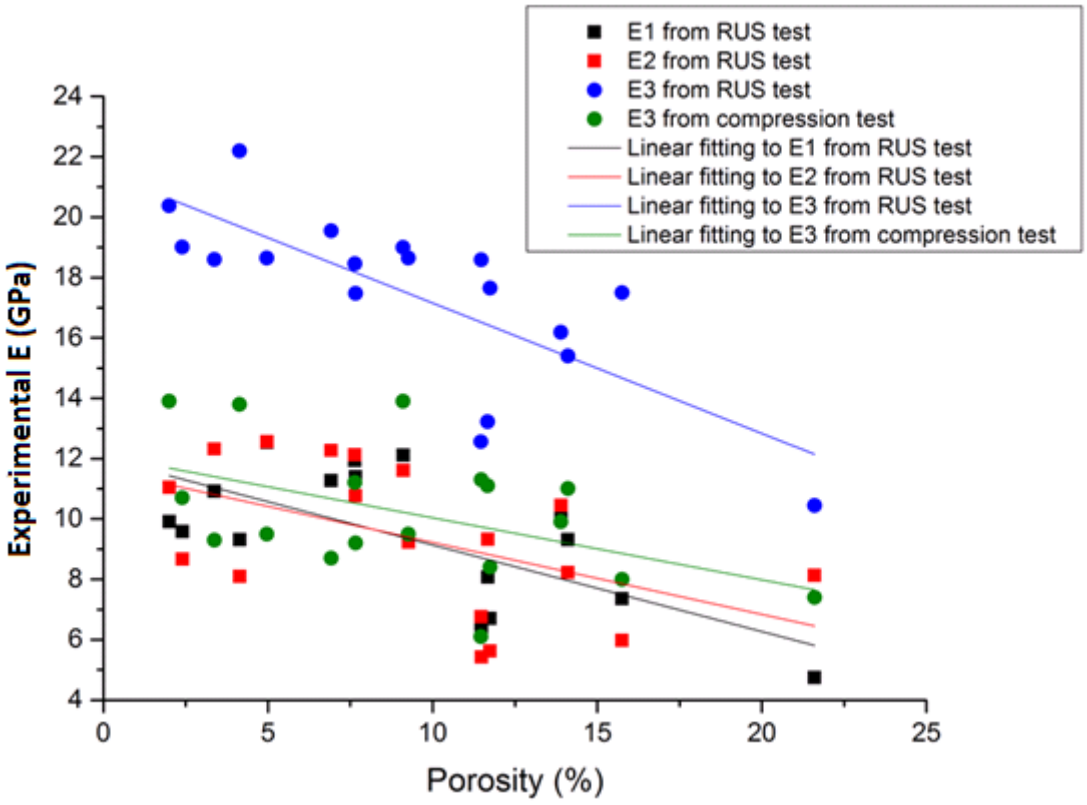


Figure 5.3.1. Experimental elastic moduli against porosity.

5.4 Extraction of bone properties using PReMISe

PReMISe software provides a non-destructive way to extract the apparent elastic modulus of bones with different pore networks in different loading directions. Two factors influence the simulated apparent elastic modulus (E) of cortical bone in PReMISe model. They are a combination factor E/E_0, which is influenced by the size, geometry, orientation and content of pores inside the bone volume, and the intrinsic elastic modulus of bone matrix with zero observed porosity (E_0) [210].

5.4.1 The combination factor E/E_0

E/E_0 obtained from PReMISe represents the influence of the visible pore network on the overall apparent elastic modulus. All the obtained results of E/E_0 and porosity for each part of individual bone sample in different loading directions (axes in *Figure 5.1.1* (a)) from PReMISe are

summarized in *Table 10.2.1* in Appendix. The data are summarised as a function of porosity in *Figure 5.4.1*. This shows similar behaviour in both x and y loading directions, and consistent behaviour between the individual sections of the volumes.

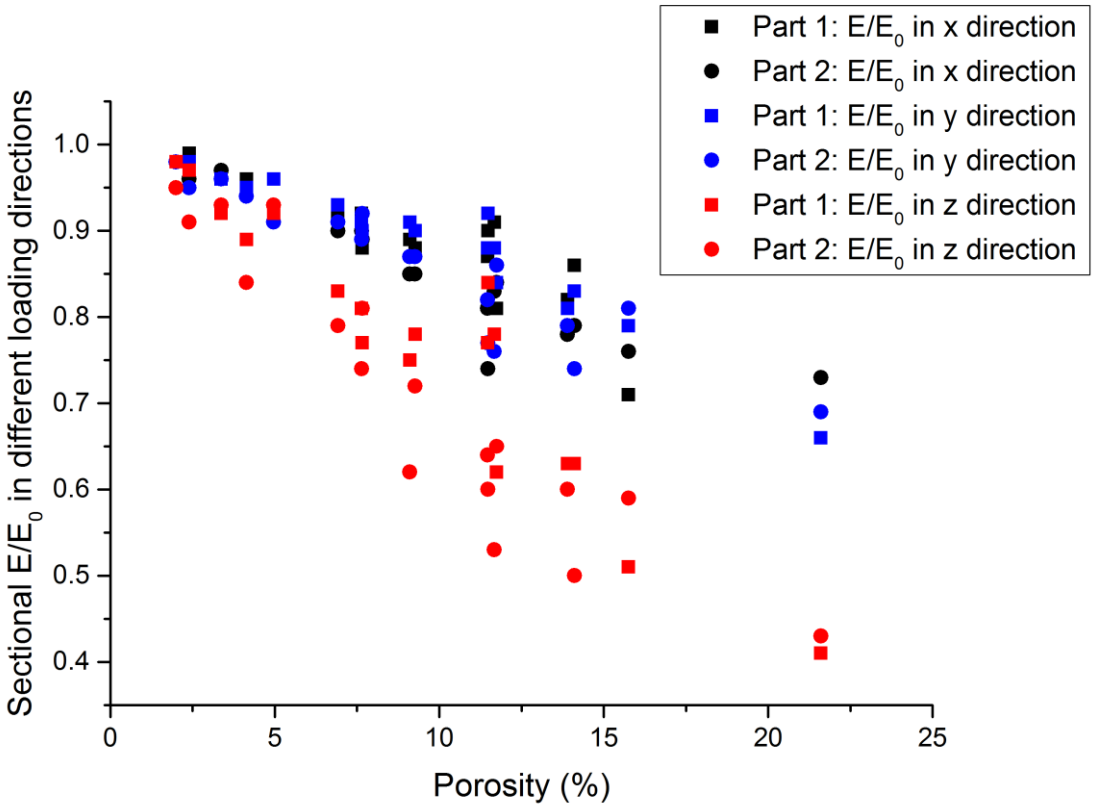


Figure 5.4.1. Sectional E/E_0 in different loading directions vs porosity.

In order to obtain the average E/E_0 of individual bone specimen based on E/E_0 values from their individual sections, a rule of mixtures [230] [231] has been employed to account for the differences in microstructure and elastic properties. According to the loading direction and the arrangement of the sections (*Figure 5.4.2*), different equations are applied.

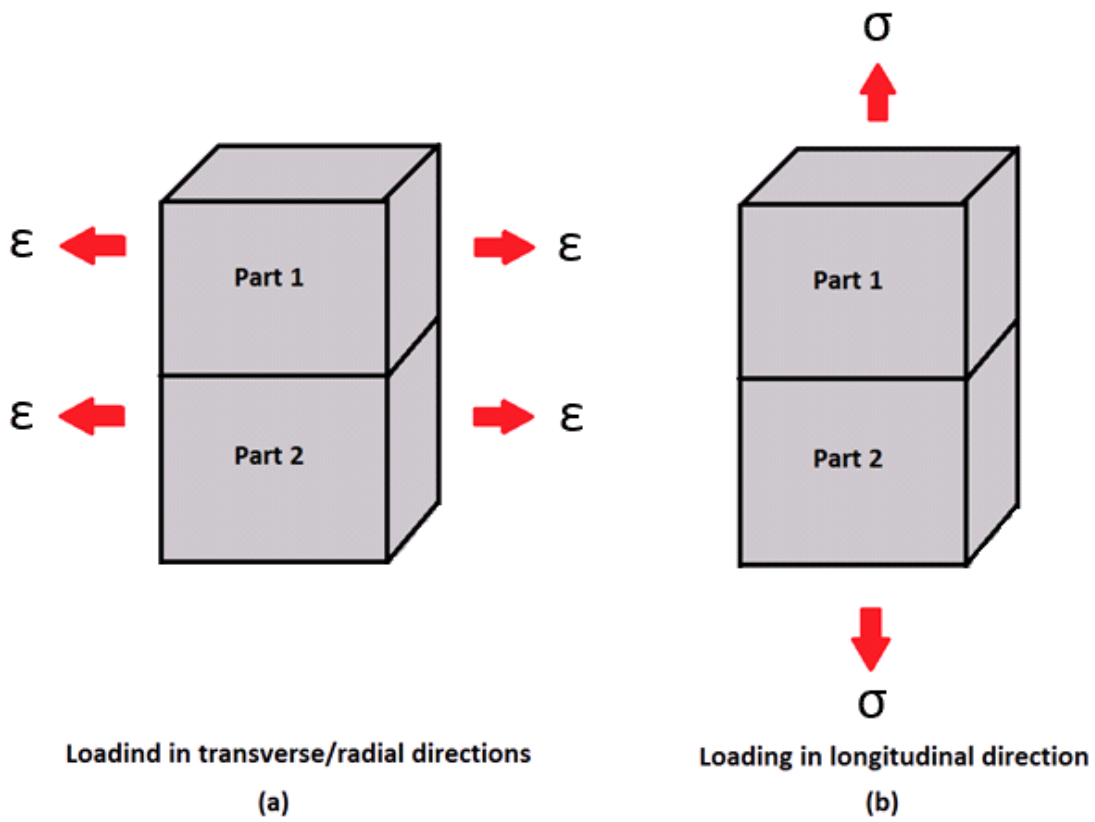


Figure 5.4.2. The simulated loading condition for each part of an individual sample: (a) Load the sample in the transverse/radial direction; (b) Load the sample in the longitudinal direction.

For loading in transverse/radial directions, it is assumed that the two volumes are loaded in parallel and that the strain (ε) applied to different parts is the same, which is described as

$$\varepsilon_{overall} = \varepsilon_{part\ 1} = \varepsilon_{part\ 2} \ldots\ldots = \varepsilon_{part\ n} \qquad \textit{Equation 5.4.1}$$

where *n* stands for the number of parts that the bone is divided into.

The overall stress (σ) applied to the whole volume of bone is then expressed as following:

$$\sigma_{overall} = f_{part1}\sigma_{part\ 1} + f_{part2}\sigma_{part\ 2} \ldots + f_{partn}\sigma_{part\ n} \qquad \textit{Equation 5.4.2,}$$

where *f* represents the volume fraction of each part. In this case, because the volume of each part is the same, the equation can be simplified into

$$\sigma_{overall} = \frac{1}{n}\sigma_{part\ 1} + \frac{1}{n}\sigma_{part\ 2} \ldots + \frac{1}{n}\sigma_{part\ n} \qquad \textit{Equation 5.4.3}$$

Therefore the overall apparent Young's modulus can be written as

$$E_{overall} = \frac{\sigma_{overall}}{\varepsilon_{overall}} = \frac{\frac{\sigma_{part\,1}}{\varepsilon_{part\,1}} + \frac{\sigma_{part\,2}}{\varepsilon_{part\,2}} \ldots + \frac{\sigma_{part\,n}}{\varepsilon_{part\,n}}}{n} = \frac{E_{part1} + E_{part2} \ldots\ldots\ldots\ldots + E_{partn}}{n} \qquad \textit{Equation 5.4.4}$$

Assuming that E_0 is the same within the same bone specimen, the overall E/E_0 in transverse/radial directions is calculated as

$$\frac{E}{E_0}_{overall} = \frac{\frac{E}{E_0}_{part1} + \frac{E}{E_0}_{part2} \ldots\ldots\ldots\ldots + \frac{E}{E_0}_{partn}}{n} \qquad \textit{Equation 5.4.5}$$

When the loading direction is parallel to the osteon longitudinal axis, the volumes are loaded in series. Hence the stress (σ) applied to each part is the same, which is written as

$$\sigma_{part\,1} = \sigma_{part\,2} \ldots\ldots = \sigma_{part\,n} \qquad \textit{Equation 5.4.6}$$

The overall strain (ε) is the sum of the contributions of ε from different parts:

$$\varepsilon_{overall} = f_{part1}\varepsilon_{part\,1} + f_{part2}\varepsilon_{part\,2} \ldots + f_{partn}\varepsilon_{part\,n} \qquad \textit{Equation 5.4.7}$$

In this case, because the volume of each part is the same, the equation can be simplified into

$$\varepsilon_{overall} = \frac{1}{n}\varepsilon_{part\,1} + \frac{1}{n}\varepsilon_{part\,2} \ldots + \frac{1}{n}\varepsilon_{part\,n} \qquad \textit{Equation 5.4.8}$$

Therefore $\frac{1}{E_{overall}}$ can be written as

$$\frac{1}{E_{overall}} = \frac{\varepsilon_{overall}}{\sigma_{overall}} = \frac{\frac{\varepsilon_{part\,1}}{\sigma_{part\,1}} + \frac{\varepsilon_{part\,2}}{\sigma_{part\,2}} \ldots + \frac{\varepsilon_{part\,n}}{\sigma_{part\,n}}}{n} = \frac{1}{n}\left(\frac{1}{E_{part1}} + \frac{1}{E_{part2}} \ldots\ldots + \frac{1}{E_{partn}}\right) \qquad \textit{Equation 5.4.9}$$

Assuming that E_0 is the same for individual bone, the overall E/E_0 in longitudinal is calculated as

$$\frac{1}{\frac{E}{E_0}_{overall}} = \frac{1}{n}\left(\frac{1}{\frac{E}{E_0}_{part1}} + \frac{1}{\frac{E}{E_0}_{part2}} \ldots\ldots\ldots + \frac{1}{\frac{E}{E_0}_{partn}}\right) \qquad \textit{Equation 5.4.10}$$

The E/E_0 values of different parts are plotted against overall averaged values of E/E_0 of bone specimens loading in different directions in *Figure 5.4.3*. Data points at one specific averaged E/E_0 value are individual calculations of E/E_0 for parts from the same bone specimen. Linear fitting has been applied to sectional E/E_0 values in x, y and z directions with R^2 of 0.88 and the slope value of 1.00 $\pm$ 0.062, R^2 of 0.87 and the slope value of 1.00 $\pm$ 0.065, and R^2 of 0.87 and the slope value of 1.02 $\pm$ 0.064, respectively. It indicates a good correlation between sectional E/E_0

and averaged E/E_0 in both directions and thus confirms the fidelity of the averaging methods used to obtain overall E/E_0. The resultant average E/E_0 of individual bone specimen in different loading directions are summarized in *Table 5.4.1.*

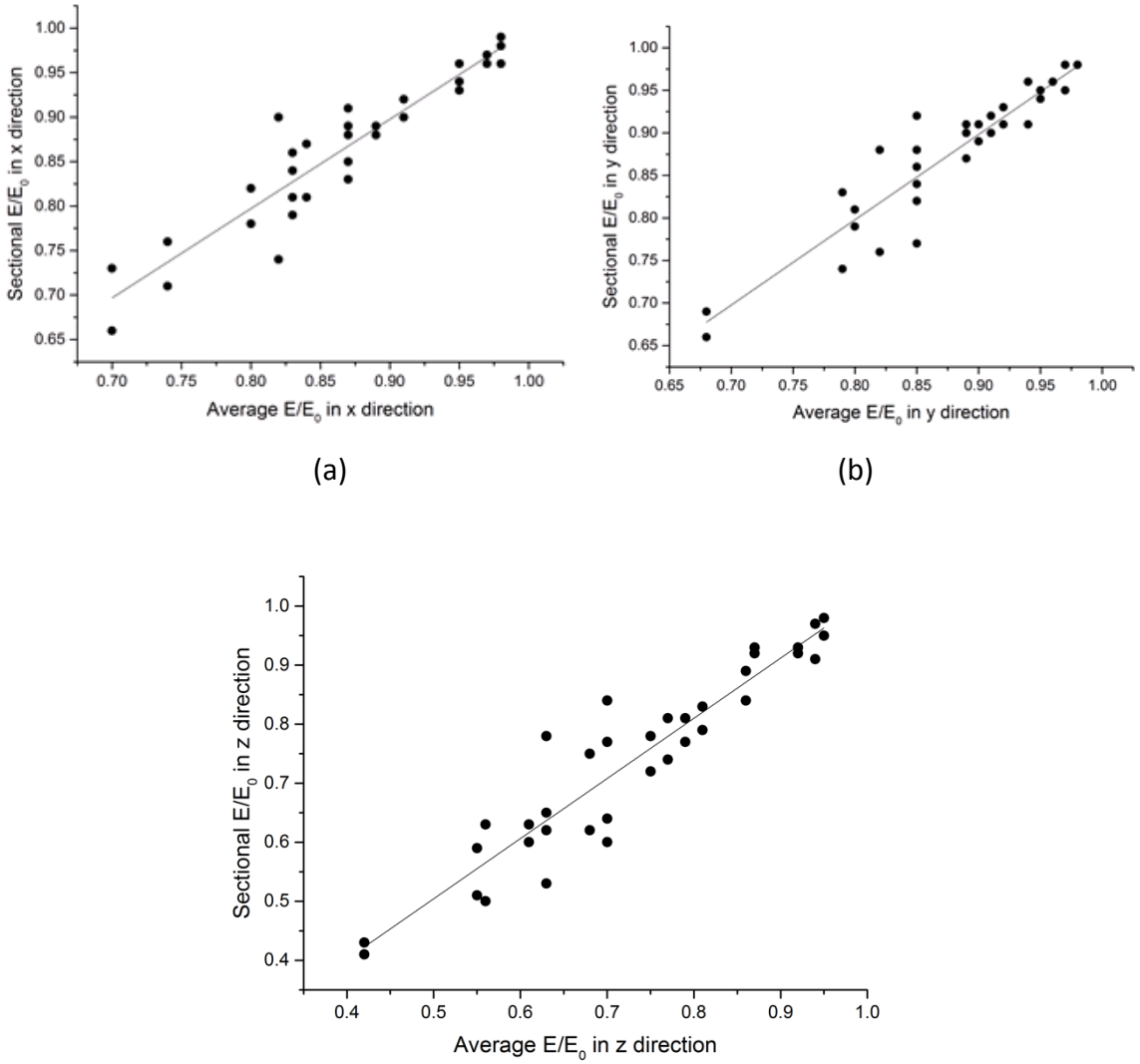


Figure 5.4.3. Sectional E/E_0 against averaged E/E_0: (a) in x direction; (b) in y direction; (c) in z direction.

Table 5.4.1. The resultant average E/E_0 value and porosity of individual bone sample simulated from PReMISe software.

Sample name	Porosity after binning (%)	Averaged E/E_0 in x direction	Averaged E/E_0 in y direction	Averaged E/E_0 in z direction
THR111	2.00	0.98	0.98	0.95
THR110	2.40	0.98	0.97	0.94
THR106b	3.37	0.97	0.96	0.92
THR63	4.14	0.95	0.95	0.86
THR103a	4.97	0.95	0.94	0.87
THR108a	6.92	0.91	0.92	0.81
THR79	7.64	0.91	0.90	0.77
THR107	7.66	0.89	0.91	0.79
THR69	9.11	0.87	0.89	0.68
THR91c	9.27	0.87	0.89	0.75
THR82	11.47	0.84	0.85	0.70
THR75	11.48	0.82	0.85	0.70
THR76	11.67	0.87	0.82	0.63
THR104	11.74	0.83	0.85	0.63
THR74a	13.90	0.80	0.80	0.61
THR04b	14.11	0.83	0.79	0.56
THR72	15.75	0.74	0.80	0.55
THR83	21.60	0.70	0.68	0.42

5.4.1.1 The relation between E/E_0 and porosity

The relation between averaged E/E_0 and porosity is presented in *Figure 5.4.4*. In general, E/E_0 decreases with increasing porosity in both transverse/radial and longitudinal directions. However, porosity is not the only factor which determines E/E_0. For the same specimen with a certain amount of porosity, a much higher E/E_0 is observed in transverse/radial directions compared with longitudinal direction. This is because the orientation of the pores is an important factor that contributes to E/E_0.

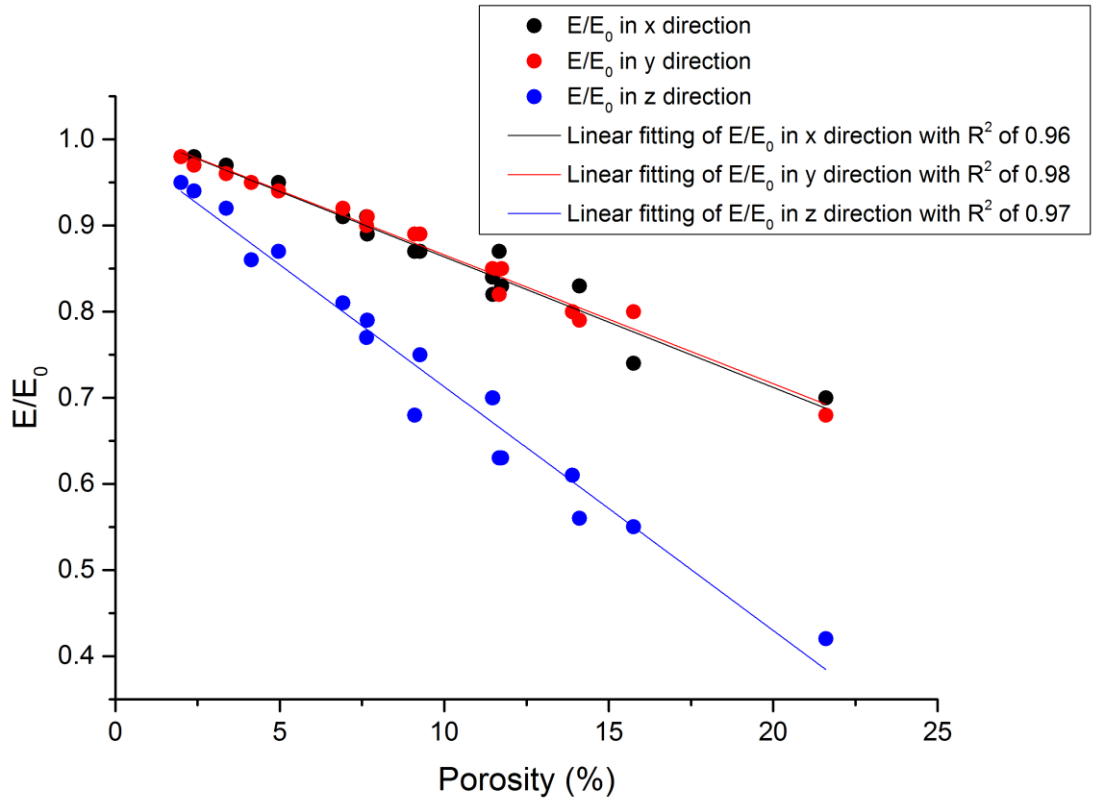


Figure 5.4.4. E/E_0 versus porosity in different directions.

5.4.2 The intrinsic elastic modulus, E_0

The porosity is an important determinant for mechanical properties of bones at the meso-scale [68] [80], but the influence of bone matrix on elastic properties of bones is still under discussion [64]. Calculation of the geometric effect of pores (i.e. E/E_0) from PReMISe allows the effective E_0 to be extracted from the measured apparent elastic moduli (E) of the individual cortical bone specimens from experiment.

By combining the dynamic experimental results obtained from the RUS tests (*Table 5.3.1*) and the E/E_0 from PReMISe from the same batch of samples (*Table 5.4.1*), the value of E_0 in different directions can be derived. The results are listed in *Table 5.4.2*. Because measured E from RUS tests in transverse and radial directions (*Figure 5.3.1*) and simulated E/E_0 in x and y directions (*Figure 5.4.4*) are close to each other and no investigation has been done to identify the relation of transvers/radial directions used in RUS experiments to x/y directions for the simulation,

averaged E and E/E_0 in radial/transverse direction are used for the extrapolation of E_0 in current stage.

Table 5.4.2.The E_0 values of cortical bones in different axis directions using the calculated E/E_0 and the RUS measurement of E. The averaged E_0 in transverse/radial direction is 10.58±2.15 GPa and The averaged E_0 in longitudinal direction is 24.33±3.45 GPa.

Sample name	Porosity after binning (%)	Averaged E in transverse /radial direction from RUS test (GPa)	Averaged E/E_0 in transverse /radial direction	E_0 in transverse /radial direction (GPa)	E in longitudinal direction from RUS test (GPa)	Averaged E/E_0 in z direction	E_0 in longitudinal direction (GPa)
THR111	2.00	10.48	0.98	10.69	20.38	0.95	21.45
THR110	2.40	9.13	0.98	9.32	19.01	0.94	21.68
THR106b	3.37	11.62	0.97	11.98	18.60	0.92	20.22
THR63	4.14	8.71	0.95	9.17	22.19	0.86	25.80
THR103a	4.97	12.55	0.95	13.21	18.64	0.87	21.43
THR108a	6.92	11.77	0.92	12.79	19.55	0.81	24.14
THR79	7.64	12.03	0.91	13.22	18.46	0.77	24.10
THR107	7.66	11.08	0.90	12.31	17.48	0.79	22.13
THR69	9.11	11.86	0.88	13.48	19.00	0.68	27.94
THR91c	9.27	9.27	0.88	10.53	18.64	0.75	24.85
THR82	11.47	6.65	0.85	7.82	12.56	0.70	17.94
THR75	11.48	5.92	0.84	7.05	18.59	0.70	26.56
THR76	11.67	8.70	0.85	10.24	13.23	0.63	21.00
THR104	11.74	6.17	0.84	7.35	17.65	0.63	28.02
THR74a	13.90	10.30	0.80	12.88	16.19	0.61	26.54
THR04b	14.11	8.77	0.81	10.83	15.40	0.56	27.5
THR72	15.75	6.67	0.77	8.34	17.50	0.55	31.82
THR83	21.60	6.35	0.69	9.20	10.44	0.42	24.86

The data are plotted in Figure 5.4.5 and shows the derived E_0 has no clear trend with porosity. In general, the obtained E_0 in longitudinal direction is higher than E_0 in transverse/radial directions for each specimen. Because the mechanical properties of cortical bone matrix are affected by a combination of factors including the mineralization degree, aspect ratio of mineral, the orientation of collagen fibre and the arrangement of bone chemical components [60] [61] [62], the anisotropy of E_0 is understandable, which was also reported by Z.Fan et al [55].

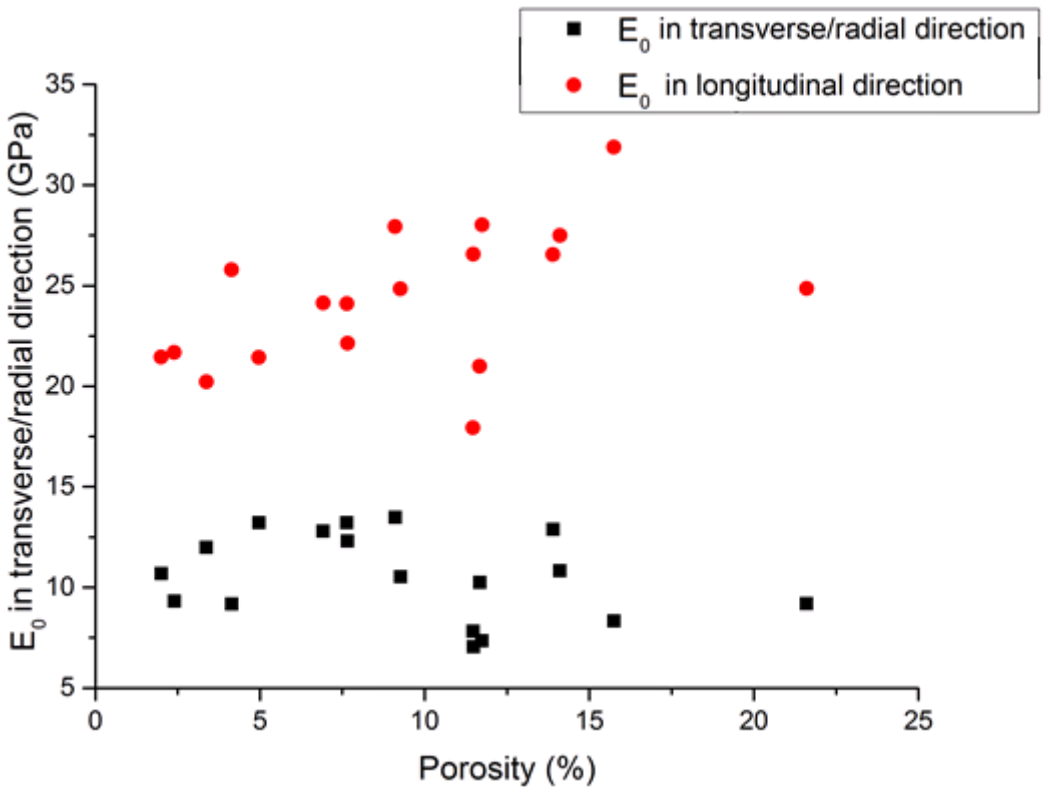


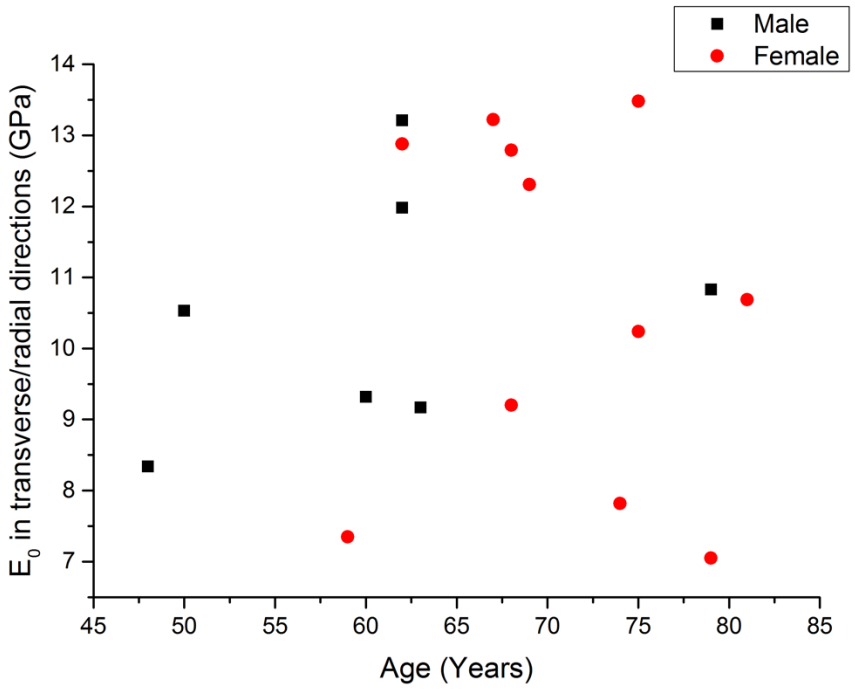
Figure 5.4.5. E_0 in different directions versus porosity.

A few papers [55][60][61][62] have studied the elastic modulus of cortical bone using nano-indentation, which are used for comparison with simulated E_0. Intrinsic elastic modulus measured by nano-indentation is affected by the building blocks of the bone matrix (osteonic and interstitial lamellae), instead of the whole bone structure which has been significantly influenced by the network of pores. The reported values of E_0 in the literature [55] [62] [60] [61] using nano-indentation (longitudinal: 20-27 GPa and transverse/radial: 16-20 GPa) are similar to the calculated average E_0 in both longitudinal direction (24.33 $\pm$ 3.45 GPa) and transverse/radial directions (10.58 $\pm$ 2.15GPa) obtained in this work (*Table 5.4.2*). Two possible reasons can contribute to the difference between E_0 obtained in this work and nano-indentation tests: 1) because nano-indentations are done on osteon lamellae structure or interstitial lamellae, this would reduce the influence of the interface between the bone matrix phases. 2) The samples tested by RUS in this work are in the wet condition and the involvement of fluid inside the microstructure can influence E_0 values compared to dehydrated cortical bones usually used in

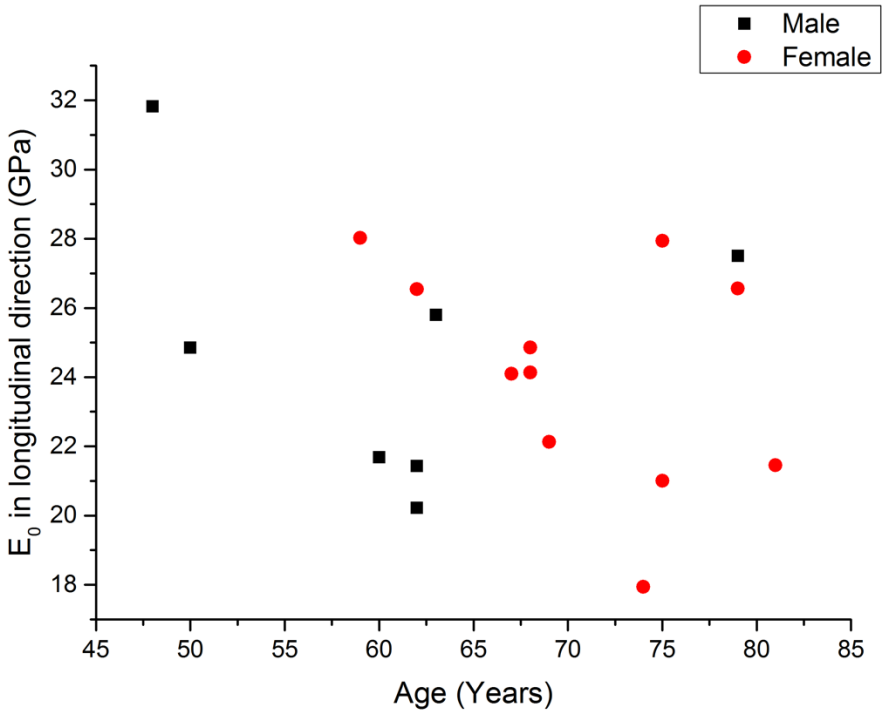
nano-indentation tests [55] [60] [61]. In conclusion, E_0 values calculated in the study are reasonable.

5.4.2.1 The relation between patients' conditions and E_0

Relations between E_0 and conditions of patients are also investigated. For the investigation of the relation between gender and E_0, samples are divided into two groups: female and male. E_0 in different directions for both gender groups are plotted against age, which are depicted in *Figure 5.4.6*. Due to the limited number of samples in both gender groups within the overlapping age range, no conclusion can been drawn on the relation between gender and E_0. Regardless of gender, there is no obvious link between age and E_0 in transverse/radial and longitudinal directions because of scattered data points against age. The same observations have been reported by C.E. Hoffler et al. who stated the elastic modulus of bone matrix of trabecular tissue is unrelated to age [77] and J.Y. Rho et al. who found a very weak link between age with lamellae elastic modulus [80]. However, there is a possible decreasing trend of E_0 with age in longitudinal direction shown in *Figure 5.4.6* (b), but this requires more data to confirm it.



(a)



(b)

Figure 5.4.6. E_0 in different directions versus age in different gender groups: (a) E_0 in transverse/radial directions; (b) E_0 in longitudinal direction.

5.4.3 Bone anisotropy

It is well acknowledged that cortical bone has anisotropic elastic properties [47] [68] [84]. In this section, degrees of contribution of pore network and E_0 to overall anisotropy ratio of cortical bone will be discussed. The pore geometric anisotropy, which is caused by the pore network, is calculated as

$$Pore\ geometric\ anisotropy\ (\ longitudinal{:}\ x\ direction) = \frac{\frac{E}{E_0}_{loading\ in\ z\ direction}}{\frac{E}{E_0}_{loading\ in\ x\ direction}} \quad \textit{Equation 5.4.11}$$

$$Pore\ geometric\ anisotropy\ (longitudinal{:}\ y\ direction\ ) = \frac{\frac{E}{E_0}_{loading\ in\ z\ direction}}{\frac{E}{E_0}_{loading\ in\ y\ direction}} \quad \textit{Equation 5.4.12}$$

Matrix anisotropy is calculated as

$$\textit{Matrix anisotropy (longitudinal: transverse/radial)} = \frac{E_{0\ longitudinal\ direction}}{E_{0\ transverse/radial\ direction}} \quad \textit{Equation 5.4.13}$$

The experimental anisotropy, directly from *E1*, *E2* and *E3* obtained using RUS experimental data, represents the general anisotropic property of cortical bone, and is calculated as

$$Experimental\ anisotropy\ (\ longitudinal{:}\ transverse\ direction) = \frac{E_3}{E_1} \quad \textit{Equation 5.4.14}$$

$$Experimental\ anisotropy\ (\ longitudinal{:}\ radial\ direction) = \frac{E_3}{E_2} \quad \textit{Equation 5.4.15}$$

The calculated pore geometric anisotropy, matrix anisotropy and experimental anisotropy are listed in *Table 5.4.3* and are plotted against porosity in *Figure 5.4.7.*

Table 5.4.3.Anisotropic ratios of cortical bones.

Sample name	Pore geometric anisotropy (longitudinal : x direction)	Pore geometric anisotropy (longitudinal :y direction)	Matrix anisotropy (longitudinal : transverse/radial)	Experimental anisotropy (longitudinal : transverse)	Experimental anisotropy (longitudinal : radial)
THR111	0.97	0.97	2.01	2.06	1.84
THR110	0.96	0.97	2.33	1.98	2.19
THR106b	0.95	0.96	1.69	1.70	1.51
THR63	0.91	0.91	2.81	2.38	2.74
THR103a	0.92	0.93	1.62	1.49	1.48
THR108a	0.89	0.88	1.89	1.73	1.59
THR79	0.85	0.86	1.82	1.55	1.52
THR107	0.89	0.87	1.80	1.53	1.62
THR69	0.78	0.76	2.07	1.57	1.64
THR91c	0.86	0.84	2.36	2.00	2.02
THR82	0.83	0.82	2.29	1.92	1.86
THR75	0.85	0.82	3.77	2.90	3.43
THR76	0.72	0.77	2.05	1.64	1.42
THR104	0.76	0.74	3.81	2.63	3.13
THR74a	0.76	0.76	2.06	1.60	1.55
THR04b	0.67	0.71	2.54	1.65	1.87
THR72	0.74	0.69	3.82	2.38	2.93
THR83	0.6	0.62	2.70	2.20	1.28

In general, porosity has a weak impact on the total bone anisotropy (experimental anisotropy) shown in *Figure 5.4.7* (c), but it is clearly shown that the geometric anisotropy shows a strong positive relation to porosity (*Figure 5.4.7* (a)) while matrix anisotropy shows a weak positive relation to porosity (*Figure 5.4.7* (b)). The weak positive relation of matrix anisotropy to porosity which may be due to two possible reasons: (1) unresolved pores due to tomograph resolution limitation. However the possibility of this reason is very small because the influence of unresolved pores on simulated E_0 is negligible as it is explained in *Section 5.5.2.2*. (2) The most possible reason is the different conditions of bone matrix (e.g. the orientation of collagen fibres, mineralization degree [55,57–62]) caused by conditions of patients. The disease of osteoarthritis, which patients suffer from, influences bone mineral density and thus porosity [49] as well as bone matrix including mineralized collagen [232], the orientation of which contributes to matrix anisotropy [55,73–75]. Therefore the relation

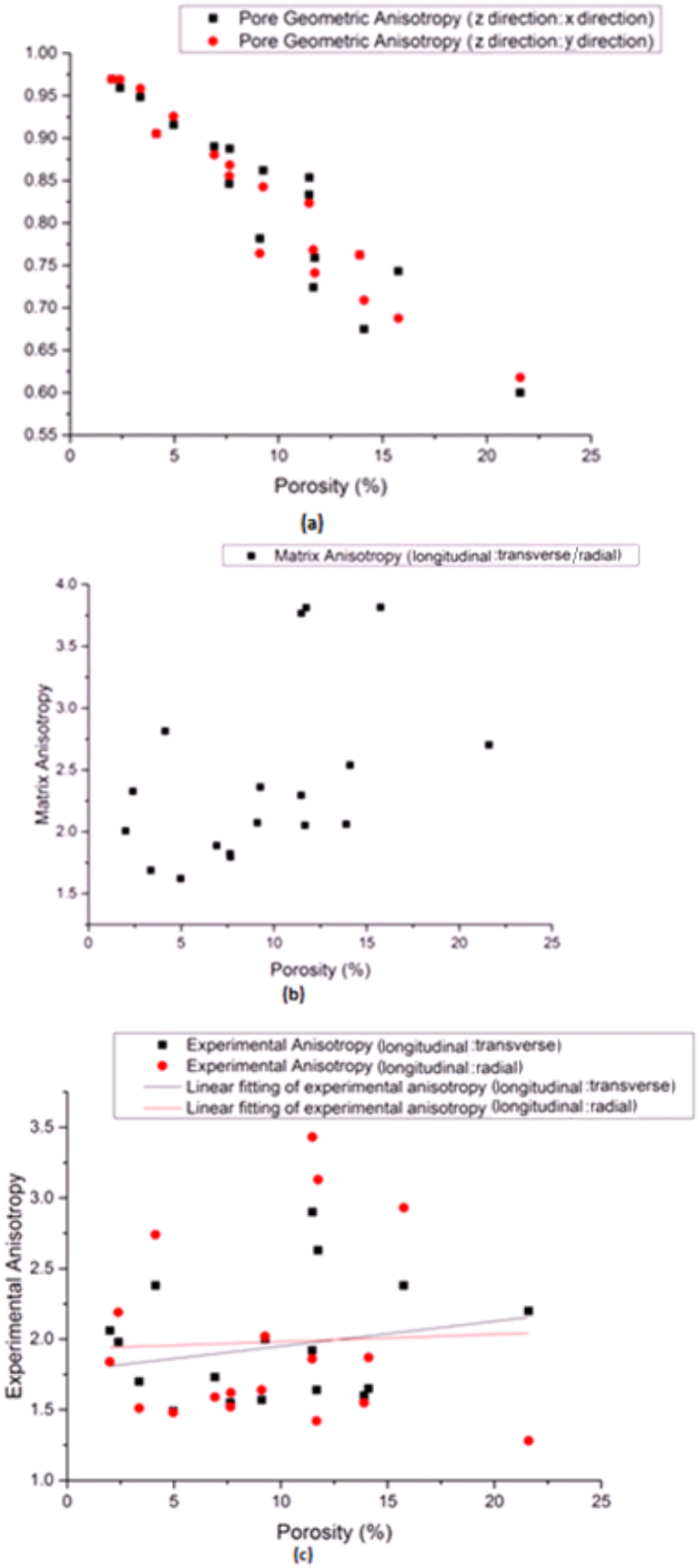


Figure 5.4.7. Anisotropic ratios obtained from different factors against porosity: (a) pore geometric anisotropy; (b) matrix anisotropy; (c) experimental anisotropy.

between matrix anisotropy and porosity is not directly related to porosity but the influence of osteoarthritis on bone matrix. In addition, the observation from *Table 5.4.3* is in agreement to Q. Grimal et al. [67] and Z.Fan et al. [55] who found that the bone matrix is a major contributor to the overall bone anisotropy.

5.5 Discussion

5.5.1 Porosity

5.5.1.1 Porosity measurement

In this chapter, a reliable way for pore calculation has been proposed. Unlike the method adopted by Dong [68], calculating the overall bone porosity based on one representative cross section, the whole volume of bone has been considered in this study.

The necessity of using whole volume bone for porosity measurement can be explained. Take one bone specimen with an overall porosity of 7.64% as an example. Porosities of cross-sections along the longitudinal direction of bone are calculated using Avizo in an interval of 0.0069 mm (one pixel size of tomograph) and are plotted against the position of the selected cross-section in longitudinal direction in *Figure 5.5.1*. The position of the bottom cross-section is set to be 0 in x axis in *Figure 5.5.1*. As it is clearly shown in *Figure 5.5.1*, there are large and continuous variations in porosities calculated from cross sections compared with the bone porosity calculated from the whole bone volume. Therefore it can be difficult to find a representative cross section which coincidently has the porosity similar to the overall bone porosity. Detailed information of calculated porosities on different cross sections are listed in Appendix *Table 10.2.2*.

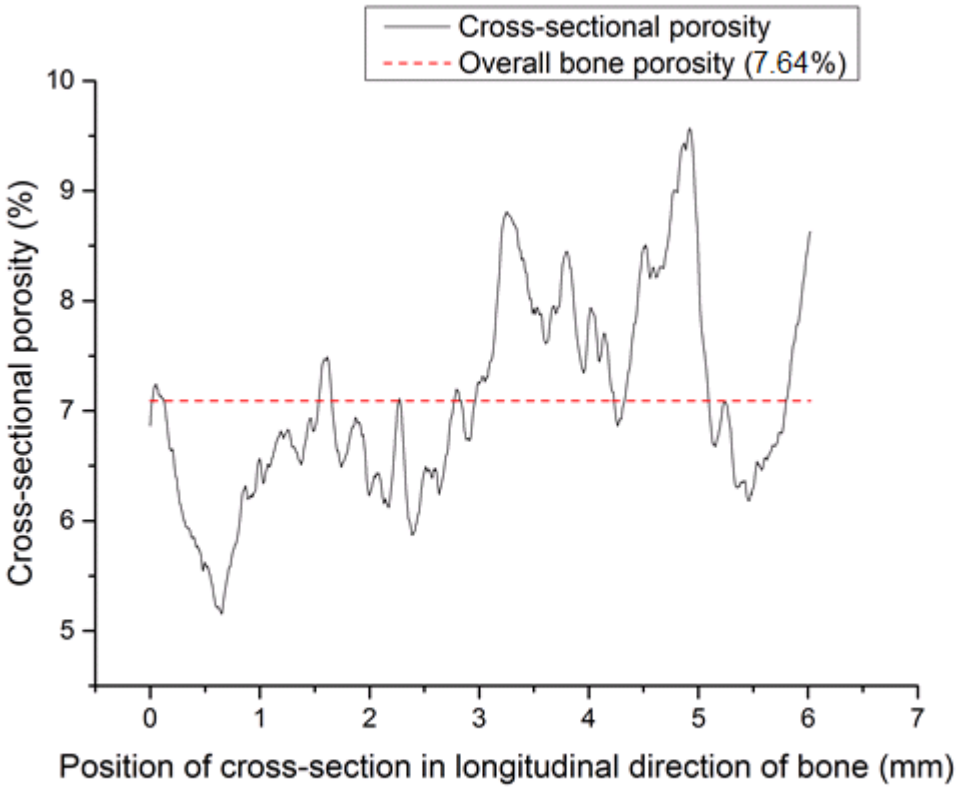


Figure 5.5.1. Cross-sectional porosity distribution.

5.5.1.2 The relationship between patients' conditions and porosity

In this chapter, unlike literature [51] [76], no obvious relation between age and gender to porosity is observed, which may due to a few reasons: 1) there are not enough samples to see the relation between porosity and age as well as gender. Khosla [76] used hundreds of samples to draw a conclusion (i.e. *Figure 2.2.3* (b)). 2) The age span of this study is not wide enough to see the significant change in mineral loss and thus porosity. In literature [76], a large age range from 20-100 years old was adopted (i.e. *Figure 2.2.3* (b)) to find a much clearer trend. (3) The location for the sample cutting. Significant change in porosity occurs in the transition region between trabecular bone and cortical bone which results in decreased cortex with age [78].Therefore, although all the samples in this study are cut in the same region from the femoral neck, the distance between where the cortical bones are cut and the transition region

will influence the extent of porosity change of the cortical bone observed due to aging. (4) The influence of osteoarthritis on patients' bone porosities.

5.5.2 PReMISe analysis of E/E_0 and E_0

The approach proposed to obtain E/E_0 and E_0 uses the microstructural information of pores within porous materials to acquire elastic properties. With the combination of real microstructural information of bone matrix and pores from X-ray tomograph, a simple model PReMISe, and experimental results from RUS, the intrinsic elastic properties of cortical bones have been successfully extracted and the influence of the pore network on the bone elastic properties have been revealed.

The results show that the increasing porosity has a negative effect on apparent bone modulus. The orientation of the pore network contributes to the enhanced elastic modulus in longitudinal direction of bone which is parallel to the Haversian canals. The anisotropy of bone matrix is also shown, which has a direct relation with overall bone anisotropy while the orientation, porosity, size, geometry and distribution of pores has weaker effect on the bone anisotropic ratio. In addition, it is found that anisotropy introduced by pores increased with increasing porosity of cortical bones. The influences of age and gender on elastic property of bone matrix have also been examined, and no clear relations can be drawn due to the limitation in sample availability. Overall the obtained results have a good agreement with literatures of cortical bones and it indicates the suitability of using this approach to assess the mechanical properties of cortical bone.

5.5.2.1 The intrinsic elastic modulus of bone material

The extraction of intrinsic elastic modulus of bone matrix with a combination of tomographs of bone samples, RUS tests and PReMISe simulation has the advantage of avoiding the difficulty of sample preparation for nano-indentation tests. It can be applied to specimens at larger length-scales. The small standard deviations present among different samples in E_0 may indicate the

possibility to use average E_0 obtained in the chapter as standard values for the future prediction of apparent elastic modulus of other cortical bone samples using PReMISe. However, it still requires further assessment by testing the fidelity of using the obtained E_0 for the prediction of apparent elastic moduli of other cortical bone samples, compared with their experimental results.

Compared with E_0 obtained by extrapolating the value of E with zero porosity via linear regression of RUS results (*Figure 5.3.1*), the obtained E_0 is 11.74 $\pm$ 0.80 GPa in transverse direction, 11.21 $\pm$ 1.01 GPa in radial direction and 20.40 $\pm$ 1.07 GPa in longitudinal direction. There are less than 16% difference in the extrapolated values with average values obtained using PReMISe. Therefore it is possible to use linear regression method to obtain average E_0 in different directions using experimental results. However, the linear regression approach can only provide average value of E_0 in different directions and cannot provide information of E_0 for each individual specimen, which has different bone matrix conditions and thus different bone matrix elasticity. In addition, the obtained values from linear regression method based on experimental results highly depend on the type of mechanical test. For example, the extrapolated value of E_0 in longitudinal direction tested by compression test (12.09 $\pm$ 0.90 GPa) which is almost half the value of that obtained by RUS test in this study.

The approach developed in this chapter is a simple and straightforward method to calculate intrinsic elastic modulus of bones and it provides good agreement between simulations and nano-indentation results [55] [62] [60] [61] of E_0 and at the same time determines the anisotropy of the bone matrix.

5.5.2.2 The use of PReMISe for extraction of bone properties

PReMISe uses E_0 as an individual factor. Using the anisotropy of bone matrix increases the accuracy of elastic moduli simulation compared with the model published by Sevostianov and Kachanov who considered the bone matrix as an isotropic material [56]. In addition, the real

pore network has been introduced by different bone samples into consideration for the improved simulation accuracy. Assumptions have been made when using PReMISe that the elastic properties of matter inside of pores are neglected, the influence of which is believed to be small because studies show the elastic moduli of the content within pores including blood vessels, osteocytes, nerves et are in the magnitude of a few KPa or MPa [233] [234] while the elastic modulus of bone matrix is in the order of GPa.

However, other issue exists that might affect the simulation results from PReMISe (e.g. the resolution of the detailed microstructural information being input into the model) and thus it requires further investigation. This issue is a result of the resolution limitation of the X-ray tomography images and image-processing tools such as ImageJ (the algorithm used for making binary and downsizing the image into 100x100x100 pixel^3). The pore network in cortical bone consists of Haversian's and Volkmann's canals as well as the resorption cavities, the diameters of which range from a few to hundreds microns [66]. These are resolved by tomography, but some small pore features (a part of lacunae and canaliculi) cannot be resolved in the resultant binary .bmp images imported into PReMISe for the microstructural information.

The influence of small pores on simulation results can be assessed by using higher resolution cortical bone tomographs, which were taken by the author with a resolution of approximately 2 um (*Section: 3.1.2*). In these tomographs, small pores can be identified in red circles (*Figure 5.5.3*). Due to the sample limitation, only two cortical bones with a porosity of 4.88% and 14.68%, respectively were scanned with this higher resolution.

The obtained E/E_0 of the two samples in x, y and z direction are plotted together with previous 18 samples and highlighted with crosses (*Figure 5.5.2*). The simulated results of both samples are listed in *Table 5.5.1*. The averaged E/E_0 values of both samples are similar to the values obtained by PReMISe based on tomographs with lower resolutions of bones with similar porosities (THR04b with a porosity of 14.11% and THR103a with a porosity of 4.97%).

The influence of small pores on E_0 can also be further evaluated using these data. Because the majority of small pores are unable to be segmented after thresholding and binning, 5 100x100x100 pixel^3 volumes of bone matrix only containing small pores are randomly selected for each specimen in different regions (*Figure 5.5.3*). These were distributed randomly in each sample with no overlapping and represent regions that were purely matrix in the lower resolution simulations. The volume fraction of these small pores, which are only observed at high resolution, is around 1% depending on different specimens and different locations. At this small level of porosity, there is therefore no significant effect of these small pores on E_0. The obtained results for the ratio between E_0 values influenced and not influenced by these pores confirm this, and are summarized in *Table 5.5.2*. This is consistent with literature [56] that the apparent elastic moduli in transverse, radial and longitudinal directions are insensitive to the unresolved small pores, which are in the length scale between 1um-5um.

Table 5.5.1. E/E_0 simulated by PReMISe based on high resolution tomographs. X,y and z indicate x,y and z loading directions used in PReMISe.

THR61b	Part 1			Part 2			Average		
	x	y	z	x	y	z	x	y	z
Porosity (%)	14.3			15.05			14.68		
E/E_0	0.81	0.79	0.64	0.80	0.77	0.59	0.81	0.78	0.61
THR91a	Part 1			Part 2			Average		
	x	y	z	x	y	z	x	y	z
Porosity	5.48			4.27			4.88		
E/E_0	0.94	0.94	0.91	0.95	0.95	0.94	0.95	0.95	0.92

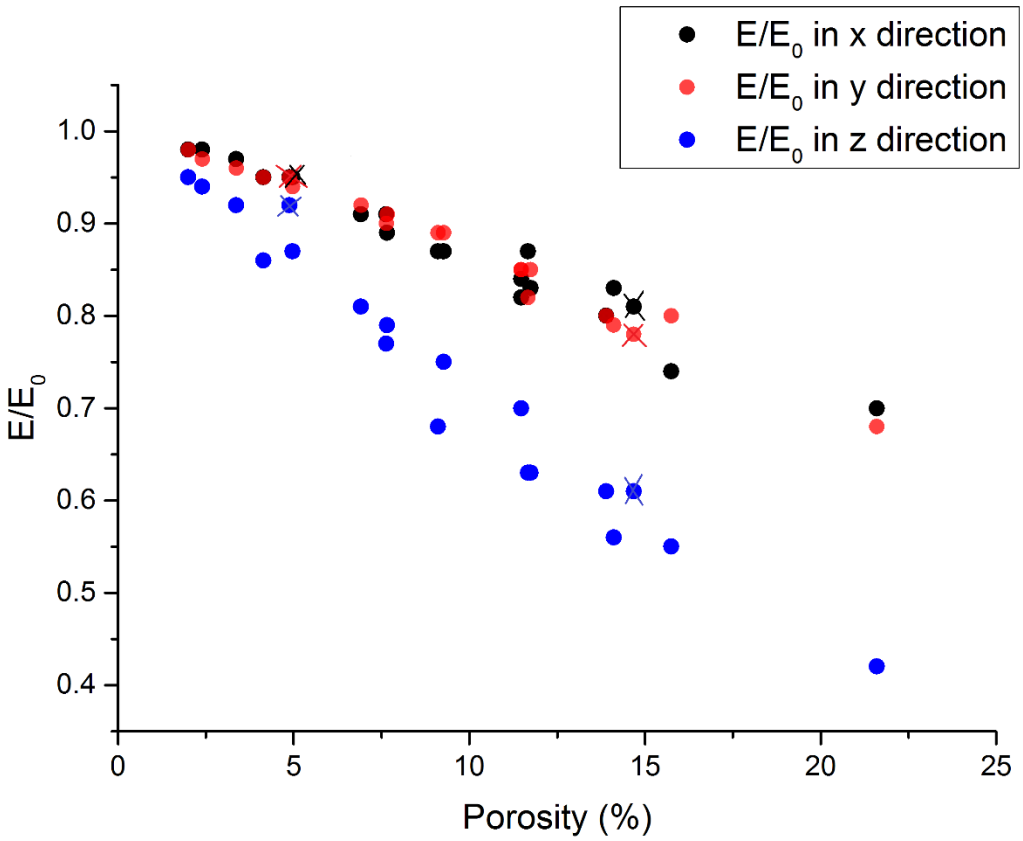


Figure 5.5.2. E/E_0 vs porosity of all bone specimens with two samples in high resolutions highlighted in crosses.

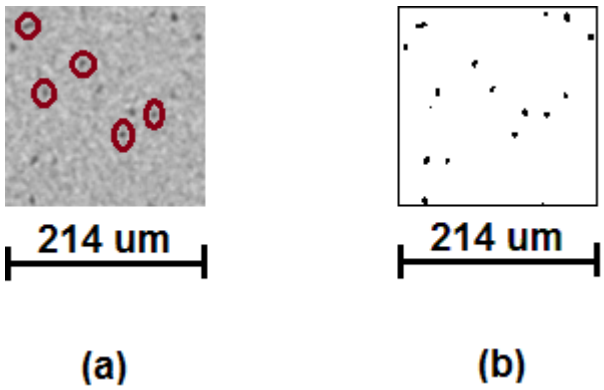


Figure 5.5.3. Bone matrix between osteons in high resolution tomograph (2.14 um) of cortical bone with a porosity of 4.88%. (a) before binning; (b) after binning.

Table 5.5.2. The simulated ratio between E_0 values influenced and not influenced by small pores.

Sample with porosity of 14.68%	Loading direction	Porosity (%)	E/E_0
Volume 1	x direction	0.85	0.99
	y direction		0.99
	z direction		0.99
Volume 2	Loading direction	Porosity (%)	E/E_0
	x direction	1.24	0.98
	y direction		0.99
	z direction		0.98
Volume 3	Loading direction	Porosity (%)	E/E_0
	x direction	1.42	0.98
	y direction		0.98
	z direction		0.97
Volume 4	Loading direction	Porosity (%)	E/E_0
	x direction	1.01	0.99
	y direction		0.99
	z direction		0.99
Volume 5	Loading direction	Porosity (%)	E/E_0
	x direction	1.07	0.98
	y direction		0.99
	z direction		0.98

(a)

Sample with porosity of 4.88%	Loading direction	Porosity (%)	E/E_0
Volume 1	x direction	0.90	0.99
	y direction		0.99
	z direction		0.99
Volume 2	Loading direction	Porosity (%)	E/E_0
	x direction	1.05	0.99
	y direction		0.98
	z direction		0.98
Volume 3	Loading direction	Porosity (%)	E/E_0
	x direction	1.00	0.99
	y direction		0.99
	z direction		0.98
Volume 4	Loading direction	Porosity (%)	E/E_0
	x direction	0.51	0.99
	y direction		0.99
	z direction		0.99
Volume 5	Loading direction	Porosity (%)	E/E_0
	x direction	0.59	0.99
	y direction		0.99
	z direction		0.99

(b)

Chapter 6

6 Fracture toughness of trabecular bone

This chapter develops a methodology to evaluate the fracture toughness of trabecular bone using an image-based analysis method. It is divided into two sections: crack segmentation and fracture toughness calculation. In the crack segmentation section, several methods for crack segmentation have been used and compared, as trabecular bone has a complicated pore network and the cracks developed cannot be readily identified in tomographs. Using these data, the development of crack length with increasing load is investigated. In the second section, pre-processing of data has been investigated and developed in order to use an FE method (JMAN) for J integral calculation and then *K* calculation. The relation between the obtained J integral/*K* and load is then studied.

6.1 Background

Raw tomography data of one randomly selected trabecular bone specimen, tested under flexural loading were provided by Dr. Shaocheng Ma, from Imperial College, London for the author to develop a methodology to calculate the J integral for a loaded crack. The data were collected in an experiment (EE 11204-1) on beamline I12 at the Diamond Light Source. The sample collection had full ethical approval (Imperial Tissue Bank number R13004).

The trabecular bone was cut from hip-fractured femoral head into a semi-core shape with a size of 12 mm in length x 7 mm in thickness x 3.5 mm in height. The geometry of the sample is sketched in *Figure 6.1.1*. A sharp notch with a length of 0.8 mm and a width between 0.15-0.2 mm was introduced using a razor blade. Tomographs of trabecular bones under loading were recorded by Shaocheng Ma on the I12 beamline using module 3 optics with a 180° rotation scan. The applied monochromatic energy beam was 112 KeV and the exposure time was 90 seconds per radiograph, with 3000 projections per tomograph. The scan time was approximately 10 minutes. Trabecular bone sample was loaded using the three-point bending test rig shown in *Figure 6.1.2* (a) (b) and (c), and tomographs were obtained under static load with 5 N intervals until the sample failed, beginning from a pre-load of 5 N. This specimen is reported to have failed at an applied load of 37 N.

The bending rig employs three fixed rollers (*Figure 6.1.3*), the diameter of which is 2 mm. The pre-notched trabecular bone was kept wet by spraying water onto the sample before scans. The reconstructed tomograph (*Figure 6.1.4*) doesn't include the whole volume of the sample in x direction but it realizes a complete visualization of notch and crack. The author takes no credit for the scanning experiment and tomograph reconstruction.

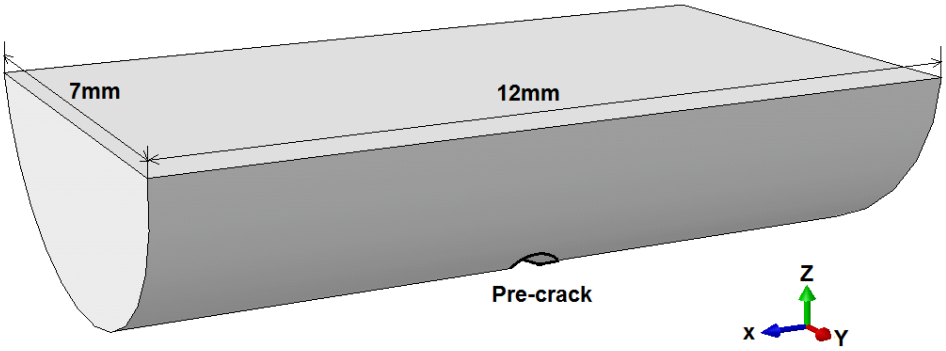
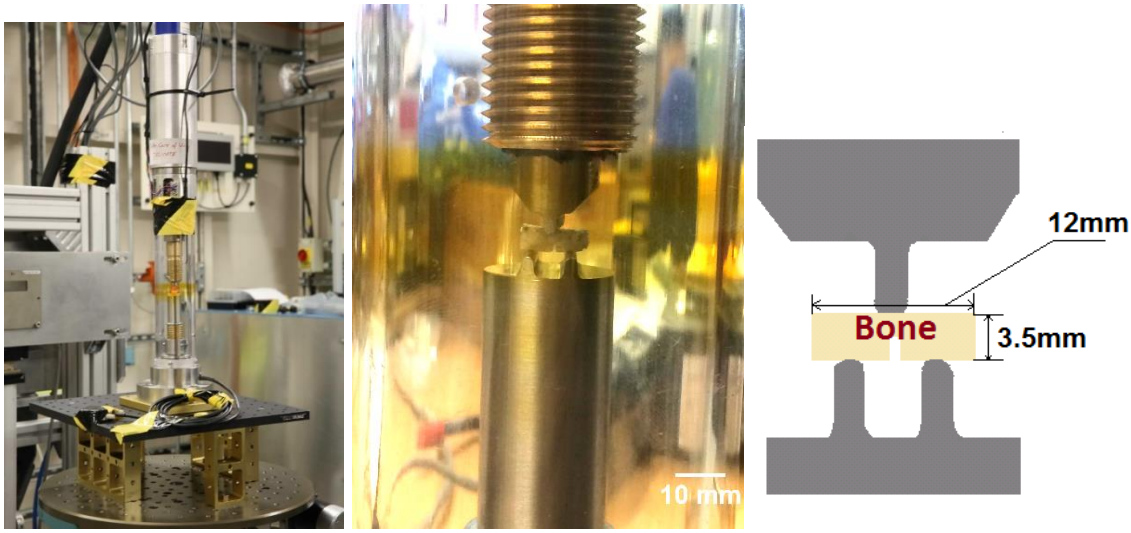


Figure 6.1.1. Sketched geometry and size of pre-notched trabecular bone.



(a) (b) (c)

Figure 6.1.2. Three point bending test on trabecular bone. (a) Set-up of three-point bending test rig in synchrotron. (b) Section view of three-point bending test on pre-notched bone. (c) Schematic image of section view of three-point bending test rig on pre-notched bone.



Figure 6.1.3. The applied fixed roller with a diameter of 2mm.

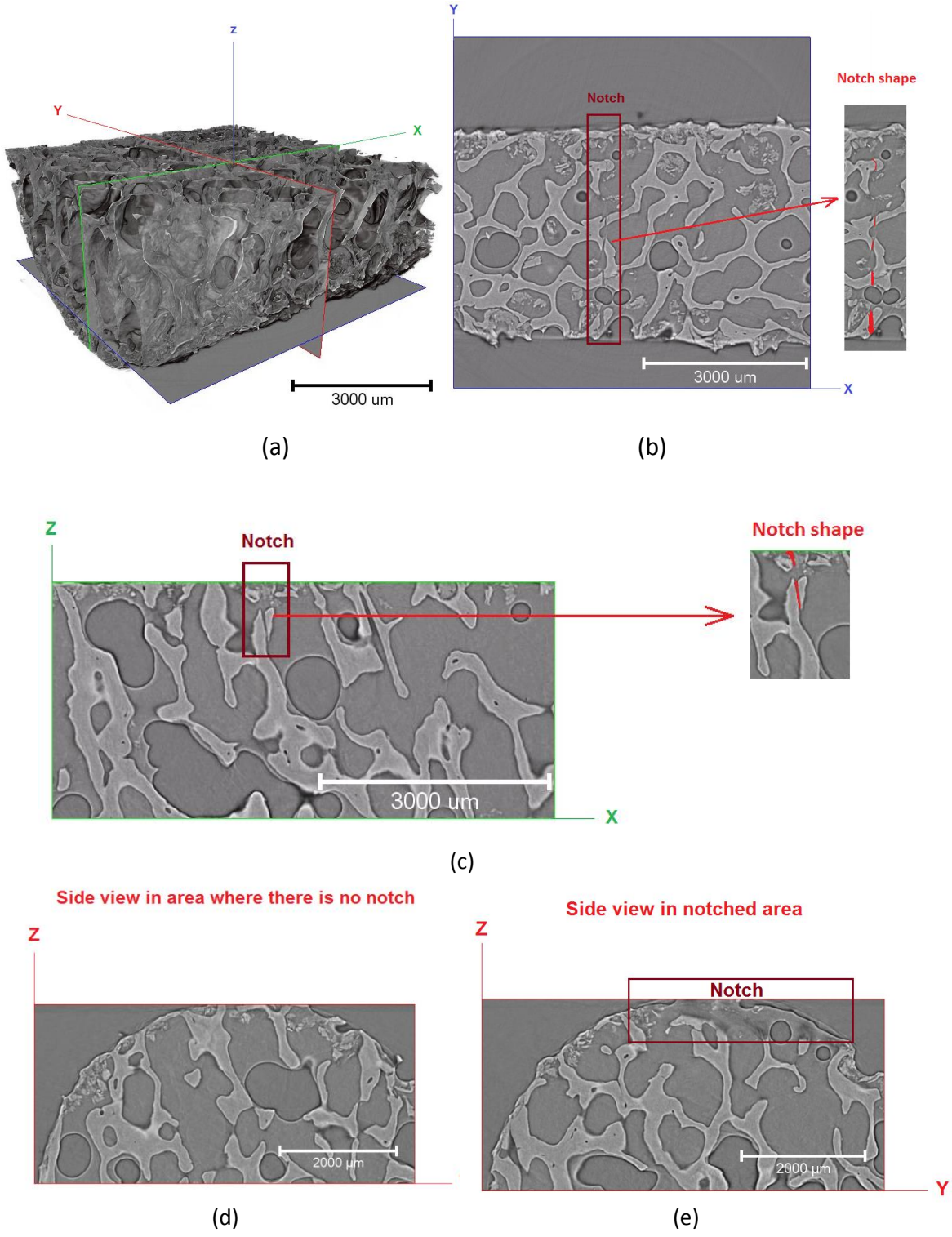


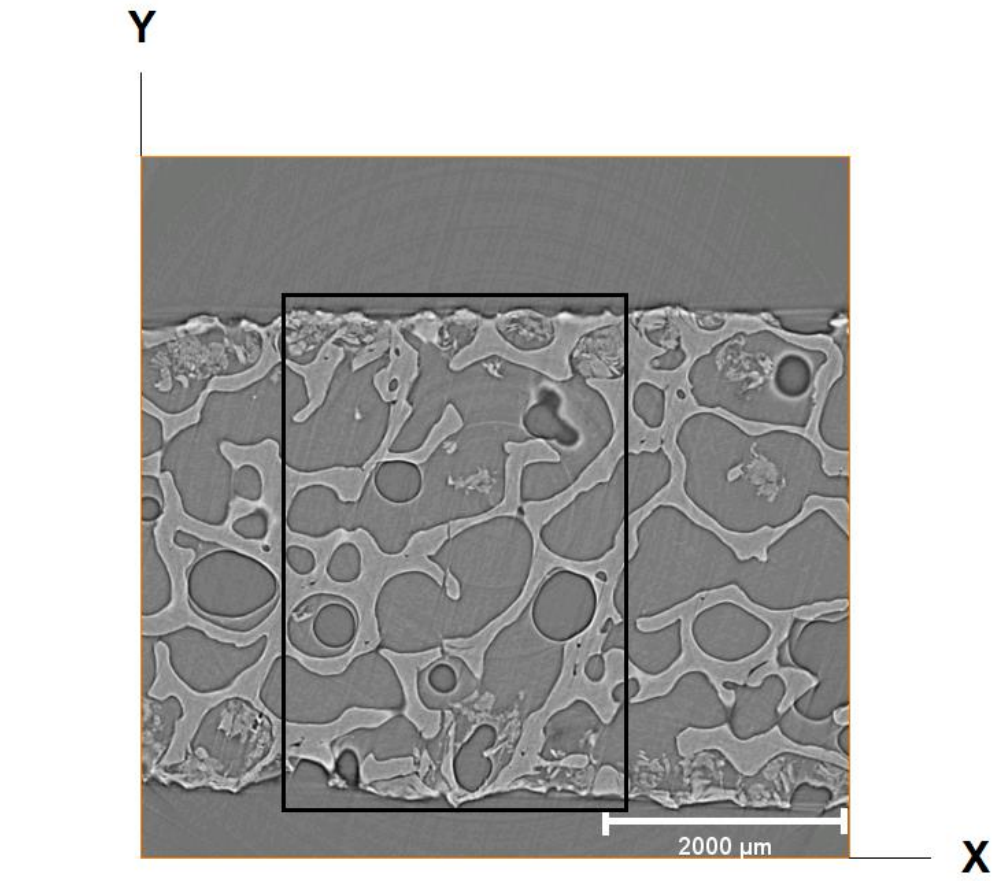
Figure 6.1.4. Tomographs of trabecular bone under its preload state. (a) 3D volume of bone; (b) XY plane view; (c) XZ plane view with emphasized notch shape; (d) YZ plane view in area where there is no notch; (e) YZ plane view in notched area. Pre-notch from razor blade is emphasized in red square.

6.2 Crack segmentation

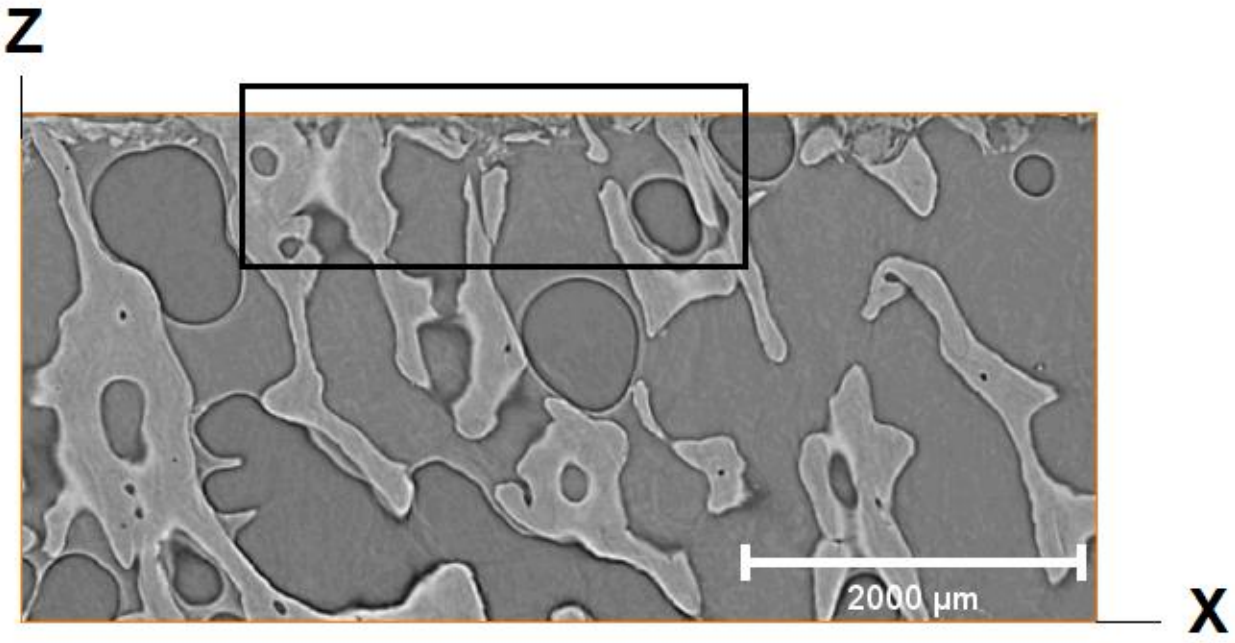
Data was cropped (marked in black square in *Figure 6.2.1*) to contain the information of the notch plus crack and at the same time save computational time. Visual crack segmentation is difficult, as shown in *Figure 6.2.2*, which demonstrates that no clear crack can be observed at the notch tip even at the maximum load applied (35N) before fracture compared with preload state. Therefore, several ways have been tried for the segmentation of notch plus potential crack at the tip, under different loadings.

6.2.1 Crack segmentation (watershed and manual methods)

The conventional method to segment cracks is threshold methods, which can be implemented using Avizo software (version 9.2.0). In this software, different material phases are seeded by painting voxels in regions representing air, pores, bone matrix and notch plus crack using *brush* option in the *segmentation* editor, as shown in *Figure 6.2.3*. The watershed option was then used to grow seeds to identify the phases in *Figure 6.2.4* that present different materials based on the greyscale gradient map. In this method, plateaus in the intensity map represent different materials and the boundaries between phases are peaks in gradient map (*Figure 6.2.5*). The watershed option allows the growth of painted voxels located in different regions until the boundaries between different phases are reached based on the gradient map [235]. However, due to the complicated geometry of notch plus crack, which is interconnected with a large amount of pores in the trabecular bone, the seeding procedure requires a slice by slice manual definition of the notch and crack to avoid the involvement of the pores that are linked with it. The manual result of the notch plus crack in trabecular bone at a load of 35 N is shown in *Figure 6.2.6*. However, this method is very time-consuming and therefore other methods were needed for the crack segmentation.



(a)



(b)

Figure 6.2.1. Data was cropped in the region of black cuboid. (a) Cropped region on xy plane; (b) Cropped region on xz plane.

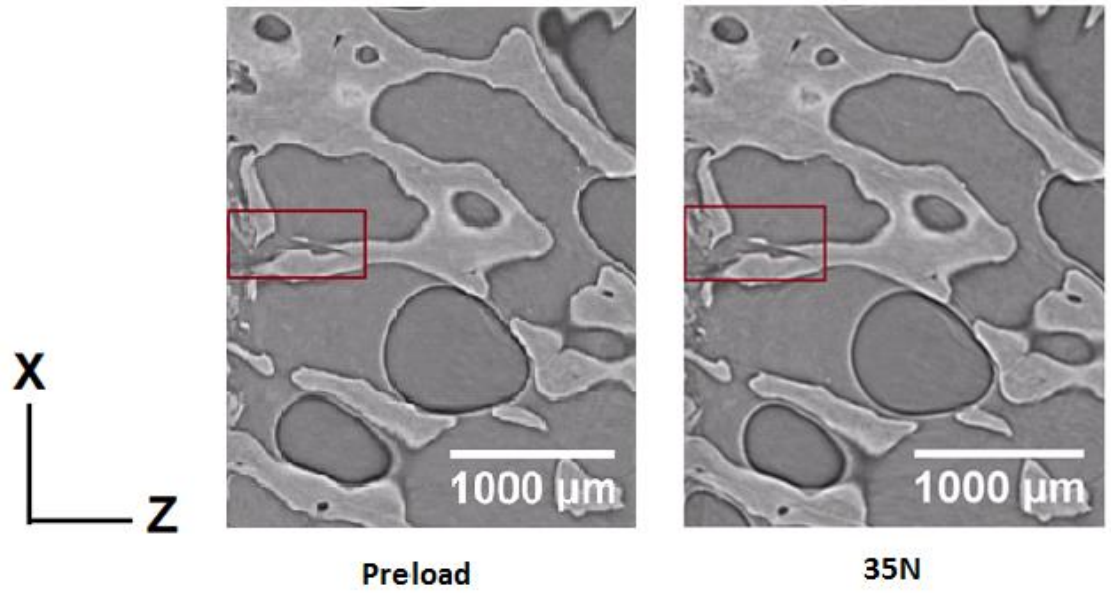
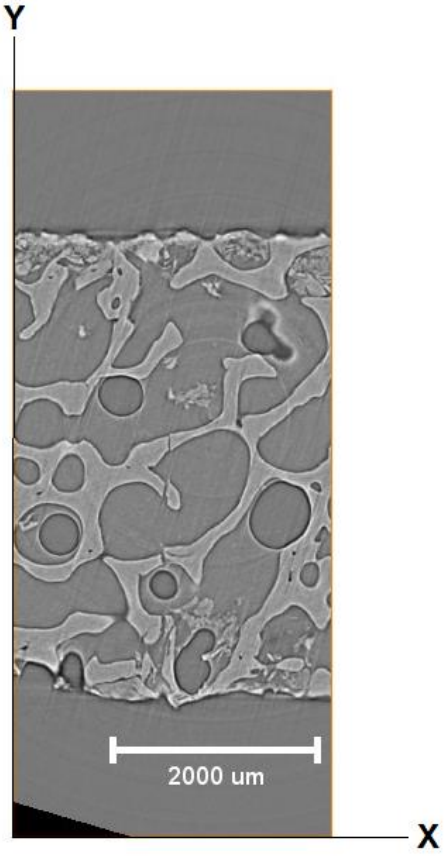
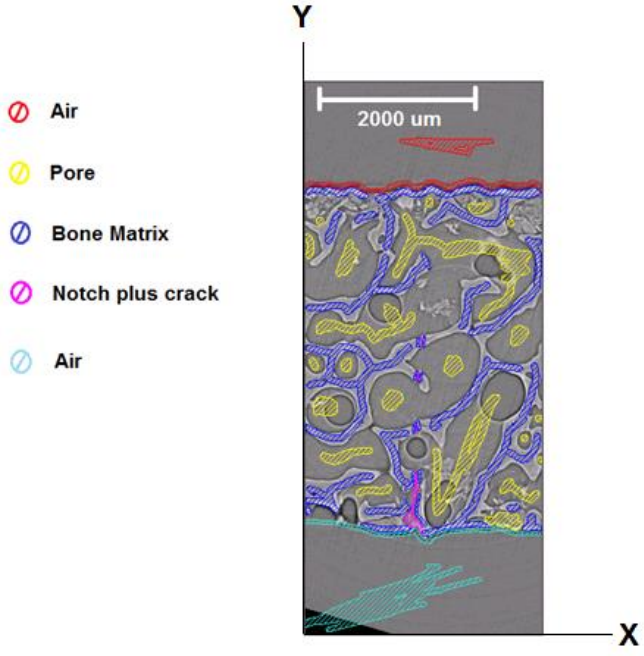


Figure 6.2.2. The notch plus crack marked in red square within trabecular bone under a load of 35N compared with preload state.

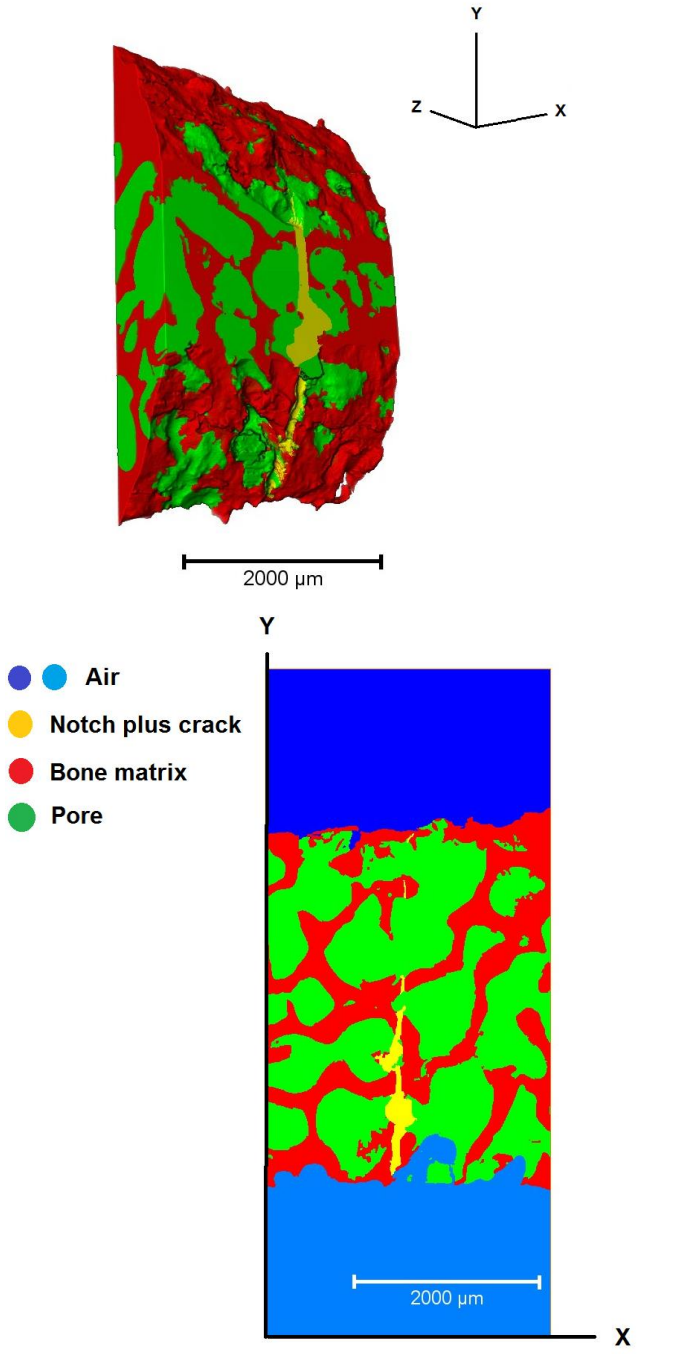


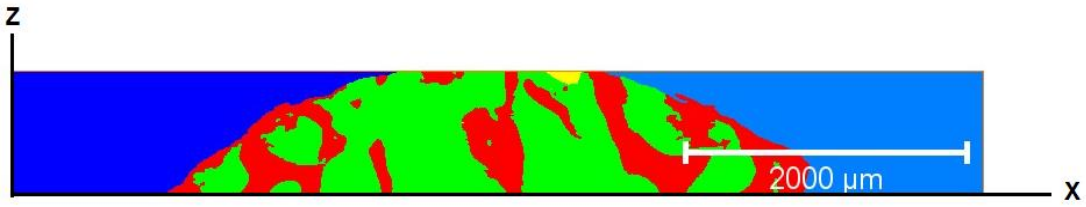
(a)



(b)

Figure 6.2.3. The seeding procedure for different phases present in tomograph of bone under a load of 35N. (a) Original orthoslice before seeding; (b) Orthoslice after seeding.


Y
Z
X
2000 µm
Y
Air
Notch plus crack
Bone matrix
Pore
2000 µm
X
(a)
(b)
Z
2000 µm
Y
(c)



(d)

Figure 6.2.4. Different materials grow into different phases after watershed procedure. (a) 3D volume of bone under a load of 35 N with bone matrix, pore and notch plus crack highlighted in red, green and yellow, respectively. (b) XY plane view. (c) YZ plane view. (d) XZ plane view.

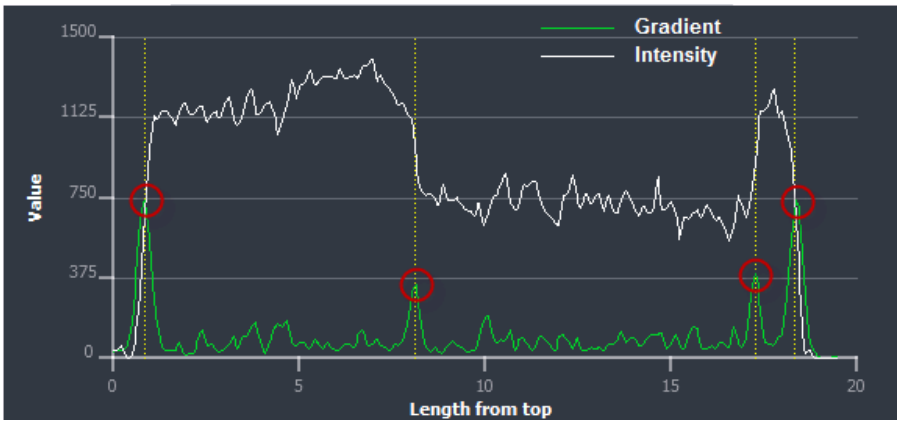
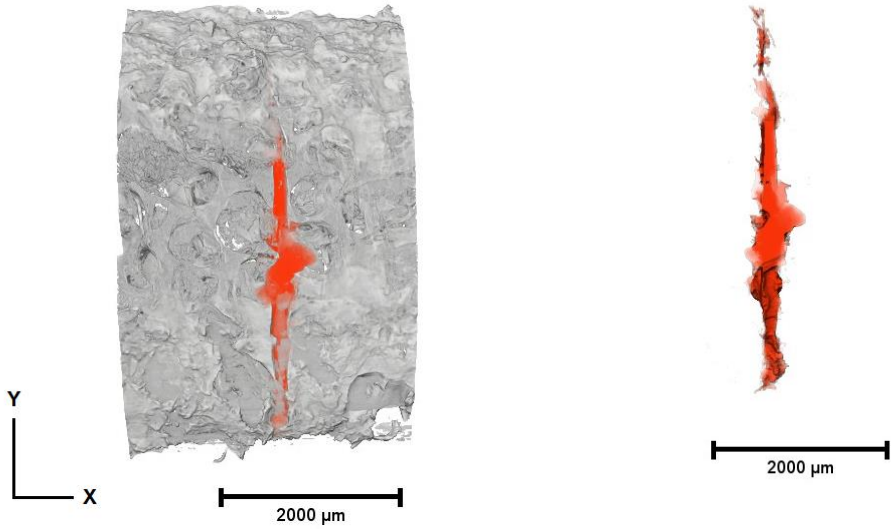
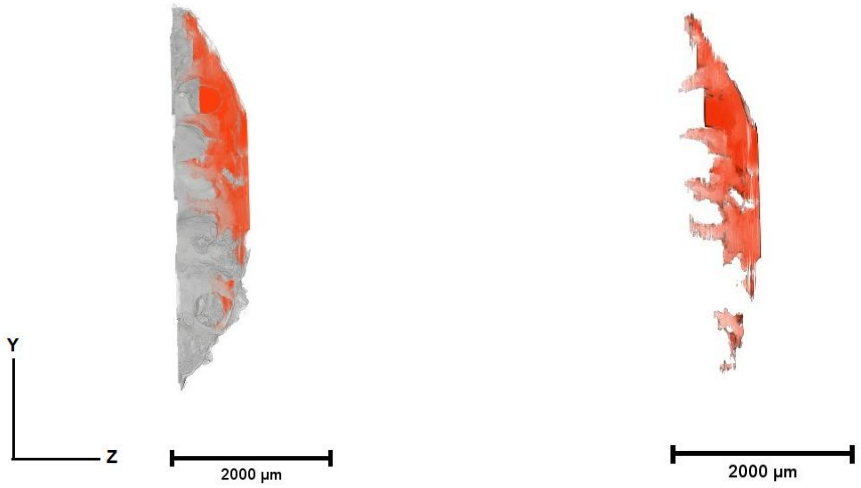


Figure 6.2.5. Intensity and gradient maps from Avizo User's Guide [235].



(a)



(b)

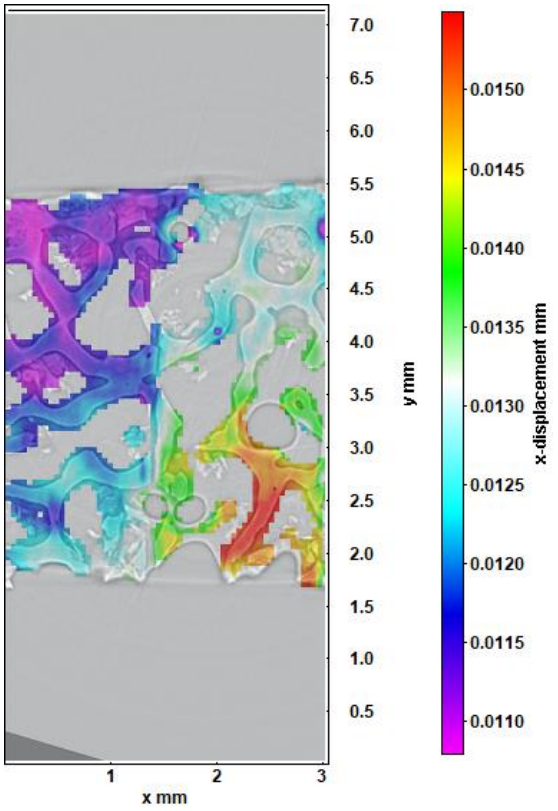
Figure 6.2.6. The segmented crack of trabecular bone under a load of 35N using Avizo. (a) Front view of notch plus potential crack with or without grey-level tomograph. (b) Side view of notch plus crack which grows in z direction with or without grey-level tomograph.

6.2.2 Crack segmentation (DVC)

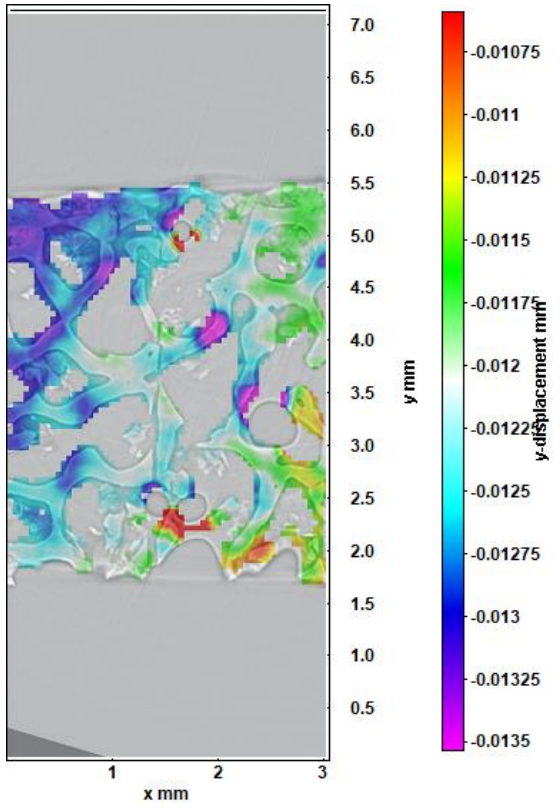
The second method for the crack segmentation used the maximum normal strain mappings from a DVC analysis. The DVC analysis used LaVision DaVis (version 8.4.0) using the FFT algorithm with a 64^3 subset with 75% overlap applied to the cropped data (*Figure 6.2.1*(a)). The resultant DVC data are shown in *Figure 6.2.7* and Appendix (*Figure 10.3.1*) for the displacement fields, and the maximum normal strains calculated from this, under different loads. A clear crack is observed with increasing loading, but at low loads (e.g. 10 N and 15 N), no obvious strain was observed in the notch region. However, at higher loads (e.g. 35N), large strains which follow the shape of notch and possible cracks are observed in the region where notch and surrounding pores lie (*Figure 6.2.7*).

By visualising the maximum normal strain data, the notch plus crack developed under different loadings can be observed (*Figure 6.2.8*). The maximum normal strain information were exported from DVC software, and then imported into Avizo and volume rendering was employed for the 3D visualization of strain map. However, the notch plus crack remains difficult to segment because of the influence of the comparable strains around pores at low loads. This is seen in the strain maps of *Figure 6.2.7* (a).

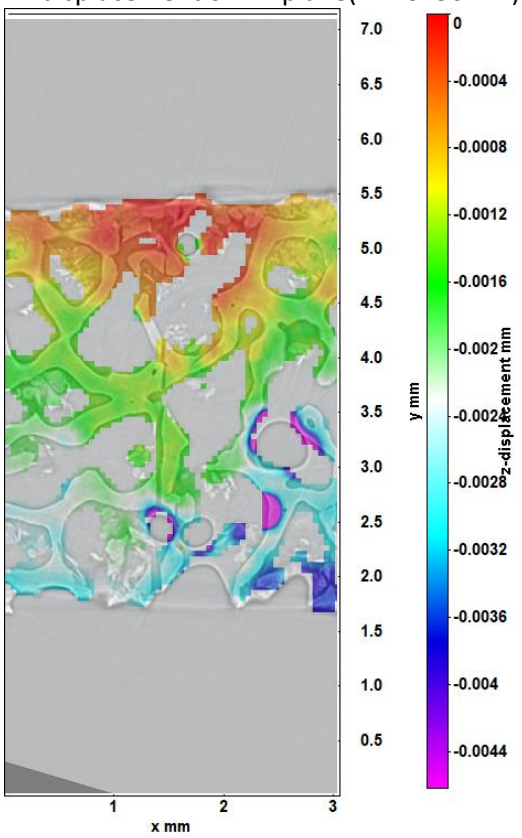
As it is shown in *Figure 6.2.8* (b), the notch extend in y direction and the crack growth in z direction with a complicated crack front under increasing loading. In addition, the notch gradually opens in x direction as it is shown in *Figure 6.2.8* (c). This method strongly depends on the quality of DVC results and requires manual adjustment of the strain range in order to avoid the unwanted strain features resulting from pores.



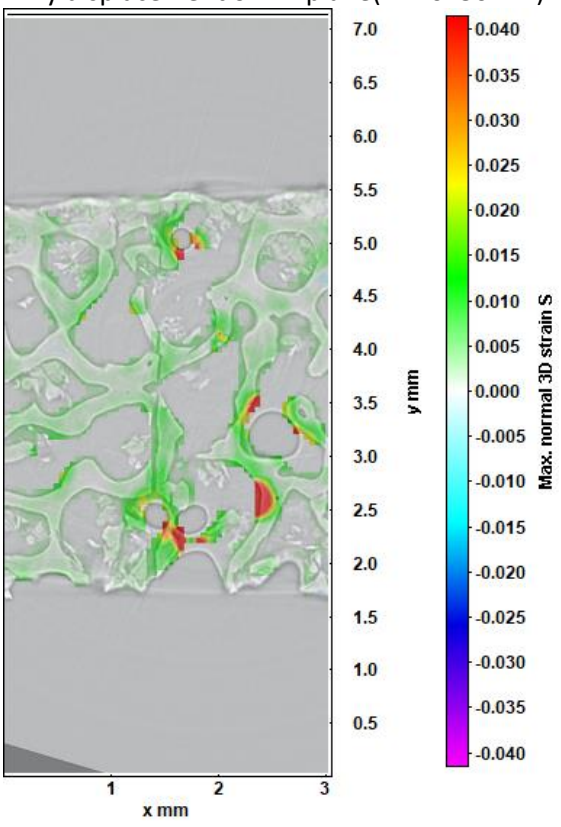
I. x displacement on XY plane(z=2.0736mm)



II. y displacement on XY plane(z=2.0736mm)

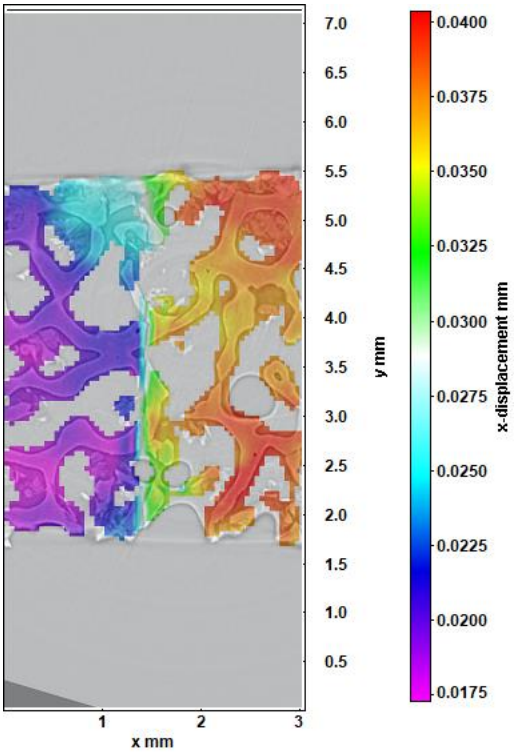


III. z displacement on XY plane(z=2.0736mm)

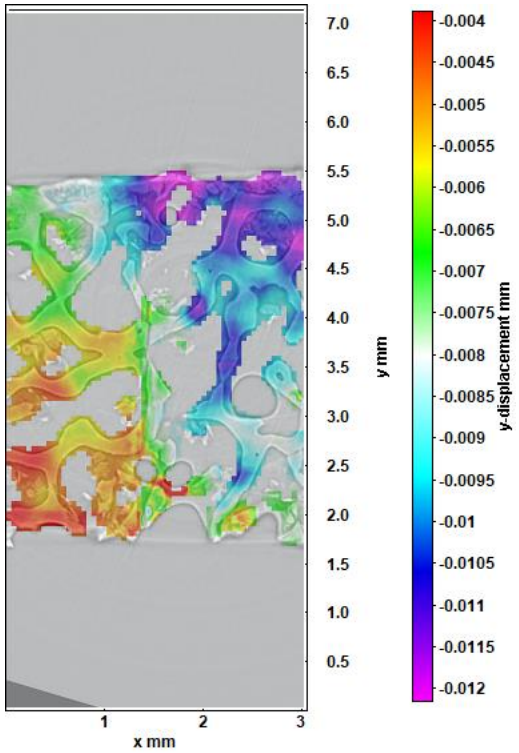


IV. max normal strain on XY plane(z=2.0736mm)

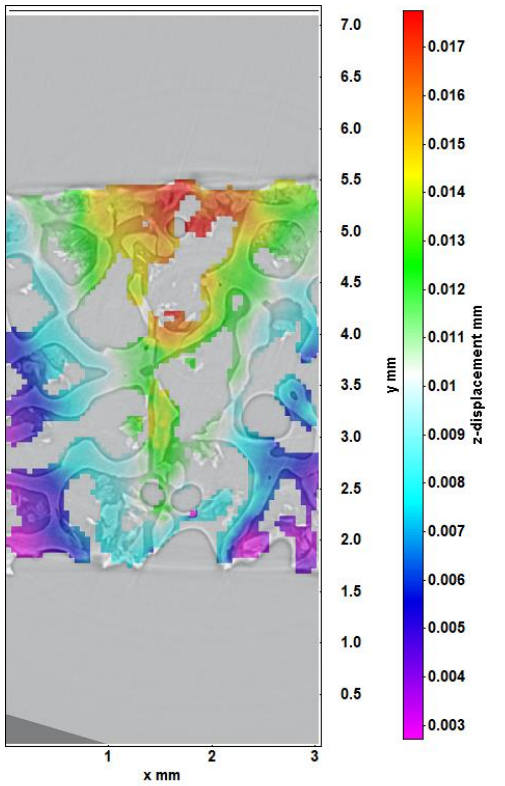
(a) 5N vs 10N



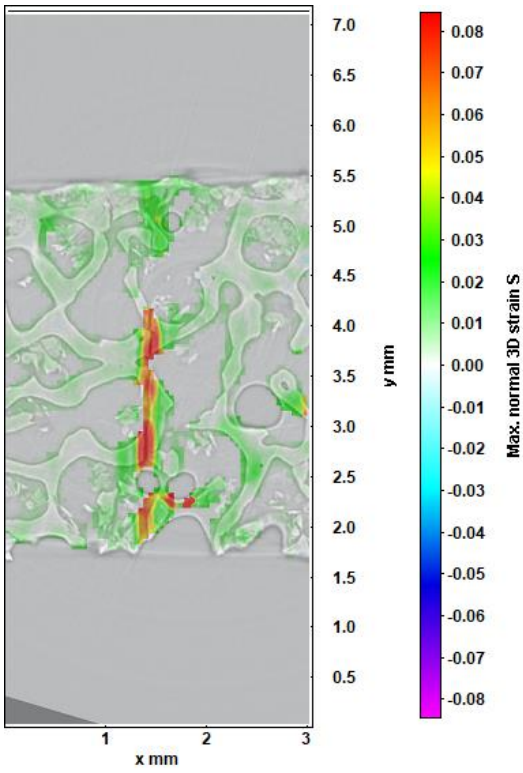
I. x displacement on XY plane(z=2.0736mm)



II. y displacement on XY plane(z=2.0736mm)



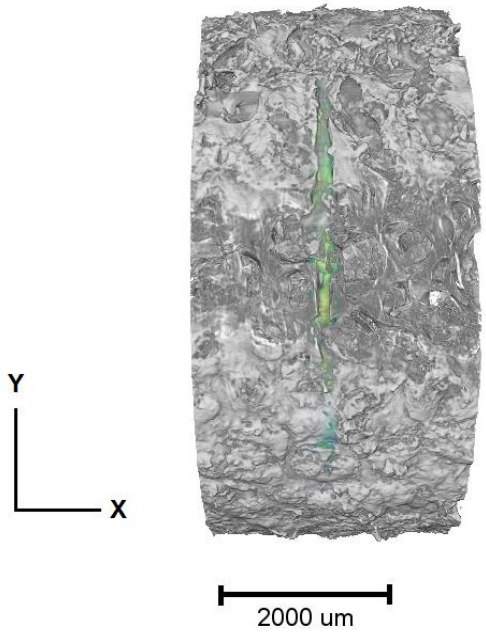
III. z displacement on XY plane(z=2.0736mm)



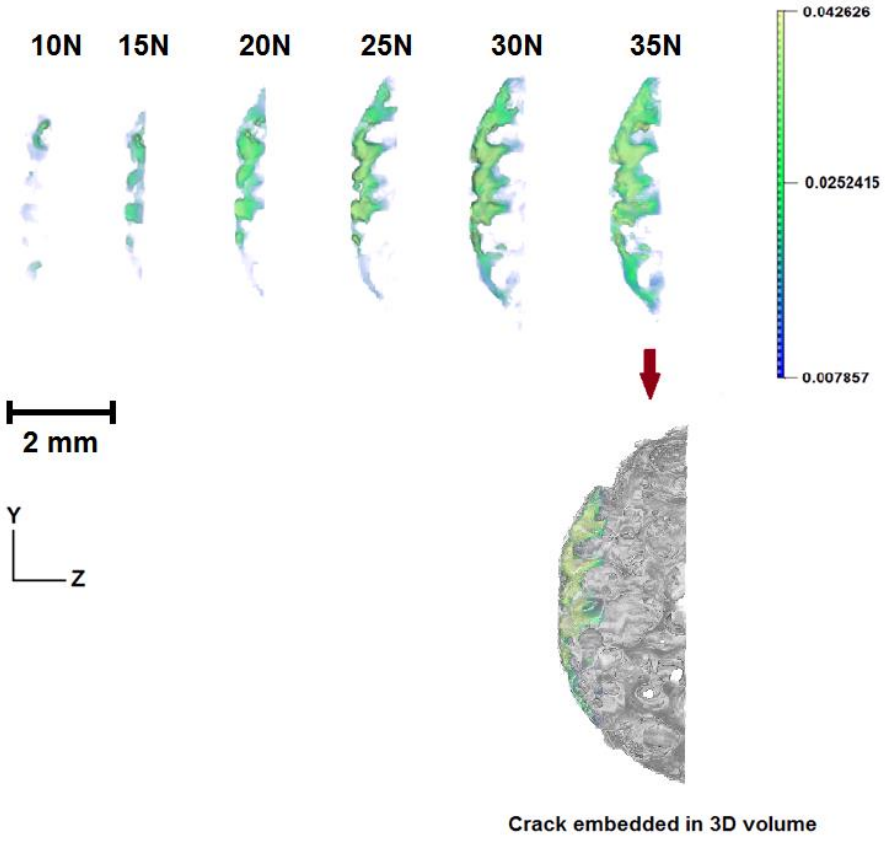
IV. max normal strain on XY plane(z=2.0736mm)

(a) 5N vs 35N

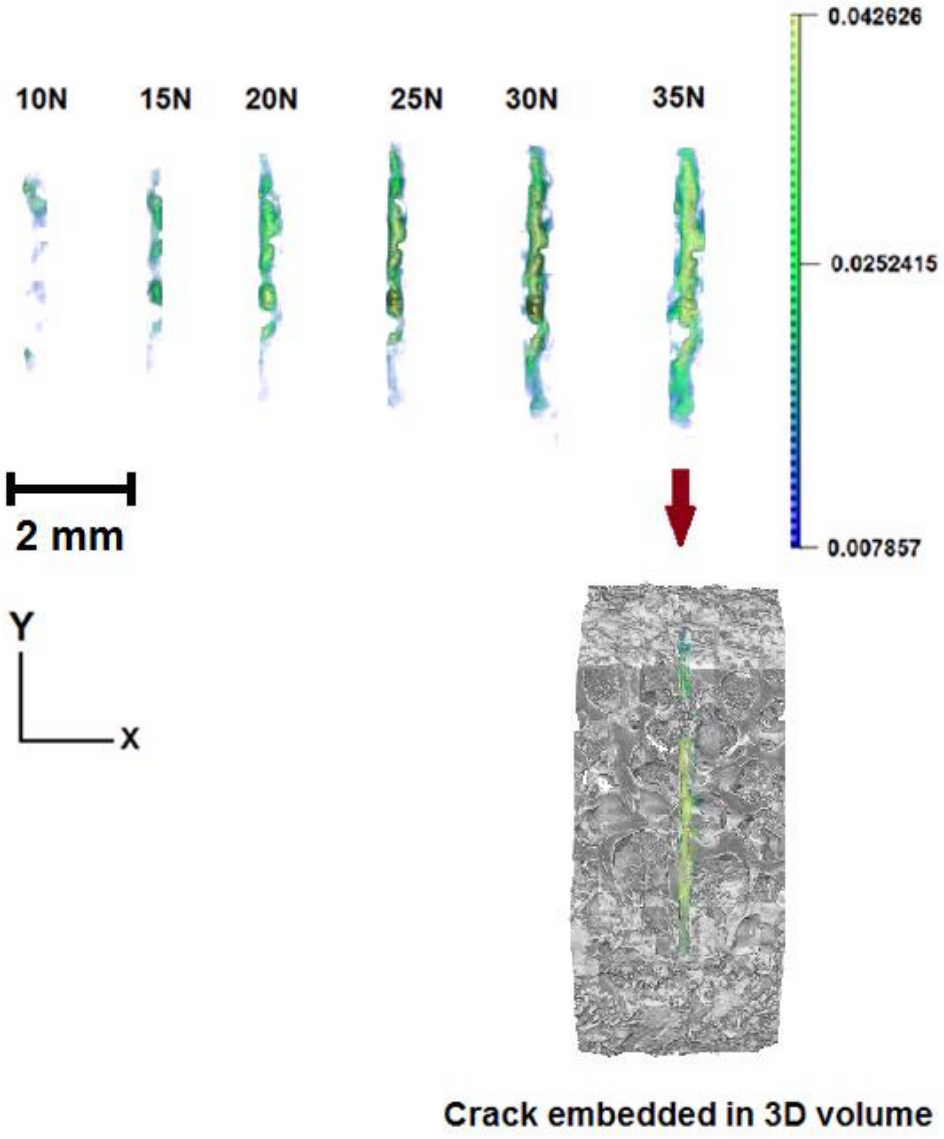
Figure 6.2.7. DVC results of displacement fields and max normal strains on XY plane (z=2.0736mm) (a) under 10N; (b) under 35N.


Y
X
2000 um

(a)


10N
15N
20N
25N
30N
35N
0.042626
0.0252415
0.007857
2 mm
Y
Z
Crack embedded in 3D volume

(b)



(c)

Figure 6.2.8. Crack segmentation based max.normal strain mapping obtained from DVC analysis. (a) 3D volume of crack embedded with bone sample; (b) side view of the development of crack with increasing load in a 5N interval; (c) front view of the development of crack with increasing load in a 5N interval .

6.2.3 Crack segmentation (phase congruency)

The third way for crack segmentation is based on the code provided by Dr. A Cinar [236], using a 3D edge detection algorithm that employs phase congruency. Phase congruency is a method for detection and quantification of cracks and crack opening based on full field displacements. It dictates points along crack or edge where maximal Fourier components in a phase with each another are present [236]. The advantage of this method is that it avoids the adjustment of

threshold value and removed the user interaction. However, its resolution is influenced by the size of subvolume used in DVC analysis [236]. The author takes no credit for the code.

As it is shown in *Figure 6.2.7*, DVC data shows that the crack opening is in x direction based on original coordinate directions of raw data (*Figure 6.1.4* (a)). To use the 3D phase congruency code, the original raw data needs to be resliced to ensure the crack opening is in the z direction (the resliced data with updated coordinate directions is shown in *Figure 6.2.9*). DVC analysis, which was prepared for 3D phase congruency, has been made based on resliced data using the FFT algorithm in a 64^3 subvolume with 75% overlap. The obtained DVC displacement fields of ux, uy and uz are the lack of DVC data (recorded as zero) in areas such as pores and background (*Figure 6.2.10* (a)). Before importing into 3D phase congruency code, DVC data was post-processed with removal of rigid body movement and rotation correction. By using 3D phase congruency code, these zero values in DVC data were first converted into NaN (in Matlab) and then replaced by interpolated values via a linear least squares approach based on known values (non-NaN data points) (*Figure 6.2.10* (b)). After that, an outlier removal method was employed in order to remove noises from images and at the same time keep the edge of notch plus crack. During this process, thresholding for removing outliers was done to remove unwanted features (*Figure 6.2.10* (c)), then the data was smoothed and each data point was replaced by the median value of its surrounding 20x20 neighbourhood (Figure *6.2.10* (d)). Lankton's region-based active contour segmentation [237] was used in 3D phase congruency code to segment notch plus crack by detecting the local discontinuity of the displacement normal to the notch plus crack (*Figure 6.2.10* (e)). The filled data, which replaces the original NaN data, was removed after the detection of the edge in the final step in order to recover the original microstructure. In order to show the clear process of crack segmentation which cannot be observed on XY plane (*Figure 6.2.9*), the whole procedure is demonstrated in *Figure 6.2.10* on XZ plane. The resulting geometries of notch plus crack under different loadings on XY planes are shown in *Figure 6.2.11*.

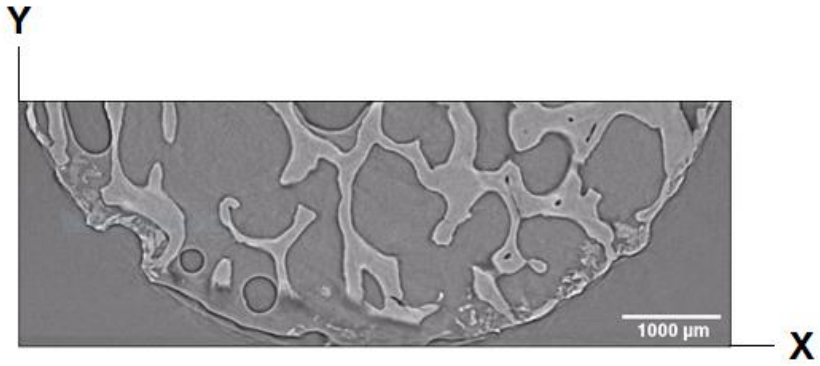


Figure 6.2.9. Resliced data for DVC analysis with crack opening in z direction.

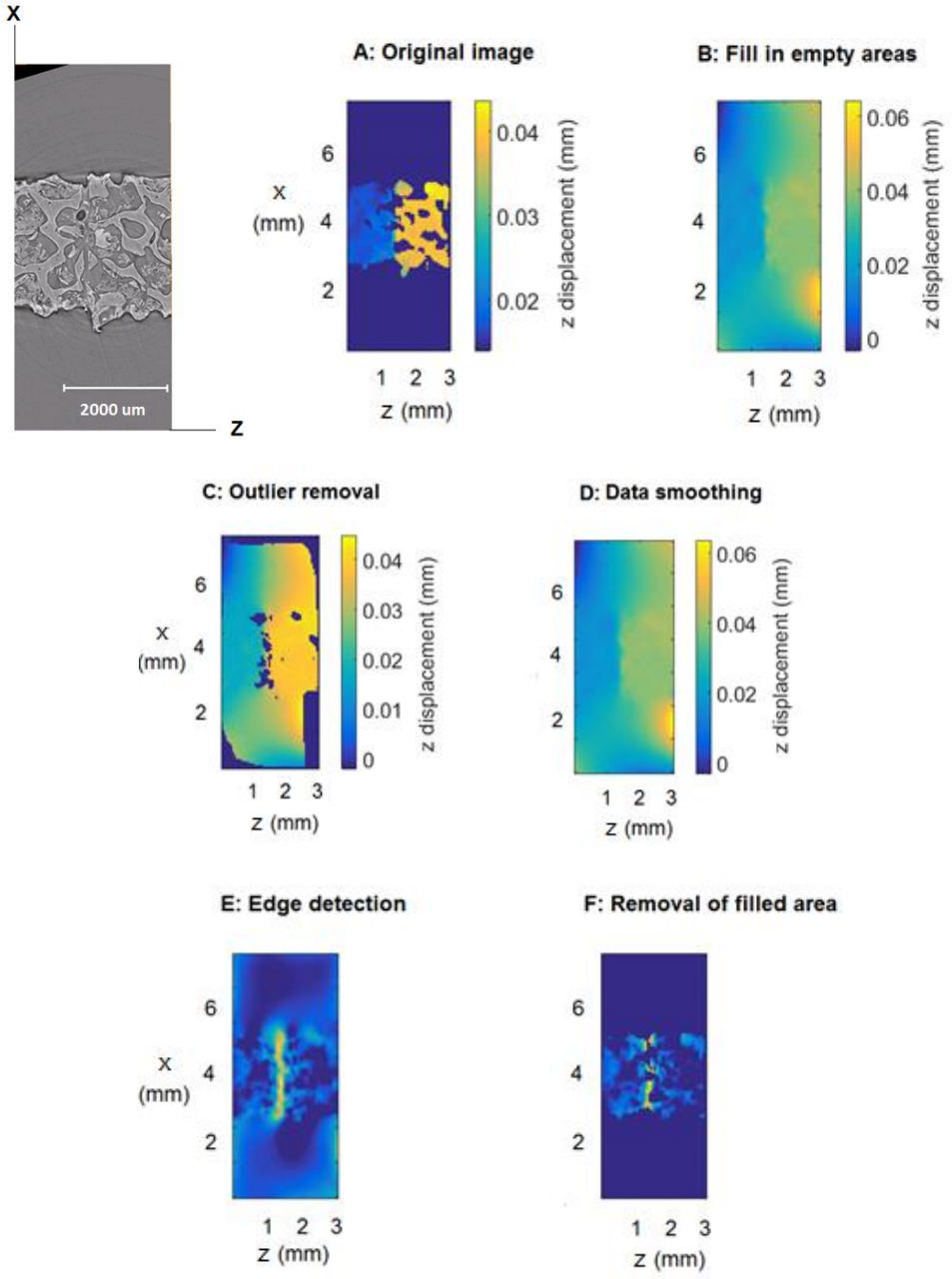


Figure 6.2.10. The procedure of crack segmentation using 3D phase congruency.

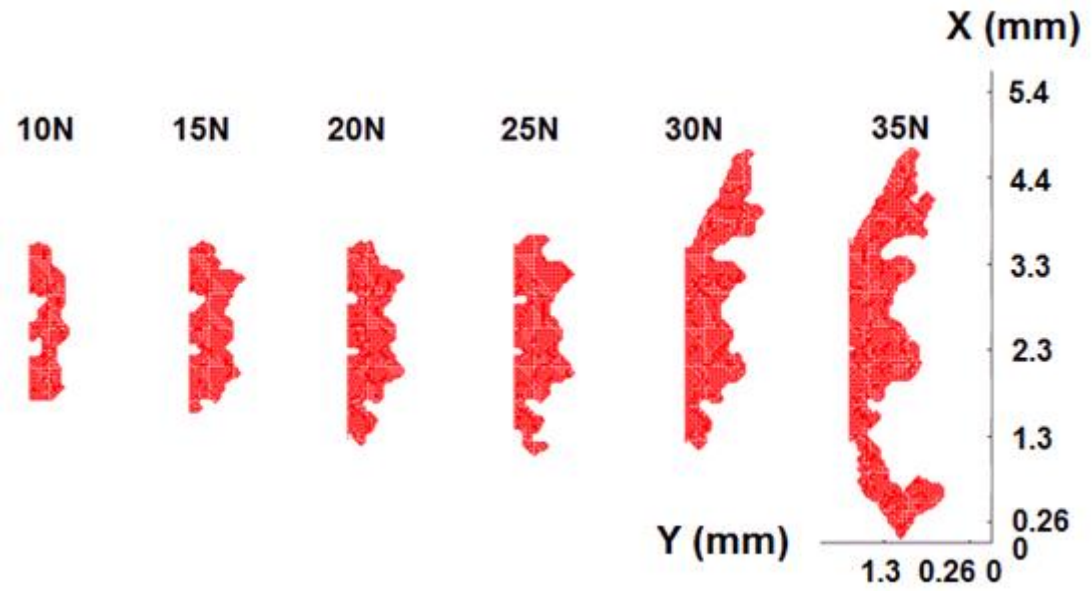


Figure 6.2.11. The development of notch plus crack (XY view) with increasing loading in 5N interval. The crack front propagates in y direction with increasing loading.

6.2.4 Development of crack length with loading

In order to investigate the development of crack length of trabecular bone under different loadings, lengths of notch plus crack segmented were measured. A simple approach has been employed to measure length of notch plus crack (difference between crack tip and crack mouth from circular surfaces). The averaged maximum length projection of notch plus crack measured at multiple Y positions on nominal YZ plane for segmentation using Avizo and strain map or at multiple X positions on nominal XY planes for segmentation using 3D Phase Congruency was considered as the notch plus crack length, which was used for the investigation of crack development with increasing loading. Detailed information of measurements of lengths of notch and crack lengths using different segmentation methods under different loadings are demonstrated in Appendix: *Section 10.3.2.* The obtained notch plus crack length under 35N based on Avizo segmentation is 0.41±0.23 mm and the obtained notch plus crack lengths under different loadings based on both DVC-strain-map segmentation and 3D phase congruency segmentation are summarized in *Table 6.2.1*.

Table 6.2.1. The notch plus crack lengths under different loadings obtained based on both DVC-strain-map segmentation and 3D phase congruency segmentation.

Load (N)	Notch plus crack length measured based on DVC-strain- map segmentation (mm)	Notch plus crack length measured based on 3D phase congruency segmentation (mm)
10	0.14±0.08	0.33±0.10
15	0.18±0.10	0.41±0.13
20	0.25±0.16	0.42±0.18
25	0.31±0.21	0.45±0.17
30	0.44±0.21	0.45±0.18
35	0.59±0.28	0.51±0.25

Shapes of segmented 3D notch plus cracks obtained from strain map and phase congruency were compared on notch opening and crack propagation planes in *Figure 6.2.12*. As it is shown in *Figure 6.2.12*, for sample under 10 N, the geometry and size of notch plus cracks obtained from strain map and phase congruency show a big difference in length, thickness and width while for sample under 35 N, a similar geometry and size of notch plus cracks were obtained by both strain map and phase congruency.

Overall, segmentation of cracks with complicated geometries using segmentation options in Avizo directly based on tomographs is not recommended because it is time consuming and dependent heavily on human factors. However, this method can still give a reasonable size estimation of notch plus crack. Both crack segmentation based on DVC max. normal strain map and 3D phase congruency code are easier for segmentation of cracks with complicated and visually ambiguous geometries. Both methods are influenced by the accuracy of DVC results. However, crack segmentation based on strain map is not accurate when the applied load is low because values of the resultant strains in crack region are close to those in other microstructural features (e.g. pores). Crack segmentations based on DVC max. normal strain and phase congruency have a high possibility in overestimation of notch opening compared with that obtained using Avizo in *Figure 6.2.12* (c). But both have improved accuracy in estimating notch plus crack lengths for sample under a higher load.

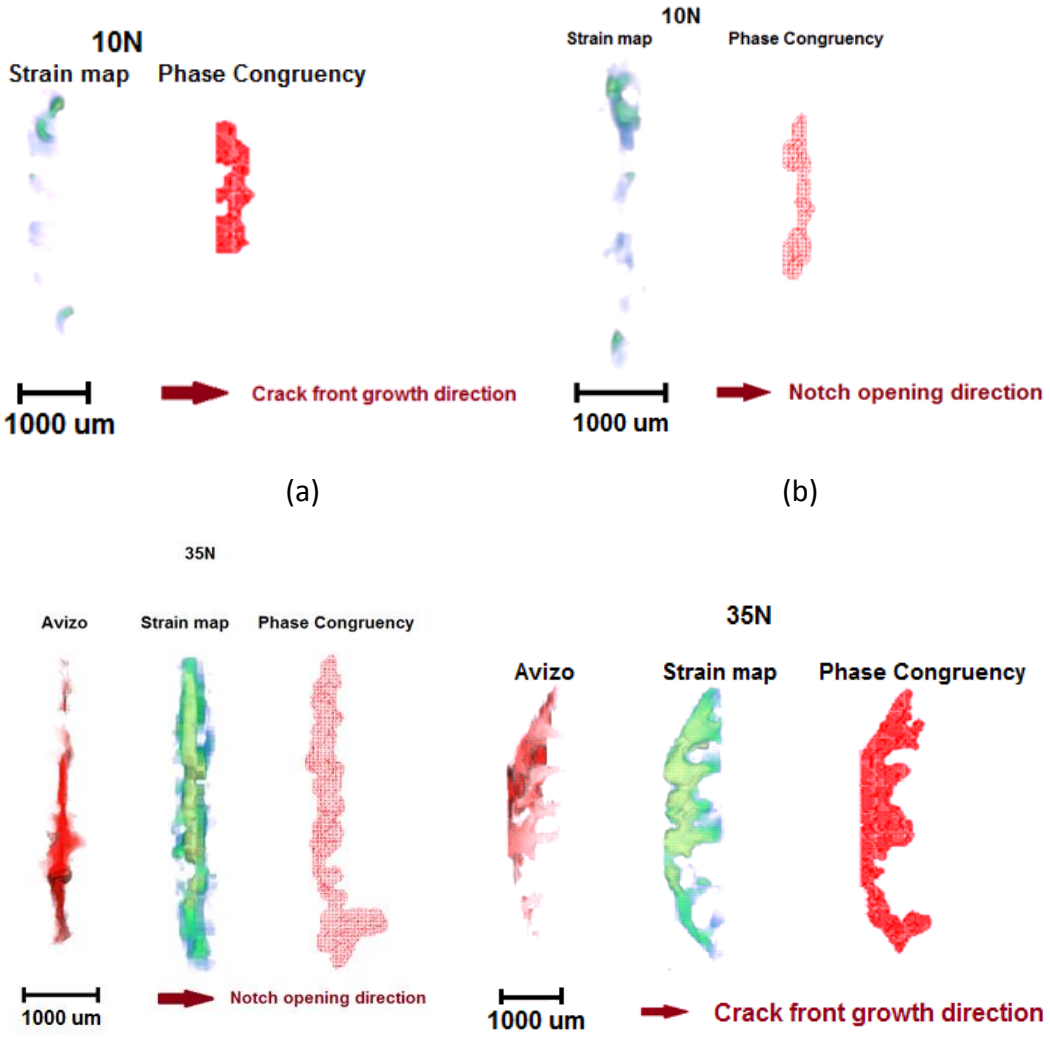


Figure 6.2.12. The comparison of notch plus crack segmented using different methods under 10N and 35 N respectively. 10N (strain map vs phase congruency): (a) crack propagation side view, (b) crack opening side view; 35N (Avzio vs strain map vs phase congruency): (c) crack propagation side view, (d) crack opening side view.

6.3 Evaluation of the J integral for a propagating crack in trabecular bone

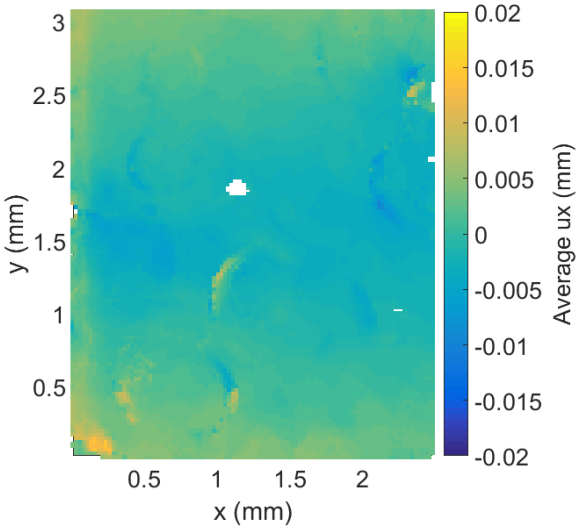
The previous section (and also appendix *section 10.3.2*) show that the three-dimensional crack shape is difficult to measure from the tomography data. It can be extracted by analysis of the displacement field, using strain or phase congruency, and this shows a general progression of the crack with an approximately straight crack front. The objective of this section of the thesis is to evaluate the strain energy release rate associated with the crack propagation, using the J-integral. The current analysis to obtain the J-integral uses a 2D model, so in the following

sections it will be shown how an effective 2D crack length is obtained, and how the 3D displacement field is sufficiently approximated as a 2D field.

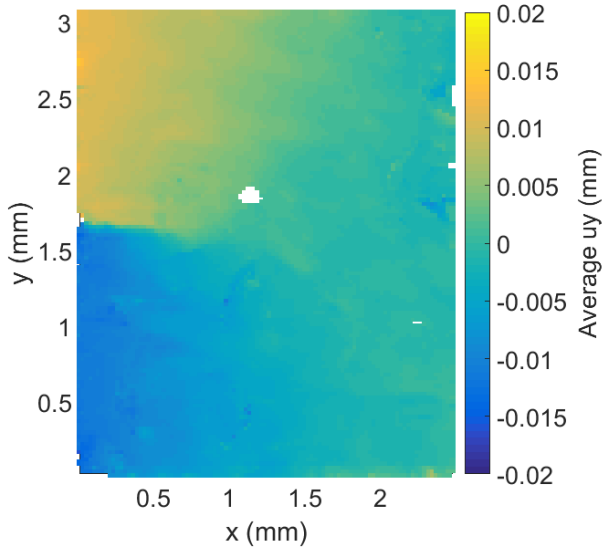
6.3.1 Pre-processing of DVC data from 3D to 2D

The tomography data were cropped around the region of crack and then rotated so crack propagation was in the x direction (original z direction), then a higher spatial resolution DVC analysis with a final subset size 32x32x32 pixel^3 with an overlap of 75% was performed (using DaVis 8.4.0) to generate a displacement field. The smaller subvolume was selected in this case rather than 64x64x64 pixel^3 in order to obtain more data points without introducing too much noise. The analysis used the Fast Fourier Transform FFT algorithm, and multiple passes were used with 2 passes with 256^3 subvolume, 2 passes with 128^3 subvolume, 2 passes with 64^3 subvolume and one pass with 32^3 subvolume. After that, data with correlation coefficient of 0.4 was discarded.

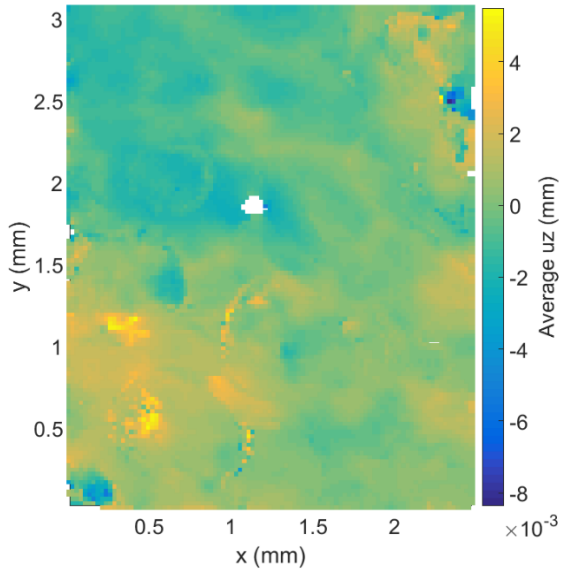
The original DVC displacement data (after rotation correction and removal of rigid body movement) contains six arrays which are x, y, z, ux, uy and uz in mm. MATLAB was used to find the same (x, y) coordinate on different xy planes in z direction and average the non-zero ux, uy and uz values for each unique (x, y) coordinate. By averaging ux, uy and uz, the majority of pore areas present in trabecular bone have been filled with average values, but some small areas are still missing data (*Figure 6.3.1*).



(a) Average x displacement



(b) Average y displacement



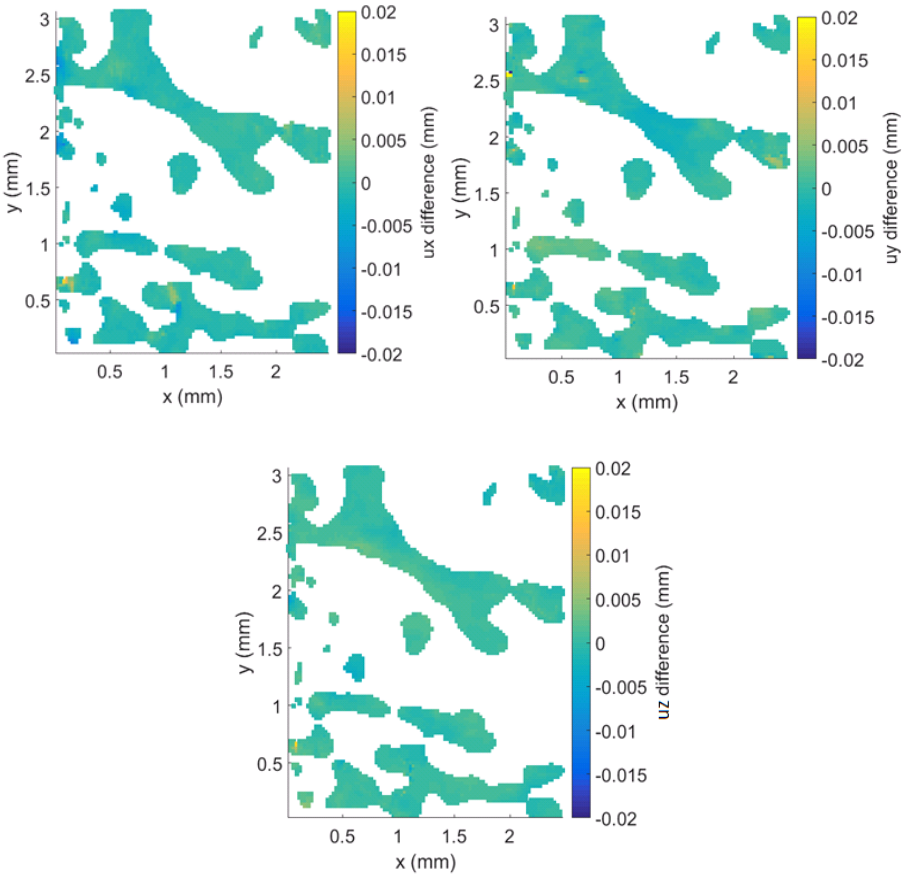
(c) Average z displacement

Figure 6.3.1.Displacement fields after averaging. A few holes with no data have been observed in the image after simple averaging of non-zero data.(a) Average ux; (b) Average uy; (c) Average uz.

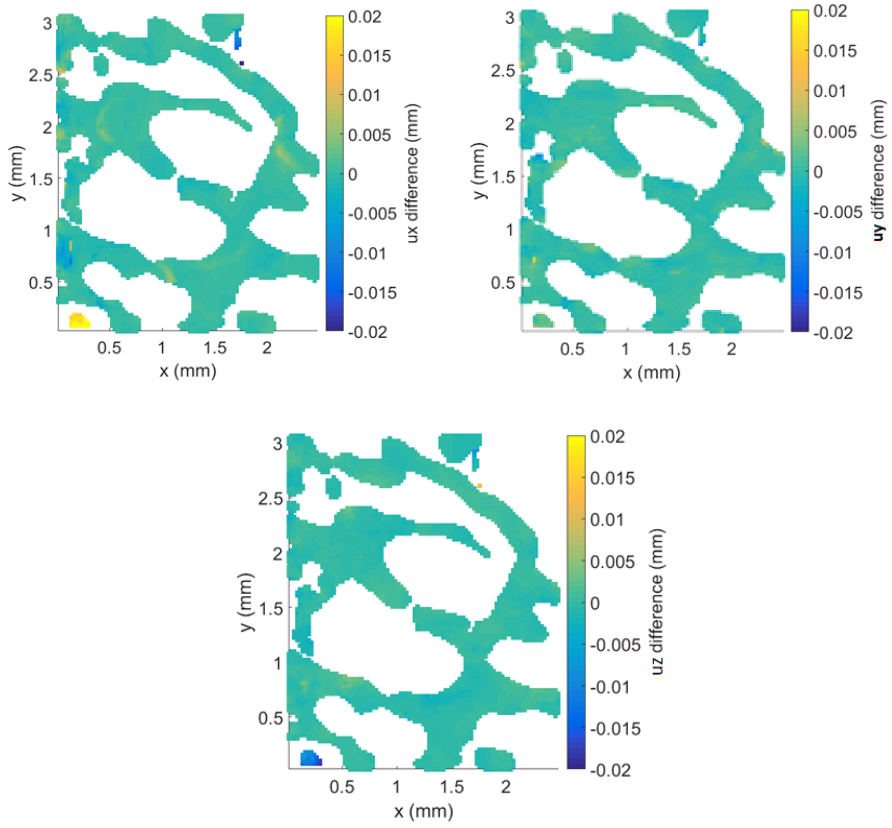
It is important to test whether the 3D deformation is adequately represented by this average 2D displacement field. The first step is to see whether there is a significant difference in x and y displacements throughout different z planes. The difference between displacement fields (ux, uy and uz) on three randomly-picked XY planes (z= 0.0128, 0.7552 and 1.3952 mm, respectively) and average ux, uy and uz (averaged z planes) are mapped in *Figure 6.3.2*. This clearly shows that differences between actual displacement fields and averaged ones are negligible compared to the magnitude of the displacements, with only a few random local variations observed. This shows the suitability of averaging the x and y displacements into one representative 2D plane for J integral calculation using JMAN code.

Further post-processing is needed to obtain 2D data that meets requirements of JMAN code: First, there should have no missing data, so the blank areas (*Figure 6.3.1*) were filled in with data interpolated via a linear least squares approach based on known values. Secondly, anomalous ux, uy and uz values were observed which are caused by edges of pores and are not good for J integral calculation. Matlab codes were applied in sequence to detect these features, remove them and smooth data using a median value of its surrounding 7x7 neighbourhood. The whole post-processing procedure is shown in *Figure 6.3.3* and the resultant 2D displacements for the bone sample at 35 N are shown in *Figure 6.3.4*.

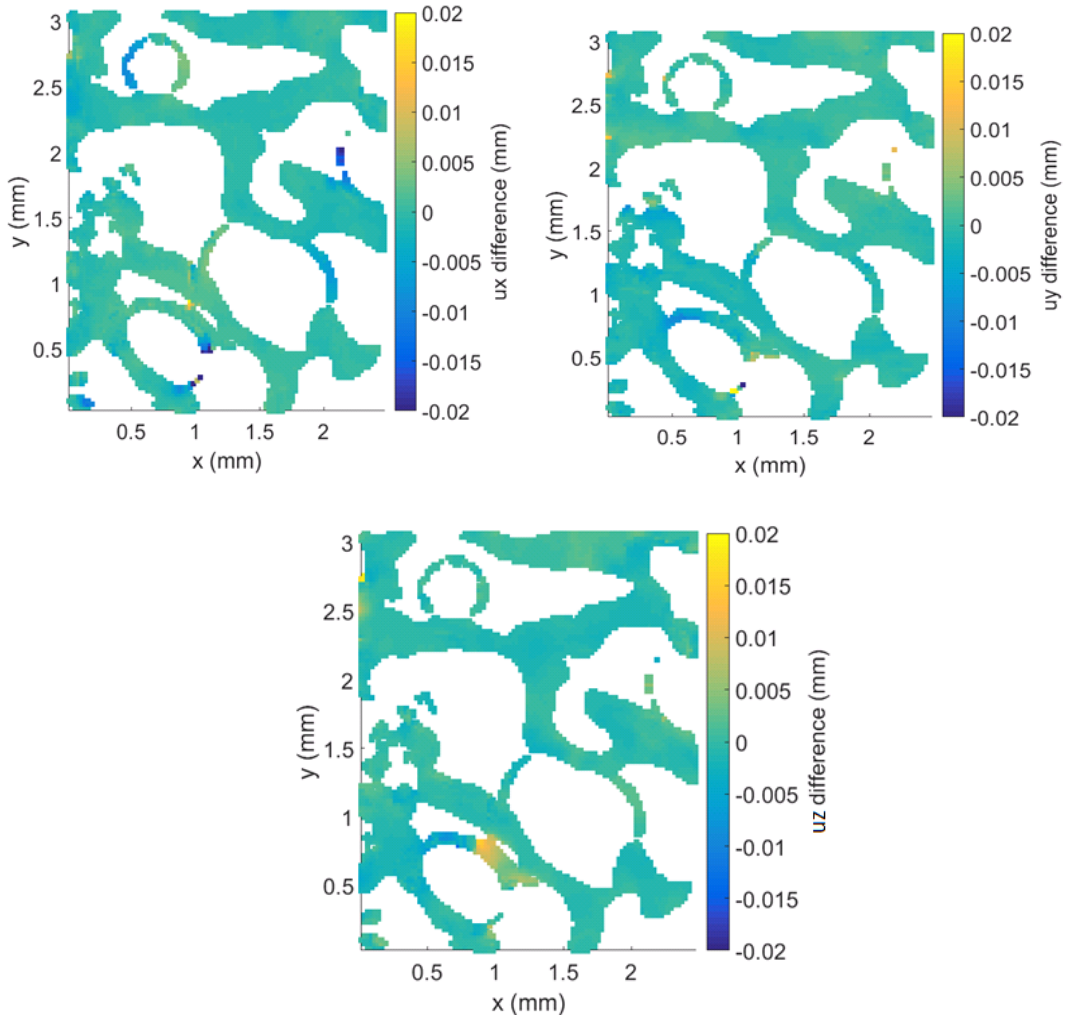
Line profiles of original and post-processed ux and uy along x=0.4992 and y = 2.5824 mm which are marked by black lines in *Figure 6.3.5* (a), are compared for the investigation of the influence of post-processing. As it is shown in *Figure 6.3.5* (b) and (c), there are no big difference in ux and uy along both lines before and after post-processing. However, post-processing results in smoother data in regions where anomalous values are present. Therefore, the data (ux and uy) after post-processing is reliable to be used for JMAN code.



(a) Z coordinate = 0.0128 mm



(b) Z coordinate =0.7552 mm



(c) Z coordinate =1.3952 mm

Figure 6.3.2. The 2D mapping of difference between x, y and z displacement on a specific XY plane and averaged x,y and z displacement on the average z plane. (a) Z =0.0128 mm; (b) Z =0.7552 mm; (c) Z =1.3952 mm.

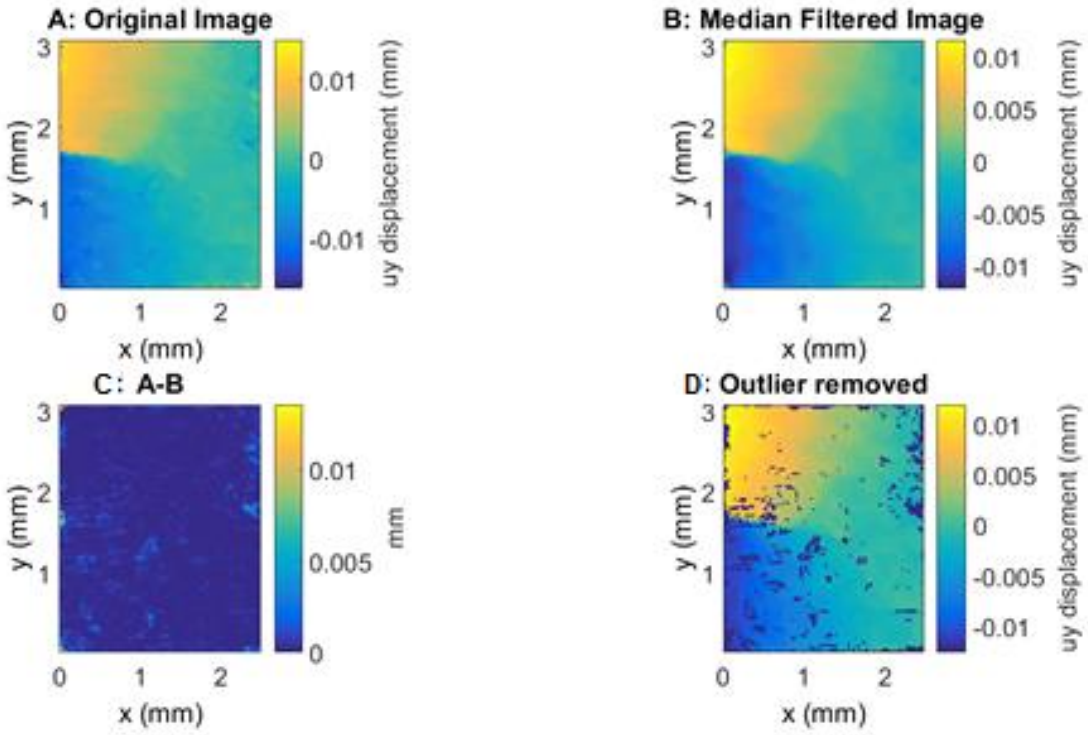
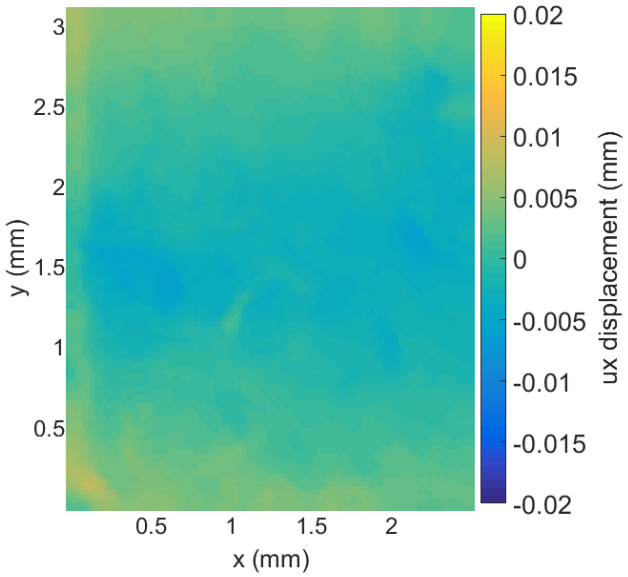
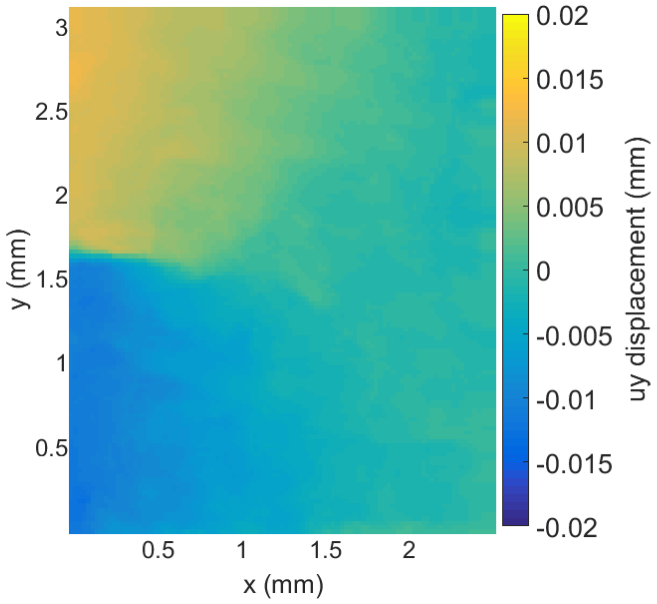


Figure 6.3.3. The process of using MATLAB to smooth data and remove unwanted features. (a) Converted y displacement field with holes filled with averaging data; (b) Data applied with Median filter. Each output pixel represents the median value of 7 x 7 neighbouring pixels around it; (c) The difference between data (a) and median-filtered data (b); (d) Features with the absolute value of difference bigger than 0.0005 are removed.

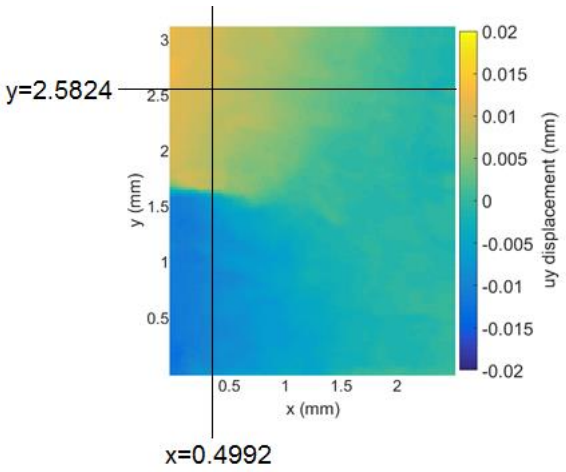


(a) Post-processed average ux.

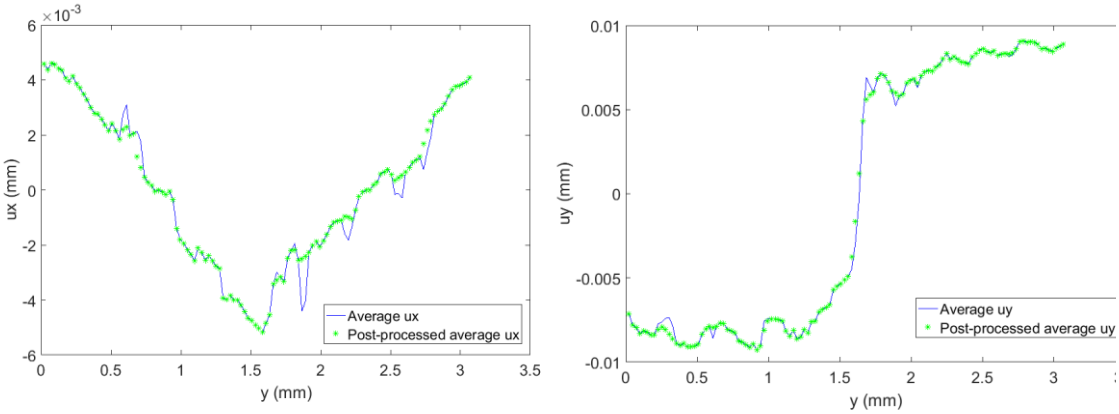


(b) Post-processed average ux.

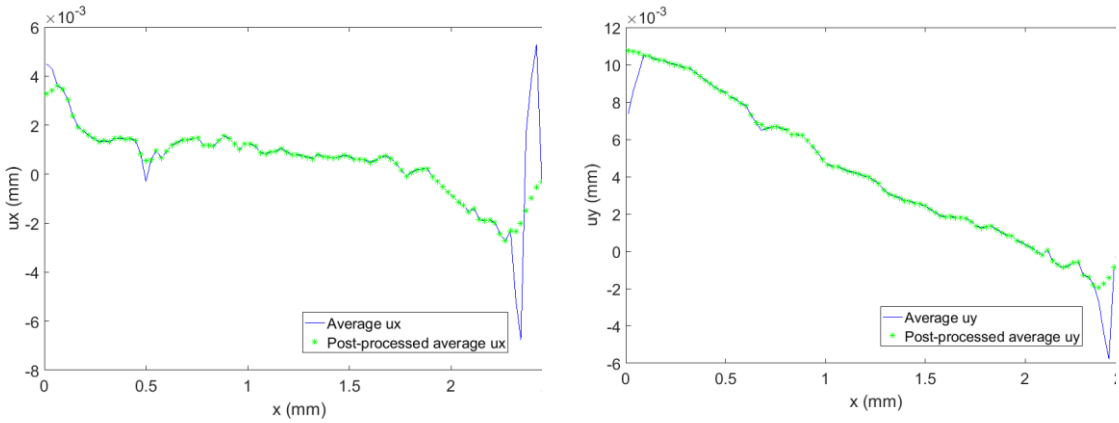
Figure 6.3.4. The resultant averaged 2D map of x and y displacement fields: (a) Post-processed ux; (b) Post-processed uy.



(a) Selected lines for line profiling.



(b) Line profile of average ux and uy along x=0.4992 mm

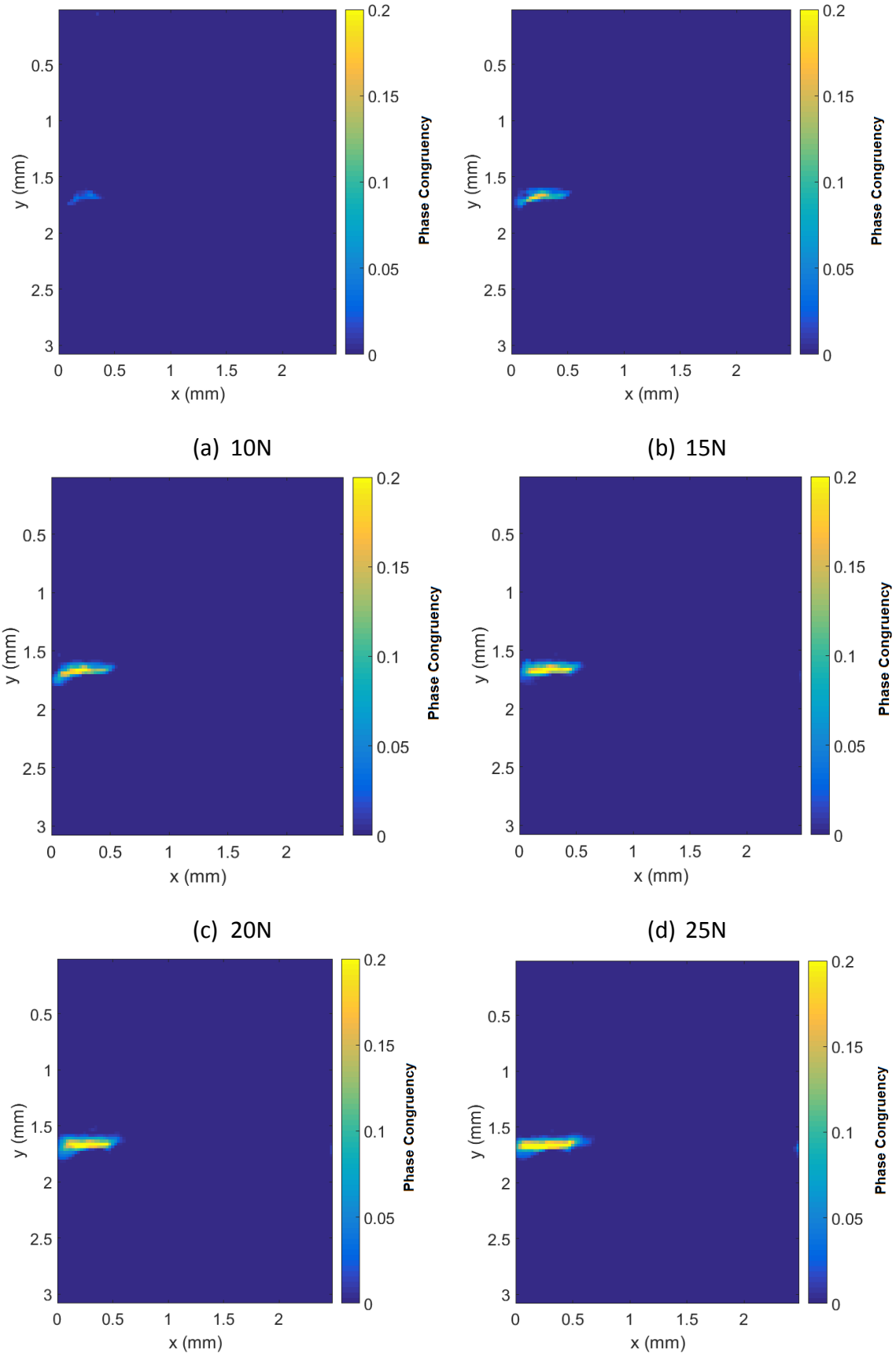


(c) Line profile of ux and uy along y=2.5824 mm

Figure 6.3.5. Comparisons between average ux and uy before and after post-processing.(a) Selected lines (x=0.4992 mm and y=2.5824 mm) for line profiles of average ux and uy; (b) Line profile of average ux, uy and post-processed ux,uy along x=0.4992 mm;(c) Line profile of average ux, uy and post-processed ux,uy along y=2.5824 mm.

6.3.2 The identification of crack tip

Before using JMAN code, it is very important to know where the crack tip is located to ensure the removal of entire crack and the accuracy of selected inner contour which must include the non-linear elastic zone at crack tip. Therefore a 2D phase congruency code written by Dr. Ahmet Cinar was used for the detection of crack. The principle of the code is similar to 3D phase congruency introduced before. A .mat file which contains post-processed average x, y and uy displacements from previous step is smoothed using a bilateral filter, which removed most of the displacement noise. After that, any edges produced by discontinuities of displacement fields are detected by an edge detector (Sobel operator). These are either due to the crack or remaining sporadic noise. The co-ordinates of the longest lines among all detected edges are found by a Hough transform and considered as the crack due to the fact that the sporadic noises will only result in short edges in the Hough map [236]. The total crack length was then found by adding the notch length to the measured crack and the obtained 2D notch plus cracks at different loads are shown in *Figure 6.3.6*. The data also provided the location of the crack and crack tip, which is needed to position the inner contour for the J integral calculation.



(a) 10N (b) 15N

(c) 20N (d) 25N

(e) 30N (f) 35N

Figure 6.3.6. Crack detections at different loads.(a) 10N; (b) 15N; (c) 20N; (d) 25N;(e) 30N;(f) 35N.

The total crack lengths (i.e. notch plus crack lengths) at different load states, measured using 2D phase congruency to identify crack tip, are summarized in *Table 6.3.1* together with calculated values of *a/w* (Notch plus crack length/Sample Thickness), which will be used for fracture toughness calculation. Because there is no sharp end of crack detected using 2D phase congruency (*Figure 6.3.6*), the uncertainty in the notch plus crack length is $\pm$ 8 pixels (0.0256mm). The result is compared with those measured using 3D geometries segmented by max. normal strain and 3D phase congruency (*Figure 6.3.7*). From *Figure 6.3.7*, notch plus crack lengths measured using 2D and 3D phase congruency show a similar trend versus load but with higher values for notch plus cracks measured from 2D method. At a load lower than 30N, the measured average length from strain map shows a big difference in average values from 2D and 3D phase congruency.

Table 6.3.1. Measured notch plus crack lengths in 2D under different loadings.

Load (N)	Averaged notch plus crack length measured based on 2D data (mm)	Notch plus crack length/Sample Thickness (3.5 mm)
10	0.3712$\pm$0.0256	0.106$\pm$0.007
15	0.4992$\pm$0.0256	0.143$\pm$0.007
20	0.5248$\pm$0.0256	0.150$\pm$0.007
25	0.5504$\pm$0.0256	0.157$\pm$0.007
30	0.5760$\pm$0.0256	0.165$\pm$0.007
35	0.6528$\pm$0.0256	0.187$\pm$0.007

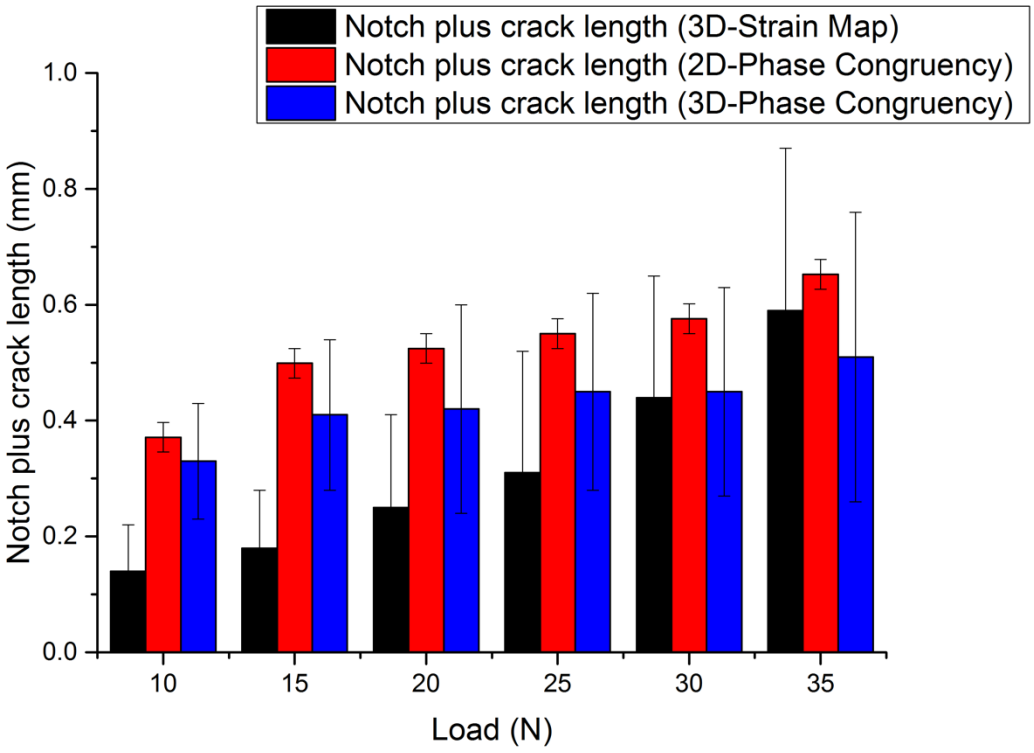


Figure 6.3.7. Comparisons of notch plus crack length vs load curves obtained from different methods.

6.3.3 The calculation of J integral

Having determined the average 2D displacement field and the position of the crack tip, the JMAN code was then applied for J integral calculation. The displacements provide the strain field, so values of Poisson's ratio and Young's modulus are required for the calculation of the stress field and eventually the J integral. Poisson's ratio is considered to be 0.3, which is a common value assumed for trabecular bone in literatures [238] [239] [240]. The elastic modulus data were provided by Dr. Shaocheng, Ma, and have an average of 0.26 GPa [92]. This modulus value was derived from a similar stress-strain curve of trabecular bone under tensile testing shown in *Figure 6.3.8*. After importing displacement field and material's properties, the JMAN code meshes the imported data into 11210 regular square grids, the centres of which are represented by the measured displacements, for finite element analysis. The whole crack is masked out manually, and an outer contour and an inner contour are manually selected. The

inside area of the inner contour contains the crack tip. The whole procedure is schematically demonstrated in *Figure 6.3.9*. The J integral calculation is based on *Equation 6.3.1* [241]:

$$J = \int_{A1}(\sigma_{ij}\frac{\partial u_i}{\partial x_i} - \overline{w}\delta_{1j})\frac{\partial q_1}{\partial x_j}dA \qquad \textit{Equation 6.3.1}$$

Where *A1* is the area between the inner and outer contours; *u* is the displacement field; δ is the Kronecker delta; *q* is a function that with the assumption that data points on the outer contour is fixed, a unit translation is imposed to the data points on the inner contour in the direction of *x1*, the crack propagation direction; $\overline{w}$ is described as *Equation 6.3.2* as the strain energy density [241]:

$$\overline{w} = \int_0^{\varepsilon_{ij}} \sigma_{ij} d_{\varepsilon_{ij}} \qquad \textit{Equation 6.3.2}$$

Equation 6.3.3 is used to calculate the resultant J integral in the code. *Equation 6.3.3* is established based on *Equation 6.3.1*. In this step, the *A1* area has been divided into rings of elements and a FE model has been created to calculate the sum of the J integral of each element [241].

$$J = \sum_{Elements\ in\ A1}\sum_{p=1}^{GP}[(\sigma_{ij}\frac{\partial u_i}{\partial x_1} - \overline{w}\delta_{1j}) \times \frac{\partial q_1}{\partial x_1} det(\frac{\partial x_k}{\partial \eta_k})]_p\ wp \qquad \textit{Equation 6.3.3}$$

where *p* presents integration points, *GP* is the total number of integration points per element, *η* is the local coordinate, *wp* is the weight related to each Gaussian integration point *p* to *GP* [241].

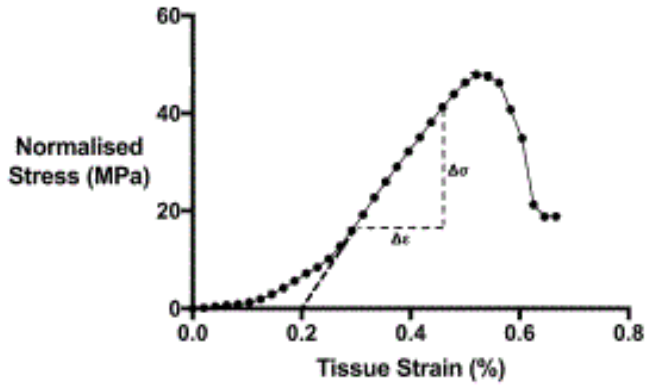


Figure 6.3.8. Stress-strain curve of trabecular bone under tension. Young's modulus was calculated using the gradient of the linear section of the curve [92].

The use of multiple contours is recommended for the calculation of J integral. With the inner contour fixed, the outer contour changes from inner contour plus one element outwards to the selected outer contour and the sum of J integral of each element within the area *A1,* which changes with increasing outer contour, has been calculated by the code using the element-based virtual crack extension formulation [242]. Theoretically, the value of J integral will reach a plateau of constant value, which is the J integral that is evaluated. The calculation assumed plane-strain condition, as the 2D dataset has been shown to be constant across the sample width and there is no significant strain in the z direction.

The masked region of the whole crack, together with the chosen inner and outer contours, are illustrated in *Figure 6.3.10*. Plots of calculated J integral of each changing outer contour (from inner contour plus one element outwards to the selected outer contour) for each load are also shown in *Figure 6.3.11*. Variable results are obtained for the contours near to the masked region, as these are more affected by data noise in the displacement field. However, the J-integral value does generally tend to a constant value with increasing contour number. The influence of contour selection on J integral calculation, which is minor, has been discussed in Appendix *Section 10.3.3.2*.

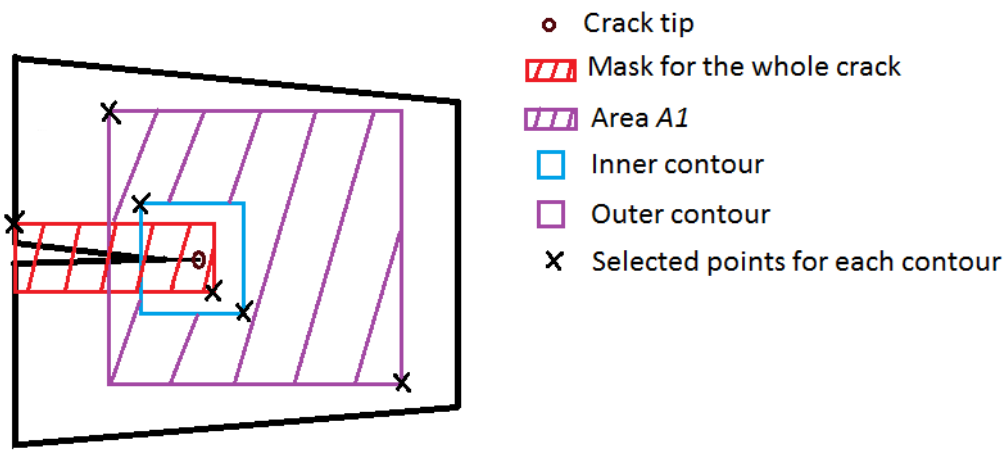
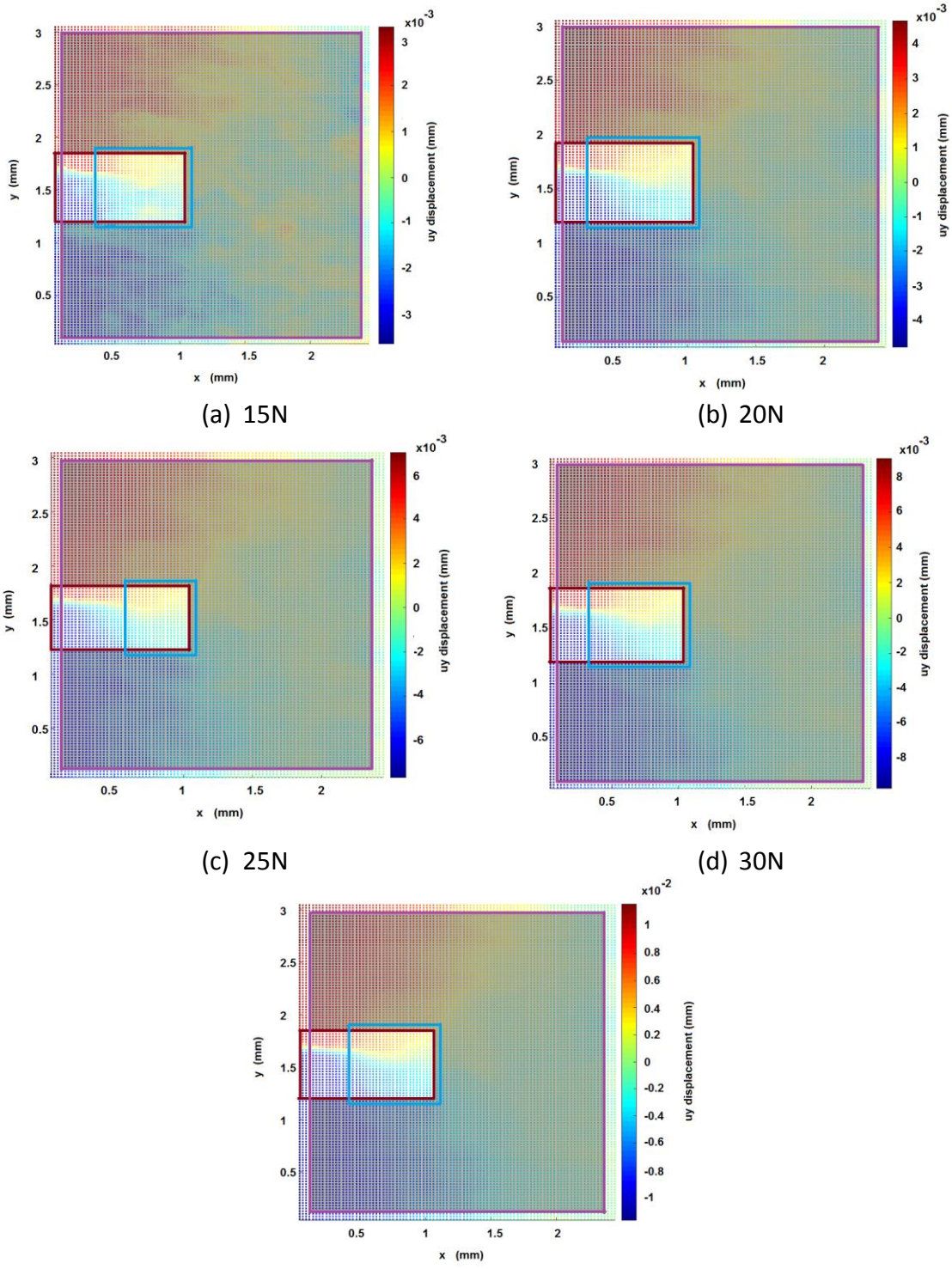


Figure 6.3.9. The procedure to select the mask of the crack and inner and outer contour for J integral calculation in JMAN code.



(a) 15N (b) 20N

(c) 25N (d) 30N

(e) 35N

Figure 6.3.10. Mask region and selected contours for JMAN calculation (Red rectangular: mask-out region of the whole crack; blue rectangular: inner contour; purple rectangular: outer contour): (a) 15N; (b) 20N; (c) 25N; (d) 30N; (e) 35N.

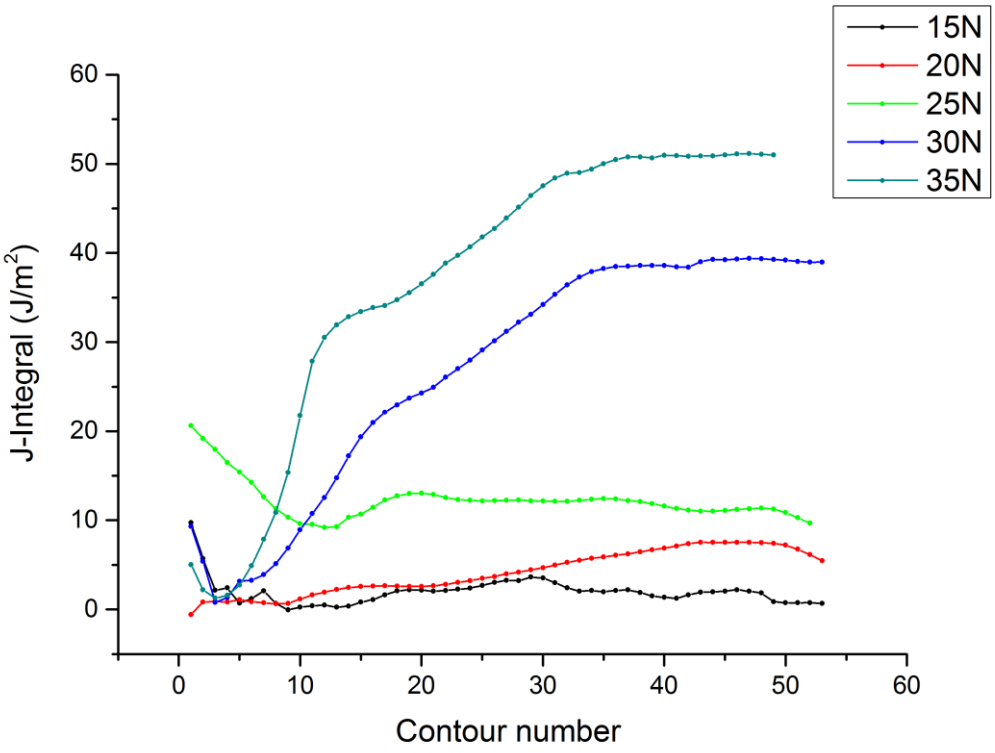


Figure 6.3.11. The resultant plot for J-integral vs contour number at different bending loads.

6.3.4 The relation between J integral and applied load

J integral in each case was evaluated using the plateau (details in Appendix: *Section 10.3.3*), with the uncertainty represented by the standard deviation in this region (typically over the last 10 contours). The obtained values are summarized in *Table 6.3.2*, and are plotted against load in *Figure 6.3.12*. This shows that the evaluated J integral increases with load, in a non-linear manner. Because the JMAN code is sensitive to signal to noise ratio [108], the J-integral could not be calculated at 10 N.

Table 6.3.2. The results of calculated J integral of trabecular bone from JMAN code.

Load/N	J integral/(J/m^2)
15	1.81±0.89
20	7.11±0.62
25	12.01±0.58
30	38.84±0.43
35	50.92±0.14

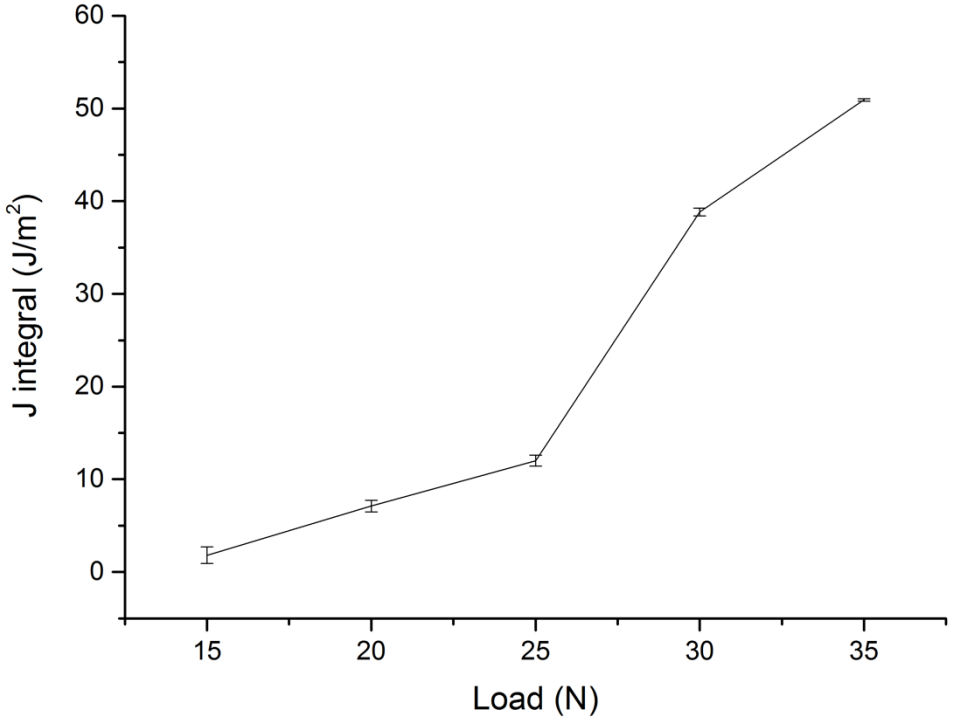


Figure 6.3.12. J integral versus load curve.

6.3.5 The stress intensity factor of trabecular bone

From the J integral, the applied stress intensity factor *K* can be calculated using *Equation 2.2.4* where $E=E/(1-\nu^2)$ for plane-strain state. The data are summarized in *Table 6.3.3* and plotted in *Figure 6.3.13*. An almost-linear relation between *K* and load is observed, with a linear fitting line of *K* = -0.029(±0.036) + 0.0043(±0.001) x load.

Table 6.3.3. Calculated K as a function of load.

Load/N	K (MPa m$^{1/2}$)
15	0.023±0.0056
20	0.045±0.0020
25	0.059±0.0014
30	0.11±0.0006
35	0.12±0.0002

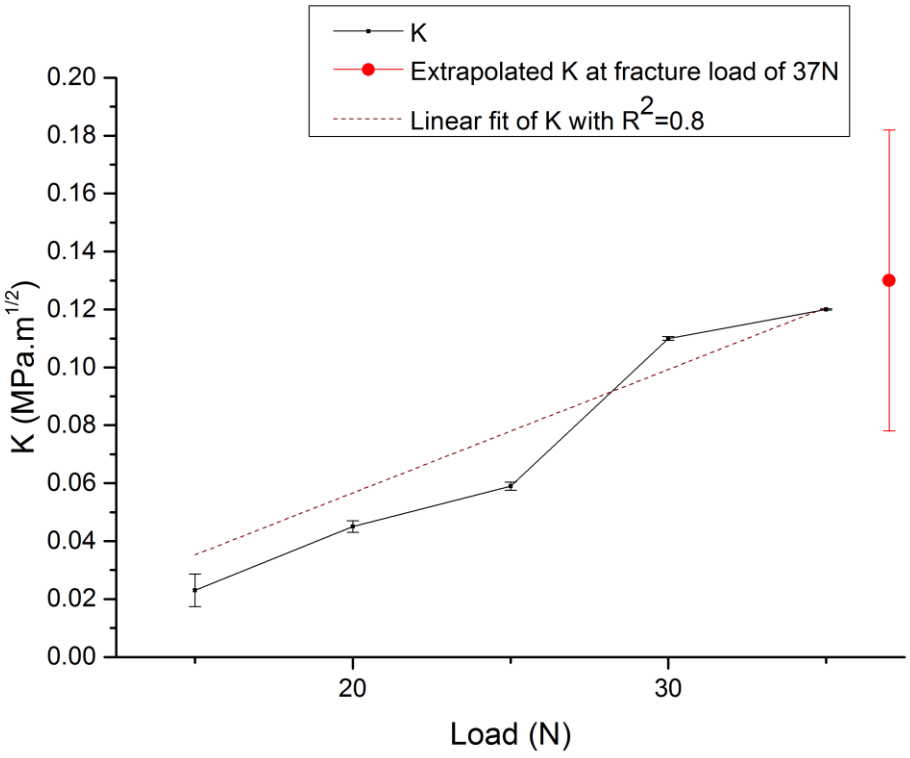


Figure 6.3.13. K vs load and the extrapolated K at fracture load of 37N marked in red dot.

6.4 Discussion

To authors' knowledge, no literature has reported J integral of trabecular bone and only values for cortical bone have been reported [98] [93]. These data have big variations among individual samples and testing methods (*Table 2.2.4*) [93,97,98,101]. Therefore, the reasonable estimation of J integral of trabecular bone using JMAN approach provides additional knowledge to bone study.

In addition, by using the evaluated J-integral to calculate the stress intensity factor, a linear relationship is found between stress intensity factor and load. This is consistent with fracture mechanics (e.g. for the loading of a single edge notch beam specimen with constant crack length). Prior to fracture, the crack length did not change significantly relative to the sample thickness with increasing load, so it is reasonable to extrapolate the trend to the failure load to estimate the stress intensity factor at unstable fracture, which is 0.13 ± 0.052 MPa $m^{1/2}$ (marked in red dot in *Figure 6.3.13*).

Values of fracture toughness of cortical bones have been reported in literature [93] [97] [98] [101] and are much higher than the obtained value of trabecular bone in this study, which can be the result of less porosity in cortical bone and thus less strain concentration sites, leading to fracture. However, literature about stress intensity factor of trabecular bone is limited. Only one literature [102] reports the relation between stress intensity factor of trabecular bone (*Figure 2.2.6*) and apparent bone density. Together with the reported relation between compression/tension elastic modulus of trabecular bone and its apparent density by Keaveny et.al [243], fracture toughness of trabecular bone with the given elastic modulus can be derived. Given the approximate elastic modulus of the bone used in this study, which is 0.26 GPa, the apparent density of bone can be estimated according to the proposed linear regression [243], $E_{app} = 8420\rho_{app} - 2430$, where E_{app} is the apparent elastic modulus of trabecular bone in a unit of MPa while ρ_{app} is the apparent density in the unit of g/cm^3. The obtained apparent density of the specimen with elastic modulus of 0.26 GPa is 0.32 g/cm^3. Then the stress intensity factor of trabecular bone with the apparent density of 0.32 g/cm^3 is calculated based on the proposed relation between K_{max} and ρ_{app} : $log\,(K_{max}) = -0.21 + 1.53 \times log\rho_{app}$ in literature [102] for sample cut parallel to trabecular structure under three-point bending test. K_{max} (in the unit of MPa m$^{1/2}$) is the stress intensity factor at the point where unstable crack starts to propagate [102] and it can be compared with the extrapolated *K* in this study at failure load of 37 N. ρ_{app} is the apparent density in the unit of g/cm^3 [102]. The resultant K_{max} of trabecular bone with the elastic modulus of 0.26 GPa based on relations proposed in literature, is 0.11 MPa m$^{1/2}$ which agrees well with the obtained *K* at 37 N which is 0.13 ± 0.052 MPa m$^{1/2}$ from JMAN approach.

Apart from that, although the geometry of the sample is not standardized, *Equation 6.4.1* of stress intensity factor calculation for edge crack based on simple linear elastic fracture mechanism has been applied to calculate the applied stress intensity factor of the specimen under a load of 35N:

$$K = \sigma\sqrt{\pi a}[1.122 - 0.213\left(\frac{a}{w}\right) + 10.55\left(\frac{a}{w}\right)^2 - 21.71\left(\frac{a}{w}\right)^3 + 30.382\left(\frac{a}{w}\right)^4]$$ *Equation 6.4.1*[244]

Where *a* is the crack length (0.6528 ± 0.0256 mm) at 35 N, *w* is the thickness of sample (3.5 mm), σ is bending stress calculated as following:

$$\sigma = \frac{mz}{I}$$ *Equation 6.4.2* [245]

Where *m* is the bending moment which is calculated as $\frac{PL}{4}$, where *P* is the applied load, which is 35 N and *L* is the distance between bending rollers [246], which is around 9 mm measured based on *Figure 6.1.2* (b); *z* is the distance between neutral axis to notch, which is calculated as $r - \frac{4r}{3\pi}$ and *r* is the radius of semi-circular YZ cross-section, which is 3.5 mm (*Figure 6.1.1), I* is the second momentum of area, which in this case is calculated as $\left(\frac{\pi}{8} - \frac{8}{9\pi}\right) r^4$ [247]. Therefore σ is simplified as $(\frac{18\pi-24}{9\pi^2-64})\frac{\mathrm{PL}}{\mathrm{r}^3} \approx 1.315\frac{\mathrm{PL}}{\mathrm{r}^3}$. The calculated σ is equal to 9.66 MPa and *K* is 0.59 ± 0.036 MPa $m^{1/2}$ at 35 N which is larger than the obtained *K* at 35 N based on JMAN calculation (0.11 ±0.0006 MPa $m^{1/2}$).

The possible reason to explain the difference between calculated value based on equations and from JMAN is due to the uncertainty of the input Young's modulus in JMAN code which influences the resultant *J* and thus back-calculated *K*. The elastic modulus of the analysed specimen was not measured, and hence the elastic modulus of trabecular bone used in the JMAN calculation is 0.26 GPa, which is an average value for trabecular bones with elastic moduli ranging from 0.1-0.4 GPa [92] (the author Dr. Shaocheng Ma provided tomographs of trabecular bone from another batch in this project). *J* and *K* of trabecular bones within the reported range of elastic modulus has been calculated based on JMAN approach with the input 2D displacement field at 35N. The resultant range of *J* is from 15.58-62.33 J/m^2 and thus *K* is 0.041-0.16 MPa $m^{1/2}$. Higher *K* is obtained with higher input elastic modulus and the input elastic modulus can be a major contributor to the difference between two measurement approaches. However, higher elastic modulus of trabecular bones has also been reported in literature [91] (*Table 2.2.3*) which

is up to 4.16 GPa and the resultant *J* value based on JMAN would then be up to 666.05 J/m^2 and *K* could be as high as 1.74 MPa $m^{1/2}$. Therefore, the *K* value calculated based on equations of linear fracture mechanism falls into the range of results using a bigger range of elastic modulus values reported [81,84,86,87,89–92].

Furthermore, the *K* value calculated based on equations of linear fracture mechanism is also expected to be higher than real *K* because the bending stress on the bone surface was calculated based on linear elasticity. This is expected to be higher than the real stress because bone has non-linear elastic behaviour and thus gives lower stress compared with the value based on the assumption of linear elasticity.

The approach used in this chapter for J integral calculation with a combination of X-ray tomograph, DVC and JMAN code has no constraints in sample preparation. For example, the sample geometry used for in-situ loading scan in this chapter is not standardized.

However, limitations still exist in current study by using JMAN code. First, for lower load, the value of J integral is difficult to converge because DVC gives results with noises which have similar magnitude as the displacements and thus the averaged data are too noisy to analyze [108]. Second, there is a possible overestimation of J integral because a constant value of linear elastic modulus has been used, which results in higher stresses around the crack tip than may be realistic. In real case, the elastic modulus of trabecular bone would decrease if microcracking occurs in the bone material, and non-linear deformation would also give larger strains than linear deformation. This would increase the calculated J-integral and over-predict the stress intensity factor. A nonlinear UMAT approach may be needed [108]. Third, the input material properties used for simulation influence the results because the elastic modulus used for the simulation is the average value of tensile results instead of bending results based on another batch of trabecular bones with similar microstructures. Testing methods can be a factor which influence the resultant elastic modulus of trabecular bone [81,84,86,87,89–91]. Forth, it is very

important to note that the obtained values can be wrong values to represent real J integral and stress intensity factor due to the large number of pores existing within the region between selected inner and outer contours, which results in significant deformation zone at crack tip and thus influences the calculation of elastic strain energy to create new crack surface in J integral calculation. However, these values can still be used to compare among different trabecular bones as another nominal standard of bone toughness.

Overall, this study provides reasonable values of *J* integral and *K* of trabecular bone, which are reasonable for future research and the proposed approach avoids the difficulty to insert the complicated crack into the sample with complicated microstructures in 3D FE modelling.

Chapter 7

7 Conclusion

Work conducted in this thesis contributes to the field of mechanical properties of biomaterials and thus provides knowledge for designs of biomimetic materials in engineering and clinic fields. A general approach with combination of X-ray tomography, digital volume correlation and modelling has been proposed in this thesis which avoids issues from conventional experiments. Two biomaterials have been looked into, which are limpet and bone, respectively.

An image-based FE models with the incorporation of the real morphology of limpet shell in macro-scale under compression has been built up with simple boundary condition using the load recorded in the experiment. The simulated distribution of strain has been compared with the strain distribution from an image-based FE model that used the 3D full displacement fields from DVC analysis as boundary conditions. Although lower strains have been predicted, due to the assumption of linear elastic behaviour, the possible fracture occurring areas have been successfully predicted. Additional information has been obtained from FE model of limpet with simple boundary condition under different loadings, which successfully extracts the apparent elastic modulus of the limpet by matching the experimental displacements with simulated displacements.

In addition, an image-based FE model of cortical bone under indentation with the incorporation of real geometry of pore network within indentation area has been built, which proves the non-elastic behaviour of cortical bone under indentation. Given the fact that larger simulated strain in indentation area, larger simulated contact area and larger simulated reaction force of the indenter with the given displacement compared with experimental measurements have been observed, crushing is expected to occur in real experiment and therefore other modelling techniques with the incorporation of crushing are required.

Due to the limited mechanical information of bone obtained from FE model, other modelling approaches have also been employed on bones to provide additional mechanical properties of bones.

In order to obtain elasticity of cortical bones, an approach by providing information of the pore network within cortical bone from tomograph to PReMISe together with apparent elastic modulus measured using RUS tests, intrinsic elastic modulus of bone material can be extracted and the anisotropy of bone matrix can be obtained. In addition, combination factors which are supposed to be only influenced by specific pore network of each individual sample have also been simulated using PReMISe. Porosities of different cortical bones which have a negative relation to apparent elastic moduli of cortical bones, have been calculated in order to investigate the relation between porosity and simulated results. The simulated combination factors of cortical bones have a negative relation to porosity while no relation has been found between porosity and simulated intrinsic elastic modulus, which is as expected. The obtained intrinsic elastic moduli have a good agreement with literature. In addition, with the knowledge of combination factor and intrinsic elastic modulus, the contribution of each factor to overall bone anisotropy can be calculated and it is found the bone matrix is the main contributor to bone anisotropy. No conclusion has been drawn on the relation between patients' conditions (e.g. age and gender) and porosity as well as intrinsic elastic modulus because of limited samples and the possible influence of osteoarthritis on bone porosity and bone tissue.

Fracture toughness of a pre-notched trabecular bone under three-point bending test has been evaluated using JMAN approach (X-ray tomograph, averaged DVC displacement fields and JMAN code). Complicated geometries of notch plus cracks under different loads developed within the specimen have been successfully segmented using different methods, which demonstrate the difficulty for fracture toughness prediction using 3D FE modelling with the incorporation of real notch geometry and thus testify the suitability of using JMAN to simplify the issue. A relatively

good agreement has been reached among these different crack segmentation methods. Lengths of notch plus cracks using different methods under different loads have been measured and compared. Stable growth of crack has been observed in all the methods until crack becomes unstable at the fracture load of 37N. The notch plus crack length from 2D phase congruency code has been used for the calculation of stress intensity factor based on equations of linear fracture mechanism, which is then compared with the value obtained from JMAN approach. The calculated *K* based on equations (0.59 MPa $m^{1/2}$) falls in the obtained range of *K* (0.041-1.74 MPa $m^{1/2}$) from JMAN approach based on the range of elastic moduli reported in literature (0.1-4.17 GPa) [81,84,86,87,89–92]. A good agreement of critical stress intensity factor has been achieved between JMAN approach (0.13 ± 0.052 MPa $m^{1/2}$) and literature-derived stress intensity factor (0.11 MPa $m^{1/2}$) with the same value of elastic modulus of trabecular bone (0.26 GPa).

Chapter 8

8 Future work

1) In-situ compression tests on complete limpets observed with synchrotron tomography can be repeated with more loading steps until fracture. Therefore, additional points of the predicted values of elastic modulus of limpet based on Image-based FE models can be obtained to further improve the accuracy and fidelity of the simulated result. Furthermore, instead of linear-elastic FE model, non-linear elastic material property can be introduced to improve the accuracy of predicted strain field given the fact limpet can grow micro-cracking under compression.
2) Nano X-ray tomography can be used in order to investigate whether microstructural information of limpet can be achieved for modelling.
3) For modelling of indentation tests on cortical bone, crushing of the indenter into specimen is an important factor which needs to be introduced into future analysis for investigation. Furthermore, instead of constant stress after deviation strain from linearity, the input stress-strain curve of cortical bone (either strain hardening [224] or strain softening *Figure 4.2.5*) in the model can be tuned in order to match simulated deformation beneath indenter with experimental one from DVC in order to extract elastic-plastic properties of cortical bone. Such an approach has been used in literature [248] [249].
4) More cortical bones can be scanned and tested afterwards using RUS tests for apparent elastic modulus measurement. With the average E_0 in different directions obtained from this thesis, the suitability of using PReMISe to predict apparent elastic moduli of cortical bones with known pore networks using tomographs can be evaluated compared with experimental results.

5) Limited literature has existed for the measurement of J integral and stress intensity factor of trabecular bones. Cortical bones rather than trabecular bones are more recommended in this case because cortical bones have less porosity and thus clearer DVC result around the crack rather than pores can be obtained. With less interference of pores, a sharper and straight crack can be expected in cortical bones which is favourable for JMAN code. In addition, more literatures of J integral and stress intensity factor of cortical bones are available for comparisons with simulated results. In addition, a non-linear UMAT approach is recommended to be incorporated into JMAN approach for the comparison with the used linear-elastic one in this project due to the fact that bone can develop micro-cracks or local damages under loading.

Chapter 9

9 Bibliography

1. Meyers MA, Chen P, Lin AY. Biological materials : Structure and mechanical properties. *Prog Mater Sci* 2008;**53**:1–206.

2. Tandon S, Faber KT. Fracture of brittle and quasi-brittle engineering materials. *Cem Res Prog* 1993:209–39.

3. Ji BH, Gao HJ. A study of fracture mechanisms in biological nano-composites via the virtual internal bond model. 2004;**366**:96–103.

4. Ridgway SA, Reid DG, Taylor JD *et al.* A cladistic phylogeny of the family Patellidae (Mollusca: Gastropoda). *Philos Trans Biol Sci* 1998;**353**:1645–71.

5. Cabral JP. Characterization and multivariate analysis of Patella intermedia, Patella ulyssiponensis and Patella vulgata from Póvoa de Varzim(Northwest Portugal). 2003;**21**:1:17.

6. Cabral JP, Jorge RMN. Compressibility and shell failure in the European Atlantic Patella limpets. *Mar Biol* 2007;**150**:585–97.

7. Barthelat F. Designing nacre-like materials for simultaneous stiffness, strength and toughness: Optimum materials, composition, microstructure and size. *J Mech Phys Solids* 2014;**73**:22–37.

8. Vermeij GJ. *Evolution and Escalation: An Ecological History of Life.* Princeton, N.J: Princeton University Press, 1987.

9. Vermeij GJ. *A Natural History of Shells*. Princeton: Princeton University Press, 1993.

10. Denny MW. *Biology and Mechanisms of the Wave-Swept Environment*. Princeton, N.J: Princeton University Press, 1988.

11. Elander J, West R, French D. Selection for increased safety factors of biological structures as

environmental unpredictability increases. 1993;**113**:1009–11.

12. Li XW, Ji HM, Yang W *et al.* Mechanical properties of crossed-lamellar structures in biological shells : A review. *Journal of the Mechanical Behavior of Biomedical Materials* 2017;**74**:54–71.

2017;**74**:54–71.

13. Boggild OB. The shell structure of the Mollusks. *Det K Danske Vidensk Selsk Skr Naturvidenskabelig og Math Afd Raekke 9* 1930;**2**:231–326.

14. Taylor JD, Layman M. The mechanical properties of bivalve (Mollusca) shell structures. *Palaeonatology* 1972;**15**:73–87.

15. Carter JG. *Skeletal Biomineralization: Patterns, Processes and Evolutionary Trends*. New York: American Geophysical Union, 1990.

16. Vermeij GJ. *A Nature History of Shells*. Princeton. Princeton, 1993.

17. Jackson A, Vincent J, Turner R *et al.* Biological materials: Structure and mechanical properties. *Soc Lond B Bio* 1988;**234**:415.

18. Menig R, Meyers MH, Meyers MA *et al.* Quasi-static and dynamic mechanical response of Strombus gigas (conch) shells. 2001;**297**:203–11.

19. Meyers MA, McKittrick J, Chen PY. Structural biological materials: critical mechanics-materials connections. *Science (80-)* 2013;**339**:773–9.

20. Kuhn-Spearing LT, Kessler H, Chateau E *et al.* Fracture mechanisms of the Strombus gigas conch shell : implications for the design of brittle laminates. *J Mater Sci* 1996;**31**:6583–94.

21. Jackson AP, Vincent JFV, Turner RM. Comparison of nacre with other ceramic composites. *J Mater Sci* 1990;**25**:3173–8.

22. Ji HM, Li XW. Microstructural characteristic and its relation to mechanical properties of clinocardium californiense shell. *JAmCeram,Soc* 2014:3991–8.

23. Ji HM, Jiang Y, Yang W *et al.* Biological self-arrangement of fiber like aragonite and its effect on mechanical behavior of Veined rapa Whelk shell. *JAmCeram,Soc* 2015;**98**:3319–25.

24. Yang W, Kashani N, Li XW *et al.* Structural characterization and mechanical behavior of a bivalve shell (Saxidomus purpuratus). *Mater Sci Eng C* 2011;**31**:724–9.

25. Yang W, Zhang GP, Zhu XF *et al.* Structure and mechanical properties of Saxidomus purpuratus biological shells. 2011;**4**:1514–30.

26. Currey JD. Further studies on the mechanical properties of mollusc shell material. *J Zool London* 1976;**180**:445–53.

27. Wegst UGK, Ashby MF. The mechanical efficiency of natural materials. *Philos Mag* 2004;**21**:2167–81.

28. Barthelat F. Nacre from mollusk shells: a model for high-performance structural materials. *Bioinspir Biomim* 2010;**5**:035001.

29. Wegst UGK, Bai H, Saiz E *et al.* Bioinspired structural materials. *Nat Mater* 2014;**14**:23–36.

30. Tang ZY, Kotov NA, Magonov S *et al.* Nanostructured artificial nacre. *Nat Mater* 2003;**2**:413–8.

31. Kato T. Polymer / Calcium Carbonate Layered Thin-Film Composites. *Adv Mater* 2010;**20**:1543–6.

32. Li YQ, Yu T, Yang TY *et al.* Bio-inspired Nacre-like composite films based on graphene with superior mechanical, electrical, and biocompatible properties. *Adv Mater* 2012;**24**:3426–31.

33. Sellinger A, Weiss PM, Nguyen A *et al.* Continuous self-assembly of organic-inorganic nanocomposite coatings that mimic nacre. *Nature* 1998;**394**:256–60.

34. Hartgerink JD, Beniash E, Stupp SI. Self-assembly and mineralization of peptide-amphiphile nanofibers. *Science* 2001;**294**:1684–8.

35. Chen L, Ballarini R, Kahn H *et al.* Bioinspired micro-composite structure. *J Mater Res* 2007;**22**:124–31.

36. Clegg WJ, Kendall K, Alford NM *et al.* A simple way to make tough ceramics. *Nature* 1990;**347**:455–7.

37. Bonderer LJ. Bioinspired design and assembly of platelet reinforced polymer films. 2007;**205411**:1069–73.

38. Munch E, Launey ME, Alsem DH *et al.* Tough, bio-inspired hybrid materials. *Science (80-)* 2008;**322**:1516–20.

39. Guldberg RE, Ballock RT, Boyan BD *et al.* Analyzing bone, blood vessels, and biomaterials with microcomputed tomography. *IEEE Eng Med Biol Mag* 2003;**22**:77–83.

40. Verhulp E, van Rietbergen B, Huiskes R *et al.* A three-dimensional digital image correlation technique for strain measurements in microstructures. *J Biomech* 2004;**37**:1313–20.

41. Hing KA. Bone repair in the twenty-first century: biology, chemistry or engineering? *Philos Trans A Math Phys Eng Sci* 2004;**362**:2821–50.

42. Rey C, Combes C, Drouet1 C *et al.* Bone mineral: update on chemical composition and structure. *Osteoporos Int* 2010;**20**:1013–21.

43. Hoskins D, Barak M. Comparing the tensile and compressive Young ' s moduli of cortical bone. 2016;**2**.

44. Carter DR, Hayes W. . The compressive behavior of bone as a two-phase porous structure. *J Bone Jt Surg* 1977;**59**:954–62.

45. Mcelhaney JH, Fogle JL, Melvin JW *et al.* Mechanical properties on cranial bone. *J Biomech* 1970;**3**:495–511.

46. Martin RB. The effects of geometric feedback in the development of osteoporosis. *J Biomech*

1972;**5**:447–55.

47. Rho JY, Kuhn-Spearing L, Zioupos P. Mechanical properties and the hierarchical structure of bone. *Med Eng Phys* 1998;**20**:92–102.

48. Fratzl P, Gupta HS, Paschalis EP *et al.* Structure and mechanical quality of the collagen – mineral nano-composite in bone. *J. Mater.Chem* 2004:2115–23.

49. Nevitt M., Lane N., Scott J. *et al.* Radiographic osteoarthritis of the hip and bone mineral density. *Arthritis Rheum* 1995;**38**:907–16.

50. Anderson AS, Loeser RF. Why is osteoarthritis an age-related disease ? *Best Pract Res Clin Rheumatol* 2010;**24**:15–26.

51. Mirzaali MJ, Schwiedrzik JJ, Thaiwichai S *et al.* Mechanical properties of cortical bone and their relationships with age, gender, composition and microindentation properties in the elderly. *Bone* 2016;**105**:196–211.

52. Reznikov N, Shahar R, Weiner S. Bone hierarchical structure in 3 dimensions. *Acta Biomater* 2014;**10**:3815–26.

53. Zebaze RMD, Ghasem-Zadeh A, Bohte A *et al.* Intracortical remodelling and porosity in the distal radius and post-mortem femurs of women: a cross-sectional study. *Lancet* 2010;**375**:1729–36.

54. Fratzl P, Weinkamer R. Nature's hierarchical materials. *Prog Mater Sci* 2007;**52**:1263–334.

55. Fan Z, Swadener JG, Rho JY *et al.* Anisotropic properties of human tibial cortical bone as measured by nanoindentation. *J Orthop Res* 2002;**20**:806–10.

56. Sevostianov I, Kachanov M. Impact of the porous microstructure on the overall elastic properties of the osteonal cortical bone. *J Biomech* 2000;**33**:881–8.

57. Ascenzi A, Bonucci E, Ripamonti A *et al.* X-ray diffraction and electron microscope study of

osteons during calcification. *Calcif Tissue Res* 1978;**25**:133–43.

58. Carando S, Barbos MP, Ascenzi A *et al.* Orientation of collagen in human tibial and fibular shaft and possible correlation with mechanical properties. *Bone* 1989;**10**:139–42.

59. Katz JL, Meunier A. Scanning acoustic microscope studies of the elastic properties of osteons and osteon lamellae. *J Biomech Eng* 1993;**115**:543–8.

60. Rho JY, Roy ME, Tsui TY *et al.* Elastic properties of microstructural components of human bone tissue as measured by nanoindentation. *J Biomed Mater Res* 1999;**45**:48–54.

61. Rho JY, Tsui TY, Pharr GM. Elastic properties of human cortical and trabecular lamellar bone measured by nanoindentation. *Biomaterials* 1997;**18**:1325–30.

62. Zysset PK, Edward Guo X, Edward Hoffler C *et al.* Elastic modulus and hardness of cortical and trabecular bone lamellae measured by nanoindentation in the human femur. *J Biomech* 1999;**32**:1005–12.

63. Cook RB. Non-invasively assessed skeletal bone status and its relationship to the biomechanical properties and condition of cancellous bone. 2005.

64. Granke M, Grimal Q, Parnell WJ *et al.* Elasticity and porosity in human cortical bone : models and experiments. 2011.

65. Currey JD. The effect of porosity and mineral content on the Young's modulus of elasticity of compact bone. *J Biomech* 1988;**21**:131–9.

66. Eneh CTM, Malo MKH, Karjalainen JP *et al.* Effect of porosity, tissue density, and mechanical properties on radial sound speed in human cortical bone. *Med Phys* 2016;**43**:2030–9.

67. Grimal Q, Raum K, Gerisch A *et al.* Derivation of the mesoscopic elasticity tensor of cortical bone from quantitative impedance images at the micron scale. *Comput Methods Biomech Biomed Engin* 2008;**11**:147–57.

68. Dong XN, Guo XE. The dependence of transversely isotropic elasticity of human femoral cortical bone on porosity. *J Biomech* 2004;**37**:1281–7.

69. Acuna RL, Dong XN, Wang X. Post-yield behavior of human cortical bone is transversely isotropic in compression. *56th Annual Meeting of the Orthopaedic Research Society*. 2009.

70. Boughton OR, Ma S, Cai X *et al.* Computed tomography porosity and spherical indentation for determining cortical bone millimetre-scale mechanical properties. *Sci Rep* 2019;**9**:7416.

71. Isaza J. Characterization of the mechanical and morphological properties of cortical bones by nanoindentation and atomic force microscopy. 2015.

72. Parnell WJ, Grimal Q. The influence of mesoscale porosity on cortical bone anisotropy. Investigations via asymptotic homogenization. *J R Soc Interface* 2009;**6**:97–109.

73. Hasegawa K, Turner CH, Burr DB. Contribution of collagen and mineral to the elastic anisotropy of bone. *Calcif Tissue Int* 1994;**55**:381–6.

74. Turner CH, Chandran A, Pidaparti RMV. The anisotropy of osteonal bone and its ultrastructural implications. *Bone* 1995;**17**:85–9.

75. Weiner S, Traub W, Wagner HD. Lamellar bone: structure– function relations. *J Struct Biol* 1999;**126**:241–55.

76. Khosla S. Pathogenesis of age-related bone loss in humans. *Journals Gerontol - Ser A Biol Sci Med Sci* 2013;**68**:1226–35.

77. Hoffler CE, Moore KE, Kozloff K *et al.* Age, gender, and bone lamellae elastic moduli. *J Orthop Res* 2000;**18**:432–7.

78. Chen H, Zhou X, Fujita H *et al.* Age-related changes in trabecular and cortical bone microstructure. *Int J Endocrinol* 2013;**2013**:213234.

79. Martin B. Aging and strength of bone as a structural material. *Calcif Tissue Int* 1993;**53**:34–

40.

80. Rho JY, Zioupos P, Currey JD *et al.* Microstructural elasticity and regional heterogeneity in human femoral bone of various ages examined by nano-indentation. *J Biomech* 2002;**35**:189–98.

81. Ashman RB, Rho JY. Elastic modulus of trabecular bone material. *J Biomech* 1988;**21**:177–81.

82. Oftadeh R, Perez-Viloria M, Villa-Camacho JC *et al.* Biomechanics and mechanobiology of trabecular bone: A review. *J Biomech Eng* 2015;**137**:010802.

83. Seeman E. Pathogenesis of bone fragility in women and men. *Lancet* 2002;**359**:1841–50.

84. Keaveny TM, Pinilla T., Crawford R. *et al.* Systematic and random errors in compression testing of trabecular bone. *J Orthopaedic Res* 1997:101–10.

85. Linde F, Hvid I, Madsen F. The effect of specimen size and geometry on the mechanical behaviour of trabecular bone specimens. *J Biomech* 1991;**24**:691–8.

86. Linde F, Hvid I. The effect of constraint on the mechanical behaviour of trabecular bone specimens. *J Biomech* 1989;**22**:485–90.

87. Jiroušek O. Nanoindentation of human trabecular bone -- tissue mechanical properties compared to standard engineering test methods. *Nanoindentation Mater Sci* 2012:259–84.

88. Gibson LJ. The mechanical behaviour of cancellous bone. *Biomechanics* 1985;**18**:317–28.

89. Townsend PR, Rose RM, Radin EL. Buckling studies of single human trabeculae. *J Biomech* 1975;**8**, DOI: 10.1016/0021-9290(75)90025-1.

90. Ryan SD, Williams JL. Tensile testing of rodlike trabeculae excised from bovine femoral bone. *J Biomech* 1989;**22**:351–5.

91. Kuhn JL, Goldstein SA, Choi R *et al.* Comparison of the trabecular and cortical tissue moduli from human iliac crests. *J Orthop Res* 1989;**7**:876–84.

92. Ma S, Goh EL, Jin A *et al.* Long-term effects of bisphosphonate therapy : perforations ,

microcracks and mechanical properties. *Nat Publ Gr* 2017:1–10.

93. Ritchie RO, Koester KJ, Ionova S *et al.* Measurement of the toughness of bone: A tutorial with special reference to small animal studies. *Bone* 2008;**43**:798–812.

94. Nalla RK, Kruzic JJ, Kinney JH *et al.* Mechanistic aspects of fracture and R-curve behavior in human cortical bone. *Biomaterials* 2005;**26**:217–31.

95. Bonfield W. Advances in the fracture mechanics of cortical bone. *J Biomech* 1987;**20**:1071–81.

96. Lucksanasombool P, Higgs WAJ, Higgs RJED *et al.* Fracture toughness of bovine bone: Influence of orientation and storage media. *Biomaterials* 2001;**22**:3127–32.

97. Phelps JB, Hubbard GB, Wang X *et al.* Microstructural heterogneity and the fracture toughness of bone. *J Biomed Mater Res* 2000;**51**:735–41.

98. Norman TL, Nivargikar SV, Burr DB. Resistance to crack growth in human cortical bone is greater in shear than in tension. *J Biomech* 1996;**29**:1023–31.

99. Williams JG, Ewing PD. Fracture under complex stress - the angled crack problem. *Int J Fract Mech* 1972;**8**:441–6.

100. Irwin GR. Analysis of Stresses and Strains Near the End of a Crack Traversing a Plate. *J Appl Mech* 1957.

101. Nalla RK, Kinney JH, Ritchie RO. Mechanistic fracture criteria for the failure of human cortical bone. *Nat Mater* 2003;**2**:164–8.

102. Cook RB, Zioupos P. The fracture toughness of cancellous bone. *J Biomech* 2009;**42**:2054–60.

103. Gibson LJ, Ashby MF. Chapter 10: Wood. *Cellular Solids: Structure and Properties, Second Edition*. Cambridge University Press, 387–428.

104. Gibson LJ, Ashby MF. Chapter 11: Cancellous bone. *Cellular Solids: Structure and Properties, Second Edition*. Cambridge University Press, 429–52.

105. Irwin GR. Onset of Fast Crack Propagation in High Strength Steel and Aluminum Alloys. *Sagamore Res Conf Proc* 1956:289–305.

106. Cherepanov GP. The propagation of cracks in a continuous medium. *J Appl Math Mech* 1967;**31**.

107. Rice JR, Rosengren GF. Plane strain deformation near a crack tip in a power-law hardening material. *J Mech Phys Solids* 1968;**16**:1–12.

108. Barhli S. Advanced quantitative analysis of crack Fields, observed by 2D and 3D image correlation, volume correlation and diffraction mapping. 2017.

109. Sakai M, Yoshimura J, Goto Y *et al.* R-Curve Behavior of a Polycrystalline Graphite : Microcracking and Grain Bridging in the Wake Region. *J. Am. Ceram. Soc* 1988;**71**:609–16.

110. Kaplan W. *Advanced Calculus*. 5th ed. Addison-Wesley, 2003.

111. Parks DM. A stiffness derivative finite element technique for determination of crack tip stress intensity factors. *Int J Fract* 1974;**10**:487–502.

112. Odgaard A, Linde F. The underestimation of Young's modulus in compressive testing of cancellous bone specimens. *J Biomech* 1991;**24**:691–8.

113. Kotha SP, Li Y, Guzelsu N. Micromechanical model of nacre tested in tension. *J Mater Sci* 2001;**36**:2001–7.

114. Evans AG, Suo Z, Wang RZ *et al.* Model for the robust mechanical behavior of nacre. *J Mater Res* 2001;**16**:2475–84.

115. Li S., Demirci E, Silberschmidt VV. Variability and anisotropy of mechanical behavior of cortical bone in tension and compression. *J Mech Behav Biomed Mater* 2013;**21**:109–20.

116. Mirzaali MJ, Bürki A, Schwiedrzik J *et al.* Continuum damage interactions between tension and compression in osteonal bone. *J Mech Behav Biomed Mater* 2015;**49**:355–69.

117. Hussein AI, Barbone PE, Morgan EF. Digital volume correlation for study of the mechanics of whole bones. *Procedia IUTAM* 2012;**4**:116–25.

118. Hurxthal LM. Measurement of anterior vertebral compressions and biconcave vertebrae. *Am J Roentgenol* 1968;**103**:635–44.

119. Simkin A, Robin G. The mechanical testing of bone in bending. *J Biomech* 1973;**6**, DOI: 10.1016/0021-9290(73)90035-3.

120. Martin RB, Boardman DL. The effects of collagen fiber orientation, porosity, density, and mineralization on bovine cortical bone bending properties. *J Biomech* 1993;**26**:1047–54.

121. Boyce TM, Fyhrie DP, Glotkowski MC *et al.* Damage type and strain mode associations in human compact bone bending fatigue. *J Orthop Res* 1998;**16**:322–9.

122. Ostojic P, McPherson R. A review of indentation fracture theory: its development, principles and limitations. *Int J Fract* 1987;**33**:297–312.

123. Chen ZW, Wang X, Atkinson A *et al.* Spherical indentation of porous ceramics : Elasticity and hardness. *J Eur Ceram Soc* 2016;**36**:1435–45.

124. Warren PD. Determining the fracture toughness of brittle materials by Hertzian indentation. *J Eur Ceram Soc* 1995;**15**:201–7.

125. Franco Jr. A, Roberts SG. Surface mechanical analyses by Hertzian indentation. *Cerâmica* 2004;**50**:94–108.

126. He LH, Fujisawa N, Swain MV. Elastic modulus and stress-strain response of human enamel by nano-indentation. *Biomaterials* 2006;**27**:4388–98.

127. Sun J, Tong J. Fracture toughness properties of three different biomaterials measured by

nanoindentation. *J Bionic Eng* 2007;**4**:11–7.

128. Spears IR. A three-dimensional finite element model of prismatic enamel: a re-appraisal of the data on the Young's modulus of enamel. *J Dent Res* 1997;**76**:1690–7.

129. Ge J, Cui FZ, Wang XM *et al.* Property variations in the prism and the organic sheath within enamel by nanoindentation. *J Biomater* 2005;**26**:3333–9.

130. Leisure RG, Wills FA. Resonant ultrasound spectroscopy. *J Phys Condens Matter* 1997.

131. Leiba R. Resonant Ultrasound Spectroscopy for arbitrarily shaped samples using Finite Element Method and Levenberg-Marquart algorithm. *Proc Acoust Eng Proj* 2014:1–4.

132. Plachy T, Padevet P, Polak M. Comparison of two experimental techniques for determination of Young's modulus of concrete specimens. *5th WSEAS Int Conf Appl Theor Mech (MECHANICS '09)* 2009:68–71.

133. Salman MM, Al-Amawee A. The Ratio between Static and Dynamic Modulus of Elasticity in Normal and High Strength Concrete. *J Eng Dev* 2006;**10**:163–74.

134. Migliori A, Sarrao JL, Visscher WM *et al.* Resonant ultrasound spectroscopic techniques for measurement of the elastic moduli of solids. *Phys B* 1993;**183**:1–24.

135. Plesek J, Kolman R, Landa M. Using finite element method for the determination of elastic moduli by resonant ultrasound spectroscopy. *J Acoust Soc Am* 2004;**116**:282–7.

136. Resonance Ultrasound Spectroscopy. *Lead NDD Technol Co*.

137. Hounsfield GN. Computerized transverse axial scanning (tomography): Part I. Description of system. *Br J Radiol* 1973;**46**:1016–22.

138. Ruegsegger P, Koller B, Muller R. A microtomographic system for the nondestructive evaluation of bone architecture. *Calcif Tissue Int* 1996;**58**:24–9.

139. Jones A et al. Assessment of bone ingrowth into porous biomaterials using MICRO-CT.

Biomaterials 2007;**28**:2491–504.

140. Genant HK, Engelke K, Prevrhal S. Advanced CT bone imaging in osteoporosis. 2008, DOI: 10.1093/rheumatology/ken180.

141. Müller R, Koller B, Hildebrand T *et al.* Resolution dependency of microstructural properties of cancellous bone based on three-dimensional mu-tomography. *Technol Health Care* 1996;**4**:113—119.

142. Jones AC, Milthorpe B, Averdunk H *et al.* Analysis of 3D bone ingrowth into polymer scaffolds via micro-computed tomography imaging. *Biomaterials* 2004;**25**:4947–54.

143. Babout L, Maire E, Buffière JY *et al.* Characterization by X-ray computed tomography of decohesion, porosity growth and coalescence in model metal matrix composites. *Acta Mater* 2001;**49**:2055–63.

144. Kelkar S, Boushey CJ, Okos M. A method to determine the density of foods using X-ray imaging. *J Food Eng* 2016;**1**:36–41.

145. Tekseth. Quantitative polychromatic X-ray computed tomography. 2018.

146. Hildebrand T, Laib A, Müller R *et al.* Direct three-dimensional morphometric analysis of human cancellous bone: microstructural data from spine, femur, iliac crest, and calcaneus. *J Bone Miner Res* 1999;**14**:1167–74.

147. Germaneau A, Doumalin P, Dupré JC. Comparison between X-ray micro-computed tomography and optical scanning tomography for full 3D strain measurement by digital volume correlation. *NDT E Int* 2008;**41**:407–15.

148. Bay BK, Smith TS, Fyhrie DP *et al.* Digital volume correlation: Three-dimensional strain mapping using X-ray tomography. *Exp Mech* 1999;**39**:217–26.

149. Smith TS, Bay BK, Rashid MM. Digital Volume Correlation Including Rotational Degrees of

Freedom during Minimization. *Exp Mech* 2002;**42**:272–8.

150. Kinney JH, Ryaby JT, Haupt DL *et al.* Three-dimensional in vivo morphometry of trabecular bone in the OVX rat model of osteoporosis. *Technol Health Care* 1998;**6**:339—350.

151. Pfeiffer F, Weitkamp T, Bunk O *et al.* Phase retrieval and differential phase-contrast imaging with low brilliance X-ray sources. 2006;**2**:258–61.

152. Arfelli F, Assante M, Bonvicini V. Low-dose phase contrast X-ray medical imaging. *Phys Med Biol* 1999;**2845**.

153. Bentley MD, Ortiz MC. The use of microcomputed tomography to study microvasculature in small rodents. *Am J Physiol Regulatory Integrative Comp Physiol.* 2002.

154. Müller R, Van Campenhout H, Van Damme B *et al.* Morphometric Analysis of Human Bone Biopsies: A Quantitative Structural Comparison of Histological Sections and Micro-Computed Tomography. *Bone* 1998;**23**:59–66.

155. Müller R, Rüegsegger P. Three-dimensional finite element modelling of non-invasively assessed trabecular bone structures. *Med Eng Phys* 1995;**17**:126–33.

156. Garcia D, Orteu JJ, Penazzi L. A combined temporal tracking and stereo-correlation technique for accurate measurement of 3D displacements: Application to sheet metal forming. *J Mater Process Technol* 2002;**125-126**:736–42.

157. Schreier HW. Advances in Light Microscope Stereo Vision. *Exp Mech* 2004;**44**:278–88.

158. Phillips DH, Lannutti JJ. Measuring physical density with X-ray computed tomography. *NDT E Int* 1997;**30**:339–50.

159. Franck C, Hong S, Maskarinec SA *et al.* Three-dimensional full-field measurements of large deformations in soft materials using confocal microscopy and digital volume correlation. *Exp Mech* 2007;**47**:427–38.

160. Benoit A, Guerard S, Gillet B *et al.* 3D analysis from micro-MRI during in situ compression on cancellous bone. *J Biomech* 2009;**42**:2381–6.

161. Basler SE et al. Towards validation of computational analyses of peri-implant displacements by means of experimentally obtained displacement maps. *Comput Methods Orthop Biomech* 2011;**14**.

162. Roberts BC, Perilli E, Reynolds KJ. Application of the digital volume correlation technique for the measurement of displacement and strain fields in bone: A literature review. *J Biomech* 2014;**47**:923–34.

163. Geers MGD, De Borst R, Brekelmans WAM. Computing strain fields from discrete displacement fields in 2D-solids. *Int J Solids Struct* 1996;**33**:4293–307.

164. Marrow J, Reinhard C, Vertyagina Y *et al.* 3D Studies of damage by combined X-ray tomography and digital volume correlation. *Procedia Mater Sci* 2014;**3**:1554–9.

165. Liu L, Morgan EF. Accuracy and precision of digital volume correlation in quantifying displacements and strains in trabecular bone. *J Biomech* 2007;**40**:3516–20.

166. Zauel R, Yeni YN, Bay BK *et al.* Comparison of the linear finite element prediction of deformation and strain of human cancellous bone to 3D digital volume correlation measurement. *J Biomech Eng* 2006;**128**:1–6.

167. Sutton MA, Wolters WJ, Peters WH *et al.* Determination of displacements using an improved digital correlation method. *Image Vis Comput* 1983;**1**:133–9.

168. Palanca M, Cristofolini L, Viceconti M *et al.* 3D local measurements of bone strain and displacement : comparison of three digital volume correlation approaches. *J Biomech Eng* 2015;**137**.

169. Brodland GW. How computational models can help unlock biological systems. *Semin Cell Dev Biol* 2015;**48**:62–73.

170. Aghili A l., Goudarzi AM, Paknahad A *et al.* Finite element analysis of human femur bone by reverse engineering modelling method. *Indian J Sci Technol* 2015;**8**, DOI: 10.1260/1750-9548.9.2.101.

171. Yosibash Z, Padan R, Joskowicz L *et al.* A CT-Based High-Order Finite Element Analysis of the Human Proximal Femur Compared to In-vitro Experiments. *Journal of Biomechanical Engineering* 2007;**129**:297–309.

172. Guldberg RE, Hollister SJ, Charras G. The accuracy of digital image-based finite element models. *J Biomech Eng* 1998;**120**:289–95.

173. Notarberardino B. Image based finite element modelling for the mechanical characterisation of complex material systems. 2010.

174. Ulrich D, Van Rietbergen B, Weinans H *et al.* Finite element analysis of trabecular bone structure: A comparison of image-based meshing techniques. *J Biomech* 1998;**31**:1187–92.

175. Jäger I, Fratzl P. Mineralized collagen fibrils: a mechanical model with a staggered arrangement of mineral particles. *Biophys J* 2000;**79**:1737–46.

176. Jackson AP, Vincent JFV, Turner RM *et al.* The Mechanical Design of Nacre. *Proc R Sooc* 1988;**234**:415–40.

177. Gao HJ. Application of fracture mechanics concepts to hierarchical biomechanics of bone and bone-like materials. *Int J Fract* 2006;**138**:101–37.

178. Espinosa HD, Rim JE, Barthelat F *et al.* Merger of structure and material in nacre and bone – Perspectives on de novo biomimetic materials. *Prog Mater Sci* 2009;**54**:1059–100.

179. Shao Y, Zhao HP, Feng XQ *et al.* Discontinuous crack-bridging model for fracture toughness analysis of nacre. *J Mech Phys Solids* 2012;**60**:1400–19.

180. Katti DR, Katti KS, Sopp JM *et al.* 3D finite element modeling of mechanical response in

nacre-based hybrid nanocomposites. *Comput Theor Polym Sci* 2001;**11**:397–404.

181. Barthelat F, Tang H, Zavattieri P *et al.* On the mechanics of mother-of-pearl: A key feature in the material hierarchical structure. *J Mech Phys Solids* 2007;**55**:306–37.

182. Dimas LS, Bratzel GH, Eylon I *et al.* Tough composites inspired by mineralized natural materials: Computation, 3D printing, and testing. *Adv Funct Mater* 2013;**23**:4629–38.

183. Linde F, Hvid I, Madsen F. The effect of specimen geometry on the mechanical behavior of trabecular bone specimens. *J Biomech* 1992;**25**:359–68.

184. Faghih SM, Mohammadi V, Rajabi H *et al.* Experimental analysis and numerical modeling of mollusk shells as a three dimensional integrated volume. *J Mech Behav Biomed Mater* 2012;**16**:38–54.

185. Neves NM, Mano JF. Structure/mechanical behavior relationships in crossed-lamellar sea shells. *Mater Sci Eng C* 2005;**25**:113–8.

186. Currey JD, Taylor JD. The mechanical behaviour of some molluscan hard tissues. *J Zool, Lond* 1974;**173**:395–406.

187. van Rietbergen B, Weinans H, Huiskes R *et al.* A new method to determine trabecular bone elastic properties and loading using micromechanical finite-element models. *J Biomech* 1995;**28**:69–81.

188. Niebur GL, Feldstein MJ, Yuen JC *et al.* High-resolution finite element models with tissue strength asymmetry accurately predict failure of trabecular bone. *J Biomech* 2000;**33**:1575–83.

189. Verhulp E, Van Rietbergen B, Huiskes R. Comparison of micro-level and continuum-level voxel models of the proximal femur. *J Biomech* 2006;**39**:2951–7.

190. Eswaran SK, Gupta A, Keaveny TM. Locations of bone tissue at high risk of initial failure during compressive loading of the human vertebral body. *Bone* 2007;**41**:733–9.

191. McElhaney J., Fogle J., Melvin J. *et al.* Mechanical properties of cranial bone. *J Biomech* 1970;**3**:495–6,IN5,497–511.

192. Keyak JH, Rossi SA, Jones KA *et al.* Prediction of femoral fracture load using automated finite element modeling. *J Biomech* 1998;**31**:125–33.

193. Pierron F, Grédiac M. Soft and Biological Materials. *The Virtual Fields Method: Extracting Constitutive Mechanical Parameters from Full-Field Deformation Measurements*. New York, NY: Springer New York, 2012, 293–327.

194. Jaecques SVN, Van Oosterwyck H, Muraru L *et al.* Individualised, micro CT-based finite element modelling as a tool for biomechanical analysis related to tissue engineering of bone. *Biomaterials* 2004;**25**:1683–96.

195. Bessho M, Ohnishi I, Matsuyama J *et al.* Prediction of strength and strain of the proximal femur by a CT-based finite element method. *J Biomech* 2007;**40**:1745–53.

196. Buonamici F, Carfagni M, Furferi R *et al.* Reverse engineering modeling methods and tools: a survey. *Comput Aided Des Appl* 2018;**15**:443–64.

197. Raja V, Fernandes K. *Reverse Engineering: An Industrial Perspective*. London: Springer, 2008.

198. Geers MGD, Borst RD, Peijs T. Mixed numerical-experimental identification of non-local characteristics of random-fibre-reinforced composites. *Compos Sci Technol* 1999;**59**:1569–78.

199. Lin LS, Li HY, Fok ASL. Characterization of Material properties using strain mapping and reverse engineering. *8th Biennial ASME Conference on Engineering Systems Design and Analysis*. Vol 1. 2006, 427–33.

200. Smith G, Flewitt P, Schlangen E. Multi-scale modelling of nuclear reactor core graphite. *J Multiscale Model* 2013;**05**:1350004.

201. Kyaw ST, Sun W, Becker AA. Effects of compositions of filler, binder and porosity on elastic

and fracture properties of nuclear graphite. *J Nucl Mater* 2015;**457**:42–7.

202. Herakovich CT, Baxter SC. Influence of pore geometry on the effective response of porous media. *Journal of Materials Science* 1999;**4**:1595–609.

203. Coble RL, Kingery WD. Effect of porosity on physical properties of sintered alumina. *J Am Ceram Soc* 1956;**39**.

204. Walsh JB, Brace WF, England AW. Effect of porosity on compressibility of glass. 1965;**48**.

205. Rice RW. Comparison of stress concentration versus minimum solid area based mechanical property-porosity relations. 1993;**28**:2187–90.

206. Lang SB. Ultrasonic Method for Measuring Elastic Coefficients of Bone and Results on Fresh and Dried Bovine Bones. *IEEE Trans Biomed Eng* 1970;**BME-17**:101–5.

207. Buskirk V, Ashman WC. The elastic moduli of bone. *Mech Prop Bone* 1981;**AMD 36. AS**:131–43.

208. Kachanov M, Tsukrov I, Shafiro B. Effective Moduli of Solids With Cavities of Various Shapes. *Appl Mech Rev* 1994;**47**:S151.

209. Eason ED, Hall GN, Marsden BJ *et al.* A model of Young's modulus for Gilsocarbon graphites irradiated in oxidising environments. *J Nucl Mater* 2013;**436**:201–7.

210. Vertyagina Y, Marrow TJ. A multi-scale three-dimensional Cellular Automata fracture model of radiolytically oxidised nuclear graphite. *Carbon N Y* 2017;**121**:574–90.

211. Element/compound/mixture selection. *Technol Natl insititute Stand Technol*.

212. Tsoulfanidis N. *Measurement and Detection Radiation*. Taylor&Francis, USA, 1995.

213. Technical procedure: phase contrast imaging. 2014:January.

214. Liu X, Grönberg F, Sjölin M *et al.* Count rate performance of a silicon-strip detector for photon-counting spectral CT. *Nucl Instruments Methods Phys Res Sect A Accel Spectrometers,*

Detect Assoc Equip 2016;**827**:102–6.

215. Evans FG, Lebow M. Regional differences in some of the physical properties of the human femur. *J Appl Physiol* 1951;**3**:563–72.

216. Xradia Versa User ' s Guide. 2014.

217. Blessing M, Bhagwat MS, Lyatskaya Y *et al.* Kilovoltage beam model for flat panel imaging system with bow-tie filter for scatter prediction and correction. *Phys Medica* 2012;**28**:134–43.

218. Simpleware Tutorial Guide.

219. Young's modulus-tensile and yield strength for common materials.

220. Typical poisson's ratio of polymers at room temperature.

221. Feng C, Kang BS. Young ' s modulus measurement using a simplified transparent indenter measurement technique. 2008:9–15.

222. Fondrk M, Bahniuk E, Davy DT *et al.* Some viscoplastic characteristics of bovine and human cortical bone. *J Biomech* 1988;**21**:623–30.

223. Viano D, Helfenstein U, Anliker M. Elastic properties of cortical bone in female human femurs. *J Biomech* 1976;**9**:703–10.

224. Zhang J., Michalenko M., Kuhl E *et al.* Characterization of indentation response and stiffness reduction of bone using a continuum damage model. *J Mech Behav Biomed Mater* 2010;**3**, DOI: 10.1016/j.jmbbm.2009.08.001.Characterization.

225. Ji BH, Gao HJ. Mechanical properties of nanostructure of biological materials. 2004;**52**:1963–90.

226. Ji HM, Li XW, Chen DL. Cymbiola nobilis shell : Toughening mechanisms in a crossed-lamellar structure. *Sci Rep* 2017:1–10.

227. Schaffler MB, Burr DB. Stiffness of compact bone: effects of porosity and density. *J Biomech*

1988;**21**:13–6.

228. W. McCalden R, Mcgeough JA, Barker M *et al.* Age-related changes in the tensile properties of cortical bone. The relative importance of changes in porosity, mineralization, and microstructure. *J Bone Joint Surg Am* 1993;**75**:1193–205.

229. Wachter NJ, Augat P, Krischak GD *et al.* Prediction of strenght of cortical bone in vitro by microcomputed tomography. *Clin Biomech* 2001;**16**:252–6.

230. Voigt W. Ueber die Beziehung zwischen den beiden Elasticitätsconstanten isotroper Körper. *Ann Phys* 1889;**274**:573–87.

231. Reuss A. Berechnung der Fließgrenze von Mischkristallen auf Grund der Plastizitätsbedingung für Einkristalle. *J Appl Math Mech* 1929;**9**:49–58.

232. Dequeker J, Luyten FP. Bone mass and osteoarthritis. *Clin Exp Rheumatol* 2000.

233. Beel JA, Groswald DE, Luttges MW. Alterations in the mechanical properties of peripheral nerve following crush injury. *J Biomech* 1984;**17**:185–93.

234. Theret D, Levesque MJ, Sato M *et al.* The application of a homogeneous half-space model in the analysis of endothelial cell micropipette measurements. *J Biomech Eng* 1988;**110**:190–9.

235. ThermoFisher Scientific. Thermo Scientific Avizo Software 9. 2018:169.

236. Cinar AF, Barhli SM, Hollis D *et al.* An autonomous surface discontinuity detection and quantification method by digital image correlation and phase congruency. *Opt Lasers Eng* 2017;**96**:94–106.

237. Lankton S, Nain D, Yezzi A *et al.* Hybrid geodesic region-based curve evolutions for image segmentation. 2007:65104U.

238. An YH, Robert AD. *Mechanical Testing of Bone and the Bone–implant Interface*., 2000.

239. Kabel J, Van Rietbergen B, Odgaard A *et al.* Constitutive relationships of fabric, density, and

elastic properties in cancellous bone architecture. *Bone* 1999;**25**:481–6.

240. Colabella L, Ibarra Pino AA, Ballarre J *et al.* Calculation of cancellous bone elastic properties with the polarization-based FFT iterative scheme. *Int j numer method biomed eng* 2017;**33**:1–16.

241. Becker TH, Mostafavi M, Tait RB *et al.* An approach to calculate the J-integral by digital image correlation displacement field measurement. *Fatigue Fract Eng Mater Struct* 2012;**35**:971–84.

242. Parks DM. The virtual crack extension method for nonlinear material behavior. *Comput Methods Appl Mech Eng* 1977;**12**:353–64.

243. Keaveny TM, Guo XE, Wachtel EF *et al.* Trabecular bone exhibits fully linear elastic behaviour and yields at low strains. *Biomechanics* 1994;**27**:1127–36.

244. Liu M, Gan Y, Hanaor DAH *et al.* An improved semi-analytical solution for stress at round-tip notches. *Eng Fract Mech* 2015;**149**:134–43.

245. Buicciarelli L. Stresses : Beams in Bending. *Engineering Mechanics of Solids*. Massachusetts Institute of Technology: MIT OpenCourseWare, 2004, 235–61.

246. Gere JM, Timoshenko SP. *Mechanics of Materials*. PWS Publishing Company, 1997.

247. Beer FP, Jr. ERJ, DeWolf JT *et al. Mechanics of Materials*. 7th ed. McGraw-Hill Education, 2015.

248. Mostafavi M, Collins DM, Cai B *et al.* Yield behavior beneath hardness indentations in ductile metals, measured by three-dimensional computed X-ray tomography and digital volume correlation. *Acta Mater* 2015;**82**:468–82.

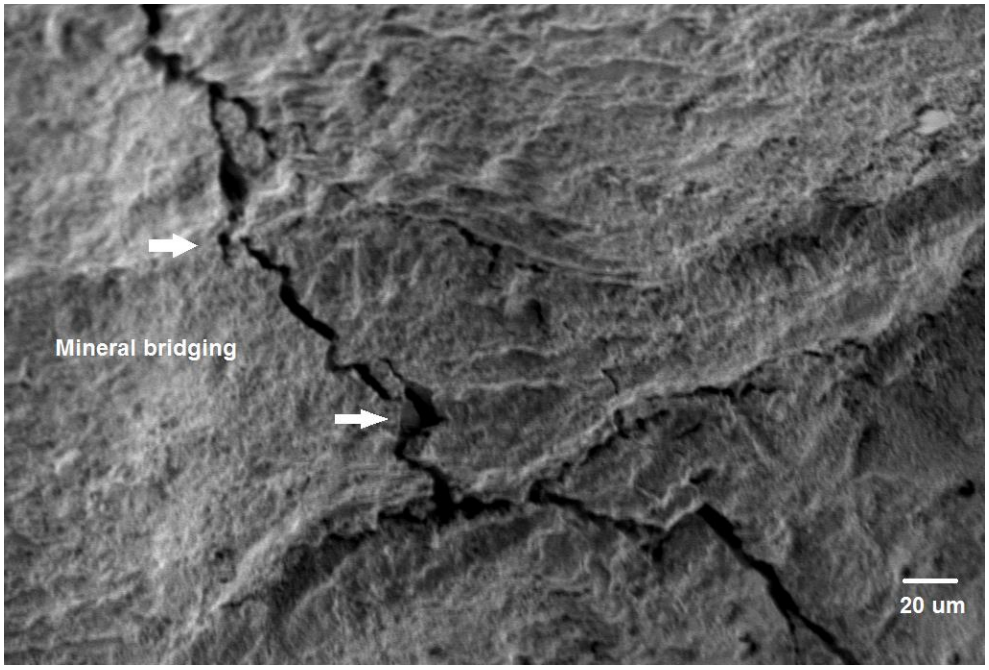
249. Mostafavi M, Bradley R, Armstrong DEJ *et al.* Quantifying yield behaviour in metals by X-ray nanotomography. *Nat Publ Gr* 2016:1–7.

10 Appendix

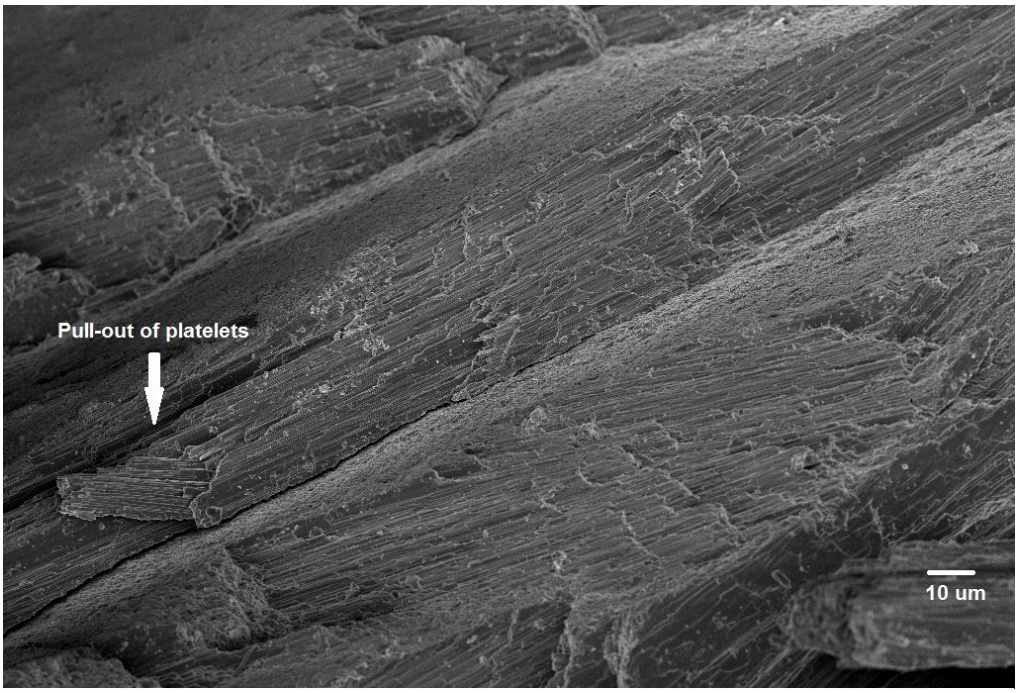
10.1 Further investigation of microstructures of limpets

British limpet consists of three layers as it is revealed by tomographs (*Figure 3.1.3*(a)). Further investigation has been done on cracked pre-notched British limpets in synchrotron to study microstructures inside these layers and the response of the complicated and hieratical microstructure on mechanical loading.

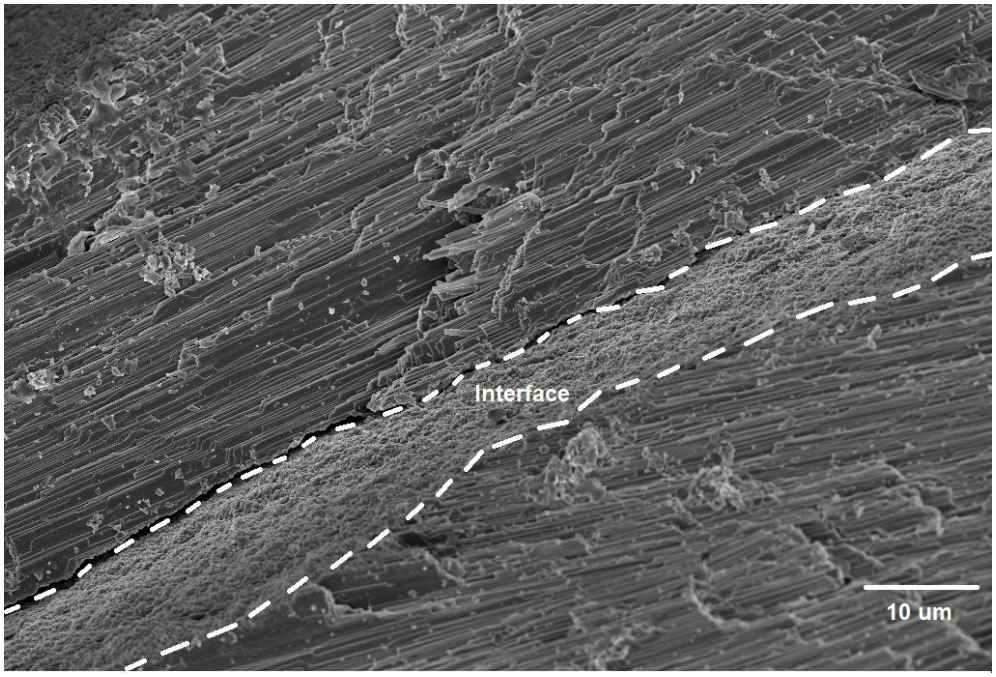
SEM images therefore have been collected with the help from Koen Evers using Merlin-60-62 scanning electron microscope (SEM) in crack region and inside the fracture surface. Complied lamellas can be easily identified by SEM images inside slimpet monolayer (*Figure 10.1.1* (b) (c) and (d)). In addition, different responses of the observed microstructures under compression loading have been learned. Apart from the crack deflection and micro-cracking observed in reconstructed synchrotron tomograph of pre-notched dry limpet 2 (*Figure 3.1.26* (b)), mineral bridging in crack path (*Figure 10.1.1* (a)) and the pull-out of platelets (*Figure 10.1.1* (b)) are also observed in SEM images. The interface between different monolayers is also observed in micro-scale (*Figure 10.1.1* (b)) which is believed to arrest the crack propagation [12]. In a monolayer, channel fracture is easily spotted in fracture surface (*Figure 10.1.1* (d)) as the crack tends to propagate along weak interface between platelets and with further development, the crack grows into stiffer platelets, causing the fracture of platelets. All these factors contribute to the complex toughening mechanisms of limpets, which make the modelling of mechanical behaviors of limpets in microscale complicated. Although SEM images revel better microstructures than X-ray tomographs, these images cannot be used for 3D volume structure rendering.



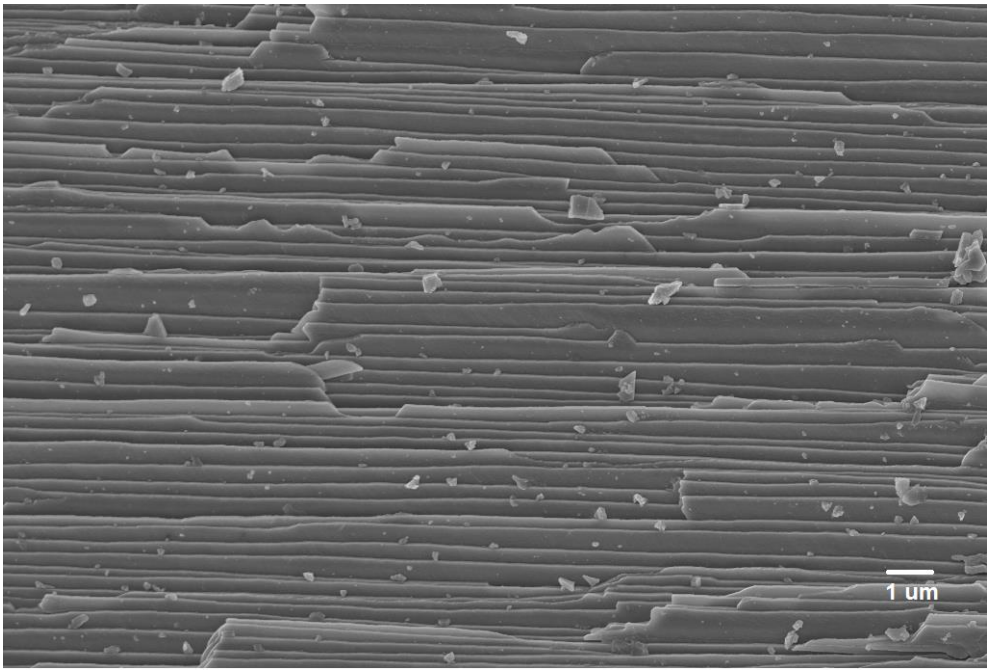
(a)



(b)



(c)



(d)

Figure 10.1.1.SEM images of crack developed in compressed shell. (a) Mineral bridging ;(b) Pull-out of stacked platelets; (c) Complicated morphology of interface between layers; (d) delaminated and cracked platelets within a monolayer.

10.2 Complementary information for Chapter 5

Table 10.2.1.Original simulated results of porosity and E/E_0 for each part of individual cortical bone sample from the selected 10 out of 18 samples for the calculation of E_0.

		Orthogonal to osteon longitudinal axis X direction in *Figure 5.1.1* as loading direction		Orthogonal to osteon longitudinal axis Y direction in *Figure 5.1.1* as loading direction		Along osteon longitudinal axis Z direction in *Figure 5.1.1* as loading direction	
		Part 1	Part 2	Part 1	Part 2	Part 1	Part 2
THR111	Porosity (%)	2.19	1.81	2.19	1.81	2.19	1.81
	E/E_0	0.98	0.98	0.98	0.98	0.95	0.96
THR110	Porosity (%)	1.36	3.43	1.36	3.43	1.36	3.43
	E/E_0	0.99	0.96	0.98	0.95	0.97	0.91
THR106b	Porosity (%)	3.48	3.26	3.48	3.26	3.48	3.26
	E/E_0	0.96	0.97	0.96	0.96	0.92	0.93
THR63	Porosity (%)	3.56	4.72	3.56	4.72	3.56	4.72
	E/E_0	0.96	0.94	0.95	0.94	0.89	0.84
THR103a	Porosity (%)	3.58	6.35	3.58	6.35	3.58	6.35
	E/E_0	0.96	0.93	0.96	0.91	0.92	0.83
THR108a	Porosity (%)	6.35	7.49	6.35	7.49	6.35	7.49
	E/E_0	0.92	0.90	0.93	0.91	0.83	0.79
THR79	Porosity (%)	6.80	8.48	6.80	8.48	6.80	8.48
	E/E_0	0.92	0.90	0.91	0.89	0.81	0.74
THR107	Porosity (%)	8.36	6.96	8.36	6.96	8.36	6.96
	E/E_0	0.88	0.89	0.90	0.92	0.77	0.81
THR69	Porosity (%)	7.66	10.55	7.66	10.55	7.66	10.55
	E/E_0	0.89	0.85	0.91	0.87	0.75	0.62
THR91c	Porosity (%)	7.93	10.61	7.93	10.61	7.93	10.61
	E/E_0	0.88	0.85	0.90	0.87	0.78	0.72
THR82	Porosity (%)	9.30	13.63	9.30	13.63	9.30	13.63
	E/E_0	0.87	0.81	0.88	0.82	0.77	0.64
THR75	Porosity (%)	6.31	16.65	6.31	16.65	6.31	16.65
	E/E_0	0.90	0.74	0.92	0.77	0.84	0.60
THR76	Porosity (%)	8.20	15.14	8.20	15.14	8.20	15.14
	E/E_0	0.91	0.83	0.88	0.76	0.78	0.53

THR104	Porosity (%)	12.22	11.25	12.22	11.25	12.22	11.25
	E/E_0	0.81	0.84	0.84	0.86	0.62	0.65
THR74a	Porosity (%)	13.15	14.64	13.15	14.64	13.15	14.64
	E/E_0	0.82	0.78	0.81	0.79	0.63	0.60
THR04b	Porosity (%)	11.58	16.63	11.58	16.63	11.58	16.63
	E/E_0	0.86	0.79	0.83	0.74	0.63	0.50
THR72	Porosity (%)	16.93	14.56	16.93	14.56	16.93	14.56
	E/E_0	0.71	0.76	0.79	0.81	0.51	0.59
THR83	Porosity (%)	22.11	21.09	22.11	21.09	22.11	21.09
	E/E_0	0.66	0.73	0.66	0.69	0.41	0.43

Table 10.2.2. Porosities measured on planes in the longitudinal direction of cortical bones in one pixel interval.

Position of cross-section in longitudinal axis of bone (mm)	Cross-sectional porosity (%)
0.000	6.86
0.007	6.99
0.014	7.07
0.021	7.10
0.028	7.14
0.035	7.21
0.041	7.24
0.048	7.23
0.055	7.24
0.062	7.20
0.069	7.21
0.076	7.15
0.083	7.14
0.090	7.13
0.097	7.14
0.104	7.12
0.110	7.11
0.117	7.11
0.124	7.10
0.131	7.07
0.138	7.01
0.145	6.93
0.152	6.90
0.159	6.82
0.166	6.76
0.173	6.71

0.179	6.65
0.186	6.65
0.193	6.63
0.200	6.66
0.207	6.63
0.214	6.58
0.221	6.50
0.228	6.45
0.235	6.40
0.242	6.38
0.248	6.29
0.255	6.27
0.262	6.22
0.269	6.16
0.276	6.15
0.283	6.12
0.290	6.08
0.297	6.04
0.304	6.02
0.311	5.99
0.317	5.99
0.324	5.95
0.331	5.94
0.338	5.93
0.345	5.94
0.352	5.93
0.359	5.92
0.366	5.90
0.373	5.86
0.380	5.85
0.386	5.84
0.393	5.86
0.400	5.85
0.407	5.81
0.414	5.80
0.421	5.76
0.428	5.77
0.435	5.77
0.442	5.73
0.449	5.74
0.455	5.70
0.462	5.70
0.469	5.62
0.476	5.57

0.483	5.54
0.490	5.59
0.497	5.62
0.504	5.61
0.511	5.58
0.518	5.58
0.524	5.59
0.531	5.56
0.538	5.53
0.545	5.51
0.552	5.46
0.559	5.44
0.566	5.42
0.573	5.37
0.580	5.33
0.587	5.29
0.593	5.25
0.600	5.22
0.607	5.21
0.614	5.22
0.621	5.22
0.628	5.21
0.635	5.19
0.642	5.18
0.649	5.15
0.656	5.17
0.662	5.23
0.669	5.28
0.676	5.33
0.683	5.37
0.690	5.40
0.697	5.45
0.704	5.49
0.711	5.54
0.718	5.58
0.725	5.58
0.731	5.58
0.738	5.64
0.745	5.67
0.752	5.72
0.759	5.74
0.766	5.75
0.773	5.79
0.780	5.78

0.787	5.80
0.794	5.83
0.800	5.89
0.807	5.94
0.814	5.98
0.821	6.05
0.828	6.13
0.835	6.19
0.842	6.25
0.849	6.28
0.856	6.28
0.863	6.31
0.869	6.32
0.876	6.27
0.883	6.22
0.890	6.20
0.897	6.20
0.904	6.22
0.911	6.24
0.918	6.22
0.925	6.21
0.932	6.24
0.938	6.22
0.945	6.25
0.952	6.26
0.959	6.28
0.966	6.36
0.973	6.45
0.980	6.50
0.987	6.54
0.994	6.56
1.001	6.56
1.007	6.52
1.014	6.45
1.021	6.40
1.028	6.34
1.035	6.35
1.042	6.36
1.049	6.41
1.056	6.45
1.063	6.48
1.070	6.51
1.076	6.52
1.083	6.49

1.090	6.49
1.097	6.51
1.104	6.53
1.111	6.58
1.118	6.58
1.125	6.62
1.132	6.64
1.139	6.67
1.145	6.69
1.152	6.72
1.159	6.73
1.166	6.76
1.173	6.76
1.180	6.79
1.187	6.81
1.194	6.82
1.201	6.78
1.208	6.78
1.214	6.75
1.221	6.77
1.228	6.79
1.235	6.79
1.242	6.80
1.249	6.82
1.256	6.83
1.263	6.82
1.270	6.80
1.277	6.76
1.283	6.73
1.290	6.69
1.297	6.67
1.304	6.67
1.311	6.67
1.318	6.67
1.325	6.64
1.332	6.62
1.339	6.62
1.346	6.59
1.352	6.56
1.359	6.55
1.366	6.54
1.373	6.51
1.380	6.52
1.387	6.55

1.394	6.58
1.401	6.65
1.408	6.68
1.415	6.71
1.421	6.75
1.428	6.82
1.435	6.83
1.442	6.88
1.449	6.91
1.456	6.93
1.463	6.94
1.470	6.91
1.477	6.85
1.484	6.81
1.490	6.82
1.497	6.82
1.504	6.86
1.511	6.87
1.518	6.90
1.525	6.98
1.532	7.06
1.539	7.11
1.546	7.18
1.553	7.23
1.559	7.31
1.566	7.39
1.573	7.44
1.580	7.44
1.587	7.47
1.594	7.47
1.601	7.47
1.608	7.46
1.615	7.49
1.622	7.47
1.628	7.42
1.635	7.35
1.642	7.27
1.649	7.19
1.656	7.09
1.663	7.01
1.670	6.94
1.677	6.86
1.684	6.80
1.691	6.72

1.697	6.68
1.704	6.63
1.711	6.64
1.718	6.61
1.725	6.55
1.732	6.53
1.739	6.49
1.746	6.49
1.753	6.52
1.760	6.53
1.766	6.54
1.773	6.56
1.780	6.59
1.787	6.60
1.794	6.62
1.801	6.64
1.808	6.70
1.815	6.72
1.822	6.76
1.829	6.81
1.835	6.83
1.842	6.85
1.849	6.85
1.856	6.86
1.863	6.88
1.870	6.94
1.877	6.94
1.884	6.92
1.891	6.88
1.898	6.89
1.904	6.90
1.911	6.89
1.918	6.86
1.925	6.82
1.932	6.77
1.939	6.79
1.946	6.74
1.953	6.67
1.960	6.62
1.967	6.53
1.973	6.38
1.980	6.32
1.987	6.26
1.994	6.23

2.001	6.24
2.008	6.26
2.015	6.29
2.022	6.30
2.029	6.35
2.036	6.37
2.042	6.41
2.049	6.39
2.056	6.39
2.063	6.44
2.070	6.42
2.077	6.42
2.084	6.43
2.091	6.40
2.098	6.38
2.105	6.34
2.111	6.29
2.118	6.22
2.125	6.20
2.132	6.15
2.139	6.19
2.146	6.20
2.153	6.17
2.160	6.16
2.167	6.14
2.174	6.12
2.180	6.15
2.187	6.22
2.194	6.29
2.201	6.34
2.208	6.40
2.215	6.48
2.222	6.57
2.229	6.65
2.236	6.77
2.243	6.86
2.249	6.98
2.256	7.06
2.263	7.07
2.270	7.11
2.277	7.11
2.284	7.06
2.291	6.98
2.298	6.84

2.305	6.74
2.312	6.65
2.318	6.53
2.325	6.43
2.332	6.30
2.339	6.21
2.346	6.11
2.353	6.01
2.360	6.01
2.367	5.99
2.374	5.96
2.381	5.92
2.387	5.87
2.394	5.87
2.401	5.90
2.408	5.90
2.415	5.92
2.422	5.96
2.429	5.98
2.436	6.02
2.443	6.05
2.450	6.08
2.456	6.13
2.463	6.19
2.470	6.28
2.477	6.31
2.484	6.37
2.491	6.40
2.498	6.44
2.505	6.47
2.512	6.49
2.519	6.48
2.525	6.45
2.532	6.45
2.539	6.47
2.546	6.46
2.553	6.45
2.560	6.41
2.567	6.39
2.574	6.39
2.581	6.44
2.588	6.47
2.594	6.45
2.601	6.48

2.608	6.45
2.615	6.39
2.622	6.32
2.629	6.27
2.636	6.24
2.643	6.28
2.650	6.31
2.657	6.34
2.663	6.38
2.670	6.40
2.677	6.44
2.684	6.50
2.691	6.55
2.698	6.59
2.705	6.61
2.712	6.64
2.719	6.71
2.726	6.81
2.732	6.86
2.739	6.92
2.746	6.94
2.753	6.97
2.760	7.01
2.767	7.07
2.774	7.10
2.781	7.14
2.788	7.17
2.795	7.20
2.801	7.18
2.808	7.18
2.815	7.13
2.822	7.11
2.829	7.09
2.836	7.09
2.843	7.04
2.850	7.02
2.857	6.92
2.864	6.82
2.870	6.80
2.877	6.75
2.884	6.73
2.891	6.74
2.898	6.75
2.905	6.75

2.912	6.73
2.919	6.75
2.926	6.79
2.933	6.86
2.939	6.93
2.946	7.00
2.953	7.04
2.960	7.09
2.967	7.11
2.974	7.17
2.981	7.23
2.988	7.25
2.995	7.26
3.002	7.25
3.008	7.26
3.015	7.27
3.022	7.30
3.029	7.32
3.036	7.31
3.043	7.30
3.050	7.26
3.057	7.28
3.064	7.31
3.071	7.30
3.077	7.31
3.084	7.38
3.091	7.40
3.098	7.45
3.105	7.45
3.112	7.47
3.119	7.49
3.126	7.54
3.133	7.61
3.140	7.67
3.146	7.76
3.153	7.87
3.160	7.96
3.167	8.07
3.174	8.15
3.181	8.22
3.188	8.32
3.195	8.45
3.202	8.56
3.209	8.64

3.215	8.70
3.222	8.74
3.229	8.76
3.236	8.78
3.243	8.78
3.250	8.81
3.257	8.80
3.264	8.79
3.271	8.77
3.278	8.77
3.284	8.77
3.291	8.76
3.298	8.74
3.305	8.73
3.312	8.70
3.319	8.70
3.326	8.67
3.333	8.67
3.340	8.66
3.347	8.62
3.353	8.56
3.360	8.49
3.367	8.47
3.374	8.46
3.381	8.45
3.388	8.37
3.395	8.39
3.402	8.38
3.409	8.37
3.416	8.31
3.422	8.26
3.429	8.26
3.436	8.24
3.443	8.14
3.450	8.08
3.457	8.04
3.464	8.02
3.471	8.02
3.478	7.98
3.485	7.91
3.491	7.88
3.498	7.93
3.505	7.90
3.512	7.88

3.519	7.91
3.526	7.94
3.533	7.93
3.540	7.93
3.547	7.88
3.554	7.87
3.560	7.88
3.567	7.88
3.574	7.84
3.581	7.75
3.588	7.69
3.595	7.65
3.602	7.62
3.609	7.61
3.616	7.62
3.623	7.62
3.629	7.64
3.636	7.68
3.643	7.77
3.650	7.83
3.657	7.90
3.664	7.92
3.671	7.95
3.678	7.94
3.685	7.96
3.692	7.94
3.698	7.88
3.705	7.89
3.712	7.93
3.719	7.94
3.726	7.94
3.733	7.96
3.740	8.01
3.747	8.13
3.754	8.25
3.761	8.33
3.767	8.35
3.774	8.39
3.781	8.41
3.788	8.43
3.795	8.45
3.802	8.45
3.809	8.42
3.816	8.40

3.823	8.36
3.830	8.30
3.836	8.30
3.843	8.24
3.850	8.17
3.857	8.07
3.864	7.96
3.871	7.89
3.878	7.82
3.885	7.76
3.892	7.67
3.899	7.63
3.905	7.59
3.912	7.53
3.919	7.50
3.926	7.45
3.933	7.41
3.940	7.38
3.947	7.37
3.954	7.34
3.961	7.37
3.968	7.40
3.974	7.48
3.981	7.56
3.988	7.66
3.995	7.77
4.002	7.85
4.009	7.91
4.016	7.94
4.023	7.93
4.030	7.92
4.037	7.89
4.043	7.88
4.050	7.87
4.057	7.86
4.064	7.75
4.071	7.68
4.078	7.61
4.085	7.51
4.092	7.46
4.099	7.45
4.106	7.48
4.112	7.51
4.119	7.57

4.126	7.64
4.133	7.67
4.140	7.71
4.147	7.70
4.154	7.67
4.161	7.63
4.168	7.59
4.175	7.53
4.181	7.45
4.188	7.36
4.195	7.29
4.202	7.24
4.209	7.19
4.216	7.17
4.223	7.17
4.230	7.12
4.237	7.04
4.244	6.98
4.250	6.93
4.257	6.89
4.264	6.86
4.271	6.89
4.278	6.91
4.285	6.93
4.292	6.92
4.299	6.93
4.306	6.99
4.313	7.04
4.319	7.07
4.326	7.10
4.333	7.14
4.340	7.19
4.347	7.24
4.354	7.29
4.361	7.34
4.368	7.37
4.375	7.41
4.382	7.48
4.388	7.57
4.395	7.64
4.402	7.68
4.409	7.73
4.416	7.79
4.423	7.80

4.430	7.84
4.437	7.89
4.444	7.97
4.451	8.06
4.457	8.14
4.464	8.22
4.471	8.28
4.478	8.33
4.485	8.43
4.492	8.44
4.499	8.48
4.506	8.49
4.513	8.48
4.520	8.51
4.526	8.48
4.533	8.42
4.540	8.36
4.547	8.30
4.554	8.24
4.561	8.20
4.568	8.24
4.575	8.27
4.582	8.31
4.589	8.30
4.595	8.29
4.602	8.25
4.609	8.24
4.616	8.21
4.623	8.22
4.630	8.24
4.637	8.28
4.644	8.30
4.651	8.30
4.658	8.32
4.664	8.31
4.671	8.30
4.678	8.29
4.685	8.31
4.692	8.37
4.699	8.41
4.706	8.45
4.713	8.47
4.720	8.51
4.727	8.55

4.733	8.62
4.740	8.71
4.747	8.75
4.754	8.84
4.761	8.94
4.768	8.98
4.775	9.00
4.782	9.00
4.789	9.00
4.796	8.99
4.802	8.99
4.809	8.98
4.816	9.06
4.823	9.16
4.830	9.23
4.837	9.33
4.844	9.37
4.851	9.39
4.858	9.41
4.865	9.42
4.871	9.44
4.878	9.41
4.885	9.37
4.892	9.42
4.899	9.46
4.906	9.51
4.913	9.55
4.920	9.57
4.927	9.56
4.934	9.53
4.940	9.46
4.947	9.39
4.954	9.29
4.961	9.16
4.968	9.01
4.975	8.90
4.982	8.78
4.989	8.66
4.996	8.49
5.003	8.30
5.009	8.09
5.016	7.93
5.023	7.84
5.030	7.74

5.037	7.67
5.044	7.60
5.051	7.55
5.058	7.51
5.065	7.44
5.072	7.39
5.078	7.31
5.085	7.24
5.092	7.09
5.099	7.01
5.106	6.93
5.113	6.87
5.120	6.80
5.127	6.75
5.134	6.69
5.141	6.70
5.147	6.68
5.154	6.67
5.161	6.70
5.168	6.73
5.175	6.75
5.182	6.77
5.189	6.82
5.196	6.85
5.203	6.91
5.210	6.94
5.216	7.00
5.223	7.05
5.230	7.07
5.237	7.07
5.244	7.09
5.251	7.06
5.258	7.06
5.265	7.02
5.272	6.97
5.279	6.93
5.285	6.88
5.292	6.83
5.299	6.73
5.306	6.63
5.313	6.55
5.320	6.47
5.327	6.40
5.334	6.35

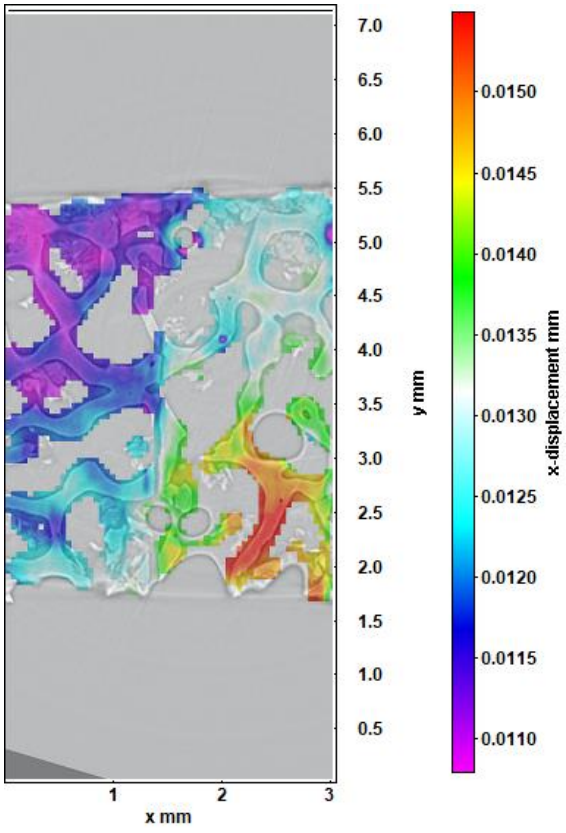
5.341	6.32
5.348	6.31
5.354	6.30
5.361	6.31
5.368	6.32
5.375	6.31
5.382	6.35
5.389	6.34
5.396	6.36
5.403	6.35
5.410	6.36
5.417	6.35
5.423	6.37
5.430	6.34
5.437	6.27
5.444	6.22
5.451	6.19
5.458	6.18
5.465	6.19
5.472	6.21
5.479	6.26
5.486	6.24
5.492	6.28
5.499	6.30
5.506	6.33
5.513	6.39
5.520	6.45
5.527	6.49
5.534	6.54
5.541	6.54
5.548	6.50
5.555	6.51
5.561	6.49
5.568	6.48
5.575	6.46
5.582	6.47
5.589	6.48
5.596	6.54
5.603	6.58
5.610	6.57
5.617	6.57
5.624	6.55
5.630	6.57
5.637	6.58

5.644	6.60
5.651	6.61
5.658	6.63
5.665	6.65
5.672	6.67
5.679	6.69
5.686	6.68
5.693	6.68
5.699	6.68
5.706	6.69
5.713	6.71
5.720	6.71
5.727	6.76
5.734	6.80
5.741	6.80
5.748	6.80
5.755	6.80
5.762	6.79
5.768	6.83
5.775	6.87
5.782	6.95
5.789	6.98
5.796	7.05
5.803	7.10
5.810	7.13
5.817	7.18
5.824	7.23
5.831	7.27
5.837	7.34
5.844	7.44
5.851	7.47
5.858	7.57
5.865	7.61
5.872	7.61
5.879	7.65
5.886	7.70
5.893	7.77
5.900	7.78
5.906	7.78
5.913	7.82
5.920	7.87
5.927	7.91
5.934	7.97
5.941	8.04

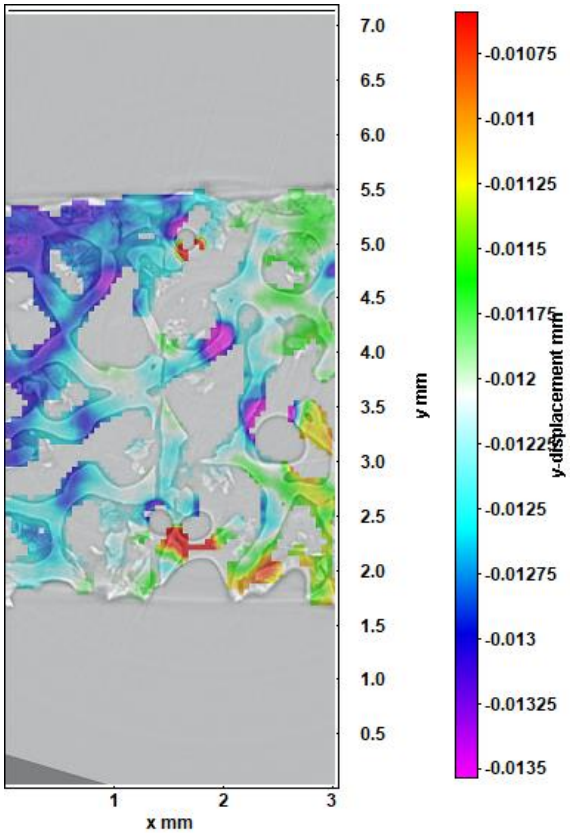
5.948	8.09
5.955	8.16
5.962	8.21
5.969	8.25
5.975	8.35
5.982	8.40
5.989	8.43
5.996	8.47
6.003	8.52
6.010	8.58
6.017	8.63
6.024	8.63

10.3 . Complementary information of Chapter 6

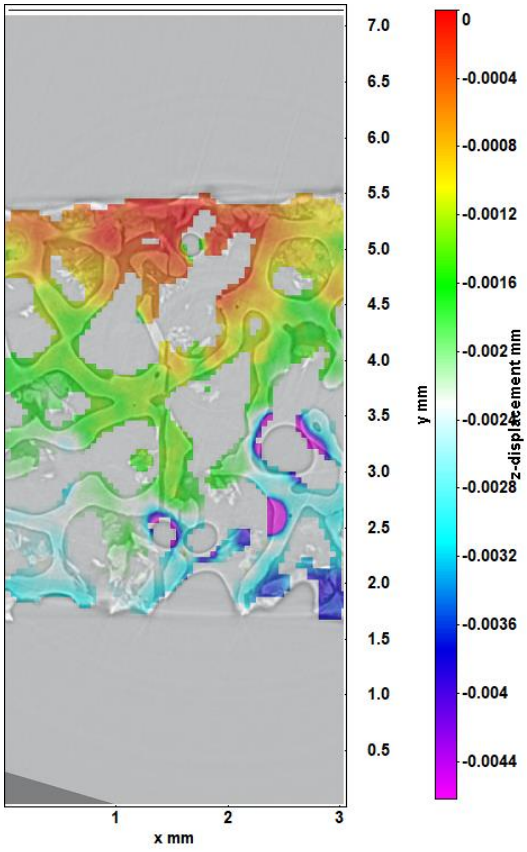
10.3.1 DVC results of trabecular bone under different loadings



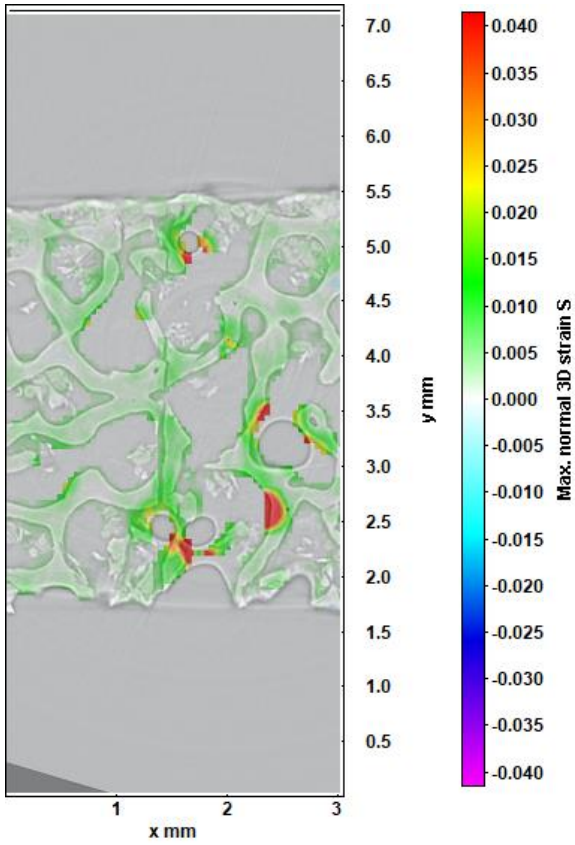
I. x displacement on XY plane(z=2.0736mm)



II. y displacement on XY plane(z=2.0736mm)

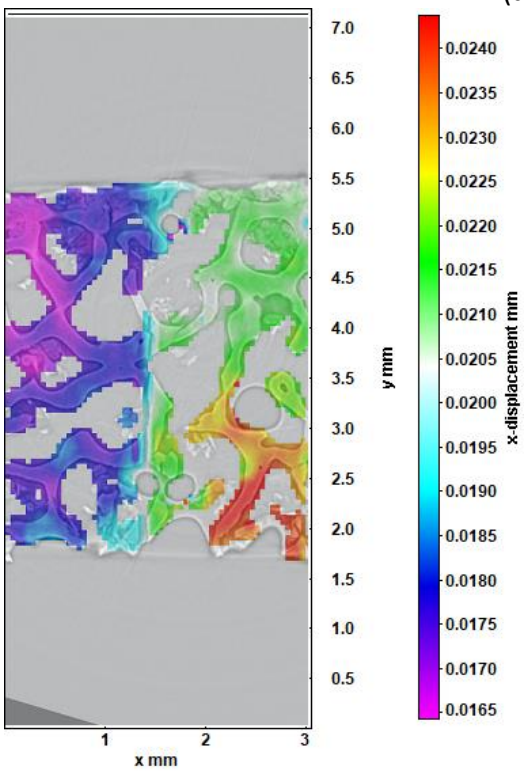


III. z displacement on XY plane(z=2.0736mm)

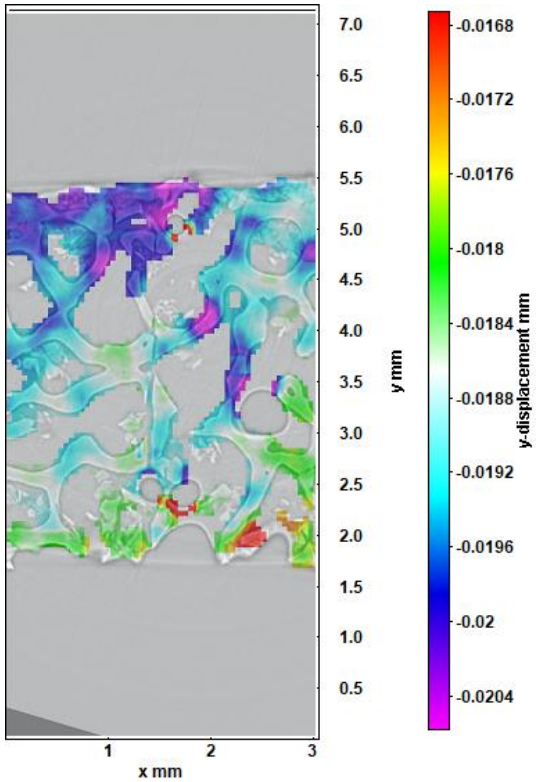


IV. max normal strain on XY plane(z=2.0736mm)

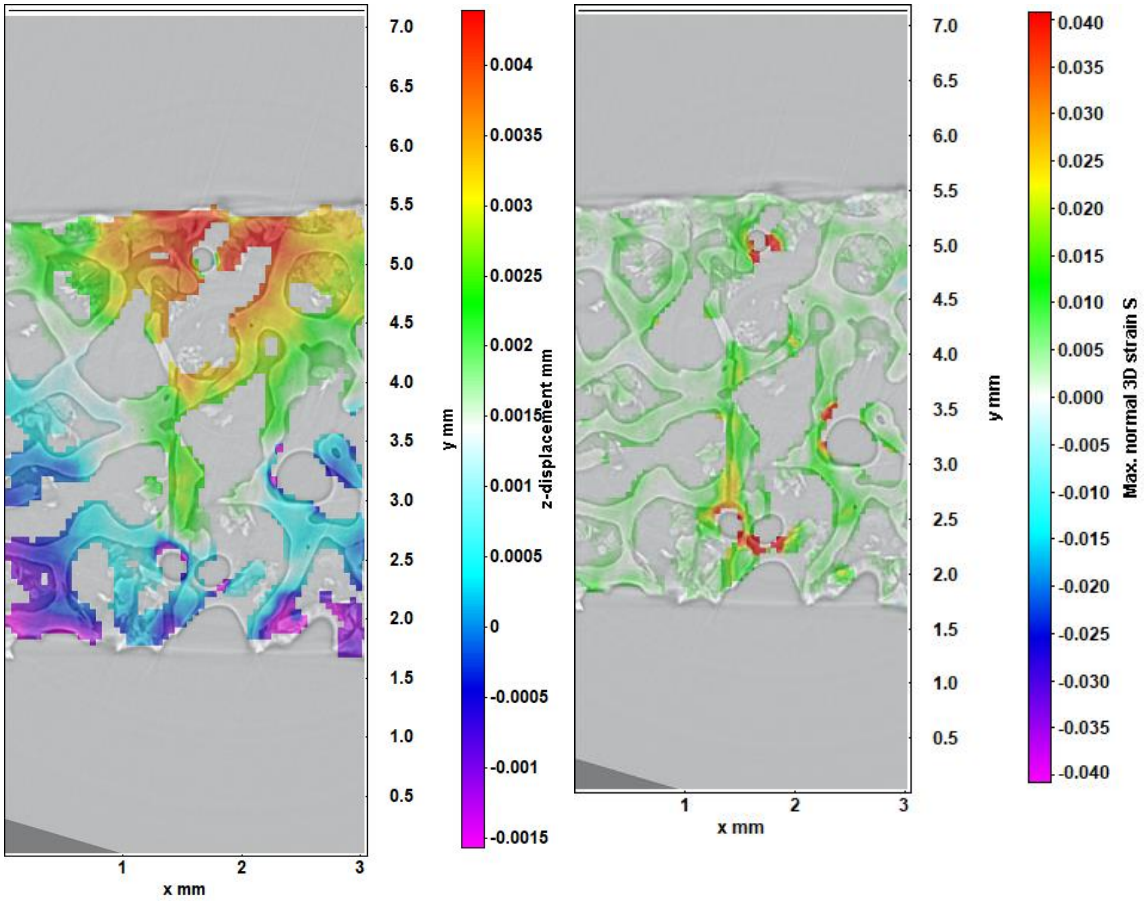
(a) 5N vs 10N



I. x displacement on XY plane(z=2.0736mm)



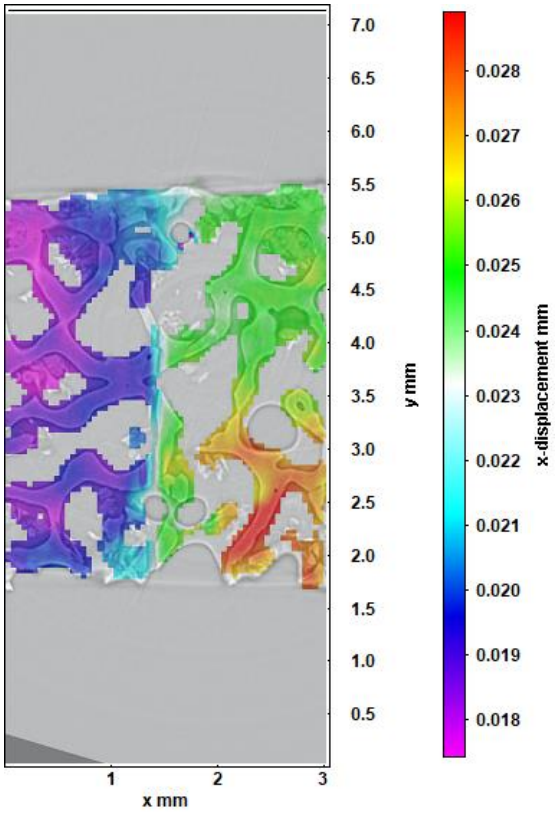
II. y displacement on XY plane(z=2.0736mm)



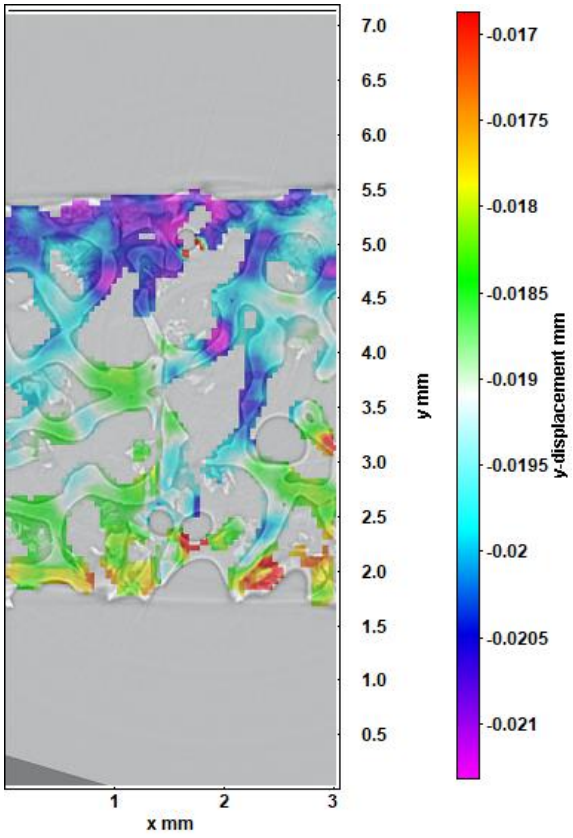
III. z displacement on XY plane(z=2.0736mm)

IV. max normal strain on XY plane(z=2.0736mm)

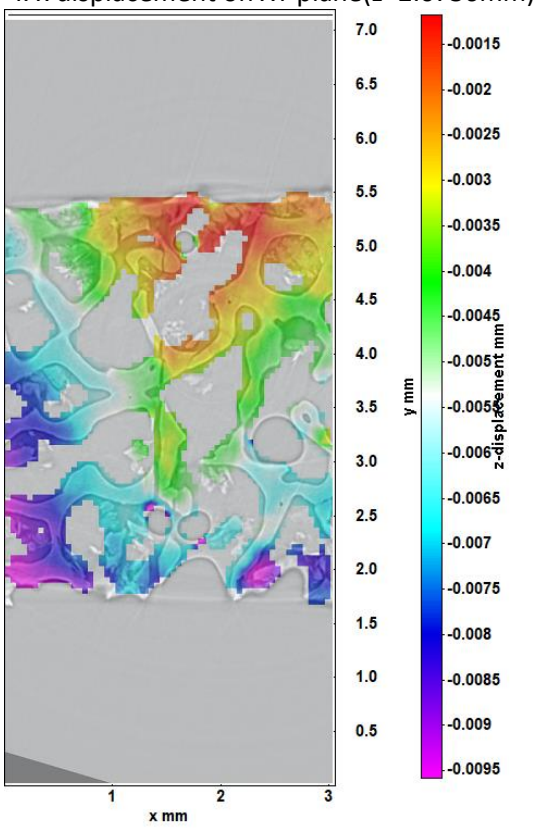
(b) 5N vs 15N



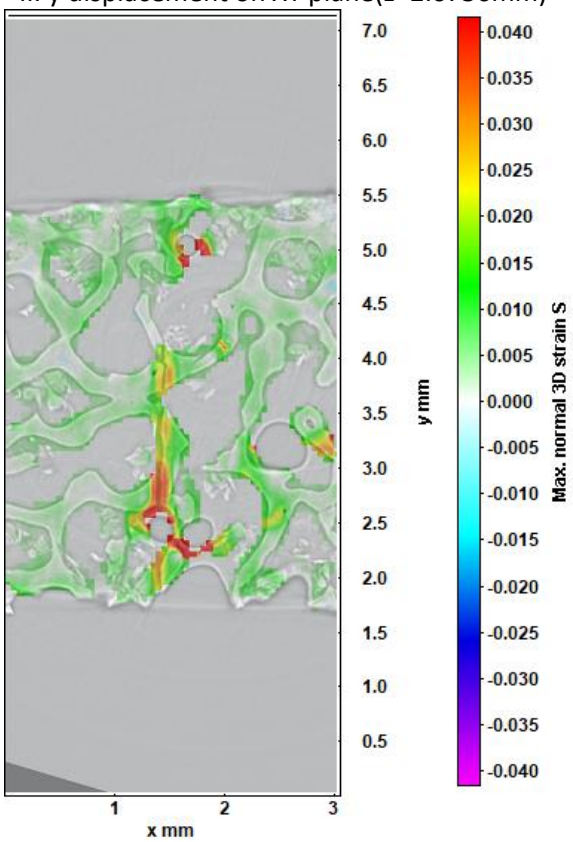
I. x displacement on XY plane(z=2.0736mm)



II. y displacement on XY plane(z=2.0736mm)

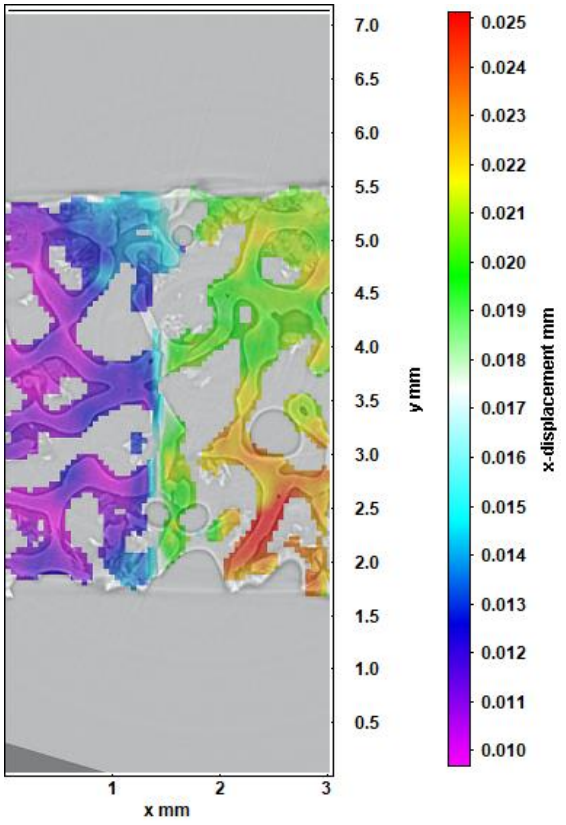


III. z displacement on XY plane(z=2.0736mm)

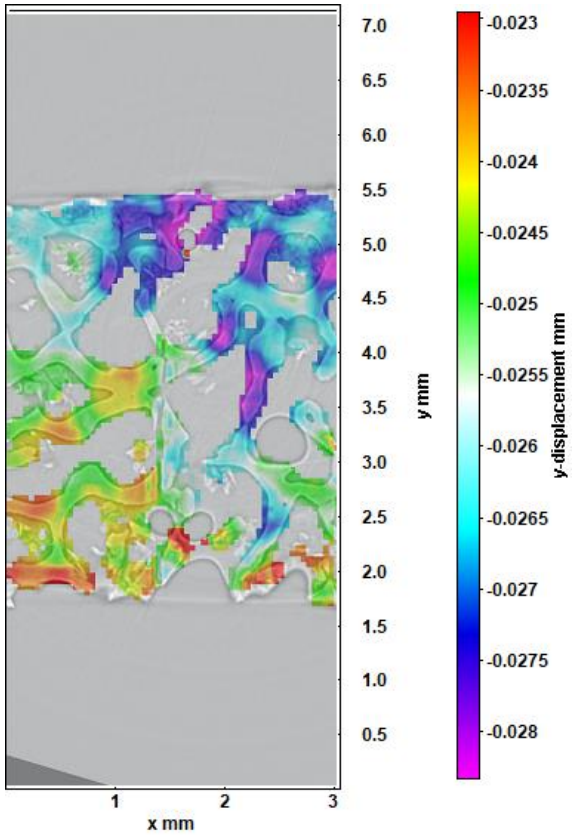


IV. max normal strain on XY plane(z=2.0736mm)

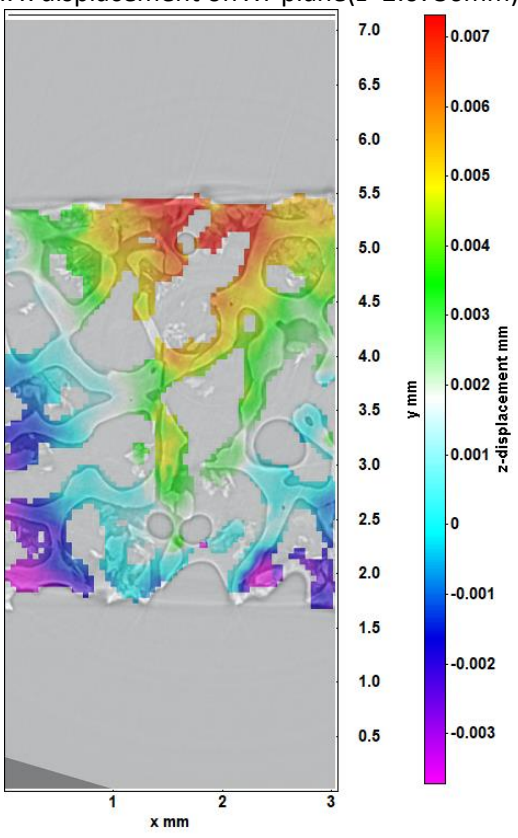
(c) 5N vs 20N



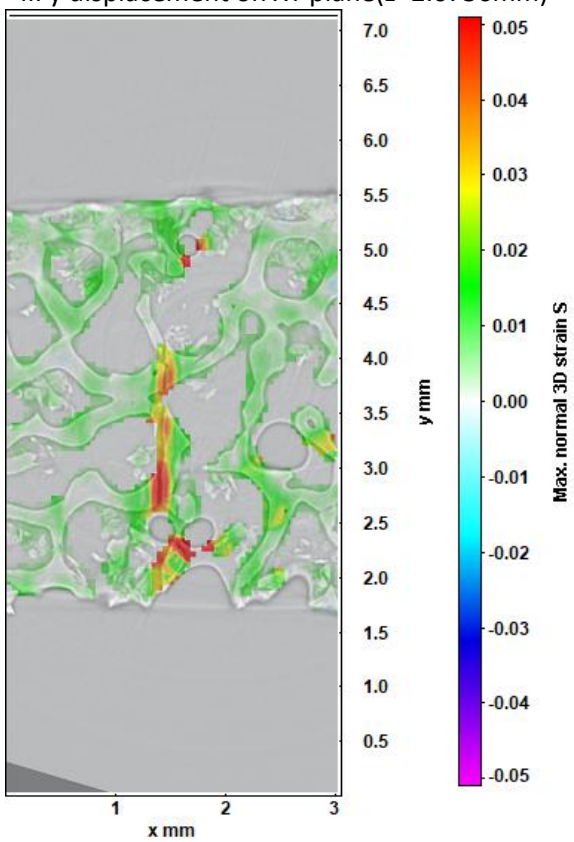
I. x displacement on XY plane(z=2.0736mm)



II. y displacement on XY plane(z=2.0736mm)

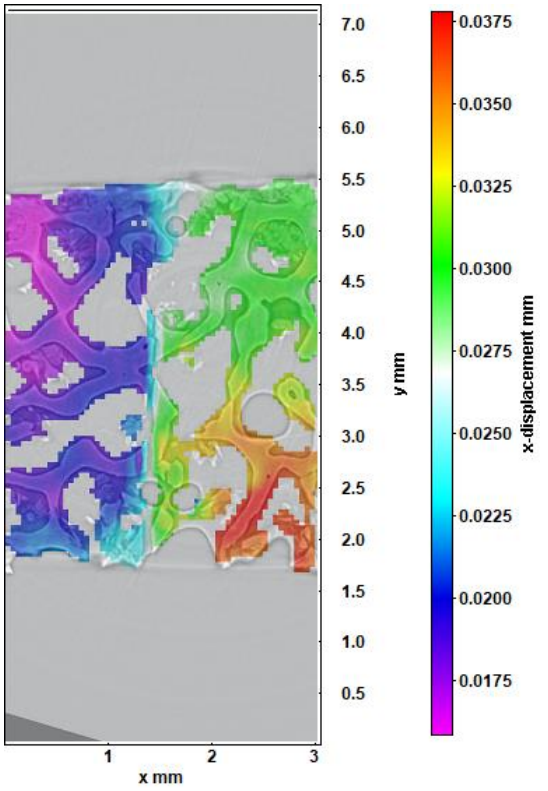


III. z displacement on XY plane(z=2.0736mm)

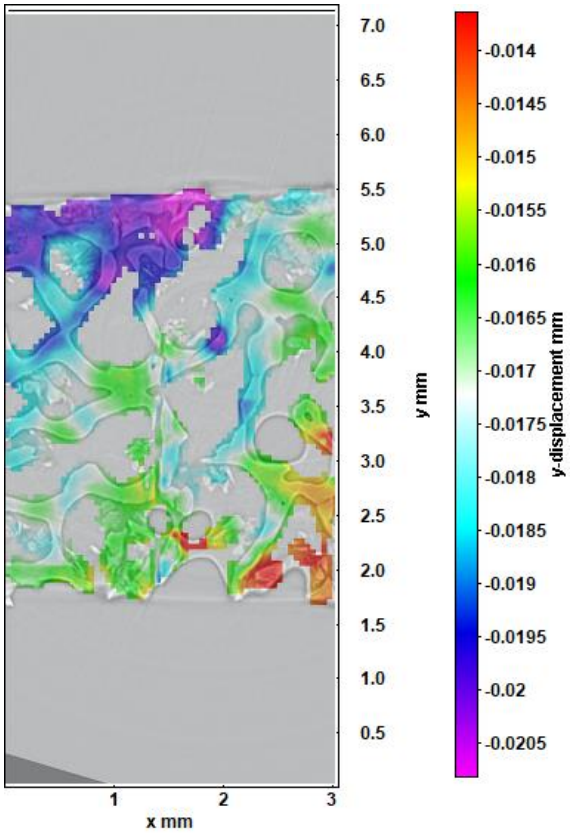


IV. max normal strain on XY plane(z=2.0736mm)

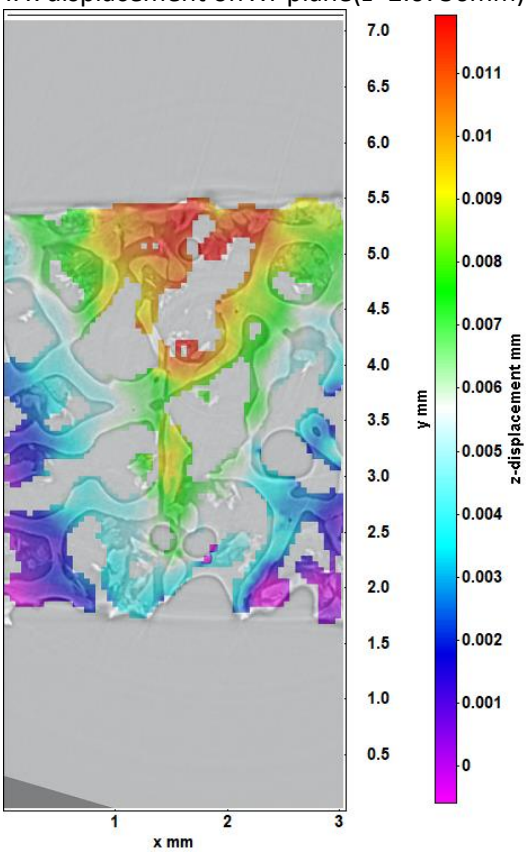
(d) 5N vs 25N



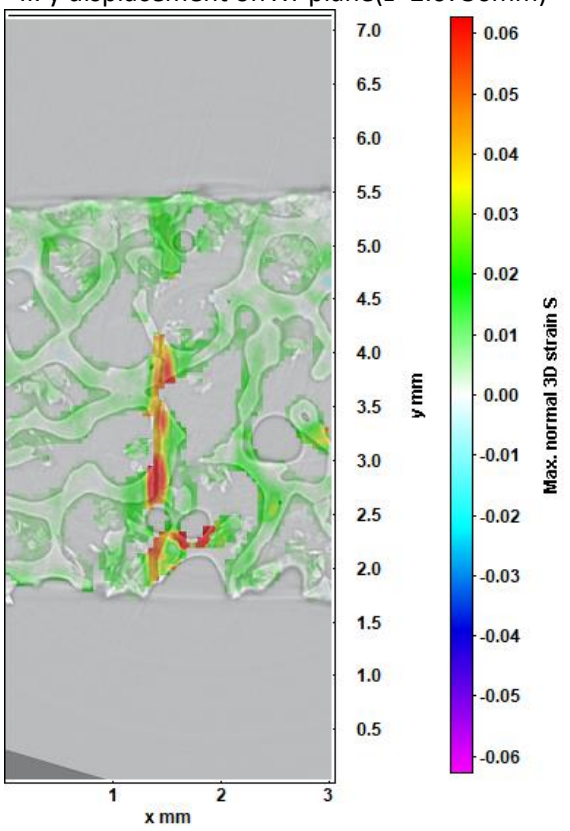
I. x displacement on XY plane(z=2.0736mm)



II. y displacement on XY plane(z=2.0736mm)

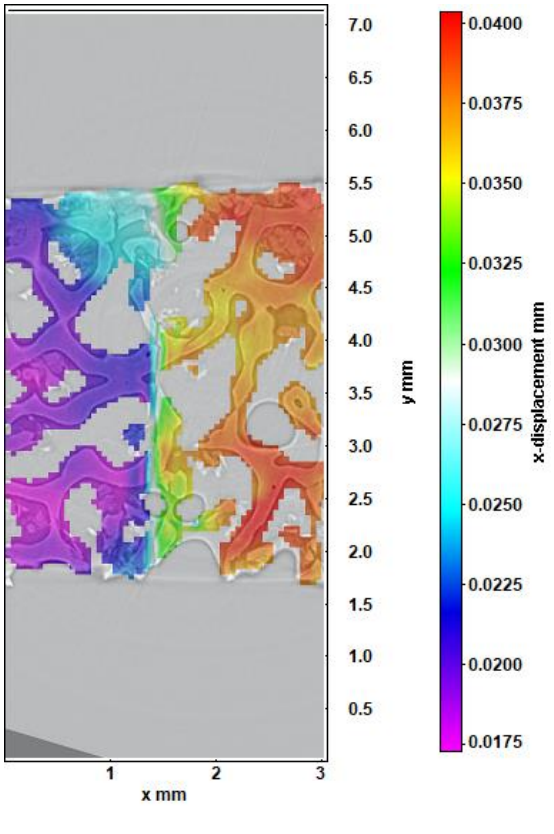


III. z displacement on XY plane(z=2.0736mm)

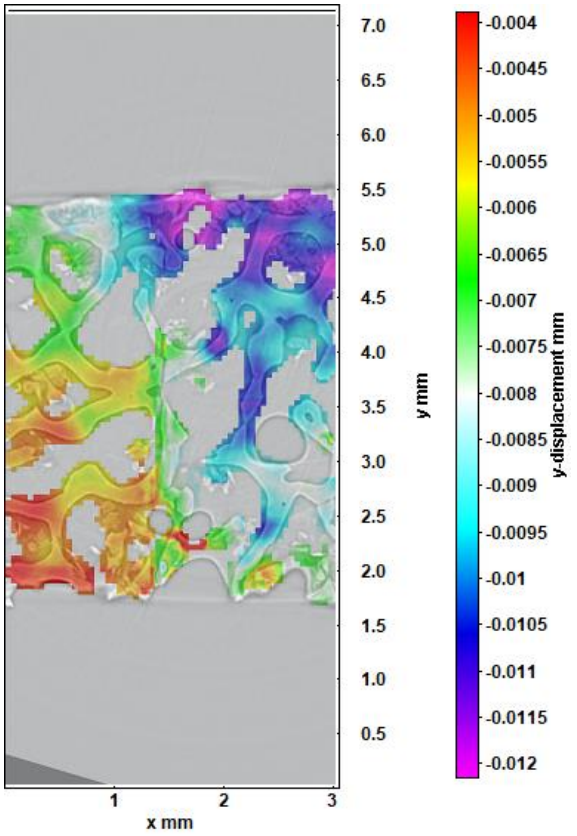


IV. max normal strain on XY plane(z=2.0736mm)

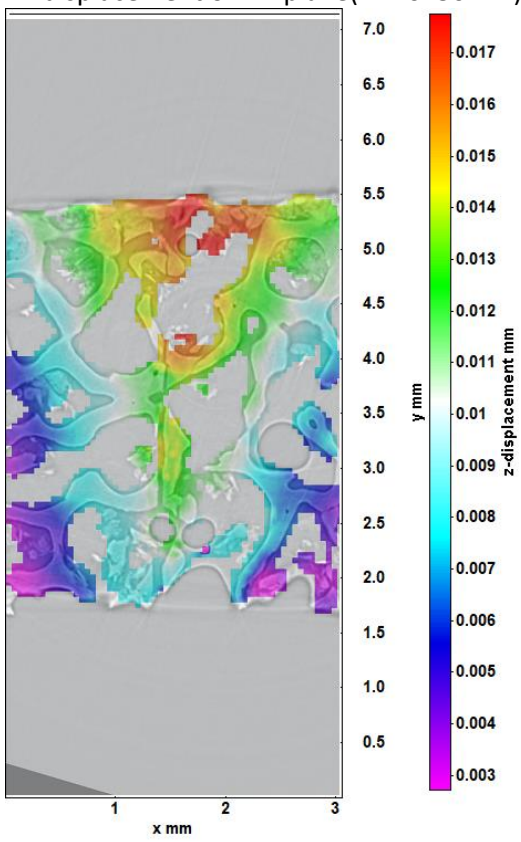
(e) 5N vs 30N



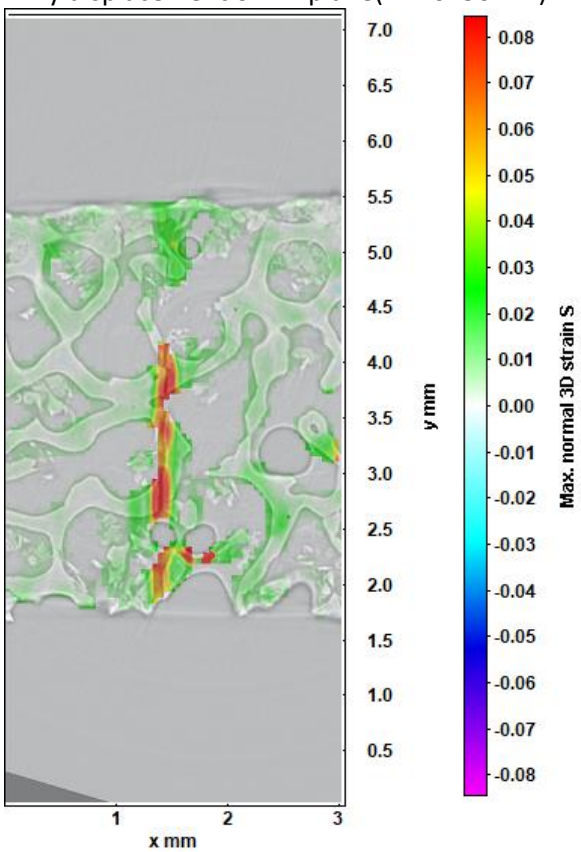
I. x displacement on XY plane(z=2.0736mm)



II. y displacement on XY plane(z=2.0736mm)



III. z displacement on XY plane(z=2.0736mm)



IV. max normal strain on XY plane(z=2.0736mm)

(f) 5N vs 35N

Figure 10.3.1. DVC results of displacement fields and max normal strains on XY plane (z=2.0736mm) under different loading states.(a) 5N vs 10N;(b) 5N vs 15N; (c) 5N vs 20N; (d) 5N vs 25N; (e) 5N vs 30N; (f)5N vs 35N.

10.3.2 Measurements of notch plus crack lengths

10.3.2.1 Notch plus crack segmented using Avizo

Due to the complex and manual nature of this method, only the notch plus crack developed under a load of 35 N using Avizo was segmented. Different Y positions (*Figure 10.3.2*) have been selected for the notch plus crack length measurement and measured lengths between crack surfaces (*Figure 10.3.2*) for different Y positions are listed in *Table 10.3.1*. The averaged length is 0.41±0.23 mm for notch plus crack developed under a load of 35 N. The same way to measure notch plus crack length at each selected position (emphasized in red in *Figure 10.3.2*) has been applied to all notch-crack length measurement in this *section 10.3.2*.

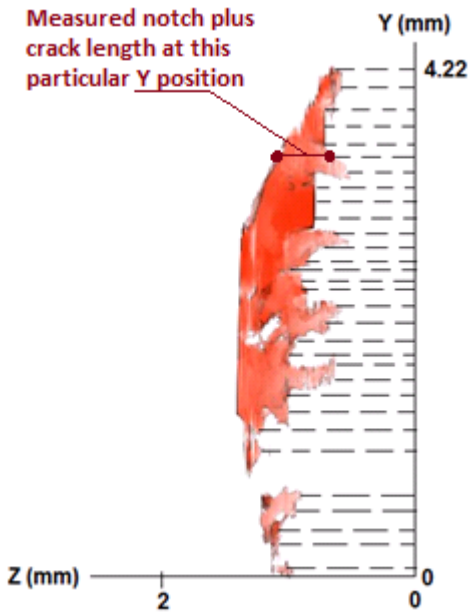


Figure 10.3.2. Different Y positions have been selected for crack measurement for segmented notch plus crack using Avizo under a load of 35N.

Table 10.3.1. Measured notch plus crack lengths at different Y positions.

Y Position (mm)	Measured notch plus crack length (mm)
0	0.08
0.08	0.12
0.16	0.06
0.43	0.16
0.53	0.27
0.63	0.31
1.02	0.16
1.19	0.16
1.36	0.42
1.46	0.43
1.60	0.77
1.68	0.76
1.75	0.41
1.85	0.45
2.06	0.65
2.16	0.81
2.30	0.54
2.40	0.51
2.46	0.47
2.51	0.55
2.65	0.79
2.76	0.79
2.87	0.52
2.98	0.52
3.15	0.42
3.28	0.61
3.35	0.46
3.47	0.31
3.58	0.19
3.75	0.16
3.89	0.25
4.22	0.10
Average	0.41±0.23

10.3.2.2 Notch plus crack segmented using DVC

Based on the development of notch plus crack with increasing loading using max normal strain map, random y positions (*Figure 10.3.3*) were selected to calculate the length of notch plus crack between crack surfaces which is grown in z direction. The measured notch plus crack length at each Y position for notch plus cracks under different load states were listed in *Table 10.3.2*. The

resultant notch plus crack length for each crack under a certain load state was the averaged value of the measured lengths at different Y positions.

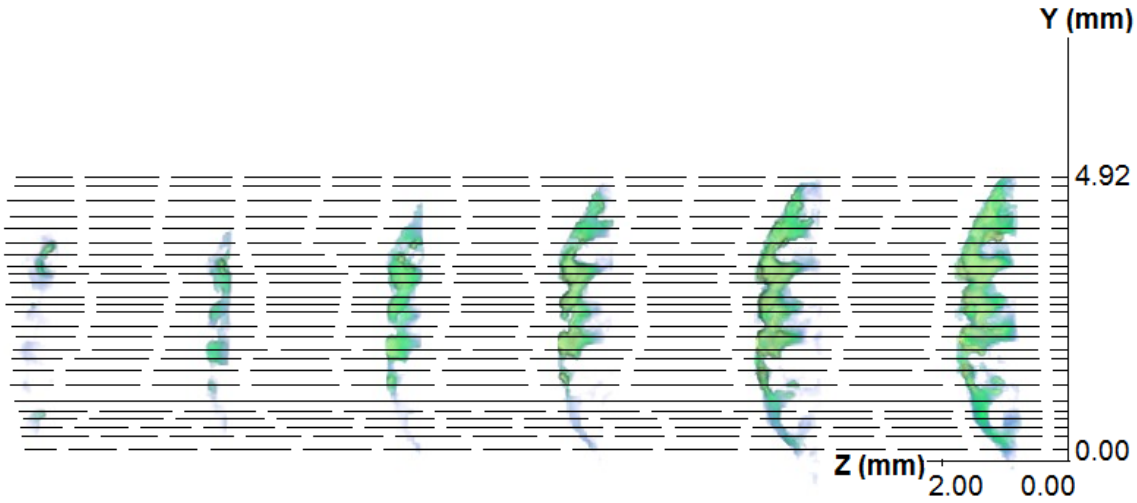


Figure 10.3.3. Randomly picked points in Y direction for the calculation of notch plus crack length, (segmented using DVC result: max. normal strain) in z direction.

Table 10.3.2. The measured notch plus crack lengths in different Y positions for notch plus cracks under different loading states.

Y position (mm)	Notch plus crack lengths (mm) at different loading states					
	35N	30N	25N	20N	15N	10N
0.00	0.11	--	--	--	--	--
0.21	0.28	0.15	0.14	0.07	--	--
0.31	0.42	0.35	0.14	0.06	--	--
0.47	0.51	0.44	0.16	0.12	0.07	0.07
0.72	0.56	0.35	0.21	0.12	0.07	0.14
0.91	0.62	0.29	0.16	0.12	--	0.14
1.01	0.34	0.34	0.23	0.12	0.07	--
1.21	0.76	0.47	0.05	0.17	0.12	0.10
1.50	0.28	0.22	0.10	0.09	--	--
1.70	0.21	0.15	0.14	0.09	0.12	0.09
1.84	0.42	0.35	0.35	0.35	0.32	0.11
2.09	1.02	0.77	0.76	0.55	0.06	--
2.31	0.95	0.77	0.23	0.15	0.22	--
2.67	0.76	0.48	0.44	0.44	0.32	0.18
2.87	0.76	0.71	0.58	0.29	0.24	0.18
3.10	0.73	0.44	0.29	0.29	0.12	--
3.18	0.51	0.50	0.36	0.55	0.29	0.29
3.35	0.84	0.59	0.59	0.55	0.30	0.30
3.55	1.05	0.96	0.84	0.29	0.29	0.09
3.75	1.07	0.36	0.36	0.26	0.07	0.07
4.04	0.36	0.32	0.28	0.36	0.12	0.10
4.24	0.91	0.66	0.55	0.28	--	--
4.38	0.74	0.55	0.24	0.12	--	--
4.60	0.51	0.29	0.26	--	--	--
4.84	0.34	0.16	0.06	--	--	--
4.92	0.21	--	--	--	--	--
Average	0.59±0.28	0.44±0.21	0.31±0.21	0.25±0.16	0.18±0.10	0.14±0.08

10.3.2.3 Notch plus crack segmented using phase congruency

Based on the information of crack geometry using 3D phase congruency code, the average value of notch plus crack length at each individual X position perpendicular to the crack growth direction in *Figure 10.3.4* has been calculated. The results are demonstrated in *Table 10.3.3*.

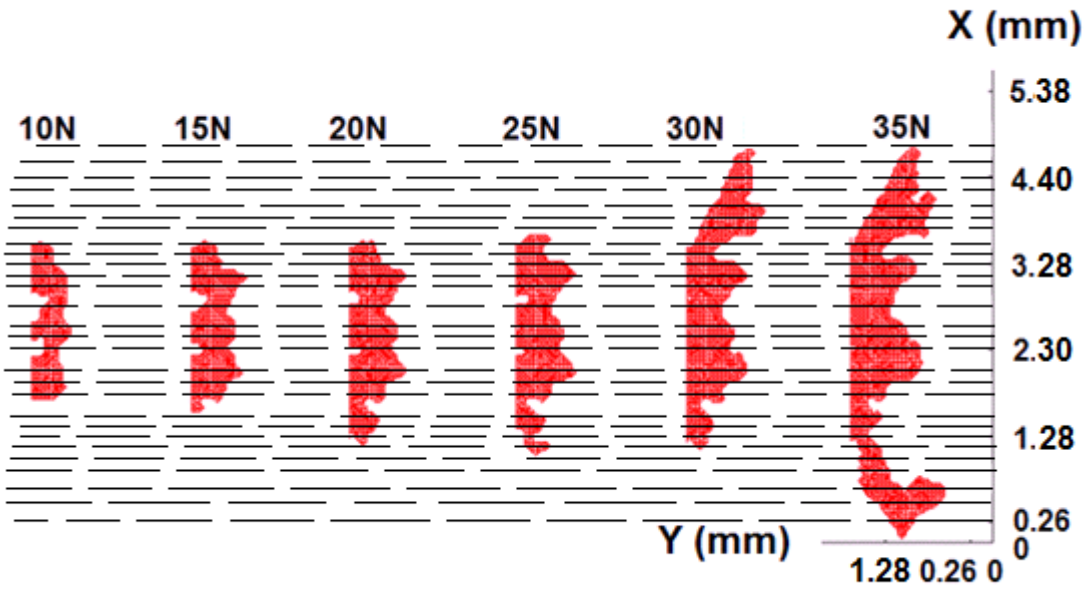


Figure 10.3.4. Randomly picked points in X direction for the calculation of notch plus crack length (segmented using phase congruency) in Y direction.

Table 10.3.3. The measured notch plus crack lengths in different X positions for notch plus cracks under different loading states.

X position (mm)	Notch plus crack lengths (mm) at different loading states					
	35N	30N	25N	20N	15N	10N
0	0.05	--	--	--	--	--
0.26	0.31	--	--	--	--	--
0.52	0.82	--	--	--	--	--
0.67	0.92	--	--	--	--	--
0.77	0.31	--	--	--	--	--
0.87	0.31	--	--	--	--	--
1.08	0.26	0.10	0.31	0.10	--	--
1.28	0.20	0.26	0.10	0.15	--	--
1.38	0.31	0.31	0.31	0.31	--	--
1.48	0.36	0.26	0.31	0.31	--	--
1.69	0.41	0.46	0.36	0.41	0.36	0.31
1.89	0.72	0.61	0.56	0.46	0.46	0.36
2.05	0.82	0.77	0.72	0.67	0.51	0.36
2.30	0.77	0.51	0.51	0.51	0.31	0.15
2.46	0.72	0.56	0.56	0.56	0.51	0.46
2.56	0.67	0.51	0.51	0.56	0.51	0.46
2.76	0.46	0.41	0.41	0.46	0.31	0.26
3.02	0.56	0.56	0.56	0.56	0.56	0.41
3.17	0.77	0.72	0.72	0.67	0.61	0.41
3.28	0.77	0.56	0.56	0.51	0.36	0.26
3.38	0.52	0.31	0.31	0.31	0.31	0.26
3.53	0.41	0.36	0.36	0.20	0.15	0.20
3.74	0.82	0.67	--	--	--	--
3.94	0.72	0.61	--	--	--	--
4.10	0.67	0.56	--	--	--	--
4.25	0.41	0.36	--	--	--	--
4.40	0.31	0.31	--	--	--	--
4.61	0.26	0.15	--	--	--	--
4.77	0.05	--	--	--	--	--
Average	0.51±0.25	0.45±0.18	0.45±0.17	0.42±0.18	0.41±0.13	0.33±0.10

The error used for each measurement (*Table 10.3.1, Table 10.3.2* and *Table 10.3.3*) was the standard deviation of all length measurements at different positions. The big standard deviation present is believed to be the result of the complicated and non-uniformly developed crack front due to microstructure.

10.3.3 J integral calculation

10.3.3.1 Calculation of average J integral using plateau in *J* vs contour number curve

In J integral vs contour curve, data points in the plateau (marked within red square in *Figure 10.3.5*) are chosen for calculating average J integral under this particular loading.

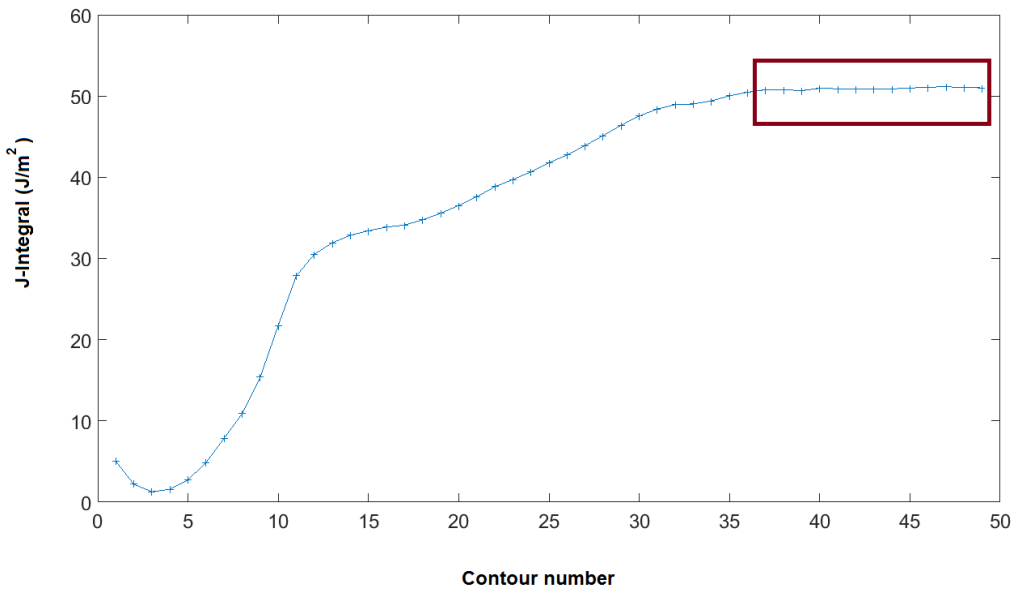


Figure 10.3.5. The obtained J-integral vs contour number curve for trabecular bone under a bending load of 35N with the plateau of the curve marked in red square.

10.3.3.2 Influence of contour selection on *J* calculation

The selection of contours for J integral calculation in JMAN can result in variations in converged J Integral calculation. Take specimen in nominal 35N as example, no converge has been achieved in J integral if the outer contour has been reduced in size with the same fixed inner contour as it is selected in *Figure 6.3.10* (e). However, with fixed outer contour (*Figure 6.3.10* (e)), the converged J integral values with different inner contours vary within an acceptable percentage

of 2%, which are shown in *Figure 10.3.6 together with result obtained from Figure 6.3.10* (e). Therefore the selection of inner counter has minor influence in calculated average J integral at plateau.

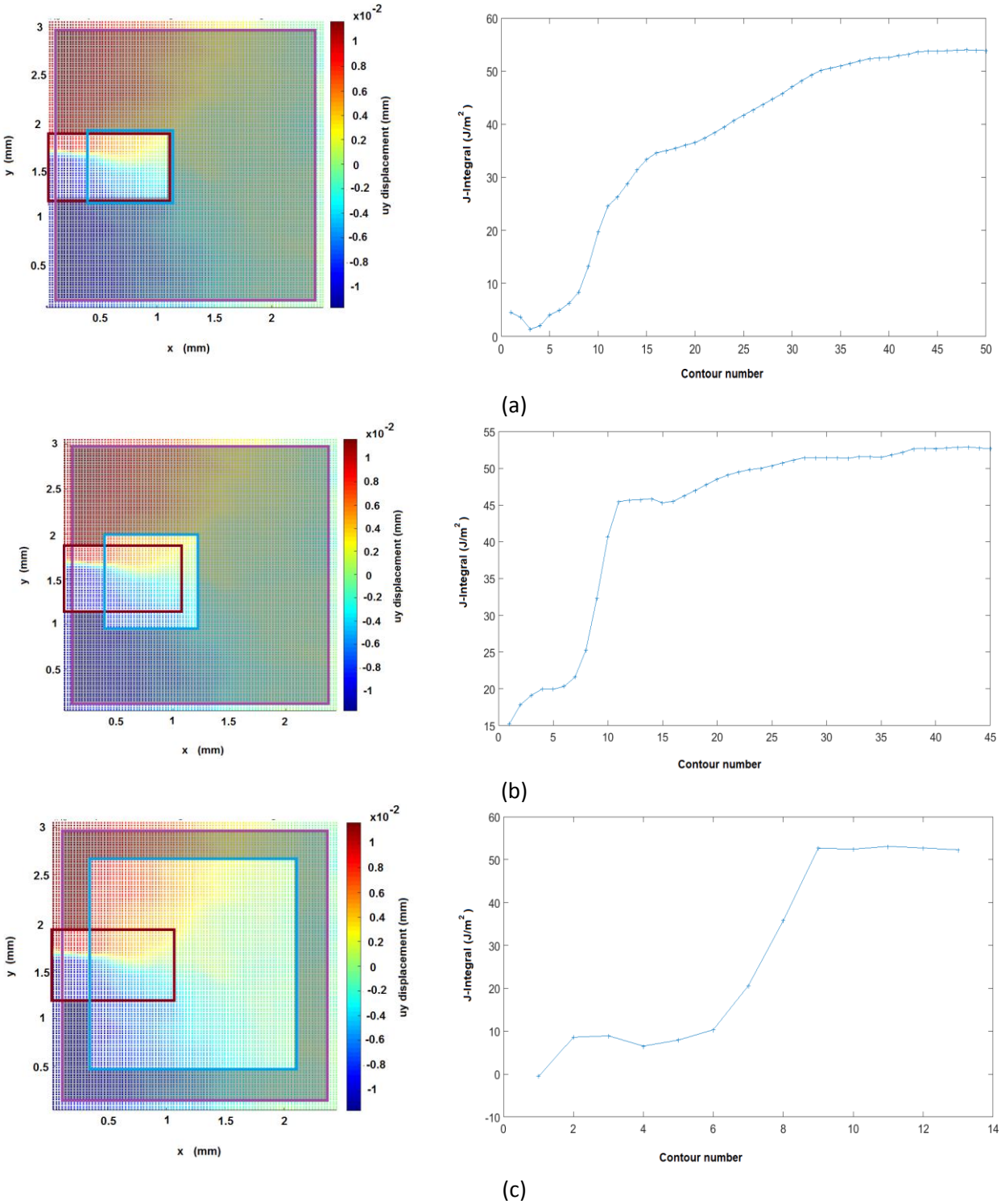


Figure 10.3.6. The computed curve and J integral vs contour number with different inner contour selections.(a) the calculated average J at plateau is 53.41±0.62 J/m²; (b) the calculated average J at plateau is 52.09±0.63 J/m²;(c) the calculated average J at plateau is 52.64±0.31 J/m².